Zusammenfassung der Arbeit

Nuclear Moments and Differences in Mean-Square Charge-Radii of Short-Lived Neon Isotopes by Collinear Laser Spectroscopy

Ziel dieser Arbeit war die Messung der Kernmomente und Kernladungsradien kurzlebiger Neonisotope mittels kollinearer Laserspektroskopie am Online-Massenseparator ISOLDE. Zur Einführung wird ein Überblick in die semiklassische Theorie der Atomspektren gegeben, und die relevanten Grössen werden für Neon berechnet. Der atomphysikalischen Theorie folgt die Beschreibung des experimentellen Aufbaus und der Methode der kollinearen Laserspektroskopie. ISOLDE stellt einen Ionenstrahl mit einer kinetischen Energie von 60 keV für Experimente zur Verfügung. Die Frequenz eines atomaren Übergangs ν_0 wird in kollinearer Laserspektroskopie durch die Doppler-verschobene Linienlage $\nu_D = \nu_0(1 \pm \beta)/\sqrt{1 - \beta^2} = \nu_L$ in Resonanz mit der Laserfrequenz ν_L bestimmt. Die Resonanzlage ist somit mit der Ionenstrahlenergie verknüpft. Die Bestimmung der Kernladungsradien erfolgt über die Messung des Feldeffekts der Isotopieverschiebung. Dieser Effekt wird mit sinkender Kernladungszahl Z kleiner, und verlangt für Neon nach einer neuen Methode zur Messung der Ionenstrahlenergie mit Hilfe des Dopplereffekts. Diese Methode wurde im Rahmen dieser Arbeit verwirklicht, sie ermöglicht eine Bestimmung der Strahlenergie mit einer Genauigkeit besser als 1 V. Nachfolgend werden die Ergebnisse der Messungen der Kernmomente und der Isotopeverschiebung in der Isotopenkette $^{17-26,28}$Ne zum Referenzisotop ^{20}Ne diskutiert. Die experimentelle Genauigkeit ermöglicht die Bestimmung des Feldeffektes der Isotopieverschiebung und der Differenzen der Kernladungsradien $\delta\langle r^2\rangle$. Die elektromagnetischen Kernmomente von ^{19}Ne, ^{21}Ne, ^{23}Ne und ^{25}Ne werden im Rahmen des Schalenmodells mit theoretischen Rechnungen für die sd-Schale verglichen. ^{17}Ne stellt eine Ausnahme unter den ungeraden Neon-Isotopen dar. Es handelt es sich ein einen p-Schalen-Kern und wird als Kandidat für einen Protonenhalo angesehen. Da keine Schalenmodelldaten zur Verfügung stehen, wird dessen magnetische Moment im Vergleich mit seinem Spiegelkern diskutiert. Die experimentellen Ergebnisse der Kernladungsradien von $^{18-26,28}$Ne werden mit verschiedenen theoretischen Modellen verglichen. Neben Daten aus der Literatur werden die Kernladungsradien mit Vorhersagen aus dem Droplet-Modell verglichen und zeigen überraschenderweise sehr gute Übereinstimmung mit diesem Modell. Der Kernladungsradius von ^{17}Ne wird wiederum separat diskutiert und theoretischen Rechnungen zur Halostruktur gegenübergestellt.

Thesis abstract

Nuclear Moments and Differences in Mean-Square Charge-Radii of Short-Lived Neon Isotopes by Collinear Laser Spectroscopy

The aim of this work was the measurement of nuclear moments and nuclear charge radii of short-lived neon isotopes by collinear laser spectroscopy at the online mass separator ISOLDE. As introduction an overview of the semiclassical theory of the atomic spectra is given and the important properties of neon are calculated. The atomic physics theory is followed by the description of the experimental setup and the description of the method of collinear laser spectroscopy. The ISOLDE online mass separator delivers an ion beam of a kinetic energy of about 60 keV. The frequency of the atomic transition ν_0 is determined in collinear laser spectroscopy by the Doppler shifted line position $\nu_D = \nu_0(1 \pm \beta)/\sqrt{1-\beta^2} = \nu_L$ in resonance with the laser frequency ν_L. Thus, the exact resonance position is connected to the ion beam energy. To measure the nuclear charge radii the isotopic field effect has to be determined from the isotope shift. This effect decreases with decreasing nuclear charge Z and required a new method to determine the ion beam energy with high precision by the help of the collinear laser spectroscopy. This method was realized within the framework of this work. This method gives the ion beam energy with an accuracy of better then 1 V. The description of the beam energy measurement method is followed by the discussion of the results of the experiments on the short-lived neon isotopes. Those yielded the nuclear moments of the odd-A isotopes and the isotopes shifts in the extended isotope chain $^{17-26,28}$Ne with respect to the reference isotope ^{20}Ne. The experimental precision enabled the determination of the field effect $\delta\nu_{FS}$ and the differences in the ms charge radii $\delta\langle r^2 \rangle$. The electromagnetic nuclear moments of ^{19}Ne, ^{21}Ne, ^{23}Ne and ^{25}Ne are discussed in the framework of the nuclear shell model and compared with theoretical calculations for the sd-shell. ^{17}Ne is an exception among the odd-A isotopes. It has a hole in the neutron p-shell and is judged as proton halo candidate. Because there were no shell model calculations for this nucleus available its magnetic moment is discussed in comparison with its mirror nucleus ^{17}N. The experimental results of the nuclear charge radii of $^{18-26,28}$Ne are compared to several collective models. Besides data published in the literature the nuclear charge radii are compared with predictions given by the droplet model. Very surprising the droplet model gives very good agreement with the experimental data. The nuclear charge radius of ^{17}Ne is again discussed separately and is compared with theoretical calculations using halo models.

Nuclear Moments and Differences in Mean Square Charge Radii of Short-Lived Neon Isotopes by Collinear Laser Spectroscopy

Am Fachbereich Physik
der Johannes Gutenberg-Universität in Mainz
Ralf Wolfgang Geithner
geboren in Mainz

Mündliche Doktorprüfung abgelegt am: 21.08.2002

For my dear parents
Renate & Karlheinz Geithner
and my grandmother
Maria Carolina Alma Geithner

"Wolfgang -
when they will be finished with you
you'll be a physicist
- and you'll even like it!"

Günther Sikler in the CERN cafeteria summer 1999

Table of Contents

List of Figures

List of Tables

List of Abbreviations

ISOLDE.............	Isotope Separation On-Line DEvice
CERN..............	Conseil Européen pour la Recherche Nucléaire
HFS................	HyperFine Structure
FS	Fine Structure
ABMR.............	Atomic Beam Magnetic Resonance
IS	Isotope Shift
MS.................	Mass Shift
FS	Field Shift
NMS...............	Normal Mass Shift
SMS................	Specific Mass Shift
ISOLDE.............	Isotope Separation On-Line DEvice
PS	Proton Synchrotron
CEC	Charge-Exchange Cell
SEM	Secondary Electron Multiplier
MCP	Measurement and Control Programme
DAC	Digital to Analog Converter
CWP...............	Chung Wildenthal Particle - interaction
CWH...............	Chung Wildenthal Hole - interaction
W-interaction	Wildenthal - interaction
USD-interaction	Universal SD - interaction
TBME	Two Body Matrix Elements
ALS................	Antisymmetric spin-orbit (LS)
OBEP..............	One-Boson Exchange Potential
WSE...............	Wood Saxon Energy-dependent
MEC...............	Meson Exchange Current
LDM...............	Liquid Drop Model
DM	Droplet Model
FRDM	Finite Range Droplet Model
BCS................	Bardeen Cooper Schrieffer
HF	Hartree-Fock
HFBCS.............	Hartree-Fock Bardeen Cooper Schrieffer
RMF	Relativistic Mean-Field
DHF	Deformed Hartree-Fock
GCM...............	Generator Coordinate Model

Chapter 1

Introduction

About 25 years ago the possibilities and advantages of using collinear laser fast beam spectroscopy for the investigation of unstable isotopes were realized [Ott77, Neu77]. Since then this method has become a prolific source of information on electromagnetic ground state properties of nuclei far from stability [Neu88]. The method is especially suited for on-line experiments with mass-separated beams of many chemical elements and nuclei. The collinear geometry involves narrow linewidths which are due to a compression of the spread of longitudinal velocity components occurring by the acceleration of ions from an ion source [Duf76, Win76, Ant78]. This compression reduces the residual longitudinal Doppler linewidth by several orders of magnitude compared to the thermal Doppler linewidth. Thus, it is possible to study nuclear properties reflected in the atomic spectra by measuring the hyperfine structure and isotope shift with high resolution.

The Mainz-ISOLDE collinear laser spectroscopy group has a long tradition of experiments at the on-line mass separator ISOLDE at CERN, Geneva (see e.g. [Neu81]). Over about 20 years the technique was improved in detection efficiency and resolution, which made it possible to explore large regions of the nuclear chart. The most important developments were two non-optical detection techniques – the detection of optical resonances by state selective collisional ionization and the use of β-NMR techniques in combination with optically polarized beams.

In recent years the experimental investigation of the light mass region of the nuclear chart was in the focus of interest. The experiments were concentrated on nuclei in the p and sd shells, namely on argon isotopes [Kle96], which were investigated by collinear laser spectroscopy with state selective collisional ionization detection. Furthermore the magnetic and quadrupole moment of ^{11}Li [Arn87, Arn92, Arn94], the quadruple moments of sodium isotopes [Kei00], and the magnetic moment of the one-neutron halo nucleus ^{11}Be [Gei00] were investigated by the use of β-NMR. So far sodium has been the lightest element for which laser spectroscopy methods were applied successfully to short-lived isotopes by the Orsay laser spectroscopy group [Hub78] for the study of nuclear charge radii from the isotope shifts.

1.1   Theoretical Background

The topic of this thesis is the study of neon isotopes in the mass region of $17 \leq A \leq 30$. The interest in the low-A region of the nuclear chart was mainly initiated by the progress

of nuclear theory, especially of the nuclear shell model in the last 20 years (see e.g. [Bro88b, Bro98a, Bro98b, Bro01a]). The shell model enabled a coherent description of the nuclei up to the sd shell ($Z, N \leq 20$) [Bro88a], and partly in the fp shell ($20 \leq Z, N \leq 40$) [Ric91] by the use of semi-empirical interactions. This model was able to explain interesting phenomena in the sd shell. As an example may be mentioned the experimentally observed breakdown of the $N = 20$ shell closure in the region of magnesium and sodium [Thi75, Det79, Gui84], the so-called "island of inversion". The masses and energy levels of nuclei in this region clearly show deformation phenomena. This could be explained by the intrusion of an fp-shell state ($2p - 2h$ states across the shell gap), which leads to a quenching of the spherical $0^+ - 2^+$ energy gap, and thus deforms the nuclear system. Predictions for neon isotopes show similar effects near $N = 20$ [Pov94, Cau98, Cau01]. γ-ray studies in this region [Pri99] indicate an onset of this intrusion mechanism already for ^{28}Ne which is expected to be within the range of the laser spectroscopy experiments.

The framework of the shell model is also used to investigate the occurrence of a new magic number $N = 16$ for drip-line nuclei around ^{24}O. This discussion came up from experiments at RIKEN [Oza00, Tan01] that revealed a kink in neutron separation energy S_n and in the interaction cross sections σ_I for nitrogen, oxygen, and fluorine. The neon isotopes do not show such a behavior, thus apparently being outside the region of this new magic number. Nevertheless, it is interesting to study the properties of ^{26}Ne with this discussion in mind.

The shell model describes the single-particle properties of exotic nuclei. Global properties can be modelled by microscopic theories which are based on relativistic mean field and Hartree-Fock methods [Lal99, Sii99, Gor01] using an effective nucleon-nucleon force. These methods are especially suited for the calculation of collective properties of nuclei like deformation and nuclear charge radii. Laser spectroscopy data to be compared to these theoretical predictions include the quadrupole moments and the isotope shifts.

A fascinating aspect of studying the neutron deficient neon isotopes is connected to the fact that the proton drip line with the lightest bound isotope ^{17}Ne can be reached experimentally. What "exotic" behavior can be expected for these proton drip-line nuclei? As the weakly bound outermost valence nucleons move in a shallow nuclear potential their wave function can spread out far beyond the core, a phenomenon which is widely known as "nuclear halo" (see e.g. [Fed93, Jen01]). The prime example of a neutron-halo nucleus is ^{11}Li (see e.g. [Han87, Zhu93]) where the halo is formed by a neutron pair outside the ^{9}Li core. The typical example for a one-neutron halo nucleus is ^{11}Be [Tan90, Fuk91] where the halo neutron is in a $2s_{1/2}$ state. The pairing force plays an important role in three-body halo systems, leading to a "Borromean" structure, where the subsystems are unstable if one of the constituents is removed (see e.g. [Jon01]).

Neutron-halo systems are nowadays well established. However, it is an open question whether similar phenomena exist for the weakly bound protons of very proton-rich systems, and if so, which nuclei are likely to develop a proton halo [Jon01]. Due to the proton charge the Coulomb barrier of the nucleus plays an important role in the possible formation of proton-halo systems, probably preventing the occurrence of proton halos for $Z > 10$ [Jon01]. The discussion on halo properties of ^{17}Ne goes back to a measurement of interaction cross sections of high energy radioactive beams with different targets [Oza94]. The low two-proton

separation energy of $S_{2p} = 0.96$ MeV identifies ^{17}Ne as a halo candidate. The authors conclude from their cross-section measurements that ^{17}Ne has a two-proton halo structure. Some theoretical studies support this conclusion [Zhu95, Kit97], interpreting the enhanced interaction cross section as an indication for an s-wave proton halo.

Nevertheless, the discussion of the ^{17}Ne case is not unidirectional. Hansen *et al.* [Han95] give a handy condition for the occurrence of s-wave halos. The binding energy has to fulfill the condition

$$S_{2p} \cdot A^{2/3} < 2 - 4 \text{ MeV} \tag{1.1}$$

which is not the case for ^{17}Ne, where $S_{2p} \cdot A^{2/3} = 6.2$ MeV. As well other theoretical calculations [Tim96, For01] disagree with the picture of a halo-like structure of ^{17}Ne. They predict a dominance of $(\pi d_{5/2})^2$ in the wave function of the weakly bound proton pair, whereas a halo requires $(\pi s_{1/2})^2$. The observables laser spectroscopy is able to provide – the magnetic moment and the mean square charge radius with respect to other isotopes – should both be sensitive to proton-halo properties, and should thus give valuable information on the puzzling structure of ^{17}Ne.

1.2   Key Aspects of This Work

The task of this work was to measure the isotope shift and the hyperfine structure of a suitable atomic transition along the neon isotope chain. Some properties of neon isotopes in the region of interest are collected in table 1.1. Collinear laser spectroscopy experiments on neon, aiming at a resolution of the effects of differences in mean square nuclear charge radii $\delta\langle r^2 \rangle$ in the isotope shift and at measuring hyperfine structure splittings, involve several experimental challenges. First to mention is the precision needed in the measurement of the isotope shift $\delta\nu_{IS}$. This quantity is connected to differences in the mean square nuclear charge radii by

$$
\begin{aligned}
\delta\nu_{IS}^{A,A'} &= \delta\nu_{MS}^{A,A'} + \delta\nu_{FS}^{A,A'} \\
&= \delta\nu_{MS}^{A,A'} + F_{el} \times \delta\langle r^2 \rangle^{A,A'} \, ,
\end{aligned}
$$

where the first term is the so-called "mass shift" $\delta\nu_{MS}$ and the second the "field shift" $\delta\nu_{FS}$. The field shift increases with the nuclear charge Z, whereas the mass shift decreases. The order of magnitude of the field shift can be estimated [Kle95]. For neon, for transitions from the metastable $[2p^5\,(^2P_{3/2}^0)\,3s]_2$ state, one obtains $\delta\nu_{FS}^{A,A+1} \approx 10$ MHz in a total isotope shift of about $\delta\nu_{IS}^{A,A+1} \approx 800$ MHz between two adjacent isotopes. At ISOLDE the ions are accelerated to a kinetic energy of 60 keV. The corresponding beam velocity causes a Doppler shift of the transition frequency, which is a function of the acceleration voltage and of the atomic mass of the isotope. The magnitude of the Doppler shift between neon isotopes of different mass is of the order of 30 GHz/u. This Doppler shift has to be measured with an accuracy of well below 3×10^{-4} to resolve $\delta\nu_{FS}$. In earlier works the uncertainty of the ion beam energy was conservatively estimated to about 30 eV if plasma ion sources were used, which is the case for noble gases (see e.g. [Kei95, Kle96]). Hence, one goal of this work was to limit the uncertainty of the ion-beam energy to less than 3×10^{-5}, corresponding to 2 V.

Table 1.1: *Ground state properties of the known neon isotopes. The fields marked with a "?" show unknown properties. The beam intensities were measured using the β-detection used in the collinear laser spectroscopy experiments, and are not corrected for beam transport losses and detection efficiency.*

A	mass [u]	spin	$T_{1/2}$	μ_I [μ_N]	Q_s [mb]	beam int. per proton pulse
17	17.017698(54)	1/2	109.2 ms	?		3.6×10^3
18	18.005697(2)	0	1.67 s			2.5×10^5
19	19.001879839(641)	1/2	17.34 s	-1.88542(8)		2×10^6
20	19.992440176(2)	0	stable			
21	20.993846744(43)	3/2	stable	-0.661797(5)	+103(8)	
22	21.991385510(232)	0	stable			
23	22.994467337(265)	5/2	37.24 s	-1.08(1)	?	3×10^6
24	23.993615(11)	0	3.38 min			3.5×10^5
25	24.99779(5)	1/2,3/2	602 ms	?	?	7×10^4
26	26.00046(6)	0	197 ms			3.2×10^4
27	27.0076(1)	?	32 ms	?	?	100
28	28.0121(1)	0	17 ms			50
29	29.0193(3)	?	200(100) ms	?	?	?
30	30.0239(9)	0	?			?

Thus, the problem to be solved was to develop a method to measure the beam energy with the desired accuracy, which is not possible with standard voltage measuring equipment.

Low production yields of isotopes far from stability are the second challenge envisaged. Especially the heavy isotopes with very short half-lives are obtained with extremely small yields from the ISOLDE target (see Tab. 1.1). To be able to extend the measurements as far as possible from the valley of stability, new limits of sensitivity and selectivity of detection were required.

The experimental technique used for the measurements on neon is the highly sensitive non-optical detection technique based on state-selective collisional ionization and ion counting. A change of the atomic state is achieved by optically pumping the atoms from the excited metastable to the ground state. The technique and the setup were developed before for measurements on short-lived xenon, krypton and argon isotopes [Neu86, Bor89b, Lie96, Kle96]. The detection of the ions produced by collisional ionization experienced several improvements to increase the sensitivity. The main limitation of this method is given by isobaric beam contaminations which give a background in the ion count rate. The most recent detection setup uses β-particle counting for the radioactive isotopes, thus suppressing all stable and long-lived contaminants [Kle96]. On the experimental foundation of the predecessor works this scheme had to be improved for the experiments on neon. For example an earlier limitation was due to non-statistical intensity fluctuations of the primary ion beam from the mass separator. By measuring the primary beam intensity it becomes possible to normalize the ion signal.

1.3   Structure of the Thesis

This thesis consists of in three major parts. Chapters 1-4 are devoted to the details of the experiment, and special attention is given to a new method to calibrate the beam energy. In chapter 5 the analysis of the experimental data and the extraction of the important nuclear physics observables is presented. Finally in chapter 6 and 7 the experimental results are interpreted in the framework of nuclear model and compared with the predictions and results of advanced microscopic calculations.

Chapter 2

Nuclear Properties from Atomic Spectra

The aim of this work was to investigate the nuclear ground state properties unstable neon isotopes. Collinear laser spectroscopy gives access to atomic spectral lines, specifically the hyperfine structure and the isotope shift. From these quantities the nuclear parameters have to be deduced.

The hyperfine structure is caused by the electromagnetic interaction of the electrons with the multipole moments of the nucleus and scales with the hyperfine-structure parameters A and B, which are proportional to the nuclear magnetic dipole moment and the nuclear electric quadrupole moment respectively. The isotope shift is due to the finite mass and the finite size of the nucleus. The part of the isotope shift which is related to the finite size of the nucleus, the so-called field shift, is proportional to the difference between the mean square charge radii $(\delta\langle r^2 \rangle)$ between two isotopes. This chapter is devoted to the theoretical description of these nucleus-electron interactions.

2.1   The Hyperfine Structure

In an atom with an ideal point-like nucleus the coulomb potential caused by the central charge has spherical symmetry. The fine-structure terms produced by LS-coupling are degenerate with respect to the total angular momentum $\boldsymbol{F} = \boldsymbol{I} + \boldsymbol{J}$ in this idealized picture. The interaction between the electromagnetic multipole moments of the nucleus and the electron shell breaks up this degeneracy. For atoms with nuclear spin $I \geq 1/2$ and fine-structure levels with angular momentum $J \geq 1/2$ this gives rise to new levels with small energy splittings, known as the hyperfine structure (HFS).

The hyperfine interaction can be described as a perturbation which is expanded in a series of multipole terms [Sch55], where the first two terms are relevant for optical spectroscopy. The first term represents the interaction of the nuclear magnetic moment μ_I with the magnetic field generated by the electrons at the site of the nucleus, $\langle H_0 \rangle = \langle JJ|\hat{H}(0)|JJ \rangle$. The second term of the expansion is due to the interaction of the nuclear spectroscopic quadrupole moment Q_s with the electric field gradient generated by the electrons at the site of the nucleus, $\langle V_{zz}(0) \rangle = \langle JJ|\hat{V}_{zz}(0)|JJ \rangle$. This quadrupole interaction only exists for nuclei with spin $I \geq 1$ and for fine structure (FS) levels with $J \geq 1$.

In first order the energy shift for an atomic level can be written as (see e.g. [Bra83], p.245)

$$\Delta E_{HFS} = \frac{A}{2}\, K + \frac{B}{4} \times \frac{\frac{3}{2}K(K+1) - 2I(I+1)J(J+1)}{I(2I-1)J(2J-1)} \; , \qquad (2.1)$$

where $K = F(F+1) - J(J+1) - I(I+1)$. In this equation the parameter A is related to the magnetic dipole interaction, the parameter B to the electric quadrupole interaction.

2.1.1 HFS Parameters of Two-Electron Configurations

In the simplest case of an atomic configuration only a single valence electron contributes to the hyperfine interaction. The neon ground-state configuration consists of a closed p shell. The transition under investigation takes place between two excited states of a single valence electron above a core configuration having one hole in the p shell. In the hyperfine interaction this hole behaves like a second valence electron and has to be taken into account in the description of the hyperfine structure. An approach to describe the hyperfine structure of two-electron configurations was formulated by Breit and Wills [Bre33].

General Considerations

In the central-field approximation of multi-electron atoms only electrons outside closed electron shells contribute to the hyperfine splitting. Electrons in closed shells couple to a "core" of angular momentum $J = 0$, and don't contribute to the multipole interaction of order $k \geq 1$.

For excited states of neon a one-electron configuration in the valence shell with a hole in the p-shell core has to be considered. To generalize, consider an electron carrying an angular momentum ℓ is missing in the shell. With respect to the magnetic dipole interaction this configuration behaves like a valence electron having the same angular momentum ℓ. For electrons in states with higher angular momentum (p, d, ...) the single electron a-factor becomes

$$a_{n\ell j} = a_{\ell \pm 1/2} = hcR_\infty \alpha^2 a_0^3 \frac{\ell(\ell+1)}{j(j+1)} \langle r^{-3} \rangle_{n\ell}\, F_r(j, Z_i)(1 - \varepsilon_{BR})(1 - \varepsilon_{BW})\frac{\mu_I}{I\,\mu_B} \; , \qquad (2.2)$$

where $(1 - \varepsilon_{BW})$ accounts for the Bohr-Weisskopf effect, and $(1 - \varepsilon_{BR})$ is the Breit-Rosenthal [Ros32]/Crawford-Schawlow [Cra49] correction.

Additionally the transition in neon under investigation involves a valence electron in the $3s$ state. The non-relativistic A-factor of a valence s-electron (hole) is given by (see e.g. Kopfermann [Kop58], p.131)

$$a_{ns} = \frac{8\pi}{3}\, h\, cR_\infty \alpha^2 a_0^3\, |\Psi(0)|^2_{ns}\, F_r(j, Z_i)(1 - \varepsilon_{BR})(1 - \varepsilon_{BW})\frac{\mu_I}{I\,\mu_B} \; . \qquad (2.3)$$

$|\Psi(0)|^2_{ns}$ is the probability density of the s-electron at the nucleus, R_∞ is the Rydberg constant in cm^{-1}, a_0 is the Bohr radius, μ_B the Bohr magneton and α is the fine-structure constant, given by [Moh98]

$$\alpha^{-1} = 137.03599976(50) \; .$$

Z_i denotes the effective nuclear charge seen by the valence electron of a multi-electron atom, when it is found inside the core of the other electrons. From empirical information usually $Z_i = Z$ for s-electrons and $Z_i = Z - 4$ for p-electrons is used.

$\langle r^{-3} \rangle_{n\ell}$ is the radial integral of an electron with $\ell > 0$, which will be discussed below. Bohr and Weisskopf [Boh50] point out, that the correction ε_{BW} can be approximated by:

$$\varepsilon_{BW} \approx \frac{Z\, r_0}{a_0} \times \left(\frac{a_0}{2Zr_0} \right)^{2(1-\sigma)} \left\langle \frac{r^2}{r_0^2} \right\rangle . \tag{2.4}$$

If a magnetization distributed uniformly over the nucleus is assumed, the expectation value becomes $\langle r^2/r_0^2 \rangle = 3/5$ [Kop58]. With this assumption the magnitude of the Bohr-Weisskopf effect for neon is found to be

$$\varepsilon_{BW} \approx 1.4 \times 10^{-4} , \tag{2.5}$$

which is substantially below the experimental resolution.

ε_{BR} can be approximated by ([Kop58], p.129)

$$\varepsilon_{BR} \approx \frac{2(1-\sigma)\sigma(2\sigma+1)}{(2\sigma-1)\Gamma^2(2\sigma+1)} \left(\frac{2Z\, r_0}{a_0} \right)^{2(\sigma-1)} . \tag{2.6}$$

ε_{BR} can be estimated to be smaller than 2×10^{-3} [Kin84] and isotopic changes of ϵ_{BR} are much smaller. Hence, both corrections can be neglected in the present case.

2.1.2 Determination of the Radial Integral

The problem of determining the nuclear magnetic moment and the nuclear quadrupole moment from the hyperfine structure of electrons with $\ell \geq 1$ boils down to the determination of the radial integral $\langle r^{-3} \rangle$ in equation (2.2). There are two commonly used empirical methods to determine this integral. Either it is calculated from the fine-structure energy-splitting, or from the hyperfine structure with the known magnetic moment.

Radial Integral from Fine-Structure Splitting

The radial integral can be estimated with the help of semi-empirical calculations from the fine-structure splitting ([Kop58], p.125ff)

$$\langle r^{-3} \rangle_{n\ell} = \frac{\delta\tilde{\nu}_{fs}}{a_0^3 R_\infty \alpha^2 \, (\ell + 1/2)\, Z_i H_r(\ell, Z_i)} . \tag{2.7}$$

The fine-structure splitting $\delta\tilde{\nu}_{fs}$ was obtained from the tables of Moore [Moo71], which are available as updated version on the internet [NIS99]:

$$\delta\tilde{\nu}_{fs} = \tilde{\nu}([2p^5\,(^2P_{1/2}^0)\,3s]_1) - \tilde{\nu}([2p^5\,(^2P_{3/2}^0)\,3s]_2) = 776.8 \text{ cm}^{-1} \tag{2.8}$$

$H_r(j, Z_i)$ belongs to a set of relativistic correction factors given by:

$$H_r(j, Z_i) = \frac{2\ell(\ell+1)}{\alpha^2 Z_i^2}(\sigma' - \sigma'' - 1) , \tag{2.9}$$

$$F_r(j, Z_i) = \frac{4j(j+1/2)(j+1)}{(\sigma(4\sigma^2-1))} , \tag{2.10}$$

$$R_r(j, z_i) = \frac{\ell(\ell+1)(2\ell+1)}{\sigma(\sigma^2-1)(4\sigma^2-1)}[3k(k+1) - \sigma^2 + 1] , \tag{2.11}$$

$$\text{where } k = \ell \pm 1 , \text{ for } j = \ell \pm 1/2 ,$$

$$G_r(\ell, Z_i) = \frac{2\ell(\ell+1)\sin[\pi(\sigma' - \sigma'' - 1)]}{\pi\alpha^2 Z_i^2} , \tag{2.12}$$

$$\text{with } \sigma = \sqrt{(j+1/2)^2 - Z_i^2\alpha^2} . \tag{2.13}$$

The expressions σ' and σ'' refer to the doublet term with $j = \ell + 1/2$ and $j = \ell - 1/2$, respectively. All the relativistic corrections are tabulated in Kopfermann ([Kop58] p.445, Tab. 8). In the case of neon, the effective charge $Z_i = Z - 4 = 6$ has to be taken. The relevant values are given in table 2.1

Table 2.1: *Relativistic correction factors for neon. Taken from ([Kop58], Tab. 8.).*

$F_r(j = 1/2)$	$F_r(j = 3/2)$	$H_r(\ell = 1)$	$G_r(\ell = 1)$	$R_r(\ell = 1, k = 2)$
1.0035	1.0008	1.0008	1.0008	1.0015

Radial Integral from HFS Data

Another approach uses hyperfine structure data to calculate the radial integral. $\langle r^{-3} \rangle$ can be determined using equation (2.2), with the well justified assumption $\varepsilon_{BW} = 0$, and $\varepsilon_{BR} = 0$. The radial integral can be calculated from

$$\langle r^{-3} \rangle_{n\ell} = a_{n\ell j} \, \frac{1}{R_\infty \, a_0^3 \, \alpha^2 \, h \, c} \, \frac{j(j+1)}{\ell(\ell+1)} \, \frac{I \, \mu_B}{\mu_I} \, \frac{1}{F_r(j, Z_i)} \; . \tag{2.14}$$

One difficulty encountered in this approach arises from the coupling of an electron in the 3s-state with a hole in the p shell, both contributing to the measured A-factor of neon. To investigate the radial integral $\langle r^{-3} \rangle$ one has to calculate the $a_{2p\,3/2}$ factor of the hole in the p shell from the A-factors of the electron-hole configuration. The single-electron contributions $a_{n\ell j}$ can be determined in the framework of the Breit-Wills theory in intermediate coupling [Bre33]. More recent formulations of this can be found in Kopfermann [Kop58], and in the publication of Kluge and Sauter [Klu74].

In the Breit-Wills theory, the hyperfine structure parameter A of a two-electron configuration splits up into contributions arising from the different electrons. With increasing nuclear charge Z the wave functions of the electrons change from the LS-coupling (Russel-Saunders-coupling) to the jj-coupling scheme which is encountered for heavy nuclei. In all practical cases, the coupling scheme is in between these extremes [Rac42], known as "intermediate coupling".

The wave functions in intermediate coupling have to be written as linear combinations of pure LS- or jj-functions, leading to a mixture of singlet and triplet states. The levels $^3L_{\ell\pm1}$ are independent of the coupling type of the electrons and the wave functions are equal to their LS/jj-counterparts:

$$\Psi(^3L_{\ell\pm1}) = \Psi_{LS}(^3L_{\ell\pm1}) = |(1/2, \ell \pm 1/2)_{\ell\pm1}\rangle \tag{2.15}$$

Where the index "$_{LS}$" is used for LS-coupling wave functions, the kets $|(j_1, j_2)_J\rangle$ represent pure jj functions. The states $^3L_\ell$ and $^1L_\ell$ have to be composed according to:

$$\begin{aligned} \Psi(^3L_\ell) &= c_1 \Psi_{LS}(^3L_\ell) \; + \; c_2 \Psi(^1L_\ell) \\ &= \alpha \, |(1/2, \ell + 1/2)_\ell\rangle + \beta |(1/2, \ell - 1/2)_\ell\rangle \end{aligned} \tag{2.16}$$

$$\begin{aligned} \Psi(^1L_\ell) &= -c_2 \Psi_{LS}(^3L_\ell) \; + \; c_1 \Psi(^1L_\ell) \\ &= \beta |(1/2, \ell + 1/2)_\ell\rangle - \alpha |(1/2, \ell - 1/2)_\ell\rangle \end{aligned} \tag{2.17}$$

The mixing coefficients c_1, c_2 can be expressed by simple trigonometric functions ([Kop58], p.151):

$$c_1 = \cos\theta_0 - \theta \qquad , \qquad c_2 = \sin\theta_0 - \theta \; . \tag{2.18}$$

The difference between the angles θ_0, and θ describes the deviation of the actual configuration from the pure Russel-Saunders case. θ_0 is given by

$$\sin\theta_0 = \sqrt{\frac{\ell}{2\ell + 1}} \; . \tag{2.19}$$
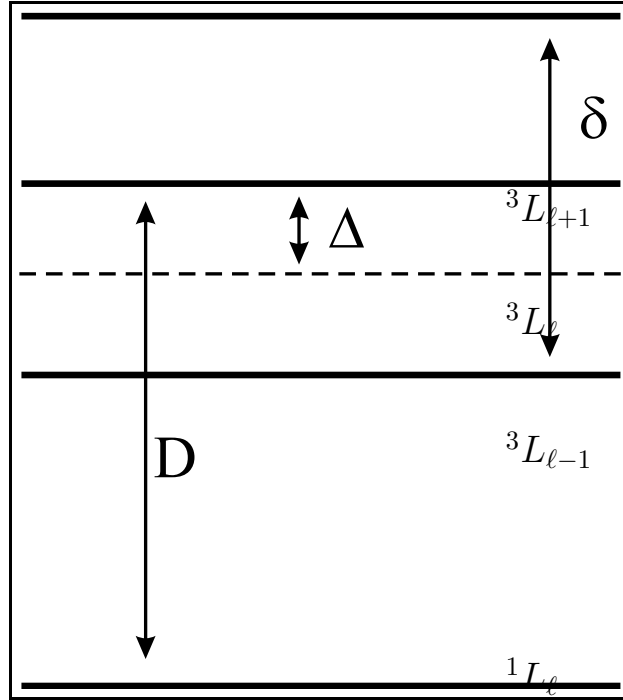
Fig. 2.1: *Illustration of the variables used to calculate the mixing angle. The thick lines represent the real level energies, the dashed line the energy in pure LS-coupling.*

The angle of intermediate coupling θ can be calculated from the level energies of the fine-structure [Wol32, Sem64], with the different quantities are displayed in figure 2.1:

$$\sin^2\theta \;\; = \;\; \frac{\Delta}{D} \, , \tag{2.20}$$

$$\text{where} \quad \Delta \;\; = \;\; \left| \frac{\ell}{2\ell+1}\left[E(^3L_{\ell+1} - E(^3L_{\ell-1})) \right] - \left[E(^3L_{\ell+1}) - E(^1L_\ell) \right] \right| \, , \tag{2.21}$$

$$\text{and} \quad D \;\; = \;\; \left| E(^1L_\ell) - E(^3L_\ell) \right| \tag{2.22}$$

In the case of neon, the four $2p^5\,3s$-levels [NIS99] have to be taken into account:

$$
\begin{aligned}
E(^3P_2) &= [2p^5\,(^2P^0_{3/2})\,3s]_2 = 134041.84 \;\text{cm}^{-1} \\
E(^3P_1) &= [2p^5\,(^2P^0_{3/2})\,3s]_1 = 134459.2871 \;\text{cm}^{-1} \\
E(^3P_0) &= [2p^5\,(^2P^0_{1/2})\,3s]_0 = 134818.6405 \;\text{cm}^{-1} \\
E(^1P_1) &= [2p^5\,(^2P^0_{1/2})\,3s]_1 = 135888.7173 \;\text{cm}^{-1}
\end{aligned}
$$

With these input data the difference in the angles becomes

$$\theta_0 - \theta = \Delta\theta = 29.54° \ . \tag{2.23}$$

From the Breit-Wills theory it is known that the $s\ell$-two-electron A-factors can be written in terms of the single-electron contributions of a two-electron $s\ell$ configuration ([Kop58], p. 152):

$$A(^3L_{\ell+1}) \quad = \quad \frac{a_s}{2(\ell+1)} + \frac{2\ell+1}{2(\ell+1)} \, a_{\ell+1/2} \tag{2.24}$$

$$A(^3L_\ell) \quad = \quad \frac{1}{2\ell(\ell+1)}\bigg\{ \Big[(\ell+1)c_2^2 - \ell c_1^2\Big] a_s + \ell(2\ell+3)c_1^2 \, a_{\ell+1/2}$$

$$+ \quad (2\ell-1)(\ell+1)c_2^2 \, a_{\ell-1/2} + 4c_1 c_2 \sqrt{\ell(\ell+1)}a_\ell'\bigg\} \tag{2.25}$$

$$A(^3L_{\ell-1}) \quad = \quad -\frac{a_s}{2\ell} + \frac{2\ell+1}{2\ell}a_{\ell-1/2} \tag{2.26}$$

$$A(^1L_\ell) \quad = \quad \frac{1}{2\ell(\ell+1)}\bigg\{ \Big[(\ell+1)c_1^2 - \ell c_2^2\Big] a_s + \ell(2\ell+3)c_2^2 \, a_{\ell+1/2}$$

$$+ \quad (2\ell-1)(\ell+1)c_1^2 \, a_{\ell-1/2} - 4c_1 c_2 \sqrt{\ell(\ell+1)} \, a_\ell'\bigg\} \tag{2.27}$$

Furthermore the factor $a_{\ell-1/2}$ can be expressed in terms of $a_{\ell+1/2}$ (use equation (2.2))

$$\frac{a_{\ell-1/2}}{a_{\ell+1/2}} \Rightarrow a_{\ell-1} = \frac{(\ell+3/2)}{(\ell-1/2)}\frac{F_r(1/2, Z_i)}{F_r(3/2, Z_i)} \, a_{\ell+1/2} \ . \tag{2.28}$$

The factor a_ℓ' stands for the short form of $a_{\ell+1/2, \ell-1/2}$ which can be expressed as well in terms of $a_{\ell+1/2}$ by using the relation

$$a_\ell' = \frac{a_0^3 \, R_\infty \, \alpha^2 \, h \, c}{2(2\ell+1)} \left\langle \frac{1}{r^3} \right\rangle G_r(l, Z)\frac{\mu_I}{I \, \mu_B} \ . \tag{2.29}$$

By expressing the radial integral $\langle r^{-3}\rangle$ with the help of equation (2.2) one obtains

$$a_\ell' = \frac{1}{2(2\ell+1)} \frac{(\ell+1/2)(\ell+3/2)}{\ell(\ell+1)} \frac{G_r(\ell, Z)}{F_r(3/2, Z_i)} \, a_{\ell+1/2} \tag{2.30}$$

Note that by the use of equations (2.28) and (2.30) the hyperfine structure can be described by the two parameters $a_{\ell+1/2}$ and $a_{\ell-1/2}$.

Finally, for the states under investigation the angular momentum is $\ell = 1$, and the Breit-Wills mixing angle as calculated above. The required relativistic corrections are listed in table 2.1. In the literature three A-factors of the $3s$-configurations of ^{21}Ne can be found. The nuclear g_I-factor of ^{21}Ne is known from La Tourrette [LT57]. A collection of HFS data is given Husson and Grandin [Hus78]. The data for the required states are:

$$[2p^5\,(^2P^0_{3/2})\,3s]_2: \quad A(^3P_2) \quad = \quad -267.68(3) \text{ MHz [Gro58]}$$

$$[2p^5\,(^2P^0_{3/2})\,3s]_1: \quad A(^3P_1) \quad = \quad -459.88(3.90) \text{ MHz [Del76]}$$

$$[2p^5\,(^2P^0_{1/2})\,3s]_1: \quad A(^1P_1) \quad = \quad -658 \text{ MHz (Delsart, Keller, priv. comm. in [Hus78])}$$

Using equations (2.24) to (2.29) and the input data from literature it is possible to calculate the single electron a-factor contributions and the radial integral.

For the analysis of the quadrupole moment the $a_{2p\,3/2}$-factors are of importance. Using the input data of the different A-factors, the single electron $a_{2p\,3/2}$-factors are obtained from solving the equations (2.24) to (2.29):

$$
\left.
\begin{array}{lll}
A(^3P_2),\ A(^3P_1): & a_{2p\,3/2} & = \quad -273.24 \text{ MHz} \\
A(^1P_1),\ A(^3P_1): & a_{2p\,3/2} & = \quad -276.19 \text{ MHz} \\
A(^3P_2),\ A(^1P_1): & a_{2p\,3/2} & = \quad -301.71 \text{ MHz}
\end{array}
\right\} \Rightarrow \overline{a}_{2p\,3/2} = -283(18) \text{ MHz} . \quad (2.31)
$$

The corresponding a_{3s}-factors, which can be used to determine the electronic factor of the field shift, are given by

$$
\left.
\begin{array}{lll}
A(^3P_2),\ A(^3P_1): & a_{3s} & = \quad -251.01 \text{ MHz} \\
A(^1P_1),\ A(^3P_1): & a_{3s} & = \quad -327.22 \text{ MHz} \\
A(^3P_2),\ A(^1P_1): & a_{3s} & = \quad -165.58 \text{ MHz}
\end{array}
\right\} \Rightarrow \overline{a}_{3s} = -248(82) \text{ MHz} . \quad (2.32)
$$

The errors given for $\overline{a}_{2p3/2}$ and for $\overline{a}_{3s}$ are the maximum difference between the mean and the three values determining the mean.

2.1.3   Evaluation of Magnetic Moments

In practice, the evaluation of magnetic moments from the measured hyperfine structures can be based on the independent knowledge of both properties for one stable isotope. As discussed in depth in the review of Büttgenbach [Büt84], the hyperfine structure constant A includes the expectation value of the product of the magnetic field produced by the electrons $\vec{H}(\vec{r})$ and the nuclear magnetization $\vec{\mu}(\vec{r})$:

$$
\begin{aligned}
A & = \frac{1}{IJ} \langle II | \vec{\mu}(\vec{r}) \cdot \vec{H}(\vec{r}) | II \rangle \\
& = \mu_I \times \frac{\langle H(0) \rangle}{IJ}
\end{aligned}
\quad (2.33)
$$

As long as the nucleus in this description can be assumed to be point-like, there are no isotopic effects included in the theory of the HFS. The magnetic field at the site of the nucleus $\langle H(0) \rangle$ is isotope independent, i.e. hyperfine anomalies are negligible (see Sec. 2.1.1). According to equation (2.33) the unknown nuclear magnetic moment of any isotope can be determined from the measured hyperfine structure by relating it to the known magnetic moment and the A-factor of another isotope of the same element:

$$
\mu_x = \mu_1 \frac{A_x I_x}{A_1 I_1}
\quad (2.34)
$$

The nuclear magnetic moment of ^{21}Ne was measured directly by La Tourrette $et\ al.$ [LT57] using the Atomic Beam Magnetic Resonance (ABMR) technique. The hyperfine parameters of the metastable lower $[2p^5\,(^2P^0_{3/2})\,3s]_2$ state of the optical transition used in our experiment have been measured with high precision by Grosof $et\ al.$ [Gro58]. The required parameters are given as:

μ_I	-0.661797(5) μ_N
$A_{[2p^5\,(^2P^0_{3/2})\,3s]_2}$	-267.68(3) MHz
$B_{[2p^5\,(^2P^0_{3/2})\,3s]_2}$	-111.55(10) MHz

2.1.4   B-factors and the Nuclear Electric Quadrupole Moment

The factor B in the hyperfine structure formula represents the quadrupole interaction ([Kop58], p.134)[1]

$$B \ = \ e\, Q'_s \times \langle V_{zz}(0) \rangle. \tag{2.35}$$

$$\ = \ \frac{e^2}{4\pi\varepsilon_0} Q'_s \frac{2j-1}{2j+2} \langle r^{-3} \rangle_{n\ell}\, R_r(\ell, j)\,. \tag{2.36}$$

As already mentioned, the B-factor of the hyperfine splitting is proportional to the expectation value of the electric field gradient at the nucleus produced by the electrons. This field gradient has to be calculated for the determination of the quadrupole moment. From equation (2.36) follows for an electron in an alkali-like one-electron state

$$\langle V_{zz}(0) \rangle = \frac{1}{4\pi\varepsilon_0}\, e\, \frac{2j-1}{2j+2} \langle 1/r^3 \rangle\, R_r(j, Z_i)\,, \tag{2.37}$$

where the relativistic factor $R_r(j, Z_i)$ is given by equation (2.11), and tabulated for neon in table 2.1. The expectation value of $\langle 1/r^3 \rangle$ was determined in the previous section.

$\langle \mathbf{r^{-3}} \rangle$ from the Fine-Structure

The lower state of the laser excitation in the experiments on neon is $[2p^5\,(^2P^0_{3/2})\,3s]_2$. For this state only the $^2P_{3/2}$-hole contributes to the quadrupole interaction, so the assumption for equation (2.37) still holds. Combining equations (2.7), (2.36), (2.37), (2.8), setting $j = 3/2$ and $\ell = 1$ leads to an expression for the (spectroscopic) quadrupole moment Q'_s:

$$Q'_s = \pm \frac{15}{2} \left(\frac{\mu_B}{ec} \right)^2 \frac{B}{\delta\tilde{\nu}_{fs}} \cdot \frac{Z_i\, H_r}{R_r} \tag{2.38}$$

Where the plus sign has to be taken for electrons, the minus for a hole in the $^2P_{3/2}$-state.

With the relativistic corrections which can be taken from (1) [Kop58], or in a graphical representation from (2) [Sch55] the quotient is found to be:

$$\frac{Z_i\, H_r}{R_r} \ = \ 5.99 \qquad (1)$$

$$\frac{Z_i\, H_r}{R_r} \ = \ 6.00 \qquad (2)$$

With the fine-structure splitting given in equation (2.8) the spectroscopic quadrupole moment can be calculated from the HFS-B-factor of the lower state of the laser-excitation:

$$Q'_s = -0.72\ \mathrm{mb/MHz} \times B_{[2p^5\,(^2P^0_{3/2})\,3s]_2}\,. \tag{2.39}$$

Using the B-factor published by Grosof *et al.* [Gro58] the uncorrected spectroscopic quadrupole moment of ^{21}Ne takes the value

$$Q'_s = 80.31(7)\ \mathrm{mb}\,. \tag{2.40}$$

The error containing only experimental uncertainties of the input parameters is mainly due to the B-factor. Empirical data indicate that the model uncertainties involved in the calculation of $\langle V_{zz}(0) \rangle$ are up to 20%.

---

1 The quadrupole moment calculated that way is valid for a spherical nucleus, and is represented by Q'_s. The effect of the deformed nucleus requires a correction, and the corresponding moment is indicated by Q_s (see below).

$\langle r^{-3} \rangle$ from the Hyperfine Structure

Using the radial integral (2.14) from the hyperfine-structure equation (2.36) for the B-factor offers an alternative equation to determine the spectroscopic quadrupole moment Q'_s. With the average $a_{2p\,3/2}$-factor given in equation (2.31) the proportionality between Q'_s and the B-factor is found to be

$$\overline{Q'_s} = -0.843(52) \text{ mb/MHz} \times B_{[2p^5\,(^2P^0_{3/2})\,3s]_2} \ . \tag{2.41}$$

Employing this and again the B-factor of Grosof $et\ al.$ [Gro58] one obtains the uncorrected spectroscopic quadrupole moment

$$Q'_s = 94.04(8)[5.8] \text{ mb} \ . \tag{2.42}$$

The error given in parentheses corresponds to the uncertainty of the B-factor and the maximum difference between the mean and the input data (2.31) contributes the error given in square brackets.

Polarization Corrections

Besides the radial integral $\langle r^{-3} \rangle$ and the relativistic corrections, the effect of the deformed nucleus on the core electrons has to be taken into account. This polarization effect is taken care of by the Sternheimer correction R [Ste51] which may result in a shielding or an anti-shielding of the nuclear quadrupole moment. The hyperfine structure of ^{21}Ne in the transitions $[^2P^0_{1/2}]_{J=1}\,4s \rightarrow [2p^5\,(^2P^0_{1/2})\,3p]_2 \rightarrow [2p^5\,(^2P^0_{3/2})\,3s]_1$ was investigated by Ducas using laser spectroscopy [Duc72]. The Sternheimer correction is included in the analysis of the quadrupole moment and is given in first order correction for ^{21}Ne by [Duc72]

$$R = 0.10(5) \ .$$

With this correction the quadrupole moment Q_s becomes

$$Q_s = Q'_s \times \frac{1}{1-R} \tag{2.44}$$

where Q'_s is the uncorrected quadrupole moment. Applying the Sternheimer correction to the quadrupole moments derived

$$\text{from fine structure:} \quad Q_s \quad = \quad Q'_s \times 1.11 = 89(5) \text{ mb} \tag{2.45}$$

$$\text{from HFS:} \quad Q_s \quad = \quad Q'_s \times 1.11 = 104(6)[6] \text{ mb} \tag{2.46}$$

The errors given in parentheses arise from the uncertainty in R, the error given in square brackets correspond to those given in equation (2.40) and (2.42).

These corrected values can be compared with the literature value of the spectroscopic quadrupole moment Q_s of ^{21}Ne measured by Ducas $et\ al.$ $Q_s = 102.9(7.5)$ mb [Duc72]. There the calculation of the radial integral $\langle r^{-3} \rangle$ follows the Breit-Wills approach based on data from the hyperfine structure, which was discussed in section 2.1.2. In contrast to the data presented in the present thesis, Ducas $et\ al.$ use more advanced wave-functions for the description of the jj-coupled states. The quadrupole moment $Q_s = 104(9)$ mb which was

calculated with the help of HFS data in the present work reproduces the reference value for the quadrupole moment of Ducas *et al.* [Duc72] very well. The present analysis in the framework of the Breit-Wills theory can thus be supported by the published data. For the further discussion the value of Ducas *et al.* [Duc72] will be used as reference value.

Neglecting model uncertainties, the spectroscopic quadrupole moment calculated from FS data does not agree with the published value within the error bars. The large deviation can be explained by the estimation of $\langle 1/r^3 \rangle$ with the help of semi-empirical methods. These are unreliable because of model simplifications like neglected spin-spin and spin-orbit terms.

With the known quadrupole moment of ^{21}Ne, the evaluation of Q_s from the B-factor essentially gives the electric field gradient at the site of the nucleus $\langle V_{zz}(0) \rangle$ which is isotope-independent. In other words the proportionality factor between Q_s and B is the same for all isotopes. The unknown quadrupole moment of an isotope is thus determined from the reference moment of ^{21}Ne by

$$Q_x = \frac{B_x}{B_{21}} \times Q_{21} \; . \tag{2.47}$$

This will be used to analyze the data of section 6.1.

Note that the quadrupole moment published by Ducas *et al.* [Duc72] was extracted by the semi-empirical method presented in the previous sections. Thus, it is sensitive to the model-uncertainties connected with this approach.

2.2   The Isotope Shift

The isotope shift (IS) arises from another correction to the basic atomic model and takes into account effects of the finite mass and size of the atomic nucleus. Reviews of the field can be found in the books of Kopfermann [Kop58], King [Kin84] and in the tables of Aufmuth, Heilig and Steudel [Auf87]. The isotope shift $\delta\nu^{A,A'} = \nu^A - \nu^{A'}$ between the transition frequencies of two isotopes of one element can be expressed by the sum:

$$\delta\nu_{IS}^{A,A'} = \delta\nu_{MS}^{A,A'} + \delta\nu_{FS}^{A,A'} = K_{MS} \times \frac{m_{A'} - m_A}{m_{A'} \, m_A} + F_{el} \times \delta\langle r^2 \rangle^{A,A'} \; . \tag{2.48}$$

The motion of the nuclei with masses m_A and $m_{A'}$ and the electrons around their common center of mass contributes the first part of the sum called mass shift (MS). The second part of the sum is the field shift (FS), which takes into account the finite size of the nuclear charge distribution.

2.2.1   Mass-Shift Effects

Since the relative mass-differences between the different isotopes is large for light elements ($Z \leq 20$), the mass shift dominates the isotope shift of light elements. For neon, the field shift contribution to the IS is of the order of 10 MHz. Compared to the mass shift of about 1 GHz between two neighboring isotopes, this 1% effect has been seen as "negligible" in the literature (see [Ami83, Ves85, Bas97]). Nevertheless, it was the aim of the present work to measure the isotope shift with high precision. Hence, the field shift, and the changes in mean square charge radii should be resolved. To extract the field shift, the exact knowledge of the mass shift is important. The mass shift term can be split up into two parts: the normal mass

shift (NMS) and specific mass shift (SMS) which have the same mass dependence. The first takes into account the effect of the reduced mass of the valence electron and the nucleus, the latter arises from the correlated movement of the electrons.

The theory of the mass shift can be found in the book of King [Kin84]. Summarizing, the normal mass shift constant K_{NMS} can be calculated by the relation

$$K_{NMS} = \nu_A \times m_e \ . \tag{2.49}$$

For the $2s^2\,[2p^5\,(^2P^0_{3/2})\,3s]_2 \rightarrow 2s^5\,[2p^5\,(^2P^0_{3/2})\,3p]_2$ transition in neon ($\tilde{\nu} = 16274.02$ cm^{-1}) this constant becomes

$$K_{NMS} = 267.644 \text{ GHz u} \ . \tag{2.50}$$

As will be shown in section 6.4.1 the normal mass shift in the quoted transition contributes only about two thirds of the total mass shift.

The specific mass shift is very sensitive to the correlation effects of electrons in the open shells. For a theoretical approach *ab initio* calculations are necessary (see e.g. [Ves85]). These calculations do by far not reach the precision needed for an exact determination of the effect in neon.

In an *ad hoc* approach the mass dependence of the mass shift $((m_{A'} - m_A)/(m_A m_{A'}))$ can be used to extract field effects. This function can to be fitted to the experimental isotope-shift data, and deviations can be ascribed to the field shift. Of course this approach neglects all field-shift contributions which have the same mass dependence as the mass shift. In a more elaborate way, using the so-called "King-Plot", K_{MS} is determined by combining absolute nuclear charge-radii measured by X-ray spectroscopy on muonic atoms with data from optical spectroscopy. This is presented in chapter 6.

2.2.2   Field Shift Effects

In the simplest model of the extended nucleus the nuclear charge density $\rho(r)$ is assumed to be constant over the nuclear charge radius

$$R = 1.2 \ A^{1/3} \text{ fm.} \tag{2.51}$$

A better approximation is used by Babushkin [Bab63], where the nuclear radius is given by

$$R = 1.115 \ A^{1/3} + 2.151 \ A^{-1/3} - 1.742 \ A^{-1} \ . \tag{2.52}$$

As a consequence of this finite nuclear size, the electrostatic potential generated by the nuclear charge deviates inside the nucleus from the Coulomb $-Ze/r$ dependence. Electrons with a non vanishing probability density inside the nucleus are sensitive to these deviations. The deviation from the Coulomb potential causes the field shift in the frequencies of atomic transitions depending on the size of the nucleus. This shift between two isotopes is given by the product

$$\delta\nu_{FS}^{A,A'} = F_{el} \times \delta\langle r^2 \rangle^{A,A'} \ . \tag{2.53}$$

This is a good approximation for light elements where contributions from higher order radial moments of the nuclear charge distribution can be neglected. In particular s-electrons have

high probability amplitudes inside the nucleus. p-states have small probability amplitudes, thus $s - p$ transitions are most suitable for the spectroscopic study of differences in nuclear mean square charge radii $\delta\langle r^2\rangle$.

2.2.3 Calculation of the Electronic Factor

For the calculation of $\delta\langle r^2\rangle^{A,A'}$ from experimental isotope-shift data, the electronic factor F_{el} has to be known. From perturbation theory the effect of the potential deviations on the transition frequency shift between two isotopes ([Kin84], p.35ff) can be calculated from

$$\delta\nu_{FS}^{A,A'} = \pi\beta|\Psi(0)|^2\frac{a_0^3}{Z}\zeta N\langle r^2\rangle^{(\sigma-1)}\delta\langle r^2\rangle^{A,A'} \; , \tag{2.54}$$

where ζ is given by

$$\zeta = R_\infty\left(\frac{2Z}{a_0}\right)^{2\sigma}\frac{1}{\Gamma^2(2\sigma)} \; , \tag{2.55}$$

and σ by equation (2.13), which for s-states becomes $\sigma = \sqrt{1 - \alpha^2 Z^2}$. The variable N is a function of the nuclear charge Z and the principal quantum number n:

$$N = \left(\frac{n+3}{n+1}\right)^\sigma\frac{1 + (1+\sigma)K/\alpha Z}{1 + (1-\sigma)K/\alpha Z} \; . \tag{2.56}$$

According to King ([Kin84], p.39) the parameter K is a function of n and Z, which for $n = 3$ takes the form

$$K = -\alpha Z\frac{7}{18}\left(1 + 0.097(\alpha Z)^2 + 0.014(\alpha Z)^4\right). \tag{2.57}$$

The quantity ζN is tabulated in the book of King ([Kin84], p.43, Tab. 4.3). For neon:

$$\zeta N = 164 \text{ MHz fm}^{-2\sigma} \; . \tag{2.58}$$

Of the nuclear properties the parameter $\langle r^2\rangle^{\sigma-1}$ is needed in the calculation of $\delta\nu_{FS}^{A,A'}$. King [Kin84] estimates $\langle r^2\rangle = 3R^2/5$, where for light nuclei the nuclear radius R is taken according to equation (2.52). The corresponding expression becomes

$$f(Z) := \zeta N\langle r^2\rangle^{(\sigma-1)} = 164.215 \text{ MHz fm}^{-2} \tag{2.59}$$

The values of $f(Z)$ for the different elements are as well tabulated in Aufmuth, Heilig, and Steudel [Auf87]. For neon

$$f(Z) = 5.455 \times 10^{-3} \text{ cm}^{-1} \text{ fm}^{-2} = 163.53 \text{ MHz fm}^{-2} \; , \tag{2.60}$$

which was used for the following analysis. With this abbreviation the shift reduces to the simple form:

$$\delta\nu^{A,A'} = \pi\beta|\Psi(0)|_{ns}^2\frac{a_0^3}{Z}f(Z)\delta\langle r^2\rangle^{A,A'} \; . \tag{2.61}$$

After calculating the dependence on several global nuclear parameters, the electron probability density at the nucleus still has to be determined.

Three approaches can be used to calculate the electron probability density at the site of the nucleus. Accurate and reliable *ab initio* calculations are available only for selected elements. Two different methods are based on empirical approaches – either the known hyperfine structure and the magnetic dipole moment is used to extract the desired probability density, or the ns level energies are related to the probability densities by the Goudsmith-Fermi-Segrè formula.

$|\Psi(0)|^2_{3s}$ from Energy Levels:

For the non-relativistic probability of finding an s-electron at the site of the nucleus a discussion is given in Kopfermann ([Kop58], p.123ff). It is shown that the probability can be related to quantities describing the energy levels by the well known Goudsmit-Fermi-Segré formula ([Fer33] and [Kop58], p.127)

$$|\Psi(0)|^2_{ns} = \frac{1}{\pi a_0^3} \frac{Z_i Z_a^2}{n_a^3} \left(1 - \left. \frac{d\xi}{dn} \right|_{n=3} \right) \tag{2.62}$$

For a 3s-electron in the electronic shell of neon, $Z_a = 1$ and $Z_i = 10$. The effective quantum numbers n_a are given by

$$n_a = \sqrt{\frac{R_\infty}{E'_{ns}}} \ . \tag{2.63}$$

These are tabulated in table 2.2 together with other relevant data needed for the calculation of $|\Psi(0)|^2_{ns}$. The level energies are taken from the NIST Atomic Spectra Data base [NIS99]. The energies E'_{ns} with respect to the ionization energy of 127110 cm^{-1} are used to calculate n_a. The quantities ξ are quantum defects defined by $\xi = n - n_a$.

Table 2.2: *Input data for the calculation of the electronic factor.*

Level	E_{ns} $[cm^{-1}]$	$E'_{ns} = E_i - E_{ns}$ $[cm^{-1}]$	n_a	$\xi(n, n_a)$
$[2p^5\,(^2P^0_{3/2})\,3s]_2$	134041.84	39887.76	1.65866	1.34134
$[2p^5\,(^2P^0_{3/2})\,4s]_2$	158601.12	1528.48	2.67564	1.32436
$[2p^5\,(^2P^0_{3/2})\,5s]_2$	165828.18	8101.43	3.68041	1.31959
$[2p^5\,(^2P^0_{3/2})\,6s]_2$	168924.65	5004.95	4.6825	1.3175
$[2p^5\,(^2P^0_{3/2})\,7s]_2$	170532.72	3396.88	5.68377	1.31623
$[2p^5\,(^2P^0_{3/2})\,8s]_2$	171473.31	2456.29	6.68402	1.31598
$[2p^5\,(^2P^0_{3/2})\,9s]_2$	172071.40	1858.20	7.68476	1.31524

For the calculation of $|\Psi(0)|^2$, $d\xi/dn$ is needed. This can be obtained by a procedure which again is described by Kopfermann ([Kop58], p.134). The dependence of the quantum defect from the principal quantum number n can be found by calculating

$$\frac{d\xi}{dn} = \frac{\dfrac{d\xi}{dE'_{ns}}}{\dfrac{d\xi}{dE'_{ns}} - \dfrac{n_a}{2E'_{ns}}} \ . \tag{2.64}$$

The derivative $d\xi/dE'_{ns}$ can be determined to good approximation by performing a linear fit to the data of $\xi(E'_{ns})$ for the terms $n = 3, ..., 9$, which yields $d\xi/dE'_{ns} = 6.8723(56) \times 10^{-7}$. One finds for the quantum defect of the 3s state

$$\left. \frac{d\xi}{dn} \right|_{n=3} = -0.03418(29) \ . \tag{2.65}$$

The shielding factor β in equation (2.61) can be chosen in analogy to the heavier noble gases to be $\beta = 1.1$. Finally the electronic factor becomes

$$F_{el} = \pi\beta|\Psi(0)|^2_{ns}\frac{a_0^3}{Z_i}f(Z) = -40(4) \text{ MHz/fm}^2 \ . \tag{2.66}$$

The error of F_{el} is estimated to about 10%, which can attributed to the uncertainty of the screening factor β and to model limitations. The error contribution of $\frac{d\xi}{dn}$ is of the order of 10^{-2} which is negligible.

$|\Psi(0)|^2_{3s}$ from Hyperfine-Structure Splittings:

Starting with equation (2.3), the electron density at the site of the nucleus can as well be determined from the a_{3s}-factor, given by equation (2.32). This factor was determined from HFS data of the stable odd-A neon isotope ^{21}Ne. From equation (2.3) the electron density becomes

$$|\Psi(0)|^2_{3s} = \frac{3\,a_{3s}\,\mu_B\,I}{8\,h\,c\,R_\infty\,\alpha^2\,F_r(1/2, Z_i)\,\mu_I} \ . \tag{2.67}$$

Using the nuclear function $f(Z)$ of equation (2.60), one arrives at an electronic factor which is based on the HFS data

$$F_{el} = \pi\,\beta\,|\Psi(0)|^2_{3s}\frac{a_0^2}{Z_i}f(Z) = -38(4)[12] \text{ MHz/fm}^2 \ , \tag{2.68}$$

again with $\beta = 1.1$. The error in parentheses belongs to the 10% uncertainty of the screening factor β, the error in square brackets arises from the uncertainty of a_{3s}. Both methods of calculating F_{el} lead to compatible results. For further use we use the F_{el}-value calculated from the fine-structure data by the Goudsmith-Fermi-Segrè approach.

Chapter 3

Collinear Laser Spectroscopy Setup at ISOLDE/CERN

The experimental environment of the ISOLDE on-line mass-separator facility at CERN involves a number of specific experimental details that have to be considered and will be described in this chapter. Furthermore, the basic physics of collinear laser spectroscopy, and details of the experimental setup used in the experiments on neon will be presented.
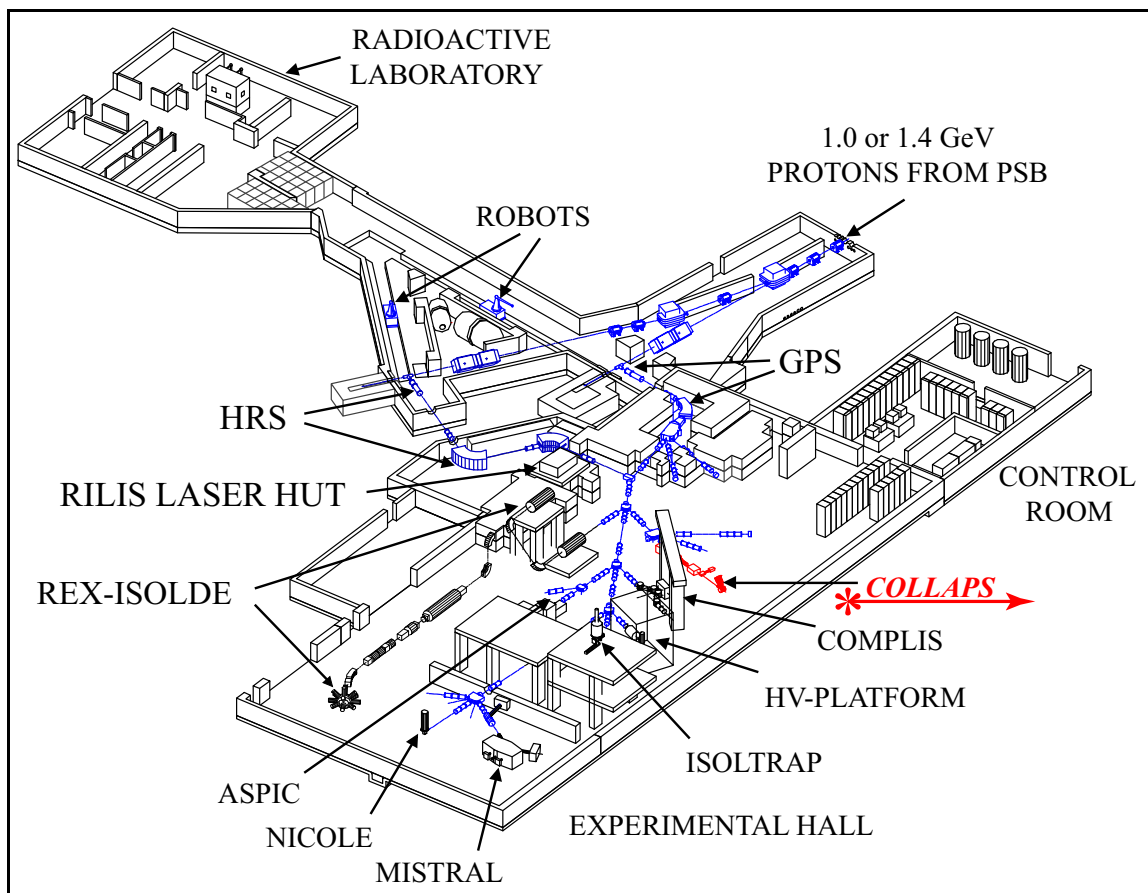
Fig. 3.1: *The layout of the ISOLDE hall. The COLLAPS experiment can be found at one of the beamline ports to the right.*

3.1 The ISOLDE Facility

3.1.1 General Remarks

The ISOLDE on-line mass-separator is an experimental facility at the European nuclear physics laboratory CERN in Geneva. A wide spectrum of radioactive isotopes, covering large regions of the nuclear chart, can be produced and delivered as mass-separated radioactive ion beams [Kug93]. The layout of the facility is shown in figure 3.1[1]. The radioactive nuclides are produced by irradiating a target material of appropriate choice with protons of 1-1.4 GeV kinetic energy which are delivered by the PS-Booster synchrotron accelerator (PS: Proton Synchrotron). The choice of the target material depends on the desired radioactive isotopes. A typical proton pulse consist of about 3×10^{13} particles impinging on the target. The proton beam from the so-called "PS-Booster" has a time structure of 2.4 μs length and a period of multiples of 1.2 s between the individual pulses. The proton pulses delivered by the PS-Booster are distributed to various facilities. 12 consecutive pulses are grouped to a so-called "supercycle", a pulse sequence with 14.4 s periodicity. A schematic plot of the time structure of the proton intensity on the target and of the beam intensity is shown in figure 3.3. The proton impact in the target material causes nuclear reactions wherefrom the radioactive isotopes are formed by fission, spallation or fragmentation. The target material is contained in a heated tube which is kept at a temperature of about 1500 K. The product isotopes evaporate from the target material and diffuse via a drift tube to a connected ion source.

The ion source can be adapted to the desired chemical element. Depending on the chemical properties of the isotopes, surface ion-sources (for elements with low work function like alkali metals) or plasma ion-sources (for elements with high ionization energies like noble gases) are used. Plasma ion-sources are often combined with a cooled "transfer line" – the drift tube between the target and the source. This suppresses elements which are less volatile, thus sticking to the wall of the tube at low temperature. The design of the plasma-source unit used for the production of noble gas beams is shown in figure 3.2.

3.1.2 Ion Beam Generation

For the present experiments on neon beams, CaO was chosen as a target material for the production of the light neutron-deficient isotopes and UC_2 for the neutron-rich isotopes. The ion source was a plasma source, in which noble gas ions can be ionized very efficiently. Further discussion shall be limited to this kind of source. A detailed discussion of the influence of the ion source characteristics on the beam energy will be presented in chapter B.3.

The principle of the plasma ion-source is based on the ionization of atoms by electron bombardment. A continuous gas flow, entering the electron-bombardment region, supplies atoms for a plasma that burns continuously. The primary plasma gas is a noble gas mixture consisting of 40% of helium, 20% of neon, 20% of argon and 20% of xenon[2]. The radioactive neon atoms evaporated from the target material are ionized together with noble gas atoms

---

1 Picture taken from the ISOLDE home page: Facility layout; online: http://www.cern.ch/ISOLDE/.

2 Uwe Georg: Private communication 01.03.2001
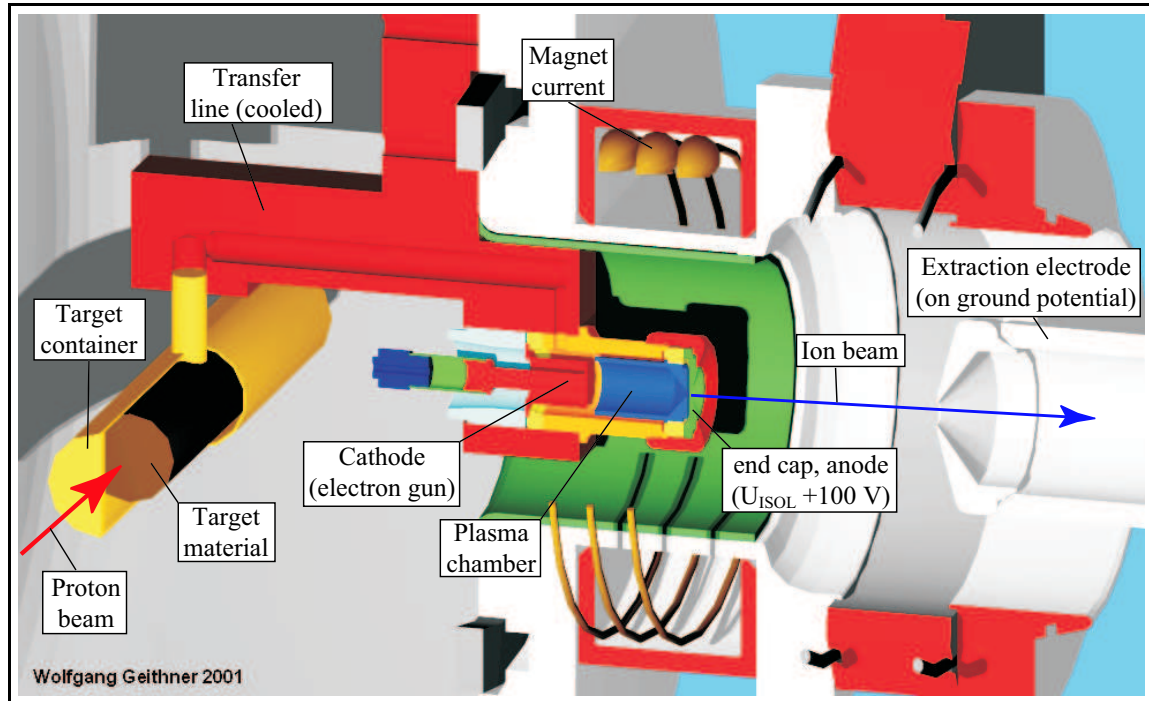
Fig. 3.2: *The ISOLDE ion source. For better visualization parts of the source are cut open. Exotic isotopes are produced by proton impact in the porous target material, and diffuse via the cooled transfer line to the plasma ion-source. All the parts shown in the graphic are kept on the main acceleration voltage besides the extraction electrode (ground potential) and the end cap (+100 V).*

from the continuous gas flow. When ionized, the ions are accelerated in an electrostatic field. The ion source and the whole target vacuum-chamber are kept at high voltage, whereas the extraction electrode and the following experimental beam lines are kept at electrical ground potential. The details of the acceleration potential in the source are of importance for the beam characteristics and are discussed in the appendix 5. The continuous ion beam generated by the plasma discharge of the noble gas mixture provides an ion beam of stable isotopes. This can be used to set and to optimize the beam-line parameters, and to do beam-energy measurements (see Chap. 5), furthermore the stable reference isotopes are available for the isotope-shift measurements (see Chap. 6).

Once extracted, the ions pass through a magnetostatic mass separator with a resolving power of $m/\Delta m = 2400$ [Kug93]. The magnetic field can be chosen to select isotopes of a given mass. The resolving power is not high enough to separate isobars. This necessitates considerations concerning the detection of isotopes produced with low yields and strong isobaric beam contaminations. The mass-separated ion beam is transported via an evacuated beam line to the different experiments placed as shown in figure 3.1.

As a result of the pulsed proton-beam structure, the ion beam from ISOLDE has a certain time structure as well. The diffusion of the isotopes out of the target material "smears out" the ion pulse emerging from the source, as illustrated in figure 3.3. The so-called "release curves" – the ion pulse shape as a function of time – depends very much on the chemical element. For neon typical ion-pulse durations are of the order of 500 ms. The timing of a measurement has to be adapted to this pulse structure. On the other hand the pulsed time

structure offers the possibility to discriminate against isotopes with different half-lives by triggering and gating methods.
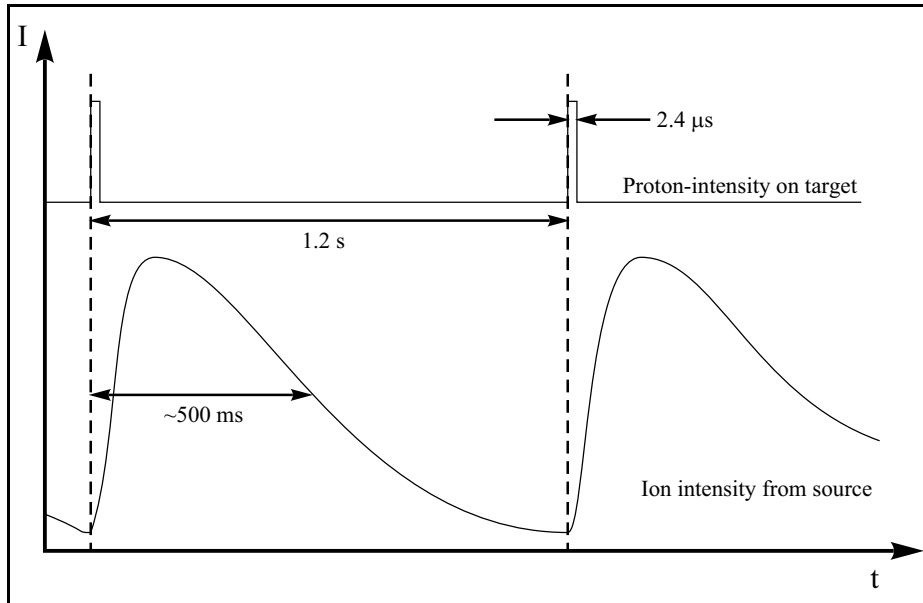
Fig. 3.3: *Time structure of proton and ion beam at ISOLDE. The plot shows schematically the time dependence of both beams, the scaling in time is not proportional.*

3.2 The Experimental Setup

3.2.1 General Description of the Setup

The experimental setup of collinear laser spectroscopy at ISOLDE is a versatile installation for experiments on radioactive isotopes. The development of this apparatus was started in the late seventies [Ott77, Neu81]. Over the years the experiment experienced many updates and extensions, increasing selectivity and sensitivity. The present setup is shown schematically in figure 3.4. It can be divided into four major parts:

- Installations for beam manipulation and beam shaping,

- Installations used for Doppler tuning (see Sec. 4.1) and neutralization

- Optical excitation and fluorescence detection region

- Gas target and atom/ion detection.

All elements used to manipulate the atom/ion beam (deflectors, quadrupole lenses, charge-exchange chamber,etc.) and the non-optical detectors are contained in an evacuated beam line. Typical residual gas pressures under experimental conditions are of the order of 1×10^{-6} mbar.
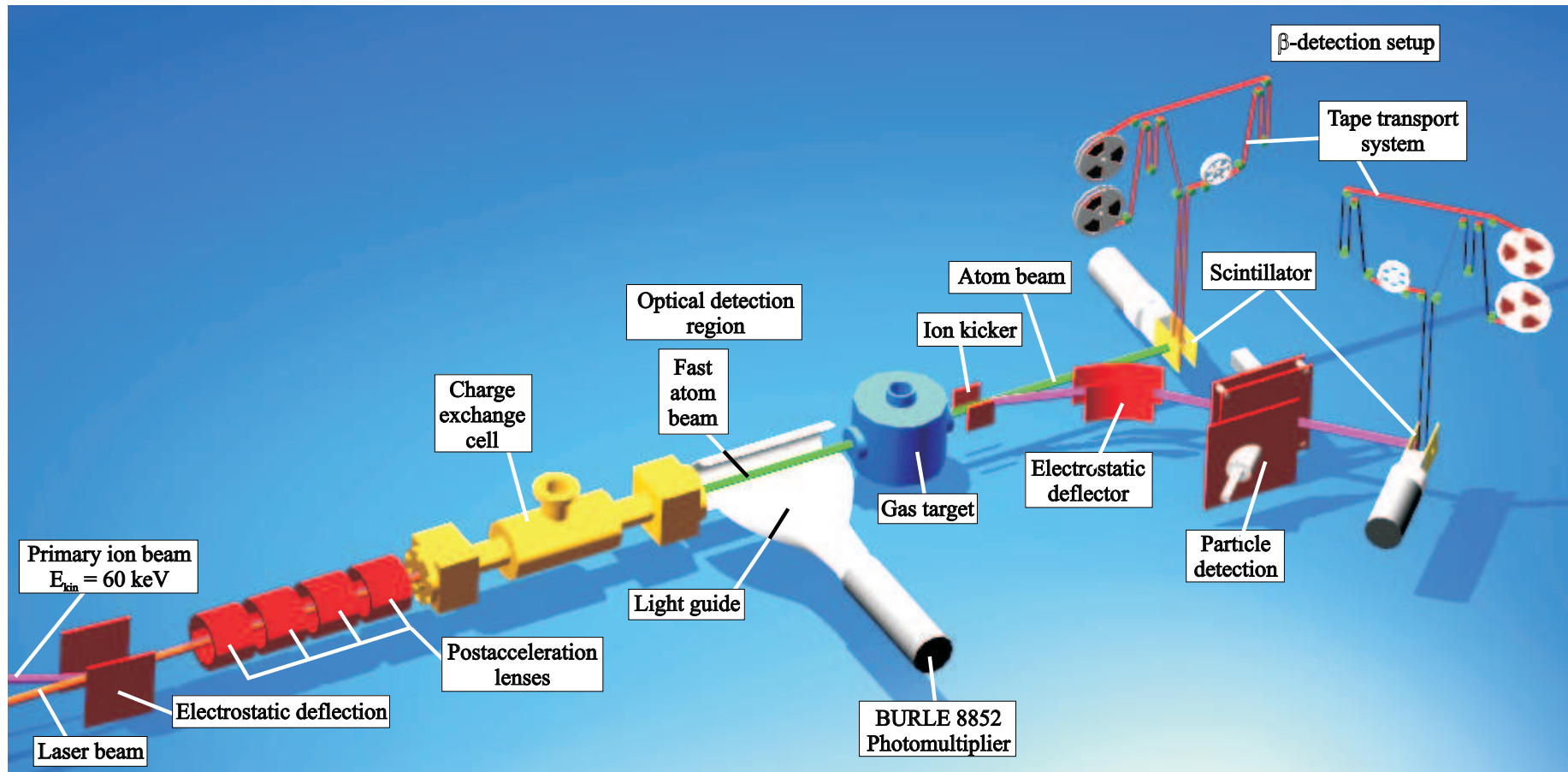
Fig. 3.4: *Schematic drawing of the major components of the experimental setup. The ion beam optics are displayed only partly for simplicity, the quadrupole lenses and the correction deflectors in front of the post-acceleration electrodes are omitted.*

Ion Beam Optics

The ion beam enters the experimental setup through a vacuum gate which is used to shut off the setup from the beam line vacuum sections. The first device used to manipulate the beam is a set of two vertical capacitor plates. These plates at voltages of about ± 2 kV are used to deflect the ion beam by $10°$ which makes it possible to superimpose the ion and the laser beam, the latter defining the axis of the apparatus. The deflector is followed by a triplet of quadrupole ion lenses, and correction elements for horizontal and vertical deflection. This gives the final possibility to shape and to steer the beam before it is neutralized. Note that these elements are not included in figure 3.4. The next important element is the post-acceleration region which is required for the Doppler tuning of the laser frequency. The post-acceleration region consists of four ring electrodes and the charge-exchange cell (CEC). All these elements can be adjusted geometrically and are decoupled electrically from ground. Each of the ring electrodes is set at a voltage which is a fixed fraction of the main post-acceleration voltage which is applied to the last ring and to the charge-exchange cell itself.

Charge-Exchange Cell
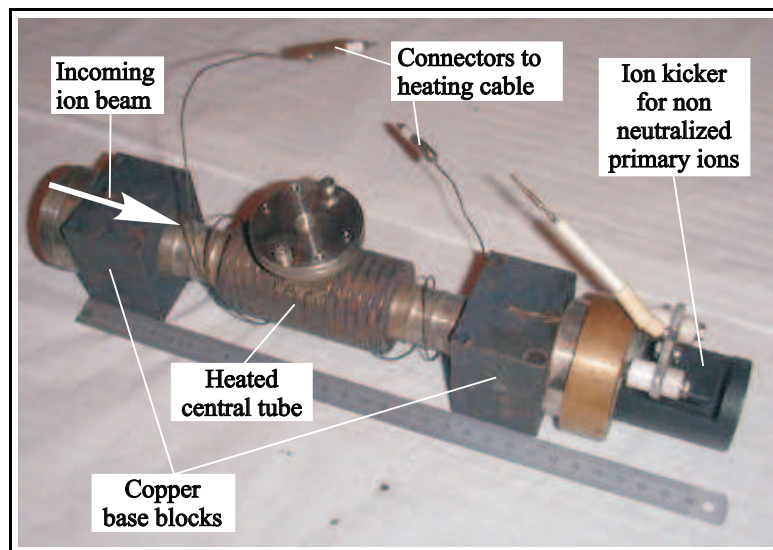
Fig. 3.5: *Photograph of the charge-exchange cell (CEC). The upper "chimney-like" part of the cell gets filled with the alkali metal used for neutralization.*

The last part of the post-acceleration region is formed by the charge-exchange cell, which is shown in figure 3.5. This device is used to neutralize the incoming ions in flight by quasi-resonant charge-transfer reaction. The design of the assembly of post-acceleration electrodes and CEC ensures the neutralization of the ions at the full post-acceleration potential. Thus, the atom beam leaving the CEC has a beam energy corresponding to the main acceleration voltage plus the post-acceleration voltage. The CEC is essentially a heated tube which contains the charge-exchange medium in the form of an alkali-metal vapor. Inside the tube a roll made out of a stainless steel mesh is inserted to take up the hot, liquified alkali metal. The tube is heated by a coaxial thermo cable.

Sodium is used as a charge-exchange medium for the neon beam. The 40 W heating power give rise to temperatures up to about 560 K at the central part of the tube. The corresponding sodium vapor-pressure is of the order of 10^{-2} mbar [Vee02]. This vapor pressure is sufficient to achieve charge-exchange efficiencies up to 95%.

The ends of the charge-exchange tube are soldered to copper blocks. The blocks are used as supports to fix the charge-exchange cell to a base plate. They are kept at lower temperatures than the central part to ensure the condensation of the alkali vapor and recirculation of the sodium inside the cell.

Optical Detection Region

After neutralization, the atoms in the beam can interact with the laser light. To be able to detect the fluorescence light, an optical detection system is installed downstream of the charge-exchange cell. This system consists of a 35 cm long drift tube. Inside this vacuum tube a half-cylinder mirror is mounted to reflect photons emitted transversally to a set of lenses which finally focus the light to a plexiglas light guide. Single photons are detected by a 2" diameter photomultiplier tube (BURLE, type 8852). To suppress background from laser stray light, the entrance and exit of the optical detection region are equipped with stacks of diaphragms increasing in diameters towards the detection region.

The Gas Target

The non-optical collisional ionization detection technique requires a gaseous "target" of up to 10^{-2} mbar pressure to ionize the incoming neon atoms in collisions (see Sec. 4.2). Technically this gas target is realized as a special vacuum vessel which was introduced by W. Borchers [Bor89a]. It is shown schematically in figure 3.6, and consists of three nested concentrical chambers to realize differential pumping from typically 2×10^{-3} mbar in the inner chamber containing the target gas, to 10^{-6} mbar in the outer vacuum system.

The target gas flows constantly through a leak valve into the innermost chamber to replace gas losses through the entrance and exit diaphragms. These diaphragms, shown in figure 3.6 had diameters of 7 mm during the measurements on neon.

Efficient pumping of the chamber is provided by two turbo-molecular pumps: a special chemically resistant one with a pumping speed of 450 l/s, evacuating the second inner chamber, and a smaller one (360 l/s) to keep the outer chamber at a pressure of 10^{-6} mbar. The pressure inside the gas target is measured by a Leybold "ViscoVac" gas pressure meter. This device measures gas pressures via the friction of a rotating ball in the thin gas atmosphere. The meter has a large dynamical range between $10^{-6} - 1$ mbar and a precision of about 4% [Ley].

3.2.2   Ion / Atom Detection Techniques

The ions produced in collisions with the target gas-molecules are deflected electrostatically out of the primary beam direction, and guided to two alternative detectors. The first one is based on ion counting by a secondary electron multiplier. This method has the advantage of being applicable to any sort of beam (stable and radioactive) but has the disadvantage of
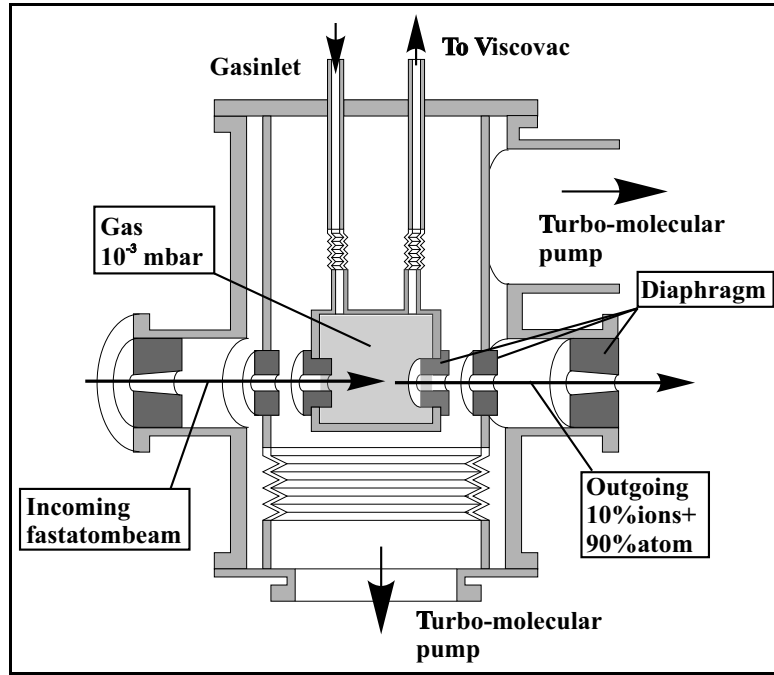
Fig. 3.6: *Schematic drawing of the gas target chamber.*

being sensitive to beam contaminations. The second method is used to suppress efficiently the non-radioactive or long-lived beam contaminations making use of β-activity counting. Both methods were already used in the work of Klein [Kle96], but some work had to be done to improve the concept and to increase the reliability and the sensitivity of the detection system.

Already A. Klein suggested to normalize the signal of the ions produced in the gas target to the intensity of the primary beam. This is necessary because intensity fluctuations or irregular sequences of proton pulses change the conditions in the ISOLDE target and the ion source, and give rise to intensity fluctuations of the ion beam that are not directly proportional to the proton-beam intensity. This leads to additional non-statistical count rate fluctuations which can hamper seriously the acquisition of spectra as a function of time. The idea of normalizing was implemented by installing detectors identical to the ones for the deflected ion, also in the forward direction to detect the neutral fraction of the beam (see Fig. 3.4). This setup was invariably used in the measurement runs on short-lived neon isotopes.

3.2.3 Measurement Modes

The pulsed ion beam from the ISOLDE ion source requires (and offers) adapted measurement modes used in the collinear laser spectroscopy experiments:

(1) The untriggered mode is used for the experiments with stable isotopes, which are based on optical detection and on state selective collisional ionization (see below). One measurement scan, consisting of n channels of width Δt (typically 20 ms) is started without any timing reference to the proton pulse impinging on the target.

(2) The triggered *channel* mode: every channel of a single scan is triggered by a proton pulse, the channel has an integration time up to the period between two consecutive

proton pulses (typically n proton pulse periods = $n\times$ 1.2 s, where n is an integer). This mode is used in the measurements with radioactive detection.

(3) The triggered *scan* mode: this mode uses the proton trigger pulse to start one scan with short channel width (typically of the order of ms). This mode is used to measure the time structure of the release curve of an isotope from the target, or for half-life measurements.

3.3 Non-Optical Detection Setups

3.3.1 Ion Counting by Secondary Electron Generation

The counting of ions produced by collisional ionization is based on the generation of secondary electrons on a metal plate. As shown in figure 3.7, the detector setup consists of a stack of two metal plates, to which a high voltage is applied. The plates are pierced, so that the impinging ion beam can pass through to the β-detection setup if the retractable stopper plate is opened. The electrons are detected by a secondary electron multiplier (SEM)(BALZERS type 217). For the neon runs a second detection setup was built and installed in the direction of the non-deflected neutral atom beam.

The SEM has an amplification of $10^8 - 10^9$ at the typical working voltage of -3500 V [Bal] and it was used to count-rates up to a few 10^6 counts/s. The advantages of the ion/atom detection lie in its suitability for long-lived and stable species. Typical applications for this kind of detection is the ion beam-energy measurement with the stable neon isotopes, which is described in chapter 5. Another application is the optical spectroscopy of the weak stable isotope ^{21}Ne and of long-lived isotopes like ^{23}Ne. As mentioned before, the ion detection
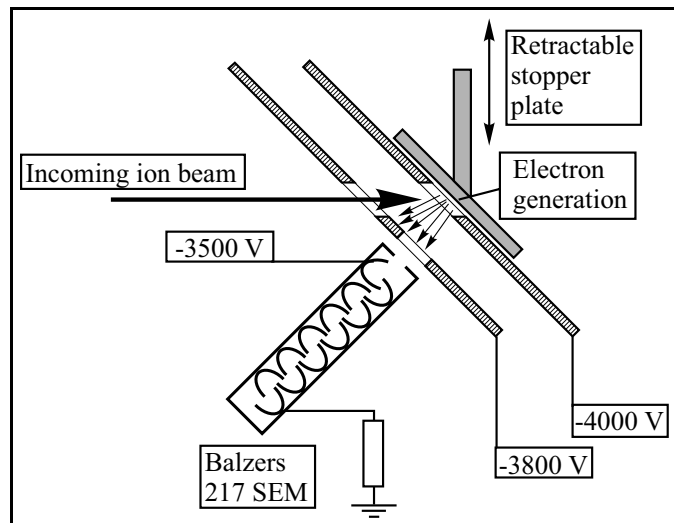
Fig. 3.7: *Schematic drawing of the particle detection setup. Electrons are generated on a retractable metal plate and get driven to a secondary electron multiplier by an electrical field.*

cannot discriminate against isobaric beam contaminations. As an example, ^{23}Ne is shadowed by a very intense beam of stable ^{23}Na. Doubly or even higher charged ions contribute as well to a background when they have the same q/m-ratio as the desired isotope.

The secondary electron detection setup can be used for fast, untriggered scans with channel step times of several milliseconds like the optical measurements. This measure mode is insensitive to the long term fluctuations of the target conditions, which have to be taken into account in the measurements with the β-detection setup.

3.3.2 β-**Activity Detection**

For the measurements on very short-lived isotopes the detection technique based on counting the β-activity of the radioactive isotopes was used. This technique eliminates the background from stable and very long-lived beam contaminations but it is of course still sensitive to background radioactivity:

(1) from radioactive isobaric beams.

(2) from accumulating radioactivity either from radioactive daughter nuclei or from the decay of the isotope under investigation if it has a half life comparable with the integration time of one measurement channel.

The first kind of background can only be suppressed either by optimizing the gating with respect to different release-times and/or half-lives of the isotopes leaving the target after the proton pulse. The other possibility is the energy discrimination, where by the counting of β-particles is suppressed when their kinetic energy is below a certain threshold.

The second type of background can be suppressed by removing all accumulating radioactivity from the detection zone. This is done by implanting the radioactive atoms into a tape system. After counting for an appropriate integration time the tape is moved, and a clean implantation zone is moved into position to take the next pulse. This procedure requires a triggered channel mode using the proton impact on the ISOLDE target as a starting signal for one measurement channel.

The β-activity detection is realized by the use of two parallel scintillator-detector plates. They are placed perpendicular to the direction of the ion beam before and behind the implantation site in the stopper tape (see Figs. 3.4 and 3.8) inside a vacuum chamber. The photons generated in the scintillation material are guided by a light guide to a photon detector (Phillips XP2262) which is placed outside the vacuum chamber. The plates are made of plastic-scintillator material (material: NE102) and have a size of $50 \times 60 \times 1$ mm. The spacing between the plates is 20 mm, thus a solid angle of about 56% of 4π is covered. The frontward plate is equipped with a hole of 12 mm diameter to be able to implant the ion beam in the stopper tape placed between the two detector plates.

3.3.3 **Improved Tape Transport System**

The tape transport system developed by A. Klein enabled the detection of radioactivity free of accumulating background. Nevertheless the reliability of the system was hampered by some mechanical weaknesses, so re-engineering of the system became necessary. The main aim of a new system was to increase the transport speed of the tape and to improve the reliability under running conditions.

The new tape system was designed to fit into the vacuum chambers used with the previous model. A schematic view of the mechanics is shown in figure 3.8. The transport mechanism is based on the "capstan" principle: one driving step-motor winds the tape and defines the winding direction. Standard VHS-video tape rolls are fixed on the axes of two 6 W dc motors. These dc motors keep the tape tight and take up the tape delivered by the stepping motor. As long as the stepping motor doesn't move, the dc motors pull the tape with a static force;
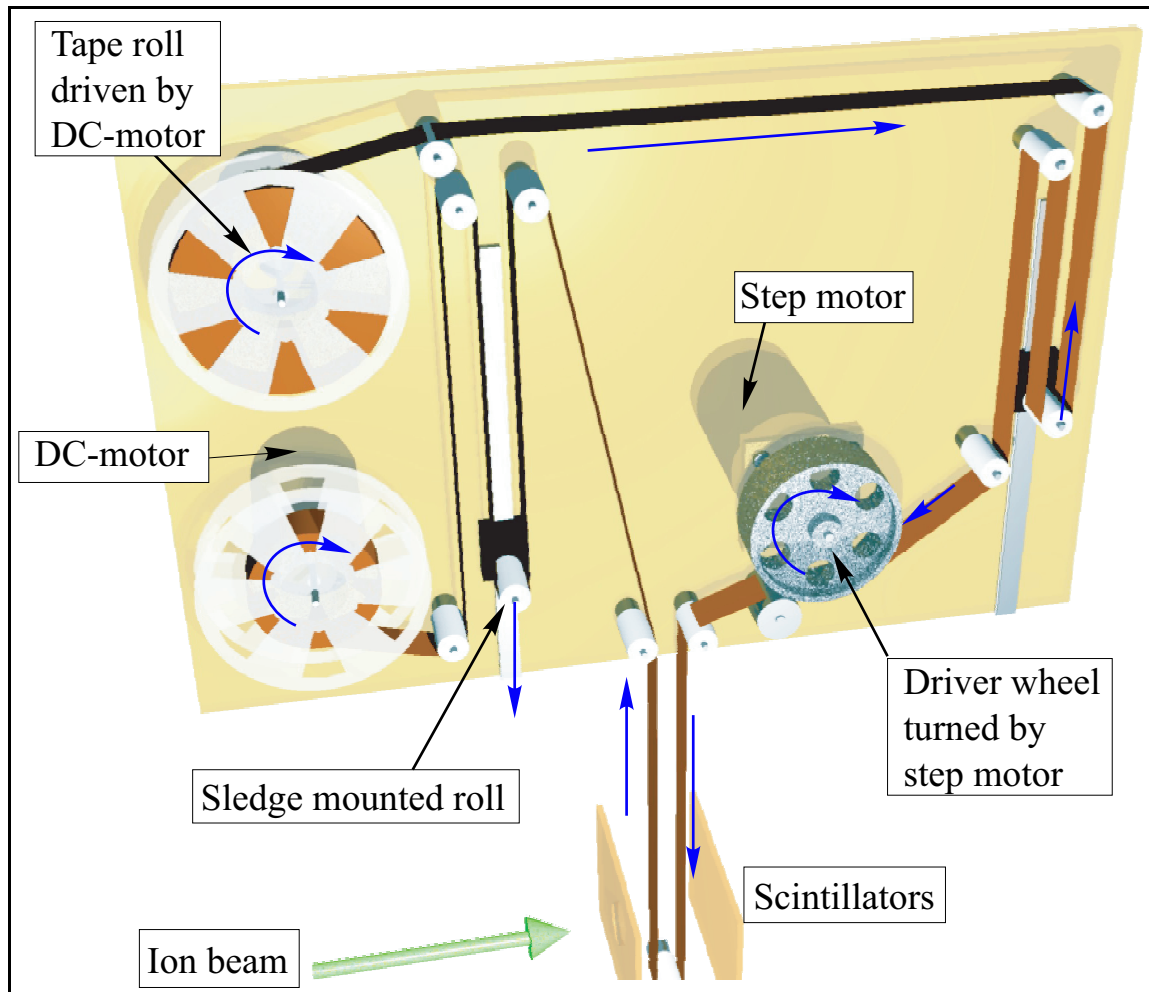
Fig. 3.8: *Schematic view of the new tape station mechanics. For better visibility the base plate is transparent.*

when the tape is moved, the tape rolls have to be accelerated. As the acceleration of the dc motors is far to small to cope with the amount of tape delivered by the stepping motor, two small sledge-mounted, spring driven rolls are installed to tighten the tape.

The tape system was designed to enable tape transport-speeds of 20 cm per 200 ms. The speed was tested off-line and a maximum of 20 cm per 150 ms was reached. In normal running operation the winding speed never exceeded 10 cm per 200 ms, which guaranteed reliable operation throughout the runs of several days.

The tape material used as implantation host was a standard VHS video-tape of various suppliers. The video-tape material provides low weight for fast transport, and sufficiently good electrical conductivity on its magnetically layered side to avoid ion losses by charging up effects on the beam. A series of measurements was used to study the diffusion of implanted neon atoms from the tape material in dependence of the side of the tape where the implantation takes place. In figure 3.9 two illustrating measurements are presented.

Both plots show the counts detected by the scintillation β-counters after a short implantation of ^{19}Ne with a half life of $T_{1/2} = 17.34$ s. The left plot represents the time behavior of the count rate when the implantation is done into the magnetized side of the video-tape.
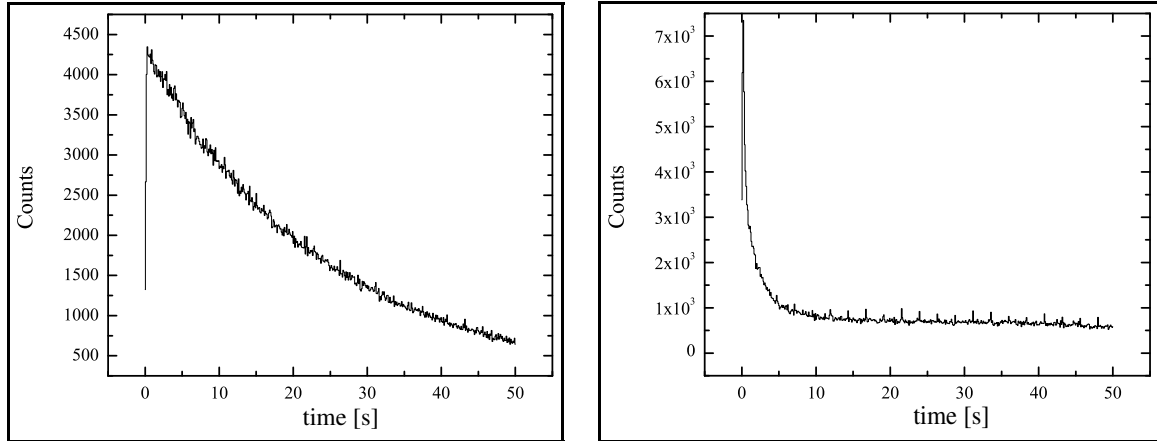
Fig. 3.9: *Diffusion from the tape material. The implanted isotope was ^{19}Ne. The left-hand picture shows the 17.34 s decay of ^{19}Ne implanted in the magnetized side of the tape and detected with β-counters. The plot on the right-hand side was obtained under the same conditions, but with implantation in the non-coated side of the tape.*

No diffusion takes place out of the magnetized side of the tape; the left plot shows a decay curve corresponding to the radioactive decay of ^{19}Ne nuclei. The right plot was achieved by implanting into the "wrong" non-coated side of the tape. The two plots show that the diffusion out of the tape material is very rapid from the non-coated side of the tape.

3.3.4   Normalization to Primary Beam Intensity
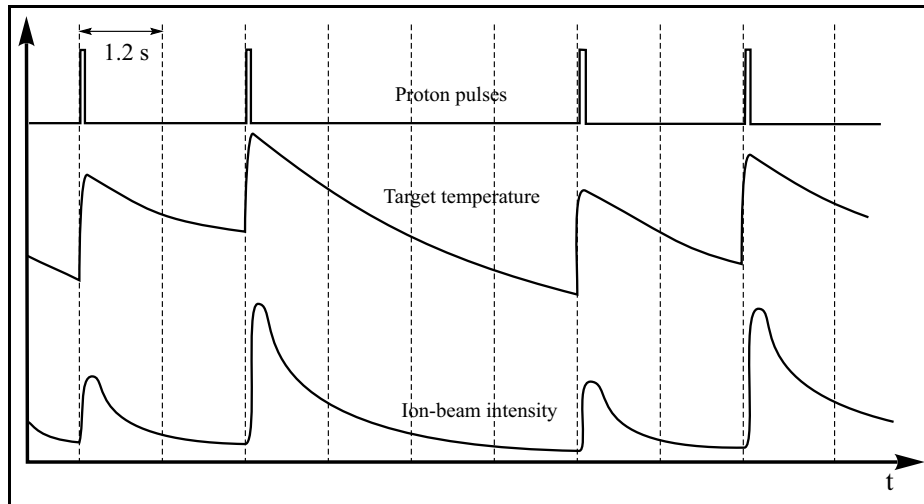
Fig. 3.10: *Schematic drawing of the effects of an irregular pulse structure on the target conditions. Long gaps between two proton pulses cause cooling of the target and lower ion-beam intensity.*

Due to proton beam fluctuations, and changing target conditions, the primary ion beam intensity varies significantly. Also the time structure of the proton-pulse sequence influences the beam intensity dramatically. This is illustrated in figure 3.10. The impact of the protons on the target causes a heating effect, which influences the diffusion of atoms out of the target. Proton-pulse sequences with changing time intervals between two consecutive pulses ("non-equidistant") cause varying target heating and cooling conditions seen as strong variations of

the primary ion beam intensity. The effect of these variations on a measurement of the ^{19}Ne hyperfine structure is shown in figure 3.11. The strongly varying count rate from channel to channel in the upper two plots can be attributed to the non-equidistant time structure of the proton pulses.
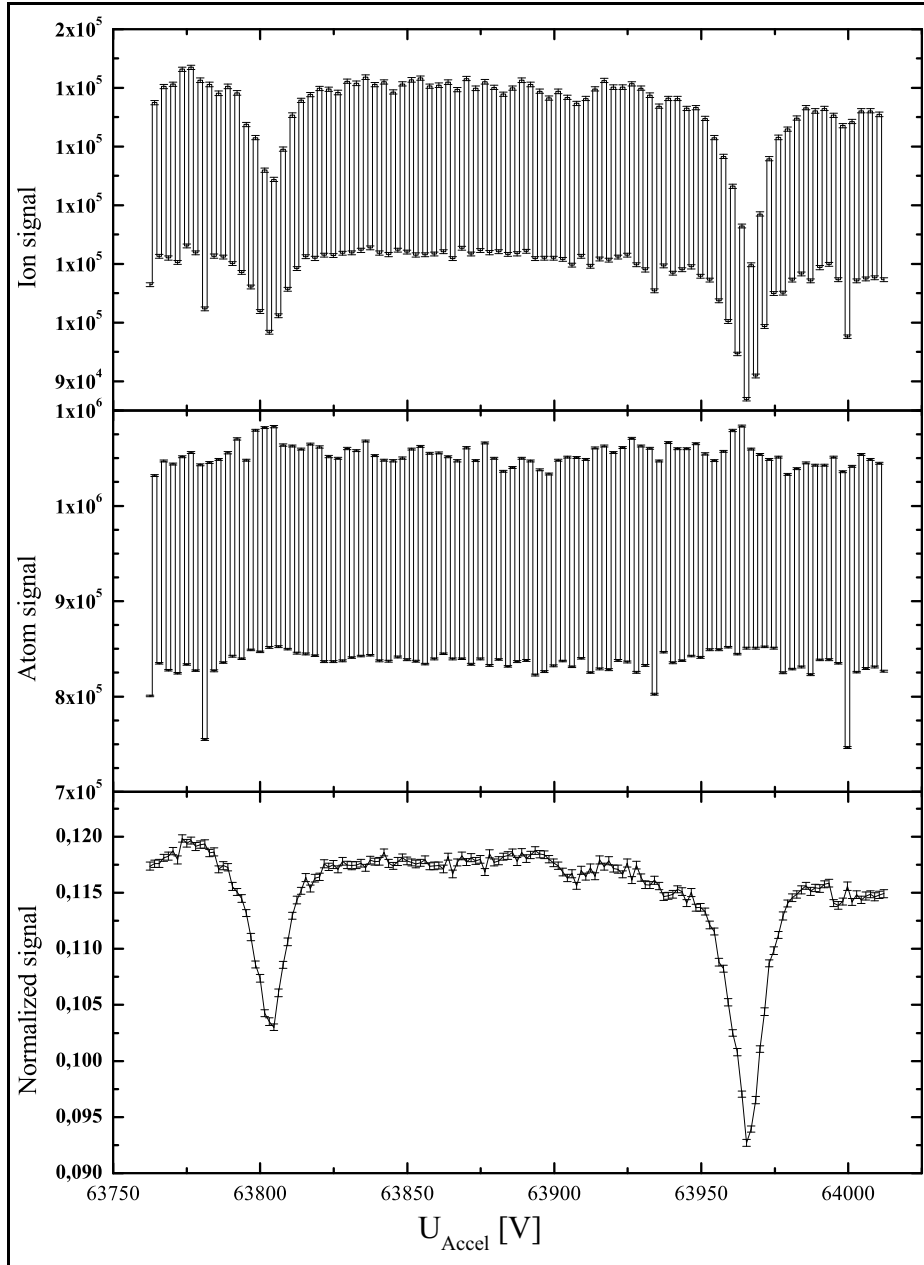
Fig. 3.11: *Example of the power of the normalization method. The pulses 3,5,9,11 of one supercycle were used in this measurement. Upper graph: ^{19}Ne hyperfine structure in the ion signal; middle: atom signal for normalization; lower: normalized signal.*

To avoid this problem, a tape system with slightly modified design was installed in the forward direction (see Fig. 3.4). Whereas the backward scintillator plate of the detector setup in the deflected ion-direction is not equipped with a hole, the backward plate of the detector in the forward direction has a hole similar to the frontward plate. Additionally the stopper tape of detection setup in the forward direction can be retracted, to give way for

the atom and the laser beam for beam alignment purposes. To avoid that laser stray-light
is guided to the photo multipliers, the holes in the scintillators are shielded with aluminum
foil. Additionally, the entrance window of the photo multiplier tube was covered with a BG3
bandpass filter. This filter suppresses the orange laser light in the range between 590-660 nm
by a factor of 10^5 and has a transmission of better than 99% for the blue scintillation light in
the range between $340 - 380$ nm [Sch]. With the normalization of the ion signal to the total
beam intensity, one obtains a signal which is independent of beam intensity fluctuations

$$S_{norm} = \frac{N(ions)}{(N(atoms) + N(ions))} .$$

(3.1)

The power of this method is illustrated in the lower, normalized spectrum of figure 3.11, which
nicely shows two components of the hyperfine structure of ^{19}Ne with errors determined by
counting statistics.

3.4   Acceleration Voltage Equipment

Of major importance for collinear laser spectroscopy is the high voltage equipment used to
accelerate the ions. This equipment can be subdivided into two subsections: (i) the main
acceleration voltage U_{accel} driving the ISOLDE primary ion beam and (ii) the voltage U_{post}
used to post-accelerate the beam in the collinear setup. Thus, the total acceleration voltage
is given by

$$U_{tot} = U_{accel} + U_{post}$$

(3.2)

An overview of the high voltage installations is shown schematically in figure 3.12.
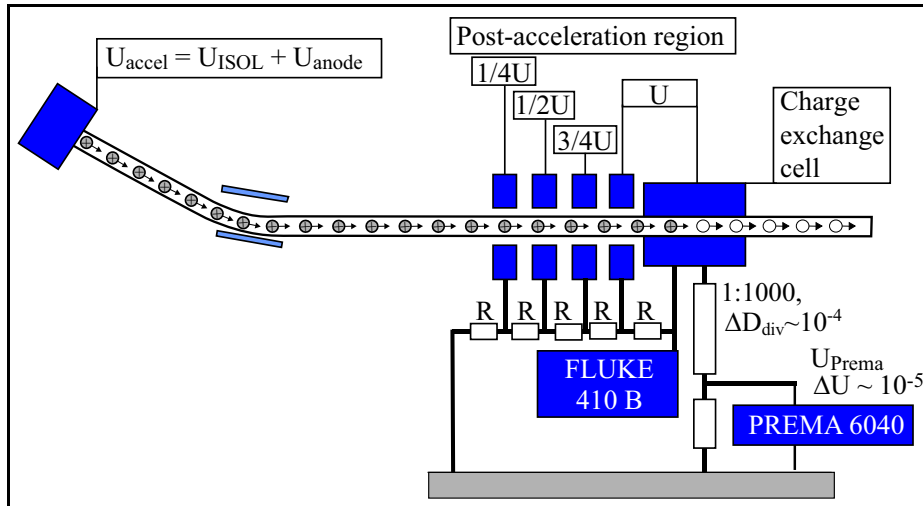
Fig. 3.12: *Schematic drawing of the different voltages important for collinear
laser spectroscopy. U_{accel} is the main acceleration voltage. It con-
sists of the high voltage U_{ISOL} and the anode voltage U_{anode}. The
optical detection, the gas target and the detection are omitted for
simplicity.*

3.4.1   The Main Acceleration Voltage

The ion beam energy is determined mainly by the positive high voltage applied to the ISOLDE ion source U_{ISOL}. This acceleration voltage is generated by a 10^{-5}-stabilized high voltage power supply [Fia92] which is typically running at a voltage of +60 kV. For the measurement the voltage is divided by a precision voltage divider with a ratio of $1:10^4$. The divided voltage is measured and digitized by a precision voltmeter, and can be read out from the ISOLDE control system. The absolute accuracy of the measurement of the main voltage is specified to 10^{-4}, corresponding to about 6 V. During the experimental runs the acceleration voltage is continuously monitored, and the readout values are saved with the data files of the "measurement and control programme" (MCP) used to control the experiment.

The total beam energy consists of the main acceleration voltage U_{ISOL} plus additional ion source-dependent voltages. These voltages vary with the type of ion source and the individual conditions inside the source. In the plasma ion source a cathode, which is kept on U_{ISOL}, emits electrons to ionize the plasma gas atoms (see Fig. 3.2). The electrons are accelerated by a voltage of about +100 V to +200 V above U_{ISOL} which is applied to the ion-source end-cap (anode). The anode is equipped with a outlet nozzle of 1 mm diameter. Ions produced close to the nozzle can leave the plasma chamber and are accelerated in the sum potential of U_{ISOL} and an unknown fraction of the anode voltage U_{anode}. This fraction is dependent on the place of ionization inside the plasma. The anode voltage is measured by a digital voltmeter and can be monitored during the measurements in a similar way as U_{ISOL}. The error of the anode-voltage measurement can be neglected.

On the other hand, the anode potential is only approximately the potential at which the ions are created. It depends on the plasma conditions inside the ion source (see appendix B.3). The corresponding true fraction of the anode voltage accelerating the ion is called U_{plasma}. This potential cannot be measured easily. It was estimated in earlier works on collinear laser spectroscopy with noble gases to be U_{anode} with an uncertainty of up to 30 V [Kei95, Kle96].

3.4.2   The Post-Acceleration Voltage

To perform the "Doppler-tuning" by post-accelerating the ions before entering the neutralization region, a variable voltage is applied to a set of electrostatic lenses and to the CEC. This variable voltage consists of a fixed offset voltage (U_{Fluke}) in the range of -10 kV to +10 kV. This voltage is supplied by precision high-voltage supplies (FLUKE 410 B). To be able to take spectra of several isotopes in a sequence, three voltage supplies are used, each corresponding to one isotope. Each voltage is set to a proper value which corresponds roughly to the resonance frequency of the isotope. Before starting a measurement on this isotope the offset voltage is applied to the post-acceleration electrodes with the use of a remotely controlled set of high-voltage switches. The post-acceleration voltage is divided by a precision voltage divider (Julie research laboratories model KV-10R), which has a divider ratio $D_{div} = 1000$ (specified error: 10^{-4} [Jul]). A more accurate calibration value of D_{div} from collinear laser spectroscopy can be found in section 5.2.2). The divided offset voltage is measured with a precision digital voltmeter (PREMA Integrating digital multimeter Type

6040). The accuracy of the voltmeter in the 10 V range and for 1 s integration time, which was used during all the experiments, is specified to

$$\Delta U_{prema} = \underbrace{1 \times 10^{-5} \text{ V}}_{\text{max. Display} \times 10^{-6}} + 4 \times 10^{-6} \times \text{ (voltage readout)} + \underbrace{1 \times 10^{-5} \text{ V}}_{\text{error last digit}} \quad \text{[PRE]} . \quad (3.3)$$

This corresponds to an error in $U_{post} = U_{prema} \times 1000$ of 60 mV for the maximum readout voltage of 10 V.

To be able to vary the post-acceleration voltage, a voltage ramp (U_{DAC}) is supplied by an 18-bit digital-to-analog (DAC) voltage source (HYTEC DAC 670 MK2 CAMAC [Hyt]), which is compatible with the CAMAC bus standard and can be driven by computer commands. The voltage range of this DAC is between -10 and +10 V, with a minimum step width of 1 mV [Hyt]. This voltage is amplified with a high-voltage amplifier (KEPCO Model BOP 500M), which has an amplification factor F_{kepco} of about 50 [Kep], so the dynamic voltage range for a measurement is -500 V $\leq U_{ramp} \leq +500$ V. This variable Doppler-tuning voltage is used to change the ground potential of the Fluke high voltage supplies. The resulting voltage applied to the post-acceleration electrodes is a voltage ramp as a function of time with a preselected width and an offset:

$$U_{post}(t) = \underbrace{U_{prema} \times D_{div}}_{U_{Fluke}} + \underbrace{\overbrace{F_{cal} \times D_{div}}^{F_{kepco}} \times U_{DAC}(t)}_{U_{ramp}} . \quad (3.4)$$

The voltage amplification factor can vary with the individual amplifier by a few percent. It varies with time, depending on factors such as the ambient temperature. The experimental amplification factor is monitored regularly by calibration measurements during the run. To calibrate, the voltage ramp used in the measurements is applied to the post-acceleration region. The applied voltage is read out by measuring the divided voltage with the precision digital voltmeter, yielding a calibration factor

$$F_{cal} = \frac{U_{kepco}/U_{DAC}}{D_{div}} = F_{kepco}/D_{div} . \quad (3.5)$$

The amplification is then determined by a straight line fit to the measured voltages. The real amplification factor of the amplifier is determined by the product of $F_{cal} \times D_{div}$, and varies only little in time. A typical time behavior is shown in figure 3.13. The amplification factor is assumed to be constant for a set of measurements, where U_{Fluke} and the sweeping voltage interval is constant.

3.5   Long-Term Laser Stabilization

To perform measurements on radioactive isotopes which are produced with low yields, one has to accept long measuring times to collect a certain count rate per channel of a spectrum. The statistical accuracy is achieved by repeating the measuring sequence of a scan (one or several ion pulses per voltage step) many times. This is realized by measuring slowly, i.e. adding up the counts of several ion pulses in one channel before the next step. Alternatively a "fast" mode can be chosen, where only the counts of one ion pulse are collected in one channel and
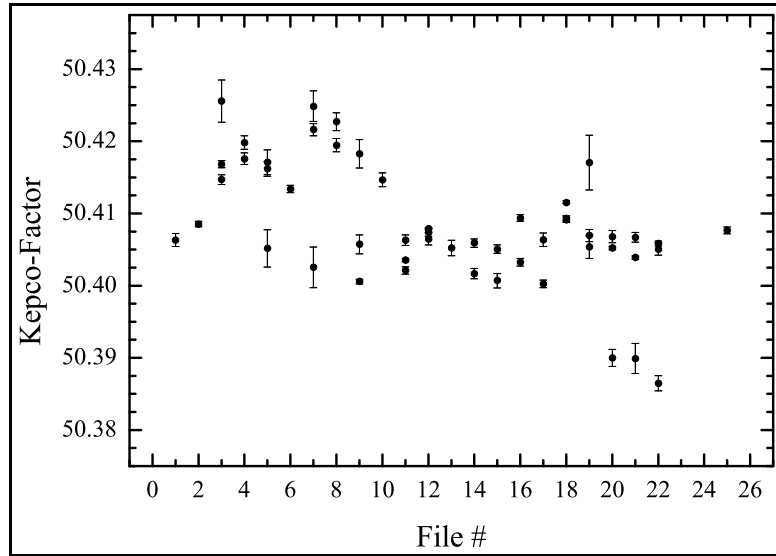
Fig. 3.13: *Measured amplification factors of the KEPCO high voltage amplifier during the run 10-1999. The data points were taken within a period of 4 days, approximately every 4-5 hours.*

the total measuring sequence is repeated many times. Thus, the long-term stability of the laser becomes important. A drift of the laser frequency causes a slow drift of the line positions in the spectra, which are taken as a function of the post-acceleration voltage, similar to a drift of the acceleration voltage itself. As pointed out in the introduction, the requirements on the precision of the determination of the optical line positions are very stringent thus requiring stable laser conditions.

The Coherent 699-21 dye laser is equipped in the standard version with a frequency stabilization, which is based on a temperature-stabilized confocal Fabry-Perot interferometer. This stabilization can efficiently be used for short-term frequency stabilization reducing the laser linewidth to about 1 MHz. The absolute long-term stability is quoted to be 10 MHz/hour [Coh], mostly due to thermal effects changing the resonance frequencies of the interferometer. As long as the measuring times are short the drift of the laser frequency is not crucial. However, measurements on radioactive isotopes can easily take hours for accumulating the required count rate. In the extreme case of ^{28}Ne measurements of the single resonance took more than 4 hours for a spectrum with good statistics.

To cope with the laser drifts, an additional long-term stabilization was developed and implemented in the laser setup. The basic components of this setup are a frequency stabilized Melles-Griot helium-neon laser and a confocal Fabry-Perot interferometer (Coherent Model number 216 free spectral range 300 MHz). The absolute frequency stability of the He-Ne laser is specified to 2 MHz/8 h and 0.5 MHz/°C [Mel]. The basic concept of the stabilization is to fix the length of the interferometer to the transmission fringes of the stabilized He-Ne laser. The observation of the transmission fringes of the dye laser in the same interferometer with a photo diode generates a voltage signal which is used for the long term stabilization of this laser.

To be able to distinguish between the He-Ne and dye-laser signals they have to be sep-
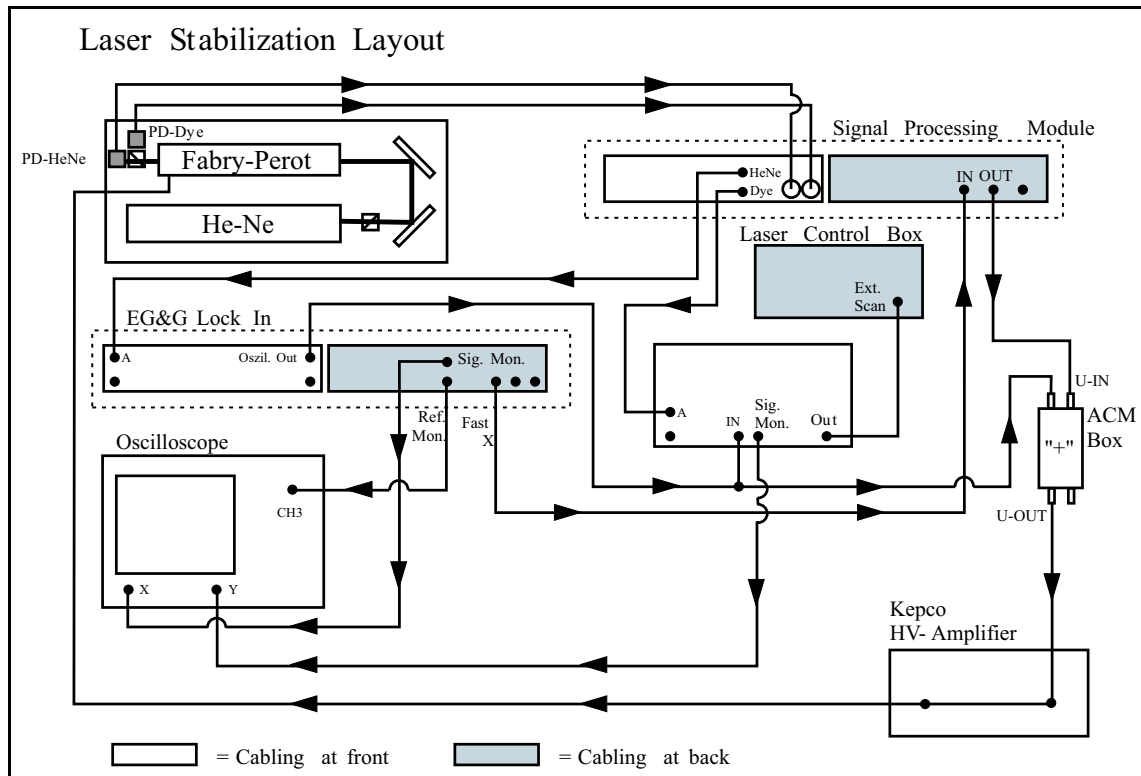
Fig. 3.14: *Schematic layout of the long-term laser stabilization. A few of the devices are shown from the front and the backside with their connections.*

arated. This is done by giving the lasers orthogonal polarizations and using beam splitter cubes for merging and separating the two laser beams. The signals delivered by two photo diodes are processed with use of lock-in techniques and are used as control voltages for an active frequency regulation. The different signal processing units and their connections are shown in figure 3.14. This long term stabilization limited the laser drifts to the required values. The absolute stability of the system was estimated to 2.8 MHz from the line positions of one resonance line under constant acceleration voltage conditions.

Chapter 4

Basic Concepts of Collinear Laser Spectroscopy

Collinear laser spectroscopy is based on the geometrical superposition of a fast atomic beam and a laser beam. There are two main advantages of this method. One is the intrinsically small linewidth measured in optical transitions. This is caused by the longitudinal compression of the velocity distribution of ions accelerated in an electrostatic field. This effect is described and briefly discussed in the papers of Kaufman [Kau76] and Wing [Win76]. Summarizing, the energy spread corresponding to the longitudinal velocity distribution is a constant in the acceleration process. This leads to a compression of the velocity spread which can be expressed by

$$\delta E = \delta \left(\tfrac{1}{2} m c^2 \beta^2 \right) = m\, c^2\, \beta\, \delta\beta = \text{const.} \,. \tag{4.1}$$

Here $\beta = v/c$ is the dimensionless relativistic parameter for the velocity in units of the velocity of light, and m is the ion mass. A description of this phenomenon in terms of an analytical formula for the velocity distribution is difficult, because it depends on the starting conditions given by the ion source. The attempt of such a description for the model of a thermal gas is presented in appendix B.

The other advantage is offered by the possibility of post-accelerating the ions in the collinear laser-spectroscopy setup (see Fig. 3.4). The movement causes a Doppler shift of the laser frequency in the rest frame of the ions or neutralized atoms. The variable voltage applied to the charge-exchange cell can thus be used to sweep the frequency in this moving frame, while the laser stays at fixed frequency. This is preferable to sweeping the laser frequency, because the relatively complicated calibration of the laser wavelength is avoided. As a result the frequency in the moving frame can be expressed as a function of the ion-beam energy.

4.1 Doppler Frequency Tuning

The Doppler shifted frequency ν' "seen" by the travelling atom is connected to the laser frequency in the laboratory system ν_L by the expression

$$\nu' = \nu_L \times \frac{\sqrt{1 - \beta^2}}{1 \pm \beta} \,. \tag{4.2}$$

To match the resonance frequency of an atomic transition ν_0 the laser frequency ν_L must be equal to the Doppler shifted resonance frequency of the moving atom ν_D and thus set according to

$$\nu_L = \nu_D = \nu_0 \pm \delta\nu_D = \nu_0 \times \frac{1 \pm \beta}{\sqrt{1 - \beta^2}} \ . \tag{4.3}$$

The $\pm$ sign depends on the direction of the laser beam with respect to the direction of the travelling atoms/ions. "+" applies when the laser beam direction is parallel to the motion of the atoms (collinear), "−" applies when it is antiparallel (anticollinear).

As the velocity of the atoms is connected with the acceleration voltage, β has to be expressed as a function of the voltage. The relativistic expression for the total energy of the atom is given by

$$E_{tot} = eU + mc^2 = \frac{mc^2}{\sqrt{1 - \beta^2}} \ , \tag{4.4}$$

where U is the total accelerating potential difference. Solving for β, one obtains

$$\beta = \frac{v}{c} = \sqrt{1 - \frac{m^2 c^4}{(eU + mc^2)^2}} \approx \sqrt{\frac{2eU}{mc^2}} \ . \tag{4.5}$$

Using equation (4.5) one obtains from equation (4.3) the full relativistic description of the Doppler-shifted frequency as a function of the acceleration voltage:

$$\nu_L = \nu_0 \times \frac{mc^2 + eU \pm \sqrt{eU(2mc^2 + eU)}}{mc^2} \ . \tag{4.6}$$

The purpose of the experiments is to measure the isotope shift $\delta\nu_{IS}$. The laser frequency remains fixed, and the two atomic resonances of the isotopes occur at different voltages fulfilling the condition

$$
\begin{aligned}
\nu_L &= \nu_0^{(1)} \frac{m_1 c^2 + e\, U^{(1)} \pm \sqrt{e\, U^{(1)}(2m_1 c^2 + e\, U^{(1)})}}{m_1 c^2} \\
&= \nu_0^{(2)} \frac{m_2 c^2 + e\, U^{(2)} \pm \sqrt{e\, U^{(2)} (2m_2 c^2 + e\, U^{(2)})}}{m_2 c^2} \ , \\
\text{where} \quad \nu_0^{(2)} &= \nu_0^{(1)} + \delta\nu_{IS} \ .
\end{aligned}
\tag{4.7}
$$

By solving equation (4.7) the full relativistic formulae for the isotope shift are derived, which can be found in Appendix C.4.

To estimate the order of magnitude of the frequency shifts for neon, the transition $2s^2\,[2p^5\,(^2P^0_{3/2})\,3s]_2 \to 2s^2\,[2p^5\,(^2P^0_{3/2})\,3p]_2$ with a transition wave number of 16274.01942(11) cm^{-1} [Jun82] was chosen. With the atomic mass of ^{20}Ne, $m(20) = 19.992440176(3)$ u [Aud93], the following values of practical interest are calculated.

- Doppler shift for ^{20}Ne caused by the primary acceleration voltage of 60 kV: $\delta\tilde{\nu}_D = +41.36$ cm$^{-1} \equiv 1.240$ THz.

- Isotopic Doppler shift (see appendix C.3) between ^{20}Ne and ^{21}Ne: $\delta\nu_{iso}^{20,21} = 29.10$ GHz.

- Frequency interval corresponding to the voltage sweep range of the post-acceleration (± 10 kV) for ^{20}Ne: $\Delta\tilde{\nu}_D = 6.927$ cm$^{-1} \equiv 207.7$ GHz.

- Differential Doppler shift for ^{20}Ne (see appendix C.2) at a beam energy of 60 keV: $\delta\nu_{diff} = 10.35$ MHz/V.

4.2 Detection Methods Used for Neon

Traditionally the detection of atomic excitations by laser light is done by detecting the fluorescence light emitted by the atoms. This light emitted in the optical detection region (see Fig. 3.4) is collected by a light guide and detected by a photomultiplier. The efficiency of photon detection is rather low. Limitations are due to a small solid angle of $\approx 2\%$ covered by the collection optics, the quantum efficiency of the photomultiplier of $\approx 10\%$, losses from optical pumping and charge exchange which altogether lead to an overall efficiency of detecting fluorescence photons of about 10^{-4}. The laser beam travelling through the apparatus causes stray-light background in the optical detection of typically a few thousand counts/(sec mW). To be able to detect a proper resonance the signal to noise ratio should be larger than: $S/\sqrt{N} > 1$; with the above estimate for the stray light one ends up with about 100 counts/sec in the resonance.

The experiment on neon relies on optical pumping from the metastable $2p^5\,3s$ state to the ground state (see Figs. 4.1, and 4.2). Taking the spectroscopic transition as an example, the branching ratio of pumping to the ground state compared to the decay back to the metastable state is 43%. Thus, the atom will emit in average only two fluorescence photons before it is pumped to the ground state. Taking the estimates altogether the optical detection limit is about 10^6 atoms/sec for a spin $I = 0$ neon isotope. For isotopes with $I \neq 0$ the beam fluxes have to be even higher, because the transition strength is distributed over the hyperfine structure components.

4.2.1 Detection Methods Used in Collinear Laser Spectroscopy

From the last section it became clear that a more sensitive detection techniques for isotopes produced with low yields is needed. This was the starting point of a development of non-optical detection techniques. The collinear laser-spectroscopy experiment utilizes in general four detection methods to investigate nuclei far from stability:

- Fluorescence detection of the optical resonance.

- Resonance detection based on state selective *neutralization* [Ver92] and state preparation by optical pumping.

- Resonance detection by the use of collisional *ionization* [Neu86].

- The β-asymmetry method which is based on spin polarization by optical pumping with circularly polarized laser light and detection of the β-decay [Arn87].

Of these four techniques, the optical detection and the collisional ionization method were used in the present experiments on neon. While the optical detection is straightforward, the collisional ionization detection requires some explanation.

4.2.2 Populating the Initial State by Charge-Exchange Neutralization

The collisional ionization detection-method is based on differences in the ionization energy of two atomic levels. The ionization cross-sections in a collisional process depend on the energy

transfer needed for ionization out of a particular atomic state. Combined with optical pumping, the collisional ionization technique can be used for detecting the change of population due to the interaction of the atoms with the laser light.

The initial state of the optical pumping process can be populated by a suitable choice of the charge-exchange partner used for neutralizing the beam. The ionization energy of the target atom in the collision has to be close to the energy of the level to be populated.

This method is especially suitable for noble gases. In the *neutralization* process the metastable level $[2p^5\,(^2P^0_{3/2})\,3s]_2$ of neon can easily be populated by choosing sodium as an appropriate charge-exchange partner. These metastable atomic levels can be excited to a $[2p^5\,(^2P^0_{3/2})\,3p]_2$ state, which decays via another $2p^5\,3s\,(J=1)$-state to the $2p^6$ atomic ground state (see Fig. 4.1). The alkali metal sodium, used for the charge exchange, has the following
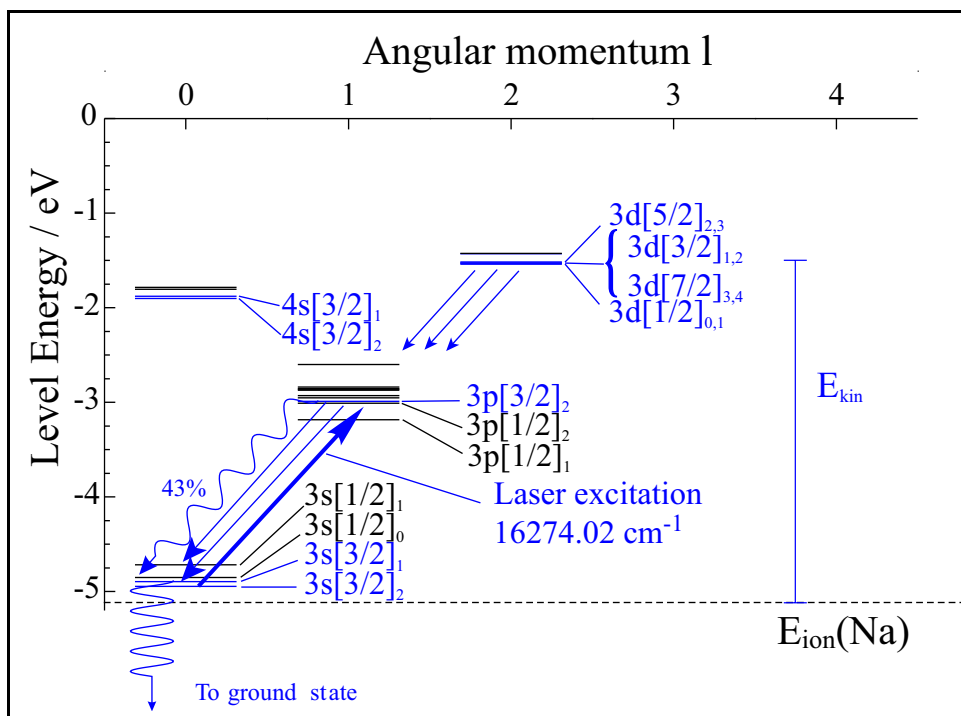
Fig. 4.1: *Level scheme for the charge-exchange process and the laser excitation. The sine like arrows indicate the decay to the ground state, the thin lined arrows the relaxation from higher levels populated in the charge-exchange process. Note the different Racah notation of the levels which was chosen for a better overview.*

physical properties [Lid00]:

Solid density: 968 mg/cm^{-3}

melting point: 370.87 K = 97.72°C

boiling point: 1156 K = 883°C

electronic configuration: $1s^2\,2p^6\,3s^1$

ionization energy: 5.1391 eV

The neutralization process populates predominantly the $[2p^5\,(^2P^0_{3/2})\,3s]_2$ state of neon which has a level energy of -4.9455 eV. The energy difference between the level energy of neon and ionization energy of sodium, $\Delta E = E_{ion}(\mathrm{Na}) - E_n(\mathrm{Ne}) = 0.1936\ eV$, has to be taken from the kinetic energy of the ions and results in a small kinetic energy shift. The process can be expressed by the equation:

$$Ne^+ + Na + E_{kin} \rightarrow Ne^* + Na^- + E_{kin} - \Delta E \tag{4.8}$$
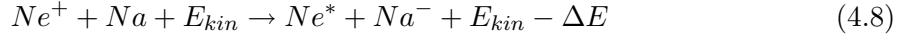
Besides the metastable $[2p^5\,(^2P^0_{3/2})\,3s]_2$ state of neon, higher levels are populated as well in the charge-exchange process. According to equation (4.8) this translates into an additional kinetic energy loss corresponding to the difference in ionization energy of sodium and the energy of the populated level. This loss in kinetic energy has effects on the observed line shape which will be discussed next section 4.3. An energy-level diagram showing some of the levels involved in the charge exchange and laser excitation is shown in figure 4.1. The figure shows parts of the level scheme of Ne I [NIS99], excluding the ground state, which has an energy of -21.5645 eV.

4.2.3   State Preparation by Optical Pumping

At resonance with the laser, the atoms are excited from the metastable $2p^5\,3s$ state to a higher level of the configuration $2p^5\,3p$. Three optical excitations were involved in the experiment (see Fig. 4.2).

(A) $2s^2\,[2p^5\,(^2P^0_{3/2})\,3s]_2 \rightarrow 2s^2\,[2p^5\,(^2P^0_{1/2})\,3p]_2$, anticollinear voltage-calibration transition (see Chap. 5), $\tilde{\nu}_0 = 16816.67$ cm^{-1}, $A_{ki} = 1.13 \times 10^7$ 1/s [NIS99]

(B) $2s^2\,[2p^5\,(^2P^0_{3/2})\,3s]_2 \rightarrow 2s^2\,[2p^5\,(^2P^0_{1/2})\,3p]_1$, collinear voltage-calibration transition (see Chap. 5), $\tilde{\nu}_0 = 16730.27$ cm^{-1}, $A_{ki} = 3.51 \times 10^6$ 1/s [NIS99]

(C) $2s^2\,[2p^5\,(^2P^0_{3/2})\,3s]_2 \rightarrow 2s^2\,[2p^5\,(^2P^0_{3/2})\,3p]_2$, spectroscopic transition,
$\tilde{\nu}_0 = 16274.01942(11)$ cm^{-1} [Jun82], $A_{ki} = 2.82 \times 10^7$ 1/s [NIS99]

Each of these levels can decay via intermediate levels to the $2s^2\,2p^6$ ground state as is shown schematically in figure 4.2. All three lines allow efficient optical pumping, so that a fast depletion of the metastable level can be achieved.
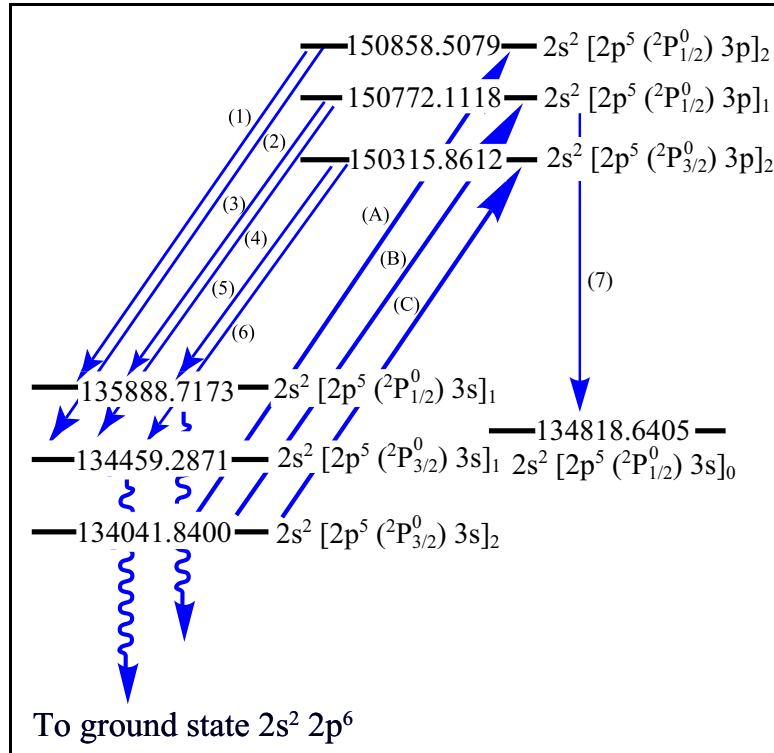
Fig. 4.2: *Optical transitions used in the neon experiments, with level energies in cm^{-1}. Radiative decays are labelled by (1)-(7), the laser excitation by (A)-(C). The transition probabilities are taken from [NIS99]:*
(1) $A_{ki} = 2.33 \times 10^7$ 1/s, (2) $A_{ki} = 1.81 \times 10^7$ 1/s,
(3) $A_{ki} = 2.17 \times 10^7$ 1/s, (4) $A_{ki} = 6.70 \times 10^5$ 1/s,
(5) $A_{ki} = 1.74 \times 10^7$ 1/s, (6) $A_{ki} = 4.16 \times 10^6$ 1/s,
(7) $A_{ki} = 2.79 \times 10^7$ 1/s,

4.2.4 State Detection by Collisional Ionization

The detection of optical pumping between the metastable state and the ground state makes use of the different ionization cross sections of the state the atom is in. The ionization energy of the $2s^2\,2p^5\,[2p^5\,(^2P^0_{3/2})\,3s]_2$ level is 4.9455 eV, whereas the ionization from the ground state takes 21.5465 eV. This energy difference causes considerably different cross sections for ionization in collisions with a gaseous partner. By the use of a special vacuum chamber downstream of the optical detection region it is possible to introduce an interaction region for the collisional ionization which can be operated at gas pressures up to 10^{-2} mbar, the so-called "gas target" (see Fig. 3.4, and Sec. 3.2.1). The cross section dependencies on the atomic state and on the collisional partner were investigated in depth in the PhD thesis of W. Borchers [Bor89a] and in the diploma thesis of U. Georg [Geo90] for the noble gases radon and xenon. It was found that molecular chlorine generally gave the highest ionization rates and the best discrimination between the two states.

In the startup phase of the experiments on neon, similar investigations were performed in a series of on- and off-line measurement. The results of the off-line tests are documented in the diploma thesis of G. Kotrotsios [Kot99]. Several gases were tested and again chlorine was judged as the most efficient collision partner for detecting the optical resonances.

Fig. 4.3: *Signal to noise ratio of ^{22}Ne. Deflected-ion signal after gas target.*
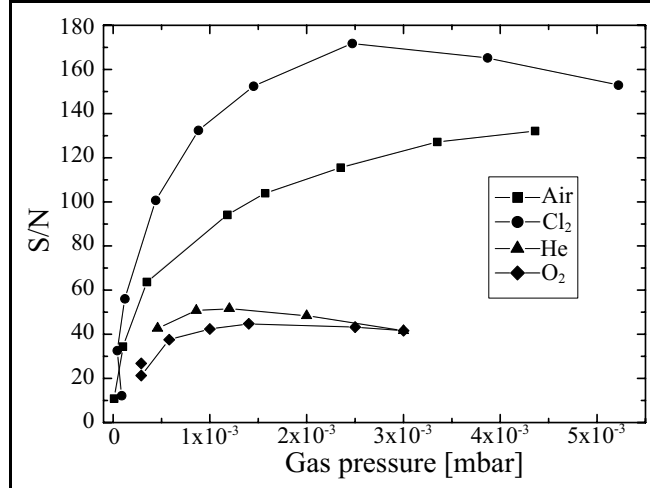
The plot shown in figure 4.3 is a summary of the tests done in the first two runs at ISOLDE. It shows the signal-to-noise ratio

$$S/N = \frac{\text{Counts(Signal)}}{\sqrt{\text{Counts(Background)}}} \; , \tag{4.9}$$

for four different gases as a function of the gas pressure inside the gas target. For neon, like for other noble gases, chlorine yields best performance as a target. A measured resonance with the quantities background and signal is visualized in figure 4.4.
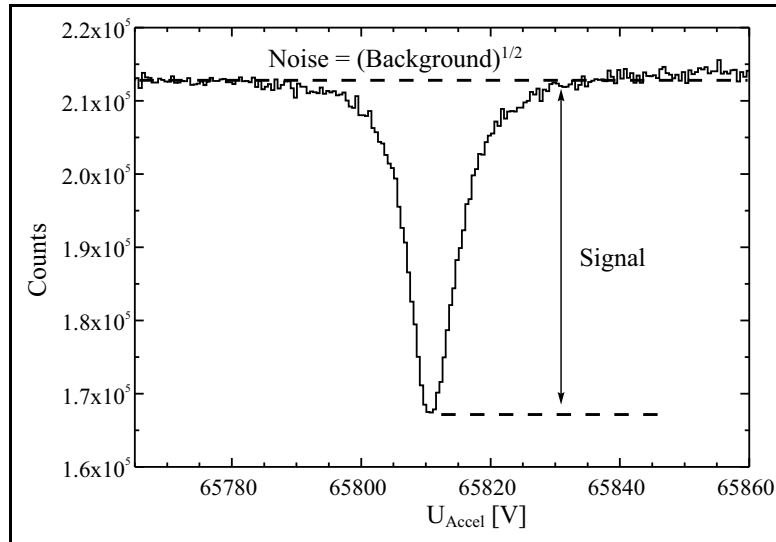
Fig. 4.4: *Line shape of a resonance in the non-optical detection. The figure shows the ion signal for the stable isotope ^{22}Ne.*

The detection of the Ne^+ ions in the beam after the gas target as a function of the laser frequency reveals the optical resonance as flop-out signal (see Fig. 4.4) corresponding to the fact that the ionization cross section is smaller in the ground state than in the metastable state.

Efficient optical pumping requires relatively high laser powers. In the optical detection

measurements typical laser powers are in the range between 600 μW to 1 mW. The typical laser power for the non-optical detection were about 10 times higher which is required a complete depopulation of the metastable level and maximum non-optical signals. These differences in laser power give an additional line broadening in the non-optical spectra. The different excitation conditions cause systematic deviations of the line positions determined from optical or non-optical spectra, due to the correlation between linewidth and line position in the fits with the asymmetric line shape introduced in the previous section. The deviations can be determined experimentally and are discussed in chapter 6.

4.3 Asymmetric Line Shapes

The resonance lines observed in collinear laser spectroscopy deviate in shape from a Lorentzian profile with the natural linewidth. This natural linewidth is of the order of 10 MHz for the transitions used in the present experiments on neon. There are several effects which change the shape and the width of the optical line: (i) The residual Doppler width contributed a broadening with an unknown line shape determined by the ion source. (ii) Saturation for efficient optical pumping broadens the Lorentzian width of the observed resonance lines from their natural width. (iii) An additional asymmetric broadening is evoked by the population of higher levels in the charge-exchange process thus causing strong deviations from the natural shape.

As discussed in the previous section, the charge-exchange process populates most efficiently the levels closest in energy to the ionization energy of sodium. Higher excited levels are populated with lower cross sections. The population of these higher excited levels has an influence on the line shape observed in the experiment. As pointed out before (see Eqn. (4.8)), atoms loose a small fraction of their kinetic energy which is equal to the difference

$$\Delta E_{kin} = E_{ion}(Na) - E_n(Ne) , \tag{4.10}$$

and depends on the neon level that is populated.

The atoms with smaller energy contribute to a low energy "tail" in the velocity distribution, and this gives the asymmetric broadening of the absorption profile. In a simple model, the population amplitude can be assumed to decrease exponentially with energy difference between the sodium ionization energy and level energy in neon. If an atom leaves the charge-exchange process in a higher excited level, it can only participate in the absorption of laser light, if this level decays to the $[2p^5\,(^2P^0_{3/2})\,3s]_2$ metastable state.

Within the time of flight through the interaction region (about 0.5 μs), every atom contributes with a power-broadened Lorentzian line shape to the detected resonance which consequentially is a sum of Lorentzians of the same width. The amplitudes of which decrease exponentially as a function of the energy difference to the ionization energy of sodium. This effect as an explanation of the asymmetrical lines is known since many years [Mue83]. It is mathematically approximated by a convolution of a Lorentzian with an exponential function:

$$F(x) = \int_{-\infty}^{+\infty} \frac{\Gamma/2}{(x - x_0)^2 + (\Gamma/2)^2} \times e^{-\frac{1}{\tau}(x - x_0 - x')^2} \, dx' \tag{4.11}$$

a Gaussian Doppler width can be taken into account, which can be done by convoluting a Voigt-profile (convolution of a Gaussian and a Lorentzian profile) with the exponential function. Experimentally such a Gaussian width was found to be negligible in the experiments on neon, meaning that the replacement of the Lorentzian by a Voigt profile in equation (4.11) did not improve the fits of experimental spectra. However, these fits show a strong dependence of the fitted line position on the asymmetry parameter τ, which has to be taken into account very carefully in the data analysis. An experimental spectrum with a broadened "tail" on the low energy side of the line is shown in figure 4.5.
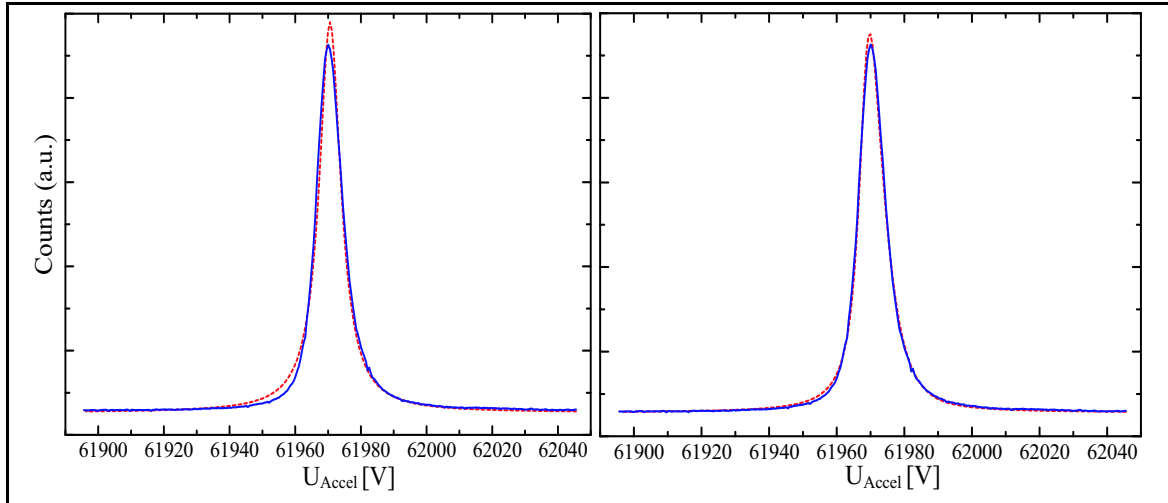
Fig. 4.5: *Comparison of Lorentzian and convoluted line fit. In blue the experimental spectrum, the fit is plotted as red dashed line. The plot to the left shows the fit of a Lorentzian line shape. The plot to the right shows the fit of a convoluted line shape Lorentzian ⊗ exponential to the same experimental spectrum.*

Chapter 5

Measurement of Beam Energies
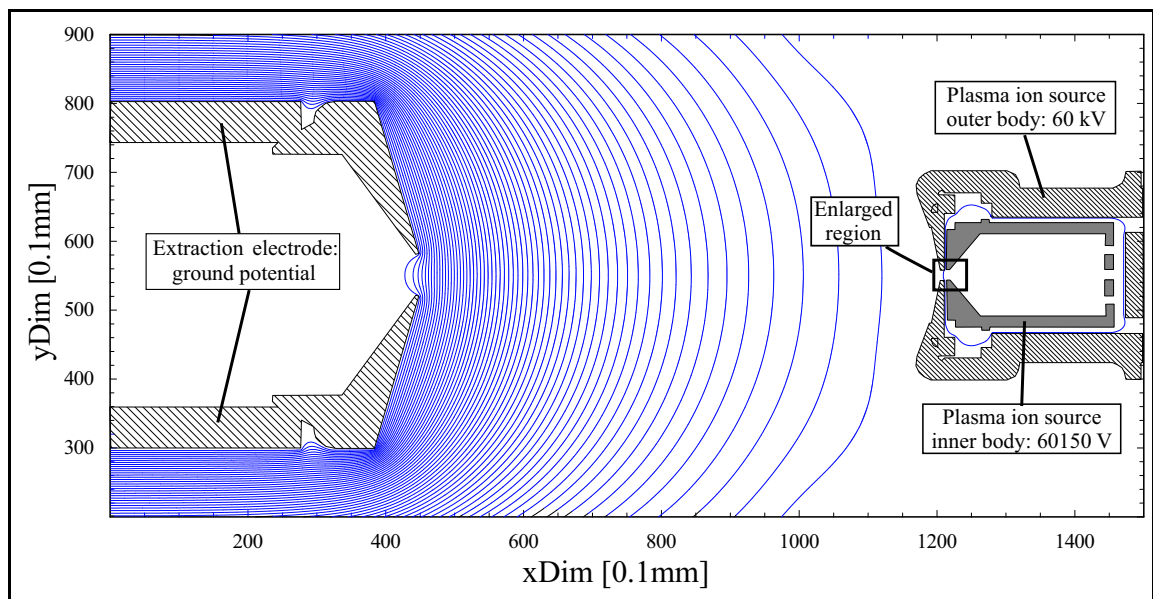
Fig. 5.1: *Field distribution between the plasma ion source and the extraction electrode. The displayed field lines represent voltage steps of 1 kV.*

As mentioned in the previous chapters, the requirements on the accuracy of the measured isotope shifts for the determination of field shifts become increasingly demanding with decreasing nuclear charge Z. The order of magnitude of the field shift in the chosen neon transition is expected to be about 10 MHz. For comparison, the isotopic Doppler shift between two neon isotopes with $\Delta m = 1$ u is of the order of 30 GHz. In the experiment the frequency positions of the optical resonance lines are measured via the beam energy at resonance which is directly linked to the electrical potential difference accelerating the ion. To determine the frequency differences between neighboring isotopes with an accuracy of 1 MHz, corresponding to a 10% accuracy of the field shift, it is necessary to know the beam energy, i.e. the accelerating voltage, to 3×10^{-5}. For the ISOLDE acceleration voltage of 60 kV this corresponds to 2 V.

Thus, the beam energy is the crucial limitation for the desired accuracy of the measurements on neon isotope shifts. It is possible to measure the applied voltages (the ISOLDE acceleration voltage, the anode voltage of the plasma ion source and the retardation volt-

ages applied to the charge-exchange region) with standard voltage measurement equipment to about 10^{-4}, but still the *real* acceleration potential seen by the ions, is not well known. The major part of the uncertainty is due to the unknown potential at which the ionization of the extracted neon atoms takes place in the plasma ion source. From experience one only knows that this potential is relatively close to the anode potential of typically about $+150$ V with respect to the main acceleration potential of about $+60$ kV.
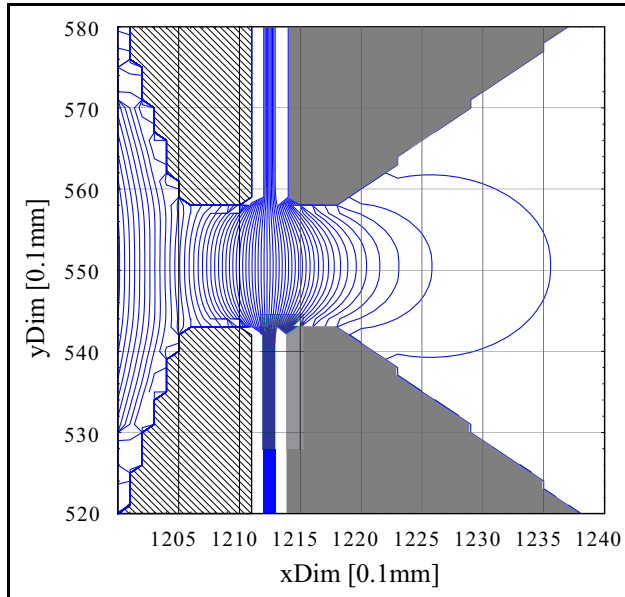
Fig. 5.2: *Enlargement of the outlet nozzle region of the plasma ion source. The potential lines shown in the figure represent steps of 3 V.*

To illustrate the conditions in the ion source, the potential distribution in the vicinity of the source was simulated utilizing the computer program SIMION™, version 7.0, as shown in figures 5.1 and 5.2. These simulations were performed without taking into consideration the plasma effects inside the ion source due to restrictions in the simulation program.

In figure 5.1, the equipotential lines represent voltage differences of 1000 V. figure 5.2 shows an enlargement of the source's outlet nozzle. Whereas the potential gradient is very small inside the source itself, it becomes quite large in the region of the nozzle (one step between the lines represents a Voltage step of 3 V). Hence, the potential "seen" by the ion becomes strongly dependent on the position of ionization. To illustrate the order of magnitude; close to the outlet nozzle a shift of the ion extraction of 0.5 mm results in a voltage difference of about 30 V, as can be seen in figure 5.2.

To meet the described requirements, a new method of measuring the beam energy was implemented. As a fortuitous circumstance, neon offers two atomic transitions which can be used in a collinear/anticollinear laser spectroscopy experiment, to measure the Doppler shift and thus to determine the velocity of the atoms in the optical excitation region. The following section is dedicated to a description of this experimental method.

5.1 Beam-Energy Measurement by Collinear Laser Spectroscopy

The idea of using laser spectroscopy in collinear geometry to determine ion beam energies, and thus to measure high voltages with high precision, was published by Poulsen [Pou82] and by Arnold *et al.* [Arn82] in the early eighties. The method used to calibrate the energy in the neon measurements relies on an excitation scheme known as "inverted Λ-configuration" or "V-configuration", a resonant excitation from a common ground state to two close lying excited levels.

In the publication of O. Poulsen the excitation scheme was a closed system, aiming at

efficient detection of the fluorescence light. In a closed system no optical pumping to levels outside the system takes place. In contrast to this, the excitation scheme in neon is open, and the optical pumping out of the V system is used for the detection. The use of such systems offer a substantial advantage: Whereas closed Lambda-systems are difficult to find, the method used in this thesis only requires two independent transitions which lie within the working range of the collinear spectroscopy setup.

5.1.1   Basic Equations

The Doppler shift caused by the atom-beam velocity depends on the parallel or antiparallel direction of the laser beam, and causes frequency shifts of opposite signs as shown in equation (4.2). The frequency shift for the excitation in the direction of the atom beam $(+\delta\nu_D)$ is positive in the laboratory system; in the opposite direction, the Doppler shift evokes a negative frequency shift $(-\delta\nu_D)$.

Because the shifts act in opposite directions, a beam velocity can be found where the energy difference between two different atomic levels gets exactly equal in the laboratory system:

Fig. 5.3: *Excitation scheme used for the collinear /anti-collinear excitation in the beam-energy measurement. The hatched arrows denote the frequency of the transitions in the laboratory system, the filled arrows in the moving frame of the atoms.*

$$\nu_L = \nu_0^{(1)} \frac{1+\beta}{\sqrt{1-\beta^2}} = \nu_0^{(2)} \frac{1-\beta}{\sqrt{1-\beta^2}} \tag{5.1}$$

As shown by the equality to ν_L, the transition can be induced by laser beams of the same frequency, but travelling in opposite directions.

The effects of the Doppler shift on the excitation of both atomic levels is illustrated in figure 5.3. The dependence of the transition frequencies on the acceleration voltage is shown in figure 5.4. The plotted graphs in the latter figure represent the two transitions of neon used in the present beam-energy measurements. To be able to calculate the beam energy, one has to take the expressions for the Doppler-shifted transition frequencies in the full relativistic form. The Doppler shifted transition frequency is given by equation (4.2). The relativistic factor β is related to the beam energy by equation (4.5). To find the voltage of equal transition frequencies one has to use expression (4.6). Both frequencies are equal in

Fig. 5.4: *Relation between frequency and voltage in the neon transitions used for the beam-energy measurement. The gray square shows the working region of the COLLAPS experiment.*

the laboratory frame if

$$
\begin{aligned}
\nu_L &= \frac{\nu_0^{(1)}}{mc^2} \cdot \left[mc^2 + e\,U + \sqrt{e\,U(2mc^2 + e\,U)} \, \right] \qquad \text{(collinear)} \\
&= \frac{\nu_0^{(2)}}{mc^2} \cdot \left[mc^2 + e\,U - \sqrt{e\,U(2mc^2 + e\,U)} \, \right] \qquad \text{(anticollinear)} \, .
\end{aligned}
\tag{5.2}
$$

Solving for the beam energy $e\,U$ yields

$$
e\,U = \frac{mc^2 \left(\sqrt{\nu_0^{(1)}} - \sqrt{\nu_0^{(2)}} \right)^2}{2\sqrt{\nu_0^{(1)}\,\nu_0^{(2)}}} \, .
\tag{5.3}
$$

The Doppler shifted frequency at this voltage can be calculated easily by the expression:

$$
\nu_{coll} = \nu_{anti} = \sqrt{\nu_0^{(1)}\,\nu_0^{(2)}}
\tag{5.4}
$$

5.1.2 The Neon Levels Used in the Experiment

As outlined, the beam-energy measurement is based on collinear/anticollinear laser spectroscopy employing two energetically close lying atomic transitions. In principle any element, delivered by the ion source, with such a pair of atomic or ionic transitions can be utilized to calibrate the beam energy, as long as their Doppler shifted transitions are crossing within the working range of the experimental setup. Corrections may have to be taken into account, e.g. when the ionization inside the ion source takes place at different potentials for different chemical elements. Preferably of course, the measurement should be done using the element to be investigated in the spectroscopy experiments.
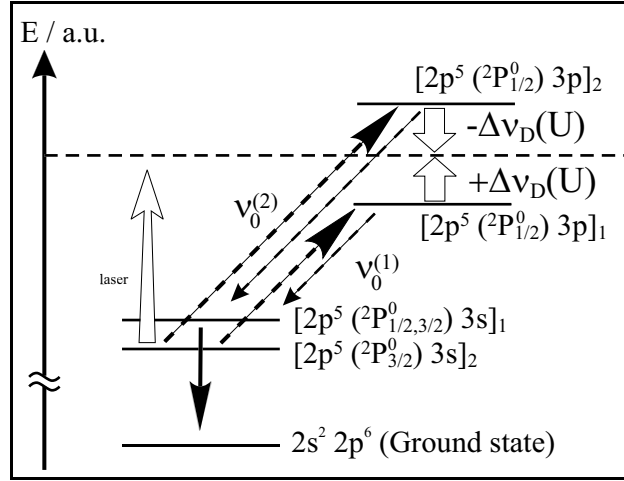
Fig. 5.5: *Transitions used for beam-energy measurement. The two transition coincide at a beam energy of 61758.77 eV.*

Neon offers the ideal transitions to calibrate beam energies of about 60 keV. These are for ^{20}Ne

$1s^2\,2s^2\,[2p^5\,(^2P_{3/2}^0)\,3s]_2 \rightarrow [2p^5\,(^2P_{1/2}^0)\,3p]_1$: $\tilde{\nu}_0^{(1)} = 16730.2704470(87)$ cm^{-1} [Zha87], used in collinear geometry, and

$1s^2\,2s^2\,[2p^5\,(^2P_{3/2}^0)\,3s]_2 \rightarrow [2p^5\,(^2P_{1/2}^0)\,3p]_2$: $\tilde{\nu}_0^{(2)} = 16816.66634(2)$ cm^{-1} [Jun82], used in anticollinear geometry.

According to equation (5.3) both transitions coincide at a beam energy of 61758.77 eV, when they are excited by laser light of $\tilde{\nu} = 16773.413$ cm^{-1}. With the transition used for the measurement on radioactive isotopes, they have in common the metastable level ($[2p^5\,(^2P_{3/2}^0)\,3s]_2$) which is populated efficiently by the near-resonant charge transfer with the sodium vapor. The excitation and optical pumping to the ground state is shown in figure 5.5. Both wave numbers are known independently ([Zha87, Jun82]) with sufficient precision, and the laser light can easily be generated with the use of Rhodamine 6G laser dye.

5.1.3 The Experimental Setup

The experimental setup used to perform the beam-energy measurement is the same as used for the collinear laser-spectroscopy experiment which is described in chapter 3. The decisive difference between the standard and the beam-energy measurement-setup is the presence of a mirror at the exit side of the apparatus. This mirror is used to reflect the laser beam in itself (see Fig. 5.6).

This kind of setup enables the simultaneous excitation and detection of the two resonances in one measurement. By using the non-optical detection, problems caused by stray light from the reflected laser beam, which would affect optical measurements, are avoided. Using the same pair of transitions for two different isotopes opens the additional possibility to calibrate independently the post-acceleration voltages which are applied to the charge-exchange cell.
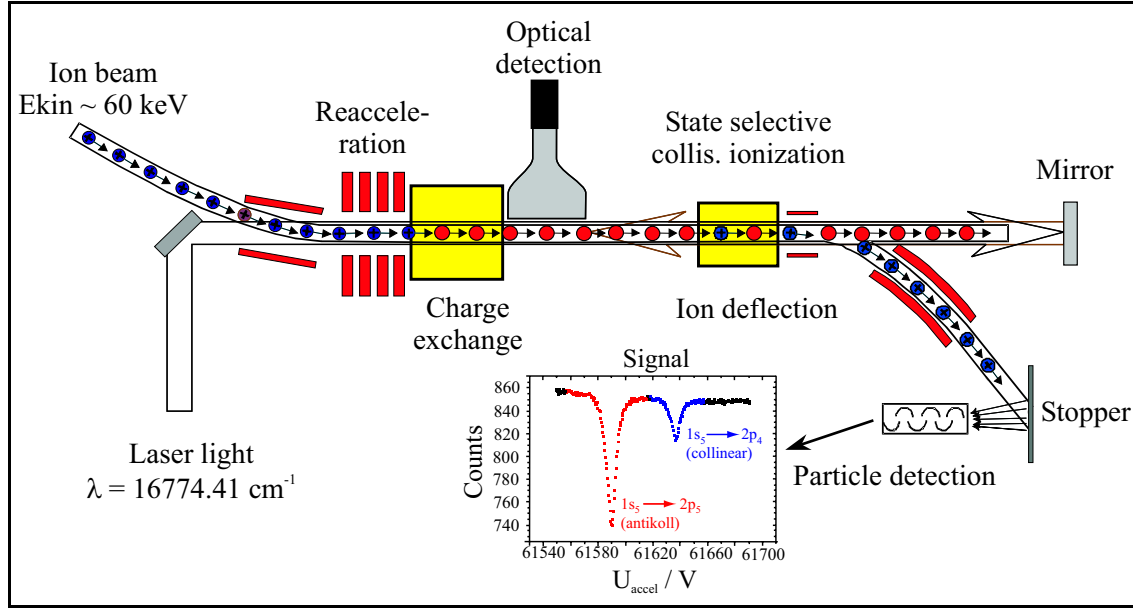
Fig. 5.6: *Experimental setup used for the beam-energy measurement. A mirror is used to retro-reflect the laser beam. It is placed at the end of the apparatus. Ions from collisions in the gas target are detected by a secondary electron multiplier (see Sec. 3.3.1).*

5.1.4   Effects of Laser Detuning

For a detailed analysis, the beam energy expressed in volts has to be split up into the voltages contributing to the total accelerating potential difference. It can be written as (see Eqn. (3.3))

$$E_{beam} = e\,U_{tot} = e\,\big[\,\underbrace{U_{ISOL} + U_{anode,plasma}}_{U_{accel},\,U_{calib}} + \underbrace{U_{DAC} \times F_{kepco} + \overbrace{U_{prema} \times D_{div}}^{U_{Fluke}}}_{U_{post}}\,\big]\,. \qquad (5.5)$$

Where $F_{kepco} \approx 50$ is the amplification factor of the Kepco HV-amplifier. U_{prema} is the readout voltage of the Prema precision digital voltmeter. Note that U_{accel} is used as symbol for the sum of voltages applied to the ISOLDE ion source and the anode, which are measured electrically. U_{calib} is used for the beam energy of the ions from the source calibrated by the collinear/anticollinear method.

For experimental reasons it is preferable not to choose the laser frequency exactly as given by equation (5.4). There the two resonances overlap and the beam energy is given by the simple formula (5.3). First of all, it is difficult to set the laser frequency with the required precision: The differential Doppler shift for ^{20}Ne is 10.35 MHz/V. The line positions have to match with a precision substantially better than 1 V. Thus, the absolute laser wave number has to be determined to better than 3×10^{-4} cm^{-1}. This corresponds to a relative precision of 2×10^{-8}, which cannot be achieved easily with standard wavelength measurement-equipment. Secondly the analysis of the two matching lines with respect to their peak positions depends critically on the assumptions on the asymmetric line shapes. Furthermore both lines have different amplitudes because of the very different efficiencies for optical pumping to the ground state. The $[2p^5\,(^2P^0_{3/2})\,3s]_2 \rightarrow [2p^5\,(^2P^0_{1/2})\,3p]_2$ transition (anticollinear) has a branching ratio of 78.5% to the ground state, and 21.5% back to the metastable level, causing large signal depths of typically 15% (see Fig. 5.5). In contrast to this the $[2p^5\,(^2P^0_{3/2})\,3s]_2 \rightarrow$

$[2p^5\,(^2P^0_{1/2})\,3p]_1$ (collinear) transition can decay via three branches: 0.5% to $[2p^5\,(^2P^0_{3/2})\,3s]_2$, 57.9% to the ground state, and 41.6% to the $[2p^5\,(^2P^0_{1/2})\,3p]_0$ level which cannot decay to the ground state and is inaccessible for the laser excitation. This gives typical signal depths of the order of about 5%. An example of a typical spectrum is shown in figure 5.7.

For these reasons a slightly different approach was chosen, where the laser frequency is detuned from the condition (5.4) by a few 100 MHz. As a result two separated resonance
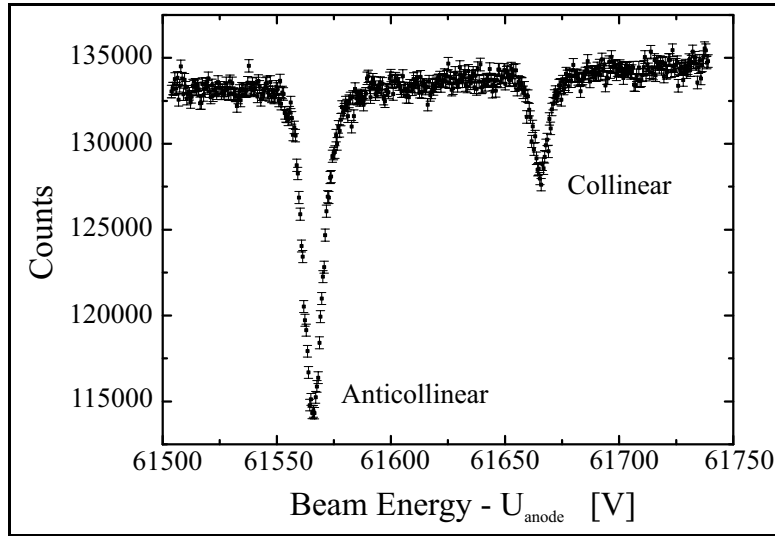
Fig. 5.7: *Typical spectrum of a voltage calibration measurement.*

lines, which can be fitted properly, are obtained in a narrow scan of the post-acceleration voltage. The separation of the line positions have to be taken into account in equation (5.5) and cause the replacements:

$$\text{Collinear line:} \quad U_{post} \rightarrow U^{(1)}_{post} \quad \text{corresponding to} \quad U_{DAC} \rightarrow U^{(1)}_{DAC} \tag{5.6}$$

$$\text{Anticollinear line:} \quad U_{post} \rightarrow U^{(2)}_{post} \quad \text{corresponding to} \quad U_{DAC} \rightarrow U^{(2)}_{DAC} \tag{5.7}$$

Incorporating these replacements in equation (5.2), the calibrated acceleration voltage has to be determined via the more complicated equation:

$$
\begin{aligned}
\nu_L &= \frac{\nu^{(1)}_0}{mc^2} \cdot \left[mc^2 + e\,U^{(1)} + \sqrt{e\,U^{(1)}\,(2mc^2 + e\,U^{(1)})} \right] \quad \text{(collinear)} \\
&= \frac{\nu^{(2)}_0}{mc^2} \cdot \left[mc^2 + e\,U^{(2)} - \sqrt{e\,U^{(2)}\,(2mc^2 + e\,U^{(2)})} \right] \quad \text{(anticollinear)} , \quad (5.8)
\end{aligned}
$$

where the total acceleration voltages are given by equations (5.5), (5.6), and (5.7). Solving the equation for U_{calib} yields the expression for the calibrated acceleration voltage which depends on the line positions measured in terms of the total post-acceleration voltage $U^{(1)}_{post}$

and $U_{post}^{(2)}$

$$
\begin{aligned}
U_{calib} \;=\;& \frac{\left(\nu_0^{(1)} + \nu_0^{(2)}\right)\sqrt{m^2 c^4 \left(\nu_0^{(2)} - \nu_0^{(1)}\right)^2 + e^2 \nu_0^{(1)} \nu_0^{(2)} \left(U_{post}^{(2)} - U_{post}^{(1)}\right)^2}}{2e\left(\nu_0^{(2)} - \nu_0^{(1)}\right)\sqrt{\nu_0^{(1)} \nu_0^{(2)}}} \\
&- \frac{1}{2}\left(U_{post}^{(2)} + U_{post}^{(1)}\right) - \frac{mc^2}{e} \; .
\end{aligned} \tag{5.9}
$$

If $U_{post}^{(1)}$ and $U_{post}^{(2)}$ in Equation (5.9) is given only by the *variable* part of the post-acceleration voltage, $U_{post}^{(1),(2)} = U_{DAC} \times F_{kepco}$, the result is the static part of the total beam energy

$$
U_{stat} = U_{ISOL} + U_{plasma} + U_{Fluke} \; , \tag{5.10}
$$

which is used for the calculation of the voltage divider ratio D_{div} which will be described in section 5.2.5.

It should be mentioned that the possibility of a finite angle between the directions of the laser beam and the ion beam has to be taken into account in the error of the calibrated value U_{calib}.

5.2   Experimental Results of beam-energy measurements

The experimental results of the beam-energy measurements and the voltage divider ratio are discussed in the following section. Besides measuring the beam energy the collinear/anticolinear method was used to calibrate the voltage divider which was used to measure the post-acceleration voltage applied to the charge-exchange cell.

5.2.1   Voltage Measurement by Collinear/Anticollinear Measurements

As discussed in the previous sections, the calibrated voltage U_{calib} is rather close to the conventionally measured voltages $U_{ISOL} + U_{anode}$. If the readout value U_{ISOL}, taken during the beam-energy measurements, and the readout of the anode voltage U_{anode} is summed, and compared with the calibrated voltage U_{calib}, the plots of figure 5.8 and 5.9 are obtained. They show U_{calib} and $U_{ISOL} + U_{anode}$ in the runs 04/2000 and 11/2000 as a function of time:

From these plots one can draw the conclusion that the ion source and a possible miscalibration produce a constant offset voltage to the readout value U_{ISOL}. This offset voltage corresponds to the position dependent potential U_{plasma} experienced by the ions inside the plasma ion source. To determine the ion beam energy in the spectroscopic measurements, the voltage readout of the ISOLDE acceleration voltage U_{ISOL}, which is recorded before every spectroscopic measurement scan, is added to U_{plasma}, calibrated the average values of

$$
U_{plasma} = U_{calib} - U_{ISOL} \; . \tag{5.11}
$$

This offset voltage changes from run to run, and the differences between the anode voltage U_{anode}, measured electrically, and the calibrated plasma voltage U_{plasma}, can become up to several tens of volts depending on the individual ion source. This is shown in the overview of calibrated voltages U_{plasma} is given in table 5.1.
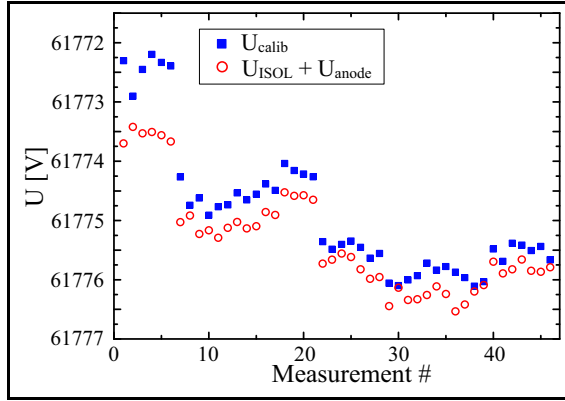
Fig. 5.8: *Plot of the calibrated main acceleration voltage in run 04/2000. The time dependence of the two data sets U_{calib} and $U_{ISOL} + U_{anode}$ is approximately the same.*
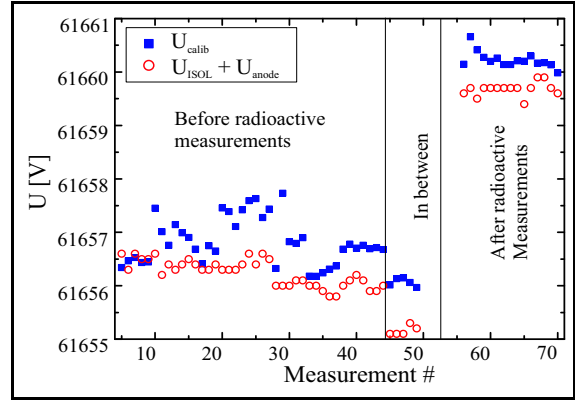
Fig. 5.9: *Plot of the calibrated main acceleration voltage in run 11/2000. Here the two data sets U_{calib} and $U_{ISOL} + U_{anode}$ show a weaker correlation than in 04/2000. Still a constant difference between the voltages can be assumed.*

5.2.2 Discussion of Systematic Errors Sources in the Beam Energy Measurement

The errors of the beam energy calibration have to be treated as systematic errors in the evaluation of the spectroscopic data. The detailed understanding of the voltage calibration errors and their sources is essential for the correct analysis of the experimental data. This section gives an overview of these errors, their origin and their role in the analysis.

Several sources contribute to the systematic error of U_{calib}. To get a closer insight into the relevant error sources, equation (5.2) has to be investigated taking into account all the different voltages used for acceleration (Eqn. (5.5)), and the effects of the laser detuning (Eqns. (5.6), (5.7)). The following parameters have to be considered in the analysis, and contribute to the total systematic error of the isotope shift:

$\nu_0^{(1)}$ **:** Uncertainty of the collinear transition frequency. Causing a systematic error of $\Delta U_{calib}^{sys}(\nu_0^{(1)}) = 0.018$ V.

$\nu_0^{(2)}$ **:** Uncertainty of the anticollinear transition frequency. This causes a systematic error of $\Delta U_{calib}^{sys}(\nu_0^{(2)}) = 0.042$ V.

$\mathbf{m_{20}}$ **:** The mass of ^{20}Ne has to be expressed in eV: $m(20) = 19.992440176(2)$ u [Aud93], where u is the atomic mass unit in eV 1 u $= 931.494013(37)$ MeV [Moh98][1]. The systematic error contribution from the uncertainty of the atomic mass unit is $\Delta U_{calib}^{sys}(u) = 0.078$ V, and with the mass error of ^{20}Ne adds in total up to $\Delta U_{calib}^{sys}(m_{20}) = 0.096$ V.

$\boldsymbol{\alpha}$ **:** Angle between the laser and the atomic beam. This angle can be estimated from the diameters of diaphragms at the entrance and exit of the collinear setup and the length of the setup. Estimating the geometric error conservatively, a deviation δz of 2 mm over a distance Δx of 1 m is assumed. Hence, the angle is given by:

$$\alpha = \arctan[\Delta z/\Delta x] = 0.114° \ . \tag{5.12}$$

---

1 As well available in the internet: http://physics.nist.gov/cuu/Constants/index.html.

The corresponding error is of the order of $\Delta U_{calib}^{sys}(\alpha) = 0.285$ V, which is the largest systematic error contribution to U_{calib}. This error estimate from geometrical considerations holds for the absolute accuracy of any calibration value, while the variation of values taken with the same beam alignment should be independent of $\Delta U_{calib}^{sys}(\alpha)$.

The total systematic error of the beam energy measurement is given by $\sqrt{\sum \left(\Delta U_{calib}(x_i)\right)^2}$ and is 0.31 V.

5.2.3   Beam-Energy Measurement by Isotope Shift Measurements

In the early runs (06/1998, 09/1998, 03/1999, 05/1999), the collinear/anticollinear beam-energy measurement method was not implemented yet. To determine the true beam energy it is possible to utilize the resonance condition for two different isotopes in collinear geometry with the known isotope shift

$$
\begin{aligned}
\delta\nu_L &= \frac{\nu_0^{(1)}}{m_1\,c^2} \cdot \left[m_1\,c^2 + U^{(1)}\,e + \sqrt{U^{(1)}\,e(2\,m_1\,c^2 + U^{(1)}\,e)} \right] \\
&= \frac{\nu_0^{(2)}}{m_2\,c^2} \cdot \left[m_2\,c^2 + U^{(2)}\,e + \sqrt{U^{(2)}\,e(2\,m_2\,c^2 + U^{(2)}\,e)} \right] \;, \\
\text{where} \qquad \nu_0^{(2)} &= \nu_0^{(1)} + \delta\nu_{IS} \;,
\end{aligned}
\tag{5.13}
$$

which can be solved for U_{calib} if the voltages $U^{(1)}$ and $U^{(2)} = U_{calib} + U_{post}^{(1,2)}$ are given by the positions of the resonance lines of the two isotopes. The required data are available as optical measurements on the stable reference isotopes ^{20,22}Ne, which are usually taken before and after each measurement on an unstable isotope. The required isotope shift $\delta\nu^{20,22}$ was determined in the runs with the collinear/anticollinear method with high precision.

5.2.4   Results of the Beam-Energy Measurements

The results of the beam energy calibration are given in table 5.1. They are given in form of plasma voltages U_{plasma} to be added to the ISOLDE voltage readout U_{ISOL} to get the real acceleration voltage U_{calib}. An assumption for this approach is that the any differences between U_{accel} and U_{calib} can be attributed to the ion source and not to a miscalibration of U_{ISOL}. The runs 10/99, 04/00, 07/00 and 11/00 are calibrated by collinear/anticollinear measurements. For the early runs the beam energy measurement was performed indirectly by utilizing the optical measurements and the isotope shift between the stable isotopes ^{20}Ne and ^{22}Ne. The isotope shift used for this was determined in the runs with collinear/anticollinear beam-energy measurement. The table shows the measured plasma voltages for seven of the eight runs on neon with its statistical and systematic errors. The systematic errors of 0.31 V are the same for all the runs with collinear/anticollinear beam-energy measurement and arise from uncertainties in the input values of the wavelengths, masses and the maximum angle between the laser beam and the atom-beam direction α. For the runs with a voltage measurement by using the isotope shift $\delta\nu_{IS}^{20,22}$ the error of the isotope shift adds an additional error of 0.12 V. The error of the divider ratio is not taken into account in the table. The values labelled U_{anode} are the readout values of the anode voltage which can be acquired from by ISOLDE control system.

Note that the differences between U_{anode} and U_{plasma} can differ by more than 30 V (run 03/99). A cross-check of the reliability of this value was done by calculating the isotope shifts $\delta\nu_{IS}^{20,22}$ of this run using U_{anode} and U_{plasma}, respectively. The utilization of U_{anode} in the calculation of $\delta\nu_{IS}$ leads to values which are about 30 MHz off from the literature value, implying a beam energy which is wrong by about 30 V. In contrast the use of U_{plasma} leads to correct isotope shifts between ^{20}Ne and ^{22}Ne. Thus, it is assumed that the different conditions inside the plasma ion source cause the different ion beam energies. This means that the true beam energy can differ appreciably from the value obtained by standard voltage measurements, which obviously necessitates the direct beam-energy measurement.

Table 5.1: *Experimental values of the calibrated plasma voltage U_{plasma} in the neon runs. The systematic error given in the table is the quadratic sum of the errors from different sources (see Sec. 5.2.2).*

run	U_{anode} [V]	U_{plasma} [V]	$U_a - U_p$ [V]	ΔU_{plasma}^{stat} [V]	ΔU_{plasma}^{syst} [V]
09/98	115.36	117.05	-1.69	0.35	0.43
03/99	172.71	138.45	+34.26	0.35	0.43
05/99	150.61	151.50	-0.89	0.14	0.43
10/99	149.59	148.29	+1.30	0.06	0.31
04/00	112.59	114.46	-1.87	0.04	0.31
07/00	190.00	190.90	-0.90	0.11	0.31
11/00	153.53	134.54	+18.99	0.04	0.31

5.2.5 Measurement of the Voltage Divider Ratio

To calibrate the voltage-divider ratio for the measurement of the post-acceleration voltage, the stable isotope ^{22}Ne is utilized together with ^{20}Ne in a collinear/anticollinear measurement. The divider ratio can be determined from the line positions of the collinear and the anticollinear line of ^{20}Ne and ^{22}Ne, which are given for the two isotopes by

$$U_{tot}^{(1),(2)\,20} = \overbrace{U_{ISOL} + U_{plasma}^{20} + U_{prema}^{20} \times D_{div}}^{U_{stat}} + U_{DAC}^{(1),(2)\,20} \times F_{cal}^{20} \times D_{div} \qquad (5.14)$$

$$U_{tot}^{(1),(2)\,22} = \underbrace{U_{ISOL} + U_{plasma}^{22}}_{U_{calib}} + U_{prema}^{22} \times D_{div} + U_{DAC}^{(1),(2)\,22} \times F_{cal}^{22} \times D_{div} . \qquad (5.15)$$

By measuring U_{stat} from the measurement on ^{20}Ne and U_{calib} from the measurement on ^{22}Ne, the four equations (5.14) can be solved for D_{div}. The divider ratio can be calculated from

$$D_{div} = \frac{U_{stat}^{22} - U_{stat}^{20}}{U_{prema}^{22} - U_{prema}^{20}} \qquad (5.16)$$

The required data are available from collinear and anticollinear measurements. Additional systematic errors for the isotope shifts of the two transitions have to be taken into account. These isotope shifts were determined from the weighted means of the results from several publications:

$\delta\nu_{IS}^{(1)\,20,22}$: Collinear line – Weighted mean: 1728.79(16) MHz,

<div align="right">from [Bas97, Bel83, Gut94, Kon92, Wik78, Zha87]</div>

$\delta\nu_{IS}^{(2)\,20,22}$: Anticollinear line – Weighted mean: 1715.3(1.8) MHz,

from [Bel83, Gut94, Kon92, Odi65]

The small error of $\delta\nu_{IS}^{(1)\,20,22}$ is mostly determined by the value of Zhao *et al.* [Zha87] (0.16 MHZ), the other values have error in the order of a few MHz. Thus, the systematic error of D_{div} is determined by the uncertainty of the isotope shift of the anticollinear line $\delta\nu_{IS}^{(2)\,20,22}$.
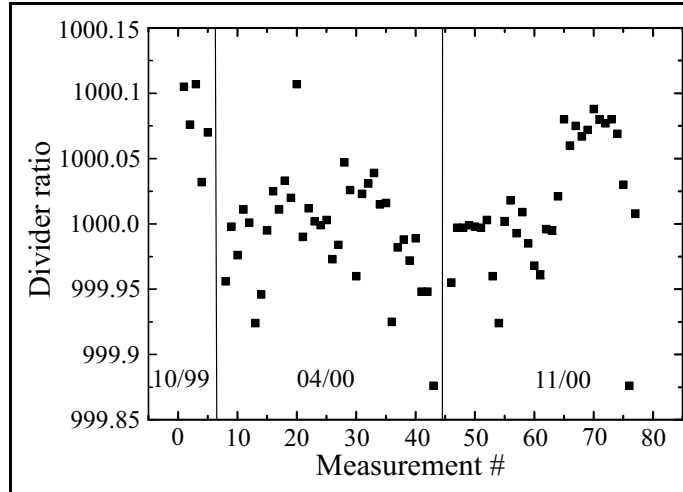
Fig. 5.10: *Voltage divider ratios measured in three different runs. The values scatter around a constant ratio throughout the different measurements.*

The divider ratio of the voltage divider, which is used to measure the dc post-acceleration voltage, is assumed to be constant throughout the runs. This can be justified by the following facts: the accuracy of the divider ratio is specified to be 1000 with an error of 10^{-4}, valid in a temperature range of $+15°$ C $- +35°$C [Jul]. The temperature inside the ISOLDE hall is stabilized to $21 \pm 1°$ C, as well are the humidity conditions.

The ratio was determined in several runs by the collinear/anticollinear method, the experimental values from the runs 10/99, 04/2000 and 11/2000 are plotted in figure 5.10. The

Table 5.2: *Mean values of the divider ratios from four last runs. The earlier runs were not calibrated with the collinear/anticollinear method.*

run	D_{div}	ΔD_{div}
10/99	1000.0780	0.0137
04/00	999.9931	0.0069
07/00	1000.0139	0.0093
11/00	999.9910	0.0034

corresponding mean values together with their errors from the different runs are listed in table 5.2. The final divider ratio is found by calculating the weighted mean of the four tabulated values which is 999.997(3). Additionally the systematic error of $\Delta D_{div}^{syst} = 0.025$ arising from the input data has to be added, which are dominated by $\Delta\delta\nu_{IS}^{(2)\,20,22}$. It is found

$$D_{div} = 1000.00(3) , \tag{5.17}$$

which verifies the specified value and decreases the error compared to the specification by a factor of 3.

Chapter 6

Experimental Results

The experimental results on the neon isotopes will be presented in this chapter. First the hyperfine splitting parameters of the odd-A neon isotopes are discussed, then the isotope-shift data on $^{17-26,28}$Ne are presented.

6.1 Hyperfine Structure and Magnetic Moments of the Odd-A Isotopes

6.1.1 Hyperfine structure analysis

Typical experimental spectra of the hyperfine structures of the isotopes ^{17}Ne, ^{19}Ne, ^{21}Ne, ^{23}Ne, and ^{25}Ne are displayed in Figs. 6.1. These were analyzed using the standard HFS-level-shift formula (2.1). The spectra of the $I = 1/2$ isotopes with large splittings (^{17}Ne, ^{19}Ne, ^{25}Ne) were measured by splitting up the measurement sequence into "windows" which covered the outer small lines and the central lines to minimize the required measurement time without loosing information. Thus, in a first step of the analysis these measurement windows were combined to one single spectrum. Examples of such spectra of ^{17}Ne, ^{19}Ne and ^{25}Ne are shown in figure 6.1.

To obtain the A- and B-factors of the lower and upper atomic state, a χ^2-minimization was performed. The spectra were fitted by the use of one single function describing the complete hyperfine spectrum. The line positions are calculated from a set of coupled equations determined by the selection rules, the nuclear spin and the hyperfine structure parameters of the lower (A_{3s}, B_{3s}) and upper (A_{3p}, B_{3p}) state. The asymmetric line shape is modelled, as discussed in chapter 3, by a convolution of a Lorentzian and an exponential function. The free parameters of the fit were the A- and B-factors of the lower and upper atomic state, the line amplitudes, the common Lorentzian linewidth, the common decay factor of the exponential, the center of gravity of the hyperfine structure, and the parameters of a linear offset to allow for a background having a slope.

To achieve consistency between the optical signal of the stable isotopes and the ion signals the optical line was fitted first by the use of the asymmetric line model. The resulting fitting parameters determine the exponential factor which was used as fixed parameter in the subsequent hyperfine structure fit. The fitting algorithm was provided by the MINUIT fitting package [Jam75].
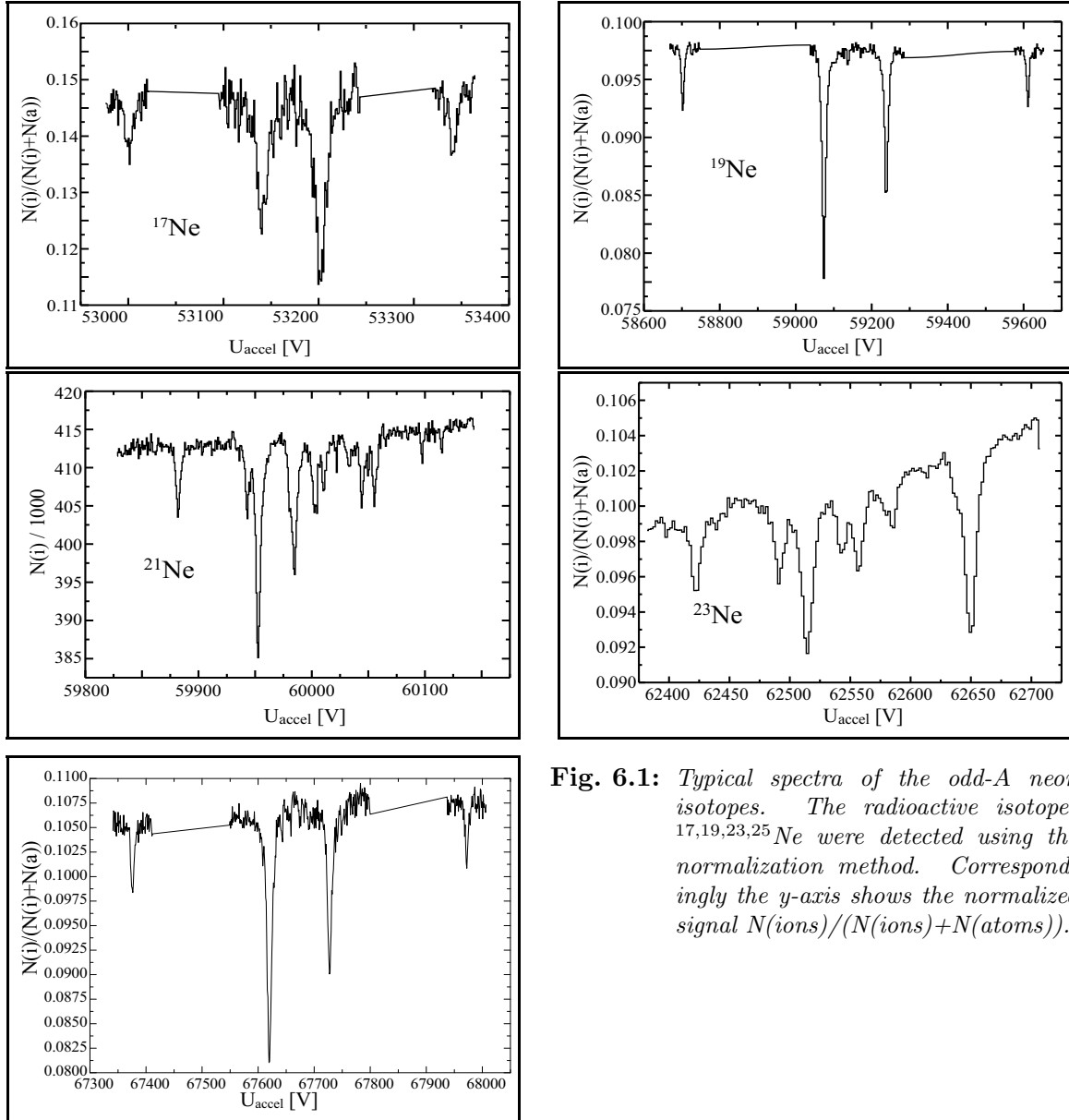
Fig. 6.1: *Typical spectra of the odd-A neon isotopes. The radioactive isotopes ^{17,19,23,25}Ne were detected using the normalization method. Correspondingly the y-axis shows the normalized signal N(ions)/(N(ions)+N(atoms)).*

The resulting A- and B-factors are compiled in table 6.1. The mean values of A_{3s}, A_{3p}, B_{3s}, and B_{3p} were determined by substituting the results of individual measurements again to a horizontal line fit yielding realistic errors. The errors given in table 6.1 were obtained by normalizing the fitting errors with the reduced χ^2 to account for the scattering of the data points, typical χ^2_{red} were of the order of 2.

The comparison with known experimental data from Grosof *et al.* [Gro58] shows good agreement between these high precision measurements and the present results. Nevertheless show the present values a deviation to smaller values. This raises the question if the errors given in table 6.1 omit additional effects which had to be taken into account. However, such effects had not been found at the present stage of discussion. Besides these, all other values have been measured for the first time.

Table 6.1: *Experimental values of the hyperfine structure parameters of the odd-A neon isotopes.*
[a] : *Reference value from Grosof et al. [Gro58].*

A [u]	I	A_{3s} [MHz]	A_{3p} [MHz]	A_{3s}/A_{3p}	B_{3s} [MHz]	B_{3p} [MHz]	B_{3s}/B_{3p}
17	1/2	+956.00 (0.66)	+665.06 (1.67)	1.4375 (0.0037)			
19	1/2	-2286.17 (0.67)	-1587.23 (0.21)	1.4404 (0.0005)			
21	3/2	-267.68[a] (0.03)	-	-	-111.55[a] (0.10)	-	-
		-267.58 (0.07)	-185.66 (0.10)	1.4412 (0.0009)	-111.82 (0.11)	-69.11 (0.25)	1.618 (0.0059)
23	5/2	-262.04 (0.78)	-181.82 (0.68)	1.4412 (0.0069)	-152.32 (3.89)	-94.55 (3.38)	1.611 (0.058)
25	1/2	-1221.11 (0.51)	-847.55 (0.20)	1.4408 (0.0007)			

Systematic uncertainties like beam energy, etc. can be neglected in this context. The largest systematic error of the hyperfine structure can be attributed to the uncertainty of the Kepco calibration factor F_{cal} and nonlinearities in the amplification curve, which causes a stretching or compression of the x-axis of the experimental spectrum. As discussed in chapter 5, the errors of the amplification are of the order of $\Delta F_{cal} = 10^{-3}$ which leads to negligible changes in the HFS parameters. Nonlinearities in the

Fig. 6.2: *Difference between the applied post-acceleration voltage and a straight line fit in an extreme case.*

amplification curve led to deviations which were smaller than 0.05 V despite a few exceptions. An example plot of an strongly nonlinear amplification curve is shown in figure 6.2, where the fit residuals are plotted against the applied DAC voltage.

These nonlinearities cause changes in the HFS parameters which are below the experimental accuracy. As an example the changes in the HFS parameters of ^{21}Ne was checked by introducing artificial nonlinearities corresponding to figure 6.2 in the x-axis of one spectrum of ^{21}Ne. The corresponding error in the HFS parameters was of the order of 0.03 MHz.

6.1.2   Nuclear Moments

From the HFS parameters given in table 6.1, the nuclear magnetic dipole moment μ and the nuclear quadrupole moment Q_s can be determined as discussed in chapter 2. To calculate these quantities, adopted reference values from the literature were used, for the magnetic

Table 6.2: *Experimental values of the nuclear moments. The errors given in parentheses were calculated from the uncertainties due to the HFS parameters, and the errors of the reference nuclear moments. The mean values $\overline{\mu_I}$ and $\overline{Q_s}$ are the weighted mean of the two corresponding values belonging to the 3s and 3p state.*

A	17	19	21 (reference)	23	25
I	1/2	1/2	3/2	5/2	1/2
$\mu_I(3s)$ [μ_N]	+0.78785(55)	-1.88407(59)	-0.66155(19)	-1.0797(32)	-1.0063(4)
$\mu_I(3p)$ [μ_N]	+0.78988(203)	-1.8851(16)		-1.0802(41)	-1.0071(6)
$\overline{\mu_I}$ [μ_N]	+0.78798(53)	-1.88419(56)		-1.0799(25)	-1.0066(4)
μ_I [μ_N] (other source)		-1.88542(8) [Mac82]	-0.661797(5) [LT57]	-1.08(1) [Dob68]	
$Q_s(3s)$ [mb]			103.15 (0.14)[7.51]	140.5 (3.6)[10.2]	
$Q_s(3p)$ /[mb]			102.9 (0.53)[7.5]	140.8 (5.1)[10.2]	
$\overline{Q_s}$ [mb]			103.0 (0.14)[7.5]	140.6 (2.9)[10.2]	
Q_s [mb] (other source)			102.9(7.5) [Duc72]		

moment of La Tourrette *et al.* [LT57], and for the quadrupole moment of Ducas *et al.* [Duc72]. The results, given in table 6.2, were calculated according to equations (2.34) and (2.47).

The nuclear moments tabulated in table 6.2 were calculated independently for the 3s, and the 3p state from the corresponding HFS factors. Subsequently the weighted mean and the weighted errors were calculated from these two values. The errors of the HFS parameters determined in this work and the values published by Grosof *et al.* were treated as statistical errors in the calculation of the nuclear moments belonging to the 3s and 3p state.

The error of the magnetic and the quadrupole moment taken from La Tourrette *et al.* and Ducas *et al.* were treated as systematic error sources. The corresponding error of μ is of the order of 10^{-6} and could be neglected. The situation is different for the spectroscopic quadrupole moments. Here the error is dominated by the systematic error given by the uncertainty of $Q_s(^{21}\text{Ne})$. The weighted mean of Q_s was calculated by the use of the statistical errors only. The systematic error can be calculated from

$$\Delta Q_s^{sys}(^A\text{Ne}) = \Delta Q_s(^{21}\text{Ne}) \times \frac{Q_s(^A\text{Ne})}{Q_s(^{21}\text{Ne})} \; .$$

The comparison with published magnetic moments of $^{19,21,23}\text{Ne}$ shows good agreement with the measurements of the present work. The accuracy of the magnetic moment of ^{23}Ne was improved by a factor of 4. Only the values of the magnetic moment of ^{19}Ne are not in agreement within their error bars. Similarly to the discussion on the HFS of ^{21}Ne the raw-data were investigated for systematic effects causing the discrepancy, but no such effects were found. Thus, it seems that the errors given in the present thesis may be underestimated.

6.2   Systematic Error of Isotope Shifts

In section 5.2.2 the different errors connected with the acceleration voltage were examined. Still missing is an investigation of the influence of these errors on the error of the isotope shift.

Additional sources contribute to the total systematic error of the isotope shifts extracted from measurements on the radioactive isotopes. Among these are the input data such as transition energies and atomic masses.

6.2.1   Additional Error Sources in the Spectroscopic Measurements

Besides the error of U_{calib} (statistical + systematic), which was discussed in chapter 5, additional error sources have to be considered in the analysis of spectroscopic isotope-shift measurements arising from the post-acceleration voltage.

D_{div} : Divider ratio of the high-voltage divider used to measure the post-acceleration voltage. The ratio was calibrated by collinear/anticollinear measurements on ^{22}Ne (see Sec. 5.2.5), and it was shown that the divider ratio error is $D_{div} = 1000 \pm 0.03$. Taking a maximum value of the post-acceleration voltage of 10 kV, one obtains a maximum error of 0.3 V for the voltage at the charge-exchange cell. The error of the voltage divider ratio D_{div} is treated as systematic error source which is invariable throughout all the runs.

F_{kepco} : Amplification factor of the Kepco voltage amplifier. The amplification factor is determined by regular calibration measurements. (see Sec. 3.4.2), and is typically about 50. The typical fitting error for the amplification factor is of the order of 10^{-3}. The calibration depends on the divider ratio $D_{div} = 1000$ with an error that is negligible compared to the direct error in F_{kepco}.

Even the maximum post-acceleration voltage error from the scanning voltage $U_{DAC} \times F_{kepco}$ of 0.01 V, including the error due to nonlinearities of the amplification factor can be neglected.

U_{prema} : Voltage readout of the DC post-acceleration voltage taken before the start of a measurement cycle on one isotope. With the precision given in section 3.4, the maximum error is $\Delta U_{post}^{sys}(U_{prema}) = 60$ mV for the maximum readout voltage of 10 V (corresponding to $U_{post} = 10$ kV) which can be neglected.

Averaging the Main ISOLDE Voltage
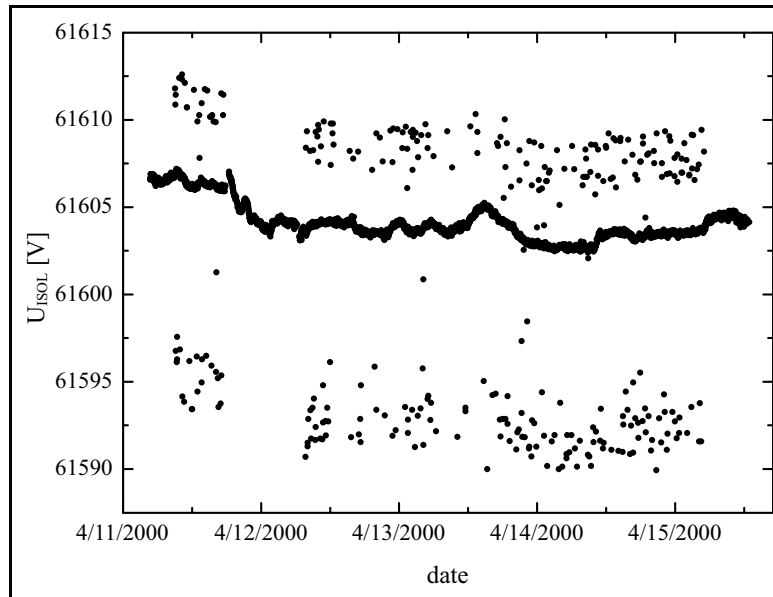
Fig. 6.3: *Plot of the ISOLDE readout voltage U_{ISOL} of run 04/2000. The plot shows the total data collected throughout the run.*

The readout of the ISOLDE main acceleration voltage fluctuates significantly with time as shown in figure 6.3. Throughout a run the ISOLDE main acceleration voltage U_{ISOL} is monitored and the readings were saved every two minutes. As can be seen in the upper plot, U_{ISOL} shows deviations of about 10-15 V from a slowly varying average trend, 10% of the data show these strongly deviating values. These dropouts can be explained by the impact of the proton beam onto the target. Because the beam ionizes the surrounding air, the high voltage is switched to ground for several milliseconds, to protect the ASTEC high voltage supplies. If the readout coincides with this proton beam impact, the monitored voltage value shows a strong deviation from the general trend. It was verified by checking the optical line positions that these fluctuations appear only in the voltage readout, but do not influence the actual measurements which are triggered by the proton pulses. Hence, these fluctuations can be omitted.

The voltage readout data during one set of measurements with stable measurement conditions are averaged over the sample region. Measurements performed under instable voltage conditions (e.g. the steep decent of U_{ISOL} in the first third of the lower plot) were taken out of the analysis. The average of U_{ISOL} is used for further calculations of the acceleration voltage U_{calib}. The statistical error due to the averaging procedure is part of the set of systematic errors contribution in the isotope shift measurements.

6.2.2 Systematic Isotope Shift Errors Related to Beam Energy

Main Acceleration Voltage

The error of U_{ISOL} is determined by the variation of the voltage readout over a number of consecutive measurements. Thus, it contributes together with U_{plasma} to the systematic

error. They add up to a total error of the acceleration voltage U_{calib}, which contributes to
the systematic error of the Doppler shifted frequency ν_D. According to A. Klein this error
has approximately the same mass dependence as the mass shift [Kle96]

$$\Delta\delta\nu_{IS} \approx K_{VS}(\Delta U_{calib}) \times \frac{m_{A'} - m_A}{m_{A'}m_A} \, , \tag{6.1}$$

where K_{VS} is the proportionality constant due to the voltage error ("Voltage Shift"). Taking
advantage of the similar mass dependencies of both the mass effect and the systematic error
in $\delta\nu_{IS}$ due to the acceleration voltage, the voltage calibration error can be eliminated in the
evaluation of the field effect of the radioactive isotopes, as shown in [Kle95, Kle96].

Even though the error of the beam-energy measurement can be eliminated in the calcula-
tion of the field shifts, it affects the isotope shifts which are the directly measured quantities.
Also the comparison and combination of results from different runs is only possible on the
basis of the voltage calibration. In discussing the effect of a calibration error, it is instructive
to investigate the validity of the approximation (6.1).

The error resulting from the error of the acceleration voltage can be estimated by testing
its effect on the isotope shift $\delta\nu_{IS}$ given in Appendix (C.7). For testing purpose an artificial
"isotope shift" was calculated from (C.7), where $U_{accel} = 60$ kV. The "line position" of the
reference isotope was set to $U_{post} = 0$ V. The line position of the isotope under investigation
was set to 2.9125 kV $\times (m_{A'} - m_{20})$ to get approximately the proper mass dependence. The
voltage of U_{prema} was chosen to reproduce the experimental isotope shift $\delta\nu_{IS}^{20,21}$. Similarly
the difference between the approximated mass dependence (6.1) of an error due to ΔU_{accel}
and the exact behavior can be investigated. The results of this investigation are summarized
in the plots presented in figure 6.4, (A), (B), (C).

Figure 6.4 (A) shows the mass dependence of the error of the isotope shift $\Delta\delta\nu_{IS}$ connected
to an error in the main acceleration voltage of $\Delta U_{accel} = +1$ V which is given by the difference

$$\Delta\delta\nu_{IS}(\Delta U_{accel} = +1 \text{ V}) = \delta\nu_{IS}(U_{accel}) - \delta\nu_{IS}(U_{accel} + 1 \text{ V}) \, , \tag{6.2}$$

where $\delta\nu_{IS}(U_{accel})$ and $\delta\nu_{IS}(U_{accel} + 1 \text{ V})$ were calculated according to equation (C.7).

The approximation in equation (6.1) was verified numerically by producing a data set
according to equation (6.2), and fitting the approximated mass dependence equation (6.1) to
these data which yielded the proportionality constant $K_{VS}(\Delta U_{accel})$. The difference between
the fit and the function is shown in plot 6.4 (B). It can be seen that within the scope of our
investigations the assumption of a voltage error with the same mass dependence as the mass
shift is valid within a few per mill of the voltage error $\Delta\delta\nu_{IS}$ and well below the statistical
errors of all isotope shift measurements.

Secondly the linearity of the error caused by ΔU_{accel} was investigated by calculating

$$\Delta\delta\nu_{IS}(\Delta U_{accel}) = \delta\nu_{IS}(U_{accel}) - \delta\nu_{IS}(U_{accel} + \Delta U_{accel}) \, ,$$

where ΔU_{accel} was varied for a fixed isotope mass (^{21}Ne). The result of this calculation
is shown in figure 6.4 (C), which shows that the error in $\delta\nu_{IS}$ increases linearly with the
error in U_{accel}. Consequently, the proportionality constant K_{VS} of the approximated mass
dependence scales as well linearly with ΔU_{accel}.

To investigate the magnitude of the error arising from ΔU_{accel}, a mass dependent data set of $\Delta\delta\nu_{IS}$ was calculated. A fit to this error plot of the form

$$\Delta\delta\nu_{IS}(\Delta U_{accel} = \pm 1 \text{ V}) = K_{VS}(\Delta U_{accel} = \pm 1 \text{ V}) \times \frac{m_A - m_{A'}}{m_A m_{A'}} \ , \tag{6.3}$$

yields the proportionality constant of the mass dependence $K_{VS}(\Delta U_{accel})$ for the typical beam energy of $e\,U_{accel} = 60$ keV

$$K_{VS}(\Delta U_{accel} = \pm 1 \text{ V}) = \pm 203.6 \text{ MHz u} \ . \tag{6.4}$$

Measured Beam Energy Voltage

The beam energy measurement was presented in chapter 5. The error of the beam energy was attributed to the unknown plasma potential U_{plasma}. The error of this plasma potential is approximately 0.5 V, thus the mass dependent voltage error is given by $K_{VS}(\Delta U_{calib}) = 101.8$ MHz u.

This result has to be compared with the mass shift constant K_{MS} which takes the value of approximately $K_{MS} \approx 360$ GHz u and will be calculated below.

Post-Acceleration Voltage

The errors related to the post-acceleration behave similarly to those from the main acceleration voltage and are dominated by the error of D_{div}. The error in U_{post} arising from ΔD_{div} can be approximated by:

$$\Delta\delta\nu_{IS}(\Delta D_{div}) \approx K_{VS}(\Delta D_{div}) \times \frac{m_A - m_{A'}}{m_A m_{A'}} \ . \tag{6.5}$$

For the dependencies of the errors in the post-acceleration voltage U_{post} a similar analysis was done as for U_{accel}. The results are plotted in figure 6.4 (D)-(F). The mass dependence is shown in plot 6.4 (D), where for test purposes an error in D_{div} of 0.1 was assumed. In plot 6.4 (E) the correctness of the approximated behavior according to Eqn (6.5) is shown. The approximation is again valid in the per mill region.

After investigating the validity of equation (6.5), the order of magnitude of the isotope shift errors in dependence of the post-acceleration errors are of interest. This error dependence was tested similarly to the dependence on U_{accel} by calculating the error arising from $\Delta D_{div} = 0.1$ and fitting the mass dependence. This fit yields

$$\Delta K_{DS}(\Delta D_{div} = \pm 0.1) = \pm 1203.3 \text{ MHz u} \ . \tag{6.6}$$

As can be seen from plot 6.4-(F) $\Delta\delta\nu_{IS}$ scales linearly with the error in D_{div} and can easily be extrapolated.

Calibrated Voltage Divider

In chapter 5 it was shown that the voltage divider used in the collinear setup can be calibrated with the collinear/anticollinear method. The calibrated divider ratio was measured to be $D_{div} = 1000.00(3)$, and this is taken as systematic error source. The errors show the mass
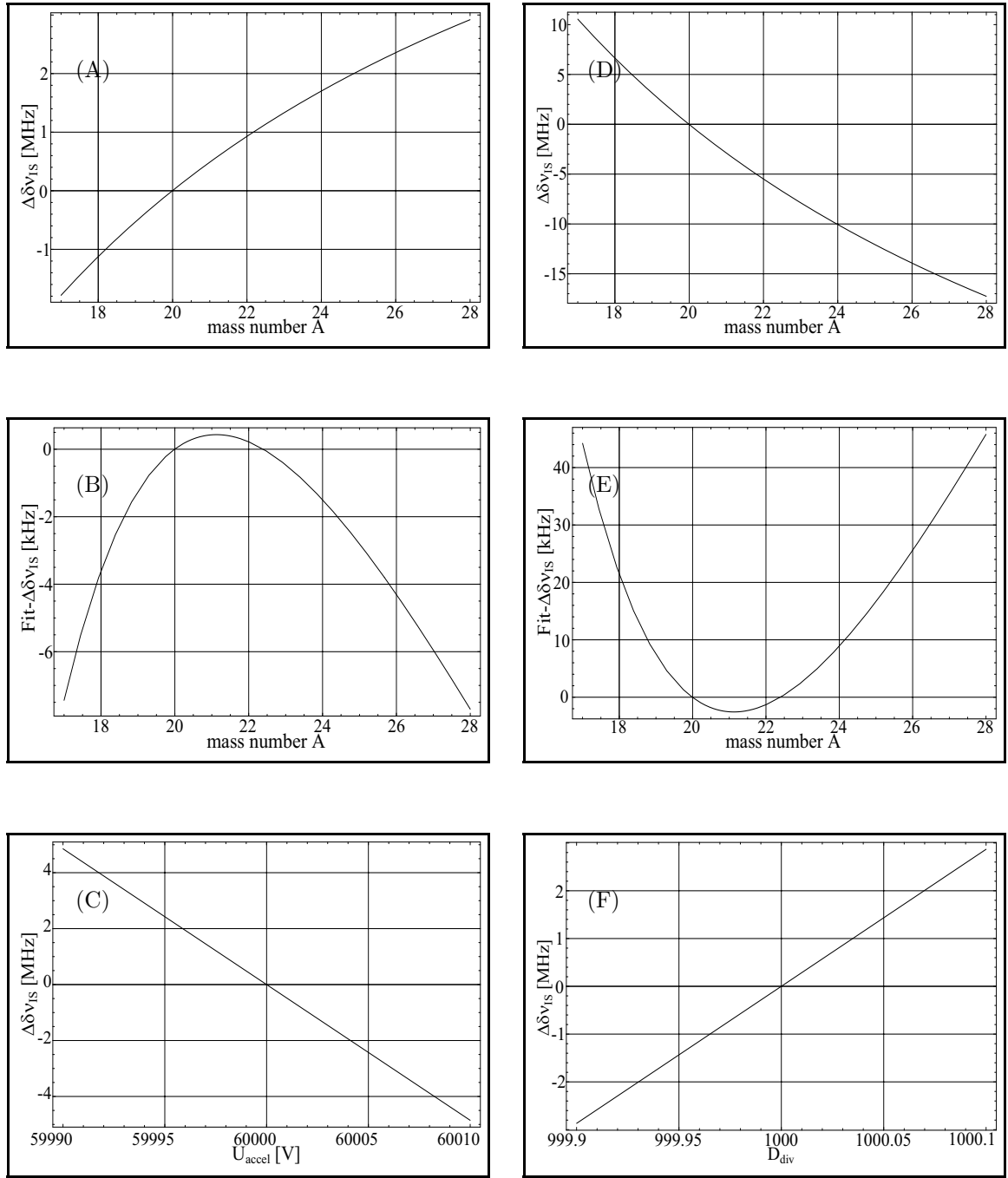
Fig. 6.4: *Dependencies of the errors in $\delta\nu_{IS}$ caused by errors in the acceleration voltages.*
(A) ΔU_{accel}: Mass dependence of $\Delta\delta\nu_{IS}$ for an error of $\Delta U_{accel} = +1$ V.
(B) ΔU_{accel}: Difference between $\Delta\delta\nu_{IS}$ and a fit of a mass dependent function of the type: $\Delta\delta_{IS}) = K \times \frac{m_{A'} - m_A}{m_A m_{A'}}$.
(C) ΔU_{accel}: Dependence of $\Delta\delta\nu_{IS}$ on ΔU_{accel}, reference isotope: ^{20}Ne, investigated isotope: ^{21}Ne.
(D) ΔD_{div}: Mass dependence of $\Delta\delta\nu_{IS}$ for an error of $\Delta D_{div} = +0.1$.
(E) ΔD_{div}: Difference between $\Delta\delta\nu_{IS}$ and a fit of a mass dependent function of the type: $\Delta\delta_{IS}) = K \times \frac{m_{A'} - m_A}{m_A m_{A'}}$.
(F) ΔD_{div}: Dependence of $\Delta\delta\nu_{IS}$ on ΔD_{div}, reference isotope: ^{20}Ne, investigated isotope: ^{21}Ne.

dependence (6.5). For the proportionality constant of the mass dependent frequency shift due to the divider ("Divider Shift") within the working range of the collinear spectroscopy ($U_{accel} = 60$ kV, $F_{kepco} = 50$) it is found

$$\Delta K_{DS}(\Delta D_{div} = 0.03) = \pm 361.00 \text{ MHz u} , \tag{6.7}$$

which is the leading error contribution due to the post-acceleration.

6.2.3   Other Error Sources

Besides the acceleration voltage, several other error sources contribute to the systematic error of $\delta \nu_{IS}$. These quantities are the definitions of the atomic mass unit u in eV, the atomic masses of the isotopes, etc. The errors arising from these parameters are listed in table 6.3 for the isotopes involved in the experiments. As can be seen from the table, most of the errors are negligible, and only the atomic masses of the most neutron-deficient and neutron-rich isotopes give an appreciable contribution to the total error of the isotope shift.

Table 6.3: *Contributions from different error sources to the systematic error of the isotope shift* $\Delta \delta \nu_{IS}$.
[1]: ^{22}Ne *as reference.*

	A									
error	17 [kHz]	18 [kHz]	19 [kHz]	21 [kHz]	22 [kHz]	23 [kHz]	24 [kHz]	25 [kHz]	26 [kHz]	28[1] [kHz]
Δu	9.3	6.1	3	2.2	5.02	6.8	9.3	12	12.7	10.6
Δm_{20}	0.1	0.1	0.1	0.1	0.1	0.1	0.1	0.1	0.1	5.9
$\Delta m_{A'}$	2065	563	21	1.3	6.4	6.8	267	1005	1205	2368
$\Delta \nu_{20}$	0.02	0.01	0.01	0.01	0.01	0.02	0.01	0.03	0.03	0.03
$\sum \Delta_i$	2075	570	24.1	3.6	11.5	13.8	277	1017	1218	2385

6.3   Corrections due to Optical and Non-Optical Line Positions

In the spectroscopic measurements resonances of at least two isotopes are required to determine the isotope shift. The common reference isotope of all measurements was ^{20}Ne, the stable isotope with the highest abundance of 90.48%. Besides this reference isotope all measurements on radioactive isotopes included the resonance of the second even stable isotope, ^{22}Ne. The resonances of both stable isotopes were detected by observing the fluorescence light emitted by the atoms in the optical detection region. All the other resonances were detected by utilizing the collisional reionization method.

Due to the different detection methods there are several effects that might influence the line shape and the line position dependent on the detection. In the optical detection saturation effects in the line shape and the corresponding homogeneous line broadening are avoided by keeping the laser power well below 1 mW. This laser power is sufficiently low to avoid optical pumping into dark states, before the atoms reach the detection zone. At the same time, the rate of detected fluorescence photons with stable beam intensities of 10–50 nA does not exceed the saturation threshold of the photomultiplier.

This is contrasted by the non-optical detection method which is used for radioactive isotopes. It relies on efficient optical pumping with laser beam powers of typically 10 mW, that cause power broadening. On the other hand the broadening effect related to the beam divergence is reduced, because the non-optically detected atoms have to pass a long path which is well defined by narrow diaphragms. Thus, atoms passing the laser beam at relatively large angles do not reach the detection region.

Independently of the detection method the line shape is asymmetric due to the charge-exchange process as described in section 4.3. Because this asymmetry only depends on the conditions for charge exchange, it is assumed to be the same for both detection methods.

Fig. 6.5: *Difference between the peak positions from fluorescence and non-optical detection. Filled circles represent data from ^{20}Ne, open circles of ^{22}Ne. The data sets were taken in each of the runs 03/99-11/00.*

All these effects accumulate and change the line shape in a way which can hardly be modelled by a mathematical description. In the model used for the line description (convolution of a Lorentzian and an exponential function, see section 4.3), the fitting parameters of the linewidth, the exponential factor and the line position are highly correlated. So it is not surprising that there is a small systematic effect which changes the line positions of the non-optically detected lines slightly against the optically detected ones. To determine this effect, numerous experiments in several measuring periods were performed, where the optical and the non-optical line shapes of the stable isotopes were compared under various conditions.

As can be seen in figure 6.5, the difference in the peak positions scatter considerably, but they can be approximated by a as systematic deviation of the optical with respect to the non-optical line positions to negative acceleration voltages. The question how much this effect depends on the conditions in the particular run cannot be answered due to the large scattering of the data. On the average a systematic shift can be found towards a negative shift of the fluorescence signals compared with the ionic signals. Thus, the shift was assumed to be the same for all the runs, and independent of the reference isotope. The mean value and the statistical error of the data shown in figure 6.5 is given by:

$$\begin{aligned} \Delta U_{corr} &= U_{Fluores} - U_{ionic} \\ &= -0.145(0.012) \text{ V .} \end{aligned}$$

This systematic shift has to be taken into account in the analysis of the isotope shifts. All signals recorded with optical detection and low laser power have to be corrected relative to the line positions of the unstable isotope by the voltage given in equation (6.8). The resulting
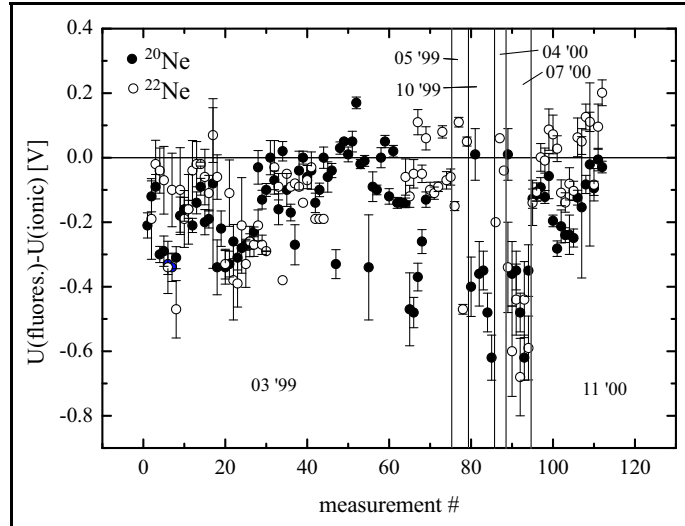
frequency shift $\Delta\nu_{IS}^{corr}$ is about -1.5 MHz.

6.4   Isotope Shifts Along the Neon Isotope Chain

The data collected in Appendix A tables A.1, A.2 and A.3 show an overview of line positions and isotope shifts of the isotopes that were obtained in several runs . The run 06/98 does not appear in the table because it was used for test purposes, run 03/99 was only on the stable isotopes to test systematic effects such as the line shift between lines detected optically and by particle detection. The values printed in bold in the Tables A.1, A.2 and A.3 are final results for the isotope shifts of the investigated neon isotopes. The errors quoted in parentheses are purely statistical and were calculated as errors of the weighted mean of the individual measurements plus the statistical error of the difference between the peak positions of the optical and non-optical signals (see appendix A).

Table 6.4: *Isotope shifts of the neon isotopes including statistical and systematic errors.*

Mass [u]	$\delta\nu_{IS}^{20,A}$ [MHz]	$\Delta^{stat}(\delta\nu_{IS}^{20,A})$ [MHz]	$\Delta_1^{syst}(\delta\nu_{IS}^{20,A})$ [MHz]	$\Delta_2^{syst}(\delta\nu_{IS}^{20,A})$ [MHz]
17	-3183.847	1.169	2.075	3.307
18	-1995.484	0.616	0.570	2.087
19	-947.424	0.741	0.024	0.986
20	– reference –			
21	874.940	0.556	0.004	0.902
22	1663.595	0.170	0.012	1.720
23	2393.810	1.379	0.014	2.470
24	3053.643	0.752	0.277	3.155
25	3654.737	0.659	1.017	3.788
26	4215.791	0.706	1.218	4.372
28	5209.596	1.396	2.385	5.416

Of the various systematic error sources, only the calibrated acceleration voltages and the differences in the line positions for optical and non-optical detection appear in the tables of appendix A. These were measured independently for every run and can be treated as statistical in the averaging over the results of the individual runs. Note that the constant voltage difference in line positions of optical and non-optical detection cause varying frequency errors of $\delta\nu_{IS}$ depending on the total beam energy of the line positions. The errors are well understood as discussed in the previous sections. This can be confirmed by looking at the consistency of the data from different runs. Note that the runs took place with time intervals of several months and under changing conditions. The individual results are consistent within the error bars.

For a better overview the data are collected in a more compressed form in table 6.4. In addition to the statistical errors $\Delta^{stat}(\delta\nu_{IS}^{20,A})$, the systematic errors are separated into two parts. The contribution $(\Delta_1^{syst}(\delta\nu_{IS}^{20,A}))$ was discussed in the previous section and arises from the uncertainties in the natural constants and masses of the isotopes. The influence of the uncertainty of the transition wave number used for ^{20}Ne is of the order of 3×10^{-4} and was neglected. The contribution to the systematic error $\Delta_2^{syst}(\delta\nu_{IS}^{20,A})$ is due to the beam-energy

measurement, and includes the systematic error of 0.31 V of U_{calib} plus the error contribution of D_{div}. This second systematic error contribution can be treated as an error of the specific mass shift constant as is shown in the following sections.

The isotope shift between ^{20}Ne and ^{22}Ne for the investigated transition was measured in several experiments before. The data of the corresponding publications are collected in table 6.5.

Table 6.5: *Isotope shift in the $[2p^5\,(^2P^0_{3/2})\,3s]_2 \to [2p^5\,(^2P^0_{3/2})\,3p]_2$ transition, published by several authors.*

	[Odi65]	[Bel83]	[Kon92]	[Gut94]	[Bas97]	weighted mean
$\delta\nu_{IS}^{20,22}$ [MHz]	1660.9(3.0)	1669(4)	1660(3)	1663.7(5.0)	1653(14)	1662.3(1.7)

The comparison between these previously published data shows good agreement with the value for the isotope shift in the transition $[2p^5\,(^2P^0_{3/2})\,3s]_2 \to [2p^5\,(^2P^0_{3/2})\,3p]_2$ found in this thesis. This holds for the results given in table 6.5 as well as for the weighted mean value given in the last column.

6.4.1 Determination of the Mass Shift

As mentioned at the end Chapter 2, the mass shift can be separated from the field shift with the help of known charge radii from X-ray spectroscopy on muonic atoms. Starting with the isotope shift equation

$$\delta\nu_{IS}^{20,A} = K_{MS}\,\frac{m_A - m_{20}}{m_A\,m_{20}} + F_{el}\,\delta\langle r^2\rangle_{muon}^{20,A}\ , \tag{6.8}$$

and dividing by the mass-dependent quotients yields

$$\underbrace{\delta\nu_{IS}^{20,A}\,\frac{m_A \cdot m_{20}}{m_A - m_{20}}}_{y} = \underbrace{K_{MS}}_{B} + \underbrace{F_{el}}_{m}\,\underbrace{\delta\langle r^2\rangle_{muon}^{20,A}\,\frac{m_A \cdot m_{20}}{m_A - m_{20}}}_{x}\ . \tag{6.9}$$

This can be regarded as an equation for a straight line, where the left-hand term is the y-coordinate, K_{MS} is the intersection with the y-axis and the electronic factor F_{el} is the slope of the straight line. The factor $\delta\langle r^2\rangle_{muon}^{20,A}\,(m_A\,m_{20})/(m_A - m_{20})$ is the x-coordinate.

As the mean square charge radii are known for the stable isotopes ^{20}Ne, ^{21}Ne and ^{22}Ne, this "King plot" can be applied for the two data points $\delta\langle r^2\rangle^{20,21}$ and $\delta\langle r^2\rangle^{20,21}$. The mass shift constant K_{MS} is determined by a χ^2-minimization of a straight line with a slope fixed to the electronic factor calculated in section 2.2.3, namely $F_{el} = -40(4)$ MHz/fm^2, with a variability within the error of F_{el}.

Errors of Charge Radii Obtained from Muonic Atoms

Absolute nuclear charge radii can be determined from X-ray spectra of muonic atoms. A large compilation of radii calculated from such spectra is given in Fricke *et al.* [Fri95]. In

general the radial moments of a nucleus are given by

$$\langle r^n \rangle \;=\; \frac{1}{Ze} \int \rho_N(r)\, r^n\, dr \;, \tag{6.10}$$

$$\text{thus} \quad \langle r^2 \rangle \;=\; \frac{1}{Ze} \int \rho_N(r)\, r^2\, dr \;. \tag{6.11}$$

In contrast to electronic transitions, muonic transition energies depend strongly on the charge distribution inside the nucleus. Due to the high mass of the muon ($m_\mu \approx 200 \times m_e$), the muon is much more tightly bound to the nucleus than an electron. This leads to appreciable variations of the wave function and of the probability density over the volume of the nucleus. The energy shift in the levels i and f participating in the transition caused by the density variation is given in first order perturbation theory by

$$\delta E_{if} = 4\pi \int_0^\infty \delta\rho_N(r) \left[V_\mu^i(r) - V_\mu^f(r) \right] r^2\, dr \;, \tag{6.12}$$

where $\delta\rho_N(r)$ is the deviation from the spherical charge distribution. In the region where $\delta\rho_N(r)\, r^2$ is large, $V_\mu^i(r) - V_\mu^f(r)$ can be approximated by the analytic expression $B\, r^k\, e^{-\alpha r}$, as suggested by Barrett [Bar70]. From perturbation theory follows that the Barrett moment

$$\left\langle r^k e^{-\alpha r} \right\rangle = \frac{4\pi}{2e} \int_0^\infty \rho_N(r)\, r^k\, e^{-\alpha r}\, r^2\, dr \tag{6.13}$$

can be deduced model-independently from the experimental transition energy E_{if}. With the Barrett moment one can define the Barrett equivalent radius $R_{k\alpha}$ via

$$3 \left[R_{k\alpha} \right]^{-3} \int_0^\infty r^k\, e^{-\alpha r}\, r^2\, dr = \left\langle r^k e^{-\alpha r} \right\rangle \;. \tag{6.14}$$

The Barrett radius $R_{k\alpha}$ is thus the radius of a sphere with constant charge density which yields the same moment $\left\langle r^k e^{-\alpha r} \right\rangle$ as the actual charge distribution.

The measured transition energies are analyzed by numerically determining the eigenvalues of the Dirac equation with an analytical function describing the nuclear charge distribution. Normally, like in Fricke et al. [Fri95], this distribution is parameterized for spherical nuclei by a two-parameter Fermi distribution of the form [Eng74]:

$$\rho(r) \;=\; \frac{\rho_0}{1 + \exp\left[4 \ln(3)\, \frac{r-c}{a} \right]} \;, \tag{6.15}$$

$$\text{where} \quad t \;=\; 4\, a\, \ln(3)$$

Here t is the parameter of the surface thickness, and c is the half-density radius. The rms radii given in table 6.6 are based on a surface thickness parameter of $t = 2.3$.

Fricke et al. [Fri95] give the charge radii of the stable neon isotopes measured by X-ray spectroscopy of muonic atoms ([Fri95], Tab. IIIA):

Table 6.6: *Nuclear rms charge radii and differences in mean square charge radii of the stable neon isotopes from the analysis of X-ray spectroscopy of muonic atoms [Fri95]. For errors see text.*

A	c	$\langle r_{ch}^2 \rangle_{model}^{1/2}$ [fm]	α	k	$R_{k\alpha}^{\mu}$ [fm]
20	2.9589(24)	3.006(2)[3]	0.0329	2.0445	3.8656(26)[33]
21	2.8941(20)	2.967(2)[3]	0.0330	2.0441	3.8162(21)[31]
22	2.8706(11)	2.954(2)[3]	0.0330	2.0439	3.7986(21)[31]

Besides the values of the nuclear charge radii $\langle r_{ch}^2 \rangle_{model}^{1/2}$, table 6.6 contains data needed to estimate the errors of $\langle r_{ch}^2 \rangle_{model}^{1/2}$.

The statistical errors of the $\delta \langle r^2 \rangle$ values used in the King-Plot were calculated from the relative statistical errors of the Barrett radii $R_{k\alpha}^{\mu}$ in table 6.6, which are given in parentheses. According to Fricke *et al.* [Fri95], the systematic errors of the mean square charge radii can be calculated by varying the skin thickness parameter t by about 10%.

Errors Due to the beam-energy measurement

The mass shift dependence of the voltage error can be determined from the isotope shift errors $\Delta_2^{sys}(\delta \nu_{IS}^{20,A})$ in table 6.4. Plotting the error data with respect to the isotope mass and fitting the mass dependence leads to a voltage error in the mass shift constant:

$$K_{VS}(\Delta U) = 378 \text{ MHz u} . \tag{6.16}$$

As was shown by Klein, the systematic errors of the isotope shift arising from the beam-energy measurement are eliminated in the evaluation of the field shift [Kle96]. This is because these errors show approximately the same mass dependence as the mass shift. The isotope shift equation, including the errors due to the beam energy can be written

$$\delta \nu_{IS}^{20,A} \pm \Delta \delta \nu_{IS}(U_{calib}) \pm \Delta \delta \nu_{IS}(U_{post}) = K_{MS} \times \frac{m_A - m_{20}}{m_A \cdot m_{20}} + F_{el} \times \delta \langle r^2 \rangle^{20,A} , \tag{6.17}$$

Where $\delta \nu_{IS}^{20,A}$ is the experimentally determined isotope shift, $\Delta \delta \nu_{IS}(\Delta U_{calib})$ is the systematic error related to the main acceleration voltage and $\Delta \delta \nu_{IS}(\Delta U_{post})$ is the systematic error due to the uncertainty of the post-acceleration voltage. These two errors can be combined to one voltage related error $\Delta \delta \nu_{IS}(\Delta U) := \Delta \delta \nu_{IS}(\Delta U_{calib}) + \Delta \delta \nu_{IS}(\Delta U_{post})$. Provided that the error related to voltage uncertainties has the same mass dependence as the mass shift, equation (6.17) can be rewritten in the form:

$$\delta \nu_{IS}^{20,A} \pm K_{VS}(\Delta U) \times \frac{m_A - m_{20}}{m_A \cdot m_{20}} = K_{MS} \times \frac{m_A - m_{20}}{m_A \cdot m_{20}} + F_{el} \times \delta \langle r^2 \rangle^{20,A} , \tag{6.18}$$

from where follows the new proportionality constant of an effective mass shift which includes the systematic error from the beam energy:

$$C_{MS} = K_{MS} \pm K_{VS}(\Delta U) = \left[\delta \nu_{IS}^{20,A} - F_{el} \times \delta \langle r^2 \rangle \right] \frac{m_A \cdot m_{20}}{m_A - m_{20}} . \tag{6.19}$$

This effectiv constant C_{MS} is obtained from the King plot of the isotope shift data, hence the systematic errors ΔU disappear in the evaluation of $\delta\nu_{FS}$ and $\delta\langle r^2\rangle$. The mass shift constant K_{MS} becomes C_{MS} with the additional error of $\pm K_{VS}(\Delta U)$.

With these assumptions the modified mass shift constant can be determined from the King plot to be

$$C_{MS} = 363.072(167)[308] \text{ GHz u} . \tag{6.20}$$

For the evaluation of field shifts this constant can be used independently of the error from the beam-energy measurement. The statistical error in parentheses is determined by the fit error in the King plot, the error in square brackets is the systematic error determined by the assumption of the 10% accuracy of F_{el} and the isotope shifts of the stable isotopes. Taken as a result for the real mass shift constant, the constant K_{MS} becomes

$$K_{MS} = 363.072(167)[308][98] \text{ MHz u} \tag{6.21}$$

with the additional error from the voltage and divider-ratio calibration.

6.4.2 Experimental Results of the Differences in Mean Square Charge Radii

After the determination of the mass shift parameter C_{MS} the experimental field shift $\delta\nu_{FS}$ and the differences in mean square nuclear charge radii $\delta\langle r^2\rangle$ can be calculated. Subtracting the mass shift from the experimental data of the isotope shift tabulated in table 6.4 yields the values for the field shift in the neon isotope chain collected in table 6.7.

Table 6.7: *Field shift and differences in mean square charge radii.*
   $\delta\nu_{FS}$; Δ^{stat}: statistical error of $\delta\nu_{FS} = \Delta^{stat}(\delta\nu_{IS})$
   $\delta\nu_{FS}$; Δ^{sys1}: systematic error of $\delta\nu_{FS} = \Delta_1^{stat}(\delta\nu_{IS})$
   $\delta\nu_{FS}$; Δ^{sys2}: systematic error of $\delta\nu_{FS}$ resulting from C_{MS}
   $\delta\langle r^2\rangle$; Δ^{stat}: statistical error of $\delta\langle r^2\rangle$
   $\delta\langle r^2\rangle$; Δ^{sys1}: systematic error arising from $\Delta^{sys1}(\delta\nu_{FS})/F_{el}$
   $\delta\langle r^2\rangle$; Δ^{sys2}: systematic error arising from $\Delta^{sys2}(\delta\nu_{FS})/F_{el}$

Mass	$\delta\nu_{FS}^{20,A}$ [MHz]				$\delta\langle r^2\rangle^{20,A'}$ [fm^2]			
[u]	$\overline{\delta\nu_{FS}}$	Δ^{stat}	Δ^{sys1}	Δ^{sys2}	$\overline{\delta\langle r^2\rangle}$	Δ^{stat}	Δ^{sys1}	Δ^{sys2}
17	−9.35	(1.17)	[2.08]	[4.15]	0.234	(29)	[52]	[104]
18	+8.34	(0.62)	[0.57]	[2.62]	-0.208	(15)	[14]	[66]
19	−0.73	(0.74)	[0.02]	[1.24]	0.018	(19)	[1]	[31]
20	– reference –							
21	+8.69	(0.55)	[0.004]	[1.13]	-0.217	(14)	[0]	[28]
22	+12.87	(0.17)	[0.012]	[2.16]	-0.322	(4)	[0]	[54]
23	+22.88	(1.38)	[0.014]	[3.10]	-0.573	(34)	[0]	[78]
24	+25.20	(0.75)	[0.28]	[3.96]	-0.631	(19)	[7]	[99]
25	+18.44	(0.66)	[1.02]	[4.76]	-0.462	(16)	[25]	[119]
26	+19.39	(0.71)	[1.22]	[5.49]	-0.485	(18)	[30]	[137]
28	+10.38	(1.40)	[2.39]	[6.80]	-0.260	(35)	[60]	[170]

The statistical errors of the field shift (in parentheses) are the same as the statistical errors of the isotope shift $\Delta^{stat}(\delta\nu_{IS}^{20,A})$ (see table 6.4). The systematic error of the field shift includes the effect of ΔC_{MS} the errors of $\delta\nu_{IS}^{21,A'}$, $\delta\nu_{IS}^{22,A'}$, and F_{el} determining the King plot.

The errors of $\delta\langle r^2\rangle$ are calculated by dividing the field shift errors by the electronic factor. The 10% error of F_{el} contributes to the error of C_{MS} and is included in the error Δ_2^{sys} of $\delta\nu_{FS}$.

The data collected in table 6.7 is plotted in figure 6.6. As can be seen, the differences in the mean square charge radii are clearly resolved. The systematic errors cause a shift in the general slope of the plot, the relative effects between the isotopes persist with changing slope. The interpretation of the results from the nuclear physics point of view will be discussed in the following chapters.
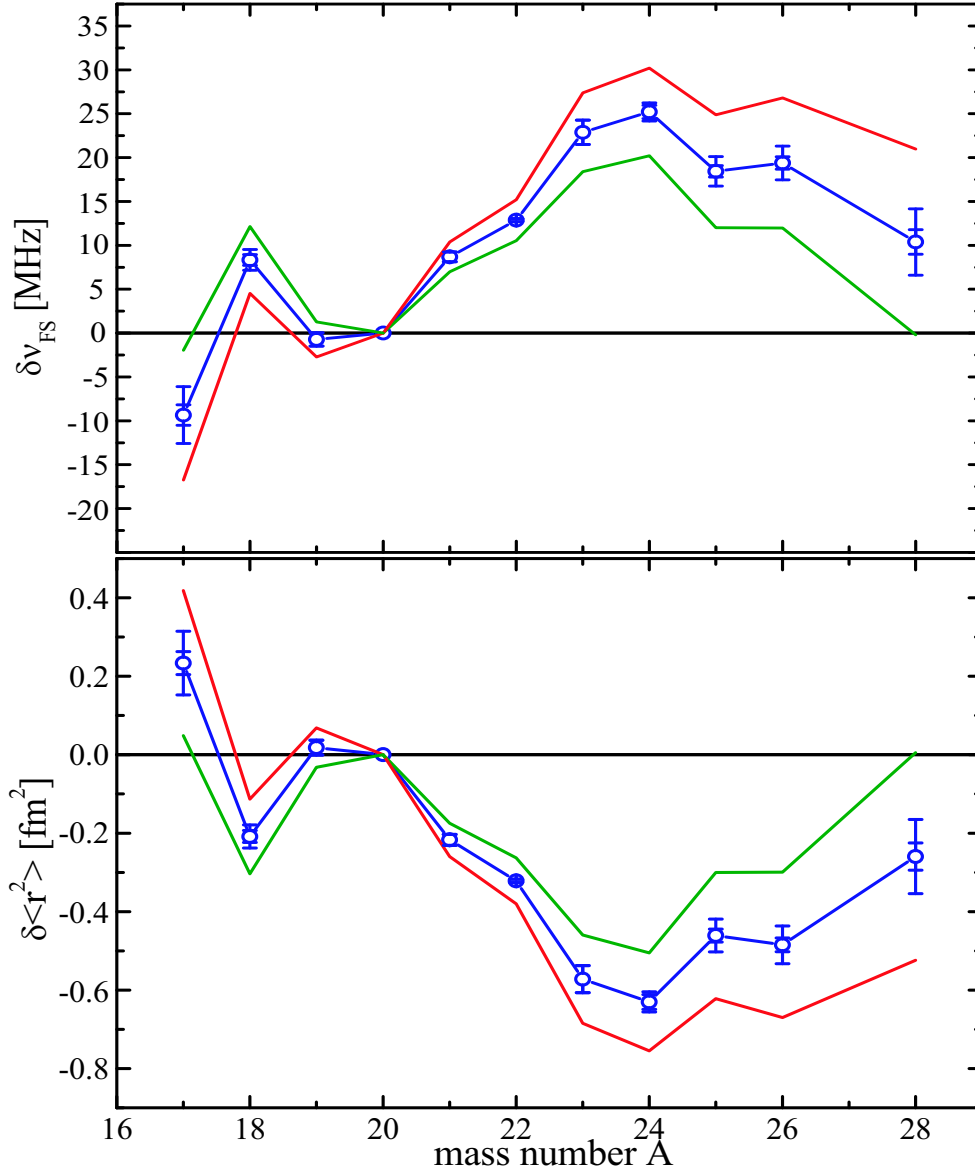
Fig. 6.6: *Plot of the field shift $\delta\nu_{FS}$ in the upper plot and the differences in mean square charge radii $\delta\langle r^2\rangle$ in the lower plot. The open circles denote the experimental data for $\delta\nu_{FS}$ and $\delta\langle r^2\rangle$ with respect to ^{20}Ne with their statistical error Δ^{stat} and systematic error Δ_1^{sys}. The two lines show the value range of the data given by the error Δ_2^{sys} related to ΔC_{MS}. Note that this systematic error changes the general slope of the curve but does not affect the relative effects.*

Chapter 7

Nuclear Moments of Odd-A Neon Isotopes

In the scope of this work five odd-A neon isotopes were investigated. The experimental values of the nuclear moments were presented in section 6.1.2. To be able to discuss the implications of the moments on the structure of nuclei in the p- and sd-shell region, a brief outline of the theoretical background shall be given.

7.1 Theoretical Description of Nuclear Moments

The theoretical description of nuclear multipole moments is summarized in the book of Ring and Schuck ([Rin80], Appendix B, p.580ff). An overview of the shell-model theory of the nuclear dipole and quadrupole moments can be found in the book of Heyde ([Hey94], p.168ff).

7.1.1 Electromagnetic Operators and Moments

The starting point of the investigation of nuclear electromagnetic moments is the interaction of the nucleus with an external electromagnetic field. The Hamiltonian of the system consisting of a nucleus and a field is given by a sum of three contributions

$$\mathcal{H} = \mathcal{H}_{nucl} + \mathcal{H}_{field} + \mathcal{H}_{int} \ . \tag{7.1}$$

The term $\mathcal{H}_{nucl}$ represents the Hamiltonian of the bare nucleus without any interaction, the corresponding eigenfunctions $\Psi_i(1, ...A)$ are assumed to be known. Following the discussion in Jackson ([Jac83], p.277), the field Hamiltonian (= field energy) is given by

$$\mathcal{H}_{field} = \frac{1}{8\pi} \int_{Vol} (\mathbf{E}^2(\mathbf{r}, t) + \mathbf{B}^2(\mathbf{r}, t)) \, d^3r \ . \tag{7.2}$$

The interaction of the nucleus with the external electromagnetic field $A_\mu(\Phi, \mathbf{A})$ is addressed by the Hamiltonian

$$
\begin{aligned}
\mathcal{H}_{int} &= -\tfrac{1}{c} \int j_\mu A^\mu \, d^3r \\
&= \int \left(\rho(\mathbf{r}, t)\Phi(\mathbf{r}, t) - \frac{1}{c} \mathbf{j}(\mathbf{r}, t) \cdot \mathbf{A}(\mathbf{r}, t) \right) d^3r \ ,
\end{aligned}
\tag{7.3}
$$

where $\rho(\mathbf{r}, t)$ stands for the nuclear charge density, and $\mathbf{j}(\mathbf{r}, t)$ is the current density inside the nucleus which is connected to the nuclear magnetic moment.

The interaction of the nucleus with the external fields causes an energy shift which can be calculated in first-order perturbation theory by

$$\Delta E_i = \left\langle \Psi_i \middle| \mathcal{H}_{int} \middle| \Psi_i \right\rangle . \tag{7.4}$$

By applying the Maxwell theory, the interaction Hamiltonian becomes

$$\mathcal{H}_{int} = \sum_{\lambda\mu} a_{\lambda\mu} \hat{Q}_{\lambda\mu} + b_{\lambda\mu} \hat{M}_{\lambda\mu} , \tag{7.5}$$

where $\hat{Q}$ and $\hat{M}$ are the electromagnetic multipole operators,

$$
\begin{aligned}
\text{electric:} \quad \hat{Q}_{\lambda\mu} &= \int \rho(\mathbf{r}) r^\lambda Y_{\lambda\mu}(\theta, \phi) \, d^3r \\
&= e \sum_{i=1}^{A} \left(\frac{1}{2} - \tau_z^{(i)} \right) r_i^\lambda \, Y_{\lambda\mu}(\theta_i, \phi_i) \tag{7.6}
\end{aligned}
$$

$$
\begin{aligned}
\text{magnetic:} \quad \hat{M}_{\lambda\mu} &= \int \boldsymbol{\mu}(\mathbf{r}) \cdot \nabla \left(r^\lambda Y_{\lambda\mu}(\theta, \phi) \right) \, d^3r \\
&= \mu_N \sum_{i=1}^{A} \left\{ g_s^{(i)} \mathbf{s}_i + \frac{2}{\lambda + 1} \cdot g_\ell^{(i)} \right\} \cdot \left(\nabla r^\lambda Y_{\lambda\mu}(\theta, \phi) \right) . \tag{7.7}
\end{aligned}
$$

Here $Y_{\lambda\mu}$ are spherical harmonics, and θ and ϕ the spherical coordinates. The expectation values for the electric and magnetic multipole moments are given by

$$\mathcal{O}_{\lambda\mu} = \left\langle \Psi \middle| \hat{\mathcal{O}}_{\lambda\mu} \middle| \Psi \right\rangle , \tag{7.8}$$

where $\mathcal{O}_{\lambda\mu}$ represents $Q_{\lambda\mu}$ or $M_{\lambda\mu}$, respectively.

The electromagnetic interaction conserves parity, so it is possible to choose $\left| \Psi \right\rangle$ as eigenstate of the parity operator. The operators $\hat{Q}_{\lambda\mu}$ and $\hat{M}_{\lambda\mu}$ have the parity $(-1)^\lambda$ and $(-1)^{\lambda+1}$, respectively, depending on the order of λ. Accordingly, the electromagnetic multipole expectation values vanish:

$$Q_{\lambda\mu} = 0 \quad \text{for} \quad \lambda = 1, 3, 5, \ldots , \tag{7.9}$$

$$M_{\lambda\mu} = 0 \quad \text{for} \quad \lambda = 0, 2, 4, \ldots . \tag{7.10}$$

Since the electromagnetic operators are spherical tensors, the Wigner-Eckart theorem (see App. E.1) can be applied for finding the eigenstates of angular momentum

$$Q_{\lambda\mu} = \left\langle J, J_z \middle| \hat{Q}_{\lambda\mu} \middle| J, J_z \right\rangle = (-1)^{J-J_z} \begin{pmatrix} J & \lambda & J \\ -J_z & \mu & J_z \end{pmatrix} \left\langle J \middle\| \hat{Q}_{\lambda\mu} \middle\| J \right\rangle \tag{7.11}$$

$$M_{\lambda\mu} = \left\langle J, J_z \middle| \hat{M}_{\lambda\mu} \middle| J, J_z \right\rangle = (-1)^{J-J_z} \begin{pmatrix} J & \lambda & J \\ -J_z & \mu & J_z \end{pmatrix} \left\langle J \middle\| \hat{M}_{\lambda\mu} \middle\| J \right\rangle . \tag{7.12}$$

Furthermore it is found that

$$\left. \begin{aligned} Q_{\lambda\mu} \\ M_{\lambda\mu} \end{aligned} \right\} \neq 0 \quad \text{only if } \mu = 0 \text{ and } 0 \leq \lambda \leq 2J . \tag{7.13}$$

7.1.2 Magnetic Dipole Moment

The magnetic dipole moment is defined as the expectation value of the magnetic dipole operator ($\lambda = 1$) in the state with maximum J_z projection, i.e. $J_z = J$. With the restrictions mentioned in equation (7.13) the only non-trivial matrix element is given by ([Hey94], p.174)

$$
\begin{aligned}
\mu &:= \sqrt{\frac{4\pi}{3}} \left\langle J, J_z = J \middle| \hat{M}_{10} \middle| J, J_z = J \right\rangle \tag{7.14} \\
&= \mu_N \left\langle J, J_z = J \middle| \sum_i g_\ell^{(i)} \hat{\ell}_{z,i} + \sum_i g_s^{(i)} \hat{s}_{z,i} \middle| J, J_z = J \right\rangle \\
&= \mu_N \left\langle J, J_z = J \middle| \sum_i \left\{ g_\ell^{(i)} \hat{j}_{z,i} + \left(g_s^{(i)} - g_\ell^{(i)} \right) \hat{s}_{z,i} \right\} \middle| J, J_z = J \right\rangle \tag{7.15}
\end{aligned}
$$

The variables g_ℓ and g_s are the gyromagnetic ratios of the orbital and the spin contribution to the nuclear magnetic moment. By applying the Wigner-Eckart theorem the magnetic moment can be expressed as

$$
\mu = \mu_N \frac{J}{\sqrt{J(J+1)(2J+1)}} \left\langle J \middle\| \sum_i \left\{ g_\ell^{(i)} \mathbf{\hat{j}}_i + \left(g_s^{(i)} - g_\ell^{(i)} \right) \mathbf{\hat{s}}_i \right\} \middle\| J \right\rangle . \tag{7.16}
$$

Single-Particle Moment: Schmidt Values

A single-particle magnetic moment is caused by one unpaired nucleon moving outside an inert core of the remaining $A - 1$ nucleons whose angular momenta couple to zero. Thus, the nuclear spin is given the angular momentum of the single particle. As is shown in the book of Heyde ([Hey94], p.174), the magnetic moment for a single particle outside a closed shell can be determined with the help of the reduced matrix elements

$$
\langle j \| \mathbf{j} \| j \rangle = (j(j+1)(2j+1))^{\frac{1}{2}} , \tag{7.17}
$$

$$
\langle j \| \boldsymbol{\sigma} \| j \rangle = \begin{pmatrix} \frac{1}{2} & \ell & j \\ \frac{1}{2} & \ell & j \\ 1 & 0 & 1 \end{pmatrix} \langle \tfrac{1}{2} \| \boldsymbol{\sigma} \| \tfrac{1}{2} \rangle (2\ell + 1)^{1/2} . \tag{7.18}
$$

The corresponding single-particle magnetic moment ("Schmidt value") follows from these formulae and can be calculated easily by utilizing the well known formula (see e.g. [Rin80], p.61)

$$
\mu_{sp} = j \left(g_\ell \pm \frac{g_s - g_\ell}{2\ell + 1} \right) \mu_N, \qquad j = \ell \pm \tfrac{1}{2} , \tag{7.19}
$$

where $g_\ell = 1$ (0), and $g_s = 5.5858$ (-3.8261) for a single proton (neutron) outside a closed shell. Plotted as a function of j the Schmidt values form two lines corresponding to protons or neutron having total angular momenta $j = \ell + 1/2$ and $j = \ell - 1/2$. These are shown in the figures 7.1 and 7.2 together with some experimental values for nuclear spin $I = j$. Most of the experimental nuclear magnetic moments fall between both lines. This can be ascribed to an interaction of the valence nucleon with the core nucleons, which effectively reduces the g_s-factor by contributing higher-order interaction terms like core polarization, mesonic exchange currents, etc. (see e.g. [Ari54]). The problem can be addressed by introducing effective g-factors, or by including these higher order effects, like configuration mixing, in the theoretical model.
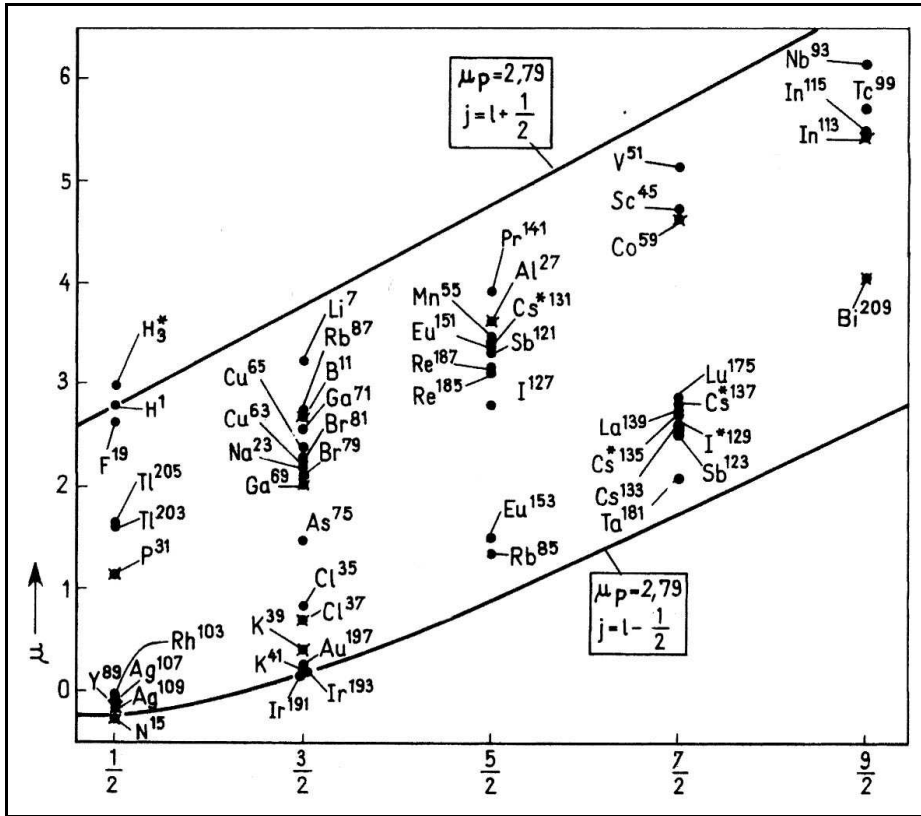
Fig. 7.1: *Schmidt lines and magnetic moments for nuclei with an unpaired proton. Taken from [May55].*
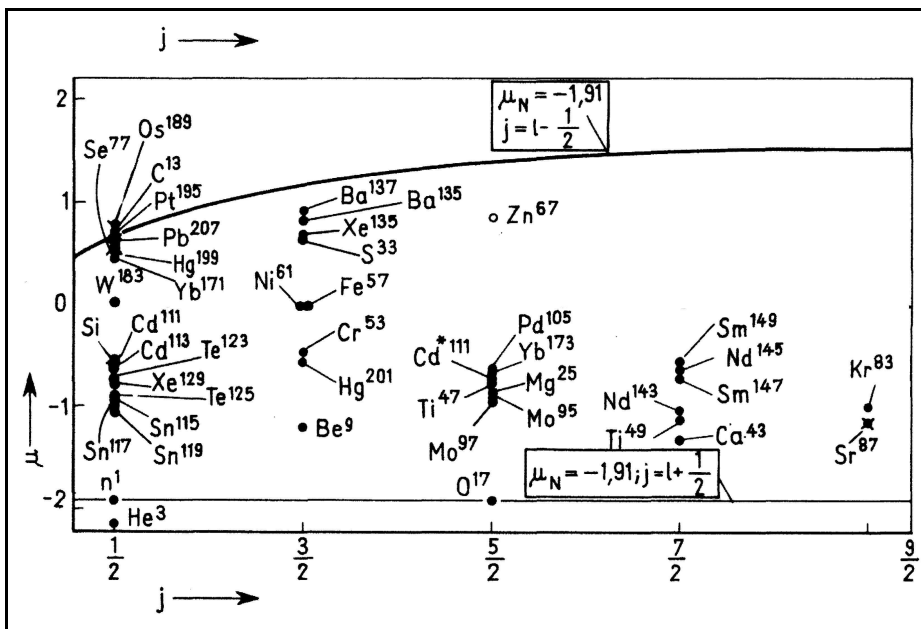
Fig. 7.2: *Schmidt lines and magnetic moments for nuclei with an unpaired neutron. Taken from [May55].*

7.1.3 Electric Quadrupole Moment

The electric quadrupole moment is defined in a similar way as the magnetic dipole moment. The second-order electric moment according to equations (7.9) and (7.13) is given by ([Rin80], p.63)

$$Q \; := \; \sqrt{\frac{16\pi}{5}} \left\langle J, J_z = J \middle| \hat{Q}_{20} \middle| J, J_z = J \right\rangle \tag{7.20}$$

$$= \; \sqrt{\frac{16\pi}{5}} \left\langle J, J_z = J \middle| \sum_{i=1}^{A} \tilde{e}_i \, r_i^2 \, Y_{20}(\theta_i, \phi_i) \middle| J, J_z = J \right\rangle . \tag{7.21}$$

In this context $\tilde{e}_i$ is the effective charge of the corresponding nucleon, $\tilde{e}_p = e$ for free protons, and $\tilde{e}_n = 0$ for free neutrons. As will be seen later, this charge of the contributing nucleons is usually found to deviate from the charges of the free particles, when the calculated quadrupole moments are compared with experimental data. Modern shell model calculations use these effective charges differing from the values of the free particle. The spherical harmonic Y_{20} is given by

$$Y_{20}(\theta, \phi) = \sqrt{\frac{5}{16\pi}} \times \left(3 \cos^2 \theta - 1\right) , \tag{7.22}$$

so that the quadrupole operator takes the well known form

$$e \, \hat{Q}_{20} = \int \rho_e(\mathbf{r}) r^2 \left(3 \cos^2 \theta - 1\right) \, d^3 r . \tag{7.23}$$

With the help of the Wigner-Eckart theorem the expectation value can be rewritten as ([Hey94], p.168)

$$Q \; = \; \sqrt{\frac{16\pi}{5}} \begin{pmatrix} J & 2 & J \\ -J & 0 & J \end{pmatrix} \left\langle J \middle| \middle| \sum_{i=1}^{A} \tilde{e}_i \, r_i^2 \, Y_{20}(\theta_i, \phi_i) \middle| \middle| J \right\rangle \tag{7.24}$$

$$= \; \sqrt{\frac{16\pi}{5}} \left(\frac{J(2J-1)}{(2J+1)(2J+3)(J+1)}\right)^{1/2} \times \left\langle J \middle| \middle| \sum_{i=1}^{A} \tilde{e}_i \, r_i^2 \, Y_{20}(\theta_i, \phi_i) \middle| \middle| J \right\rangle \tag{7.25}$$

The expressions for the quadrupole moment depend explicitly on the radial coordinate r. Hence, the radial dependence of the wave functions in the nuclear potential has to be considered in the calculation of quadrupole moments.

Single-Particle Quadrupole Moment

In analogy to the magnetic moment, a single-particle quadrupole moment can be calculated. For a single nucleon the reduced matrix element $\left\langle j \middle| \middle| Y_{20} \middle| \middle| j \right\rangle$ is given by ([Hey94], p.168)

$$\left\langle j \middle| \middle| Y_{20} \middle| \middle| j \right\rangle = \sqrt{\frac{5}{4\pi}} (2j+1) \frac{3/4 - j(j+1)}{\left(j(j+1)(2j-1)(2j+1)(2j+3)\right)^{1/2}} . \tag{7.26}$$

With the help of this result and equation (7.25), the single-particle quadrupole moment takes the very simple form

$$Q_{sp}(j) = -\frac{2j-1}{2j+1} \tilde{e} \left\langle r^2 \right\rangle , \tag{7.27}$$

If there are n nucleons in a configuration $j^n; I = j$, and n is odd, the quadrupole moment becomes

$$Q_n = Q_{sp} \times \left(1 - \frac{2n-2}{2j+1} \right) . \tag{7.28}$$

This implies that the quadrupole moments for a hole or a particle in the same state have the same absolute value, but the opposite sign.

The quadrupole moment caused by a single particle moving outside a closed-shell configuration is obtained with the nucleon charge $\tilde{e}$ as given above, while for a single hole in a closed proton (neutron) shell the effective charge becomes $\tilde{e}_h = -\tilde{e}_p$ ($\tilde{e}_h = -\tilde{e}_n$). As can be seen, the quadrupole moment is negative for a single proton outside a closed configuration, which corresponds to a oblate deformation. A single hole in a proton shell causes a positive quadrupole moment, corresponding to a prolate deformation. These situations are illustrated in figure 7.3.
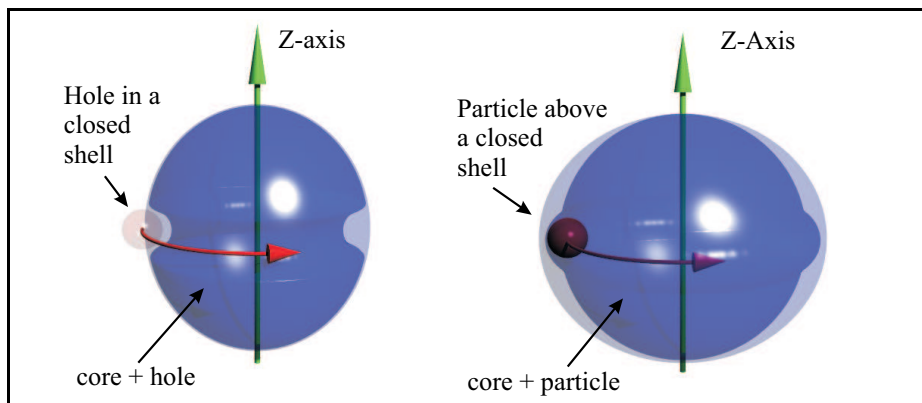
Fig. 7.3: *Simple picture of single-particle/hole quadrupole deformation. Figure according to [Hey94], p.169*

.

7.2   Nuclear Moments and Shell Model Calculations

As mentioned in the beginning of this chapter, shell model calculations are the state-of-the-art theoretical approach for the calculation of nuclear moments. After a discussion of the foundations of the theory of nuclear moments within the shell model, theoretical results will be given and compared to the experimental data.

7.2.1   General Remarks

The theoretical predictions of nuclear magnetic dipole and electric quadrupole moments presented in this work [Wil79, Bro01b] have been calculated in the framework of an extended nuclear shell model which was developed by Wildenthal and Brown in the 1980ties [Wil84, Bro88b].

Modern shell model calculations incorporate many of the multinucleon configurations arising under the assumption that all protons and neutrons in the valence shell simultaneously occupy several different, partially filled, single-particle configurations. They are thus extensions of the "classical" nuclear shell model proposed by Mayer and Jensen [May49], which

assumes a single configuration for each nuclear level, corresponding to a single nucleon in one single-particle orbit. The theoretical investigation of neon isotopes requires calculations in an sd-shell model-space ranging from $8 < N,\ Z < 20$. The magnetic moment of ^{17}Ne will be discussed separately, because it involves a proton pair in the sd shell and a neutron hole in the p shell.

A basic assumption of the shell model calculations is that only nucleons above, or holes below a closed-shell configuration contribute to effects in the calculated observables. The nucleons in the closed-shell configuration form a "core" which is considered as inert against excitations to higher configurations. For the sd shell this closed core is formed by the doubly magic ^{16}O. The N, Z closed-shell configuration above the sd shell is assumed to be ^{40}Ca (e.g. [Bro01a], p. 520).

The assumption of closed cores can be questioned, as is discussed by Warburton *et al.* [War92b]. It becomes evident that, if the cores are investigated in model spaces larger than the closed-shell configuration, they are found to have significant non-closed-shell admixtures. As an example, ^{16}O has about 50% of admixtures from higher states if it is investigated in the $(0 + 2 + 4)\hbar\omega$ model space [War92b]. To account for the simplification of an inert core, the operators and interactions used in the model space have to be renormalized by the use of effective charges.

7.2.2   The sd-Shell Model Interaction

Early attempts of a model-independent approach for the nuclear interaction were undertaken by Kuo and Brown [Kuo66, Kuo67], who developed interactions for 2-particle "$2p$" ($A = 18$) and 2-hole "$2h$" ($A = 38$) configurations above and below the closed shells. These calculations were based on the calculation of renormalized G-matrix elements, but were unapplicable for more complicated configurations. The next step was done by Chung and Wildenthal [Wil79], who developed a so called "CWP" particle interaction for the lower sd shell ($A = 18 - 24$) and a "CWH" hole-interaction for the upper sd shell ($A = 32 - 39$). These two interactions worked well in "their" mass region, but the interpolation to the mid-shell region was not successful.

The yet unpublished theoretical predictions of nuclear moments [Bro01b], presented in this work, are based on the work of Brown and Wildenthal performed in the nineteen-eighties [Bro88a, Bro88b, Wil84]. Here a model independent nuclear interaction was developed which is based on a purely phenomenological approach. This interaction, referred to as "*W-interaction*" or "*USD-interaction*", removed the shortcomings of the earlier interactions.

The interaction is determined by calculating three single-particle matrix elements and 63 two-body matrix elements (TBME). These TBMEs in the jj-coupled representation are given

by ([Bro88a], p. 197/8)

$$
\begin{aligned}
\langle \quad ab;JT \quad |V(1,2)| \quad cd;JT \quad \rangle = \\
\sum_{L,S,L',S'} [(1+\delta_{ab})(1+\delta_{ab})]^{-1/2}[(1+\delta_{AB})(1+\delta_{CD})]^{1/2} \\
\times \quad
\begin{pmatrix}
\ell_a & \frac{1}{2} & j_a \\
\ell_b & \frac{1}{2} & j_b \\
L & S & J'
\end{pmatrix}
\begin{pmatrix}
\ell_c & \frac{1}{2} & j_c \\
\ell_d & \frac{1}{2} & j_d \\
L' & S' & J'
\end{pmatrix}
\sum_{p}(-1)^{J-J'}
\begin{Bmatrix} L & S & J \\ S' & L' & p \end{Bmatrix}
\begin{Bmatrix} L & S & J' \\ S' & L' & p \end{Bmatrix}^{-1} \\
\times \quad \langle ABLSJ'T|V_p|CDL'S'J'T\rangle \,,
\end{aligned}
\tag{7.29}
$$

where the a,b,c,d are the orbitals of the particles under investigation in the model space, J is the total two-particle angular momentum and, if the isospin is conserved, the matrix elements are characterized by their isospin $T = 0$ or $T = 1$. If isospin is not conserved, then there are three sets of TBMEs for the combination *pppp*, *nnnn*, *pnpn* [Bro01a], where p =proton, n =neutron. These TBMEs together with their linear combinations are treated as the free parameters of a least-squares fit to experimental binding and excitation energies. The model includes a mass dependence of the TBMEs of the form [Bro88a, Bro88b]

$$
\langle V\rangle(A) = \frac{\langle V\rangle(A=18)}{(A/18)^{0.3}} \,,
\tag{7.30}
$$

where the power 0.3 was imposed by a least-squares fit [Bro88b] of these two-body matrix elements to experimental values. 19 of the total of 66 TBMEs are fixed to the A=18 G-matrix elements calculated by Kuo *et al.* [Kuo67]. This was done to overcome problems to in the determination of these elements to the desired precision. The remaining 47 matrix elements were fitted to 447 energy levels in the mass region $A = 18-39$ with a rms deviation of 185 keV [Wil84] with model-space dimensions below 1000 ([Bro88b], p.35). The detailed discussion of the fitting procedure and values for the TBMEs can be found in the publication of Brown *et al.* [Bro88a].

Shell Model Extensions

As mentioned by Brown [Bro98b], a big problem of the described method is the "explosion" of the model space if the calculations are extended to higher-mass regions. Successful shell-model studies have meanwhile been carried out for the pf shell [Ric91, Miz01, Cau01], but calculations in higher-dimensional model spaces are prohibited by the exponentially growing computer demands. Hence, the long standing desire for procedures to link groups of two-body matrix elements together via a fundamental or an *ad hoc* relationship, or to eliminate some of them from the variation procedure, remains a primary goal.

To study the interaction more closely, it has to be separated into its components (central, spin-orbit, tensor and antisymmetric spin-orbit terms). This can be done by transforming the jj-coupled TBMEs into a LS-coupled representation. This transformation is unique, and no additional assumptions about the interaction is necessary than its two-body nature. If the potential determining the interaction is isospin-conserving, then the antisymmetric spin-orbit (ALS) component must vanish ([Bro98b], p.12). Studies of the USD-interaction revealed only a minor dependence on the ALS component. Setting this to zero increased the rms deviation to the experimental energy values only from 185 keV to 215 keV.

In [Bro88a] an additional effort to reduce the number of parameters in the two-body interaction is described. To do so, a 14-parameter, density-dependent one-boson exchange potential (OBEP) was introduced for each component. With this OBEP it was possible to reproduce the 447 experimental binding energies which determined the USD-interaction with a rms deviation of 260 keV. The potential model defined by the OBEP is called "SDPOTA", and it was used to extend the calculations to the p shell [Ric91] and $p-sd$ cross shell [War92a]. However, calculations for the magnetic moment of ^{17}Ne based on these approaches have not been published so far.

7.2.3 Magnetic Dipole Moments

The theoretical values to be compared with the experimental magnetic moments of ^{19,21,23,25}Ne, presented in this work, are based on the CWP and CHP interactions of Wildenthal *et al.* [Wil79], and shell model calculations utilizing the USD-interaction described above [Bro01b]. None of these calculations includes predictions for ^{17}Ne, therefore an attempt to interpret the magnetic moment of ^{17}Ne will follow in a separate section.

The theoretical concept of calculating the magnetic moments is discussed in the publication of Brown and Wildenthal [Bro87]. It is found that the calculation necessitates the use of effective g-factors. These were determined on the basis of an analysis of experimental data of a number of $A = 17 - 39$ sd shell nuclei. The standard approach used in the shell model is to employ the magnetic M1 operator $\hat{\mathcal{O}}(\mathrm{M1})$ to calculate the corresponding reduced M1 matrix elements, in the notation of [Bro87]

$$
\begin{aligned}
M(\mathrm{M1}) &= \langle \mathrm{f}||\hat{\mathcal{O}}(\mathrm{M1})||\mathrm{i}\rangle \\
&= \left(\tfrac{1}{2}\right)(-1)^{T_f - T_z}
\end{aligned}
$$
$$
\times \left[\begin{pmatrix} T_f & 0 & T_i \\ -T_z & 0 & T_z \end{pmatrix} \langle \mathrm{f}|||\hat{\mathcal{O}}(\mathrm{ISM1})|||\mathrm{i}\rangle \;+\; \begin{pmatrix} T_f & 1 & T_i \\ -T_z & 0 & T_z \end{pmatrix} \langle \mathrm{f}|||\hat{\mathcal{O}}(\mathrm{IVM1})|||\mathrm{i}\rangle \right] . \quad (7.31)
$$

The corresponding magnetic moments in terms of the reduced matrix elements are given by equation (7.14)

$$
\begin{aligned}
\mu &= \sqrt{\frac{4\pi}{3}}\langle J, J_z = J|\hat{\mathcal{O}}(\mathrm{M1})|J, J_z = J\rangle \\
&= \sqrt{\frac{4\pi}{3}}\frac{J}{\sqrt{J(J+1)(2J+1)}}\langle J||\hat{\mathcal{O}}(\mathrm{M1})||J\rangle . \quad (7.32)
\end{aligned}
$$

The operators $\hat{\mathcal{O}}(\mathrm{ISM1})$ and $\hat{\mathcal{O}}(\mathrm{IVM1})$ in the reduced matrix elements are the isoscalar (IS) and isovector (IV) components of the M1 operator:

$$
\hat{\mathcal{O}}(\mathrm{M1}) = \tfrac{1}{2}\left[\hat{\mathcal{O}}(\mathrm{ISM1}) + \hat{\mathcal{O}}(\mathrm{IVM1})\right] , \quad (7.33)
$$

where

$$
\begin{aligned}
\hat{\mathcal{O}}(\mathrm{ISM1}) &= \mu_N \sqrt{\frac{3}{4\pi}} \sum_i \left[g_\ell(\mathrm{ISM1})\hat{\ell}_i + g_s(\mathrm{ISM1})\hat{\mathbf{s}}_i \right] I(\mathrm{IS}) , \\
\hat{\mathcal{O}}(\mathrm{IVM1}) &= \mu_N \sqrt{\frac{3}{4\pi}} \sum_i \left[g_\ell(\mathrm{IVM1})\hat{\ell}_i + g_s(\mathrm{IVM1})\hat{\mathbf{s}}_i \right] I(\mathrm{IS}) . \quad (7.34)
\end{aligned}
$$

The parameters $I(\mathrm{IS})$ and $I(\mathrm{IV})$ are given by 1 and $\tau^{(i)}$, respectively, where τ is the isospin of the i-th nucleon. The summation index i runs over all A nucleons in the nucleus, and the g_s and g_ℓ are the spin and orbital g-factors of the free nucleons:

$$
\begin{aligned}
g_s(\mathrm{ISM1}) &= \tfrac{1}{2}[g_s(\mathrm{p}) + g_s(\mathrm{n})] = 0.880 \ , \\
g_\ell(\mathrm{ISM1}) &= \tfrac{1}{2}[g_\ell(\mathrm{p}) + g_\ell(\mathrm{n})] = 0.500 \ , \\
g_s(\mathrm{IVM1}) &= \tfrac{1}{2}[g_s(\mathrm{p}) - g_s(\mathrm{n})] = 4.706 \ , \\
g_\ell(\mathrm{IVM1}) &= \tfrac{1}{2}[g_\ell(\mathrm{p}) - g_\ell(\mathrm{n})] = 0.500 \ .
\end{aligned}
\tag{7.35}
$$

It turns out that the theoretical values obtained with this method of using free-nucleon g-factors cannot reproduce the experimental magnetic moments very well. As mentioned by Heyde [Hey94], the approach of using the free nucleon g-factors fails because of the limitations of the model space where closed-shell nuclei are treated as an inert core. Core excitations which are not included in the model, are accounted for by effective g-factors which deviate from the free-nucleon values. The approach of Brown and Wildenthal tries to improve the discrepancies between theory and experiment by adjusting phenomenologically the values of effective g-factors. Optimum values for g^{eff} are found by performing a least-squares fit of shell-model values to a collection of 49 experimental magnetic moments and 114 experimentally determined M1 matrix elements [Bro87] as mentioned above. The authors introduce an effective M1 operator $\hat{\mathcal{O}}^{eff}$ of the form

$$
\hat{\mathcal{O}}^{eff}(\mathrm{ISM1/IVM1}) = (3/4\pi)^{1/2}[g_s\hat{\mathbf{S}} + g_\ell\hat{\mathbf{L}} + g_s\,\delta(\mathrm{M1})] \ ,
\tag{7.36}
$$

where the parameter δ is adjusted to the experimental values, and has a mass dependence of

$$
\delta(A) = \delta(A = 28)(A/28)^{0.35} \ .
\tag{7.37}
$$

Finally the effective g-factors are given by

$$
\begin{aligned}
g_s^{eff}(A) &= g_s + g_s\delta_s(\mathrm{M1}\,;A = 28)(A/28)^{0.35} \ , \\
g_\ell^{eff}(A) &= g_\ell + g_s\delta_\ell(\mathrm{M1}\,;A = 28)(A/28)^{0.35} \ , \\
g_p^{eff}(A) &= g_s\delta_p(\mathrm{M1}\,;A = 28)(A/28)^{0.35} \ ,
\end{aligned}
\tag{7.38}
\tag{7.39}
\tag{7.40}
$$

where g_p is the tensor part arising from the dipole-dipole interaction within the nucleus.

The different contributions to the g-factors are given in [Bro87] and listed in table 7.1. With these effective g-factors the theoretical magnetic moments for the sd shell were calculated by Brown [Bro01b], and they are used in figure 7.4 (C). A comparison between the experimental data and these and earlier theoretical values obtained with three different interactions is shown in figure 7.4, where the differences between experiment and theory are plotted against the isotope mass.

Table 7.1: *Effective nuclear moments in comparison with free-nucleon values. The values collected here were taken from [Bro87].*

	type	$g^{(free)}$	$g^{(eff)}$(A=28)
g_s	isoscalar	0.880	0.76
	isovector	4.71	4.00
	proton	5.586	4.76
	neutron	-3.826	-3.25
g_ℓ	isoscalar	0.5	0.519
	isovector	0.5	0.608
	proton	1.00	1.127
	neutron	0.00	-0.089
g_p	isoscalar	0	0.03
	isovector	0	0.38
	proton	0	0.41
	neutron	0	-0.35
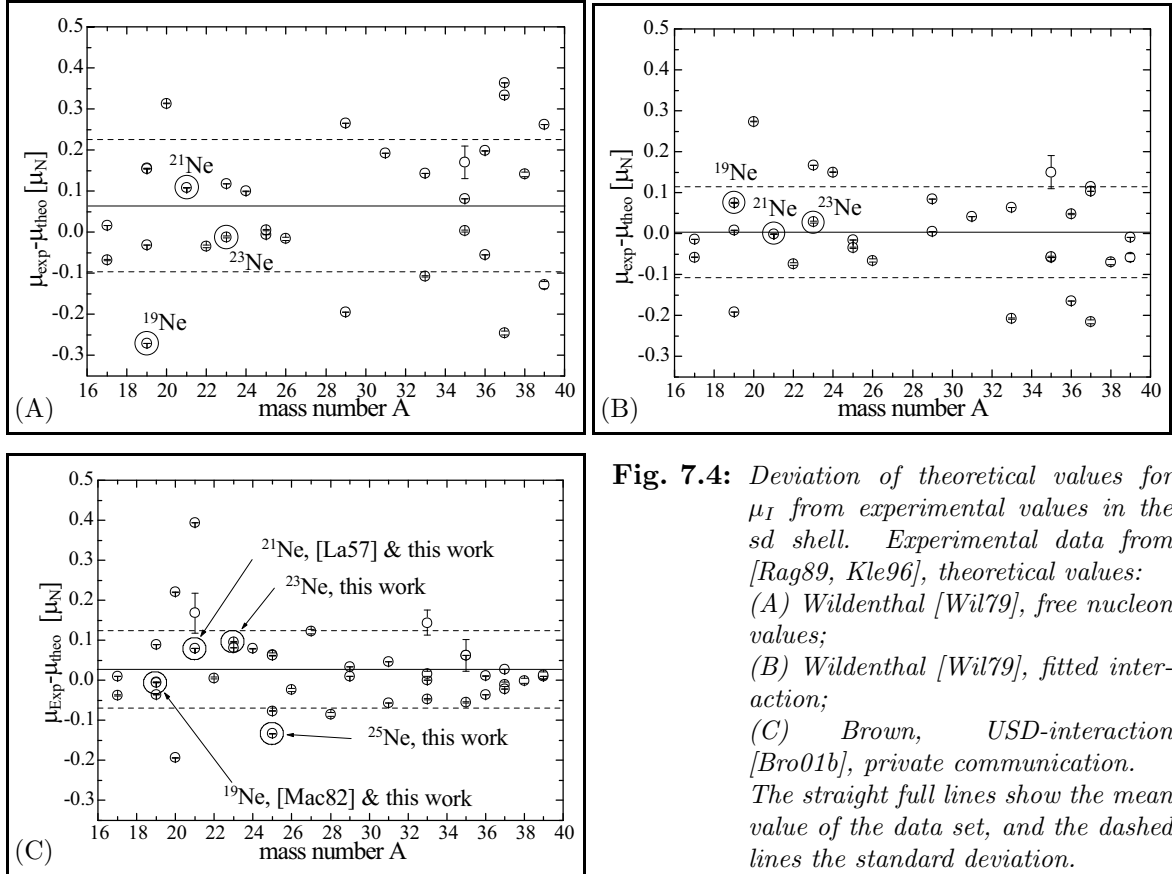
Fig. 7.4: *Deviation of theoretical values for μ_I from experimental values in the sd shell. Experimental data from [Rag89, Kle96], theoretical values:*
(A) Wildenthal [Wil79], free nucleon values;
(B) Wildenthal [Wil79], fitted interaction;
(C) Brown, USD-interaction [Bro01b], private communication.
The straight full lines show the mean value of the data set, and the dashed lines the standard deviation.

In plot (A) of figure 7.4, the theoretical values are taken from [Wil79], where the magnetic moments were calculated on basis of a shell-model approach using free nucleon g-factors. The sd-shell wave functions were calculated on the basis of two mass independent empirical Hamiltonians, one of which described the mass region $17 \leq A \leq 28$, the other the mass region $29 \leq A \leq 39$. The low-mass Hamiltonian was fitted to 200 experimental binding energies relative to ^{16}O, predominantly from the region $17 \leq A \leq 24$. The high mass Hamiltonian was obtained in a similar way by fitting to 140 binding energies in the mass range $32 \leq A \leq 39$.

Table 7.2: *Comparison of magnetic moments in the lower sd shell - experiment and theory. 6th column: single-particle magnetic moment (Schmidt value)*

isotope	Exp $[\mu_N]$	[Wil79], free $[\mu_N]$	[Wil79], fit $[\mu_N]$	μ_{SP} $[\mu_N]$	[Bro01b], USD $[\mu_N]$
^{17}O	-1.89379(9)	-1.91	-1.88	-1.91	-1.904
^{19}O	-1.53195(7)	-1.5	-1.54	-1.91	-1.621
^{17}F	+4.7223(12)	+4.79	+4.79	+4.79	+4.76
^{19}F	+2.628868(8)	+2.9	+2.82	+4.79	+2.665
^{21}F	+3.93(5)	–	–	+4.79	+3.762
^{19}Ne	-1.88419(56)	-2.04	-1.96	-1.91	-1.88
^{21}Ne	-0.66158(18)	-0.77	-0.66	-1.91	-0.741
^{23}Ne	-1.0799(25)	-1.07	-1.11	-1.91	-1.177
^{25}Ne	-1.0066(4)	–	–	-1.91	-0.873
^{21}Na	+2.8363(1)	–	–	+4.79	+2.442
^{22}Na	+1.746(3)	+1.78	1.82	–	1.74
^{23}Na	+2.2176556(6)	+2.1	+2.05	+4.79	+2.137
^{24}Na	+1.6903(8)	+1.59	+1.54	–	+1.611
^{25}Na	+3.683(4)	–	–	+4.79	+3.619
^{25}Mg	-0.85545(8)	-0.85	-0.84	-1.91	-0.918

Plot (B) shows the comparison of experiment and theory from the same publication. There effective g-factors were used which were determined on basis of the linear combinations of ten single-particle matrix elements, which were fitted to 42 experimentally known magnetic moments. The sd-shell wave functions employed to calculate the theoretical magnetic moments were the same as those used for the calculation with free g-factors.

To judge the quality of the theoretical descriptions the mean deviations were calculated and plotted as horizontal lines inside the graphs. The mean values are given as solid lines, the dashed lines show the standard deviation of the data. The corresponding systematic differences between experimental and theoretical magnetic moments are as follows:

$$
\begin{aligned}
\delta\mu &= (0.065 \pm 0.161)\,\mu_N & \text{Wildenthal, free } g\text{-factor, Fig. 7.4 (A)} \\
\delta\mu &= (0.003 \pm 0.111)\,\mu_N & \text{Wildenthal, fitted } g\text{-factor, Fig. 7.4 (B)} \\
\delta\mu &= (0.028 \pm 0.096)\,\mu_N & \text{Brown, USD-interaction, Fig. 7.4 (C)}
\end{aligned}
$$

(7.41)

7.2.4 Discussion of the Magnetic Moments

The comparison between experimental and theoretical magnetic moments in the sd shell which is presented in the previous section, shows the predictive power of recent shell-model calculations. As can be seen, the calculation based on the semiempirical W/USD-interaction yields the best results, showing the smallest deviation between theory and experiment. At first glance, it is surprising that this "best" theory reproduces the moments of ^{21}Ne and ^{23}Ne less accurate than the calculation by [Wil79]. These deviations are still within the general
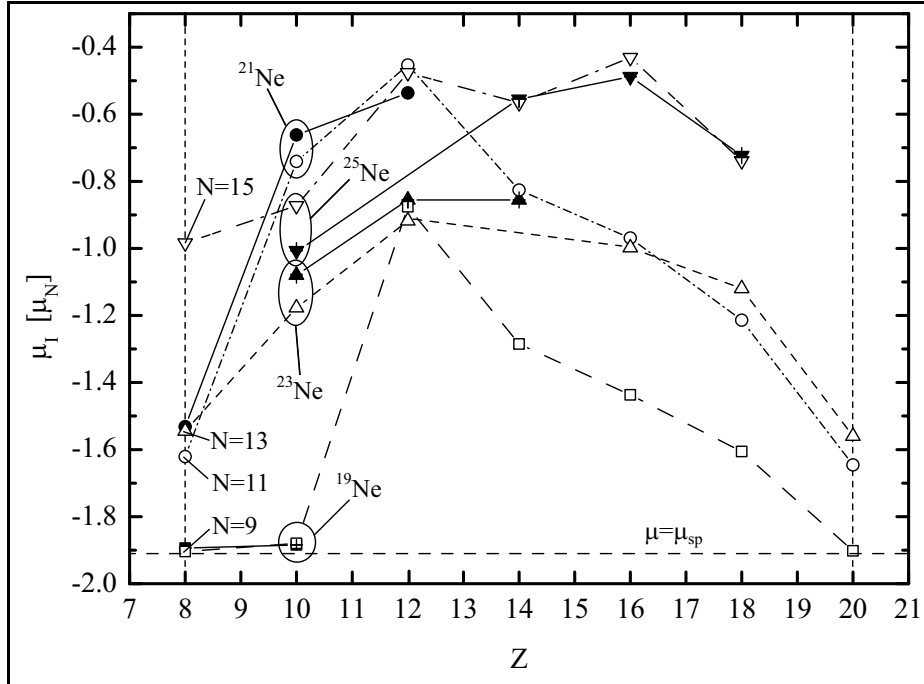
Fig. 7.5: *Plot of theoretical and experimental magnetic moments of isotones in the sd shell. The open symbols represent theoretical values provided by [Bro01b]. The filled symbols correspond to experimental data available from [Rag89] and the present study. The dashed horizontal line shows the Schmidt value of magnetic moments caused by an unpaired neutron in an ℓ + 1/2 state (-1.91 μ_N).*

trend and possibly influenced by the strong nuclear deformation which can be found in the vicinity of ^{20}Ne (for details see chapter 8). An argument to prefer the USD-theory is the fact that this theory describes the whole *sd* shell by *one* interaction, which is not the case for the calculations of Wildenthal, where the parameters had to be fitted for the low-mass and the high-mass region of the shell separately.

The behavior of the magnetic moments can be explained qualitatively by taking a look at their variation in isotonic chains. For the odd neon isotopes measured in the present work experimental magnetic moments are known for a number of isotones. These data, plotted as filled symbols, together with the theoretical values given by Brown [Bro01b] plotted as open symbols, are presented in figure 7.5. The unknown signs of the experimental data were adjusted according to the theoretical prediction which was always negative in the region shown in the plot. Additionally the single-particle magnetic moment of ℓ + 1/2 neutron configurations is plotted as a dashed horizontal line for orientation.

As can be seen, the trends of the experimental data are very well reproduced by the theory. The course of the magnetic moments along one isotone chain can be attributed mostly to the filling of protons into the *sd* shell, and thus softening the single-particle character of the configuration. The effect becomes most prominent for proton mid-shell nuclei, where the magnetic moments show the smallest absolute values and the largest deviations from the single-particle moment. Beyond the mid shell the single-particle character becomes dominant again, and the magnetic moments approach the single-particle value.

The magnetic moment of ^{19}Ne shows a deviating behavior from the general trend, having almost the same value like ^{17}O, whereas one would expect a smaller value. The ground state of ^{19}Ne is a deformed $s = 1/2$ state (see section 7.2.6) which is an exception in the chain of $N = 9$ nuclei, having $d_{5/2}$ ground states. Thus, one expects admixtures of other states than $s_{1/2}$ in the deformed configuration. Thus, a large deviation from the general trend of the magnetic moments of the $N = 9$ nuclei is expected. This deviation can be attributed to the suppression of first order configuration mixing for the $s_{1/2}$ neutron state in ^{19}Ne.

7.2.5 Electric Quadrupole Moments

The quadrupole deformation of valence orbits (i.e. the orbits included in the model space of the shell model) leads to deformation of the core orbits as well, which are not to be included in the model. This core deformation can be described in a self-consistent way as a perturbation from the coupling of $2\hbar\omega$, $J^{\pi} = 2^{+}$ core excitations to the valence orbits ([Bro01a], p.575). In the shell model space this effect can be accounted for by introducing effective charges of protons ($\tilde{e}_p = e_p^{free} + \delta e_p$) and neutrons ($\tilde{e}_n = e_n^{free} + \delta e_n$). Hence, the case of a free nucleon is given by $\delta e_{p,n} = 0$, $e_p^{free} = +e$ and $e_n^{free} = 0$. As discussed by Sagawa and Brown [Sag84], the polarization charge δe has a slight orbital dependence, and the isoscalar polarization charge $\delta e_p + \delta e_n$ takes values between 0.70 [Car86] and 0.79 [Bro88b]. The isovector polarization charge $\delta e_n - \delta e_p$ is found to be of the order of 0.2, but is more difficult to determine, because most quadrupole data is dominated by the isoscalar component [Kei00]. Taking into account only the isoscalar component the effective charges become $\tilde{e}_p = 1.35\,e$ and $\tilde{e}_n = 0.35\,e$ [Car86], whereas including the isovector component yields effective charges $\tilde{e}_p = 1.29$ and $\tilde{e}_n = 0.49$ [Bro01a] were used in the theoretical study presented below [Bro01b].

Similar to the magnetic moments, the electric quadrupole moments were calculated theoretically. Besides the privately communicated results of Brown [Bro01b], an older publication of Carchidi et $al.$ [Car86] was used to compare theoretical with experimental data. For the lower sd-shell nuclei this comparison is given in table 7.3 and shown graphically in figure 7.6

Both theoretical calculations start from the multipole operator

$$\hat{\mathcal{O}}(E, LM)_i = \tilde{e}_i r_i^L Y_{LM}(\theta_i, \phi_i) \,. \tag{7.42}$$

For of the quadrupole moment this operator with $L = 2$, $M = 0$ the expectation value takes the form of equation (7.21). The wave functions used to calculate the quadrupole moments are again based on the USD-interaction. As the quadrupole operator $\hat{\mathcal{O}}(E2)$ has a radial dependence, this has to be accounted for explicitly. Carchidi et $al.$ use three different approaches to model the corresponding Hamiltonian [Car86]. The first data set calculated by Carchidi et $al.$ [Car86] based on the Woods-Saxon potential [Bro82]

$$V_0(r) = U_0 \left\{ 1 + \exp(r - r_0 A^{1/3})/a_0 \right\}^{-1} \,. \tag{7.43}$$

The parameters given as "WSE" in [Bro82], were determined for the two doubly magic nuclei ^{16}O and ^{40}Ca. A smooth mass dependence is introduced by using for each of the Woods-Saxon parameters U_0, r_0 and a_0 the function

$$X_0 = X_a + X_b A^{-1/3} \,, \tag{7.44}$$
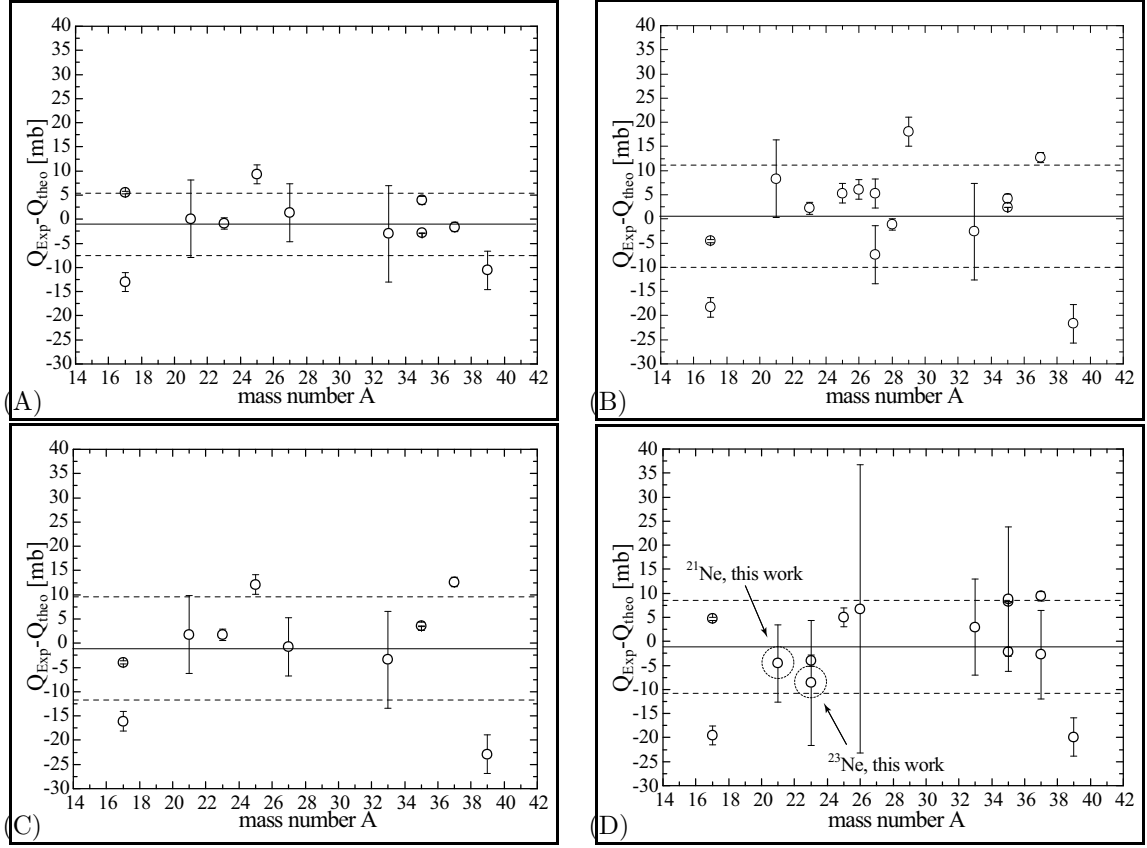
Fig. 7.6: *Deviation of theoretical values for Q_s from experimental values in the sd shell. Experimental data from [Rag89, Kle96], theoretical values with different radial wave functions:*
(A) Carchidi [Car86], Woods-Saxon potential;
(B) Carchidi [Car86], harmonic oscillator with mass dependence. The values for $^{26-29}Na$ were taken from [Kei00] (Tab. 4, column 7), where Brown calculated Q_s with the same parameter set as in [Car86];
(C) Carchidi [Car86], harmonic oscillator with experimental r_{ch};
(D) Brown, harmonic oscillator [Bro01b].
The straight full lines show the mean value of the data set, and the dashed lines the standard deviation of the data. The data in the four sets do not include all the same isotopes corresponding to availability data.

where X represents one of the parameters. The effective charges used for the calculations with the Woods-Saxon potential were $\tilde{e}_p = 1.15\ e$, and $\tilde{e}_n = 0.45\ e$. The difference between experimental and theoretical values are plotted in figure 7.6 (A)

The second theoretical data set uses a fit to the charge radii of closed-shell nuclei to determine the oscillator parameter which is obtained as

$$\hbar\omega = 45A^{-1/3} - 25A^{-2/3}\ [\text{MeV}]\ , \tag{7.45}$$

or equivalently expressed by the oscillator length

$$b = \sqrt{\frac{\hbar}{m\omega}}0.6A^{1/6}[1 - 0.556A^{-1/3}]^{-1/2}\ [\text{fm}]\ . \tag{7.46}$$

Plot 7.6 (B) shows the difference values between experimental data and the corresponding theoretical values of Carchidi *et al.* including this mass dependence.

Table 7.3: *Comparison of quadrupole moments in the lower sd shell - experiment and theory.*

isotope	Exp [mb]	[Bro01b] USD, HO [mb]	[Car86] HO(mass) [mb]	[Kei00] HO(mass) [mb]	[Car86] HO(fit) [mb]	[Car86] WS [mb]
^{17}O	-26(3)$^{(*)}$	-30.46	-21.2	–	-21.8	-31.3
^{17}F	-58(4)$^{(*)}$	-80.44	-81.7	–	-83.9	-87
^{21}Ne	+102.9(7.5)	+107.57	+94.7	–	+101.2	+102.9
^{23}Ne	+141(13)	+149.59	–	–	–	–
^{23}Na	+105.6(1.2)$^{(*)}$	+109.61	+103.4	–	+103.9	106.5
^{25}Mg	+201(3)	+194	+193.7	–	+186.9	+189.7
^{26}Na	-5.3(2)	–	–	-11.4	–	–
^{26}Al	+270(30)	+263.25	–	–	–	–
^{27}Na	-7.2(3)	–	–	-12.5	–	–
^{27}Al	+150(6)	–	+157.4	–	+150.8	+148.6
^{28}Na	+39.2(1.2)	–	–	+40.6	–	–
^{29}Na	+86(3)	–	–	+67.9	–	–
^{33}S	-64(10)	-66.96	–	–	–	–
^{35}S	+47.1(9)	+49.27	+42.9	–	+43.6	+43.2
^{35}Cl	-82.49(2)	-90.75	-84.9	–	-86	-79.6
^{35}Ar	-84(15)	-92.81	–	–	–	–
^{37}Cl	-64.93(2)	-77.4	-80.7	–	-80.6	-66.4
^{37}Ar	+76.2(9.2)	+78.96	–	–	–	–
^{39}K	49(4)	+68.89	+70.7	–	+71.9	+59.6

The third theoretical calculation uses an oscillator length b which is calculated individually for each stable isotope on the basis of experimental charge radii [Car86]

$$r_{ch}^2 = (r_p^{(0)})^2 + r_p^2 + (N/Z)r_n^2 + \frac{3}{4}(\hbar/mc)^2 \; , \tag{7.47}$$

where the oscillator length b is connected to $r_p^{(0)}$, which is the rms point proton radius for nuclei in the *sd* shell [Car86]

$$(r_p^{(0)})^2 = \left[\frac{18 + 3.5(Z-8)}{Z}\right] b^2 - \frac{3b^2}{2A} \; . \tag{7.48}$$

For r_p^2 and r_n^2 Carchidi *et al.* used the values $(0.86)^2$ and $-(0.34)^2$, respectively [Car86]. The comparison between experiment and theory is plotted in figure 7.6 (C). Both of the two calculations used an oscillator potential, and the effective charges were set to $\tilde{e}_p = 1.35 \; e$, and $\tilde{e}_n = 0.35 \; e$.

The fourth set of values given by Brown [Bro01b] includes predictions also for the more recently measured quadrupole moments as well as for ^{23}Ne. The calculational details follow the lines discussed in Keim *et al.* [Kei00]. The effective charges used in the calculation were $\tilde{e}_p = 1.29$ for the proton and $\tilde{e}_n = 0.49$ for the neutron, and a harmonic oscillator potential was assumed for the radial dependence. The comparison between the values obtained in this way and experimental data is plotted in figure 7.6 (D).

All of the four sets of theoretical values are compared with experimental data compiled by Raghavan [Rag89] and partly supplemented from the preprint of Stone [Sto01], and with data from laser spectroscopy. In a similar way as for the magnetic moments the deviation between experiment and theory is plotted in figure 7.6, together with the mean value and the corresponding standard deviation. The mean values and the standard deviations of the four data sets are the following:

δQ = (-1.1 ± 6.5) mb   Carchidi, Woods-Saxon potential, Fig. 7.6 (A) ,

δQ = $(+0.6 \pm 10.6)$ mb   Carchidi, harmonic oscillator, closed-shell fit, Fig. 7.6 (B) ,

δQ = (-1.1 ± 10.7) mb   Carchidi, harmonic oscillator, experimental r_{ch}, Fig. 7.6 (C) ,

δQ = (-1.1 ± 9.7) mb   Brown, harmonic oscillator, Fig. 7.6 (D) .

These deviations are generally of the order of the experimental errors.

7.2.6   Discussion of the Electric Quadrupole Moments

In a collective model the quadrupole moments of ^{21}Ne and ^{23}Ne can be well understood in the context of nuclear deformation, which dominates as well the behavior of the nuclear radius as will be discussed in chapter 8. The neon nuclei can be characterized by well deformed nuclear shapes and large intrinsic quadrupole moments Q_0 which is connected to the spectroscopic quadrupole moment Q_s by [Rin80]

$$Q_s = Q_0 \frac{3K^2 - I \cdot (I+1)}{(2I+3)(I+1)} \ . \tag{7.49}$$

Assuming deformed nuclei, the single-particle levels can be described in the context of the Nilsson model [Nil55], where the nuclear state is determined by the quantum numbers $[N\, n_z\, m_\ell\, , J]$. J is the total angular momentum of the nucleus, thus corresponding to the spin. The deformation properties are supported by the spins of the odd neon isotopes which contradict the spherical shell model, where the spins should be $I(^{19}\text{Ne}) = 5/2$, $I(^{21}\text{Ne}) = 5/2$, $I(^{23}\text{Ne}) = 5/2$, $I(^{25}\text{Ne}) = 1/2$. In the Nilsson model ^{19}Ne can be assigned to a $[220, 1/2]$ state, and ^{21}Ne to a $[211, 3/2]$ state, which is consistent with the spin of those isotopes.

In comparing the results of the different calculations, one finds neither the different assumptions for the radial wave function nor the modification of the effective charges within reasonable limits give a systematic improvement of the overall agreement with experimental data.

7.3   Comparison of Mirror Nuclei ^{17}Ne and ^{17}N

A long lasting dispute about the nuclear ground state structure of ^{17}Ne [Oza94, Gui95, Zhu95, Tim96, For01] has been going on for almost one decade. The community is split into two parties, favoring either a proton halo or a standard shell-model structure. Hence, a separate discussion of the possibilities to clear up the structure of ^{17}Ne from the data gathered in the present work is very interesting. Calculations of the nuclear moment in the framework of nuclear halo models or in the large-basis shell model framework have not been performed, so a qualitative approach was chosen.

The magnetic moment of ^{17}N, the mirror nucleus of ^{17}Ne, was measured by Ueno *et al.* in 1996 [Uen96]. Hence, the structure of ^{17}Ne can be discussed in the context of mirror magnetic moments as was suggested by Sugimoto [Sug73]. It is particularly interesting to combine the two magnetic moments $\mu(^{17}Ne)$ and $\mu(^{17}N)$ to an isoscalar moment, and to compare this with simple models and with the systematics of isoscalar moments [Sug73].

7.3.1 Isoscalar Moment

According to Sugimoto [Sug73], the nuclear magnetic moment of a j^n configuration of protons or neutrons can be written in an isospin-space representation:

$$\mu = \frac{1}{2}\left[g_\ell^s \left\langle \sum_i \ell_z^{(i)} \right\rangle_J + \mu_{n,p}^s \left\langle \sum_i \sigma_z^{(i)} \right\rangle_J + g_\ell^v \left\langle \sum_i \tau_z^{(i)} \ell_z^{(i)} \right\rangle_J + \mu_{n,p}^v \left\langle \sum_i \tau_z^{(i)} \sigma_z^{(i)} \right\rangle_J \right] . \quad (7.50)$$

The g_ℓ^s and g_ℓ^v represent the isoscalar and isovector orbital g-factors, the $\mu_{n,p}^s$ and $\mu_{n,p}^v$ the intrinsic nucleon magnetic moments. For details the book of de-Shalit and Talmi [Sha63] should be consulted. The upper indices s and v distinguish between components of the magnetic moment which behave like a scalar (s), or a vector (v) in isospin space. The isoscalar components have the same values for both members of a mirror pair, while the isovector components have the same absolute value, but opposite sign for both mirror partners.

The isoscalar moment of two mirror nuclei (nuclei with the same mass number $A(1) = A(2)$ and opposite isospin $T_z(1) = -T_z(2)$) is given by half of the sum of the two magnetic moments of the mirror partners

$$\frac{1}{2}\left[\mu(T_z = +T) + \mu(T_z = -T)\right] = \frac{1}{2}\left[g_\ell^s \left\langle \sum_i \ell_z^{(i)} \right\rangle_J + \mu_N^s \left\langle \sum_i \sigma_z^{(i)} \right\rangle_J \right] . \quad (7.51)$$

In the same way the isovector moment is given by the difference of the two moments

$$\frac{1}{2}\left[\mu(T_z = +T) - \mu(T_z = -T)\right] = \frac{1}{2}\left[g_\ell^v \left\langle \sum_i \tau_z^{(i)} \ell_z^{(i)} \right\rangle_J + \mu_N^v \left\langle \sum_i \tau_z^{(i)} \sigma_z^{(i)} \right\rangle_J \right] , \quad (7.52)$$

which will not be discussed in the present context.

The total angular momentum in jj-coupling is given by $J = \left\langle \sum \ell \right\rangle + \frac{1}{2}\left\langle \sum \sigma \right\rangle$. Assuming the parameter $\mu_{n,p}^s$ is given by the sum of the magnetic moments of the free nucleons $\mu_{n,p} = \mu_n + \mu_p$, and the orbital g-factor $g_\ell = 1$ as well by the free-nucleon factors, the sum moment can be written as:

$$\mu(T_z = +T) + \mu(T_z = -T) = J + \left(\mu_p + \mu_n - \tfrac{1}{2}\right) \left\langle \sum_i \sigma_z^{(i)} \right\rangle_J \quad (7.53)$$

7.3.2 Discussion of the Experimental Results for ^{17}N/^{17}Ne

Sugimoto [Sug73] gives an overview of a number of isoscalar moments of $T = 0, 1/2, 1$ nuclei. As he points out, most of the experimental isoscalar moments fall inside the limits given by the isoscalar moments calculated from the Schmidt values of the nuclei under investigation. The deviations can be addressed by correcting the single-particle moment by relativistic and

configuration-mixing effects [Noy59], while the influence of meson exchange currents (MEC) largely cancels out.

The magnetic moment of ^{17}N was measured in a β-NMR experiment using a spin polarized beam from a fragmentation reaction of ^{18}O with a ^{93}Nb target [Uen96]. The experiment yielded an absolute value of the magnetic moment $|\mu(^{17}N)| = 0.352(2)\,\mu_N$. The sign was not measured, but from shell-model considerations the sign was assumed to be negative, corresponding to a proton in the $p_{1/2}$ state.

The Schmidt moment of a $p_{1/2}$ proton (Eqn. (7.19)) is

$$\mu_S(^{17}N) = -0.264\,\mu_N\ . \tag{7.54}$$

A surprising observation is that the magnetic moment of ^{17}N is more negative than the corresponding Schmidt value, which is one of the few exceptions from the general trend shown in figure 7.1.

The magnetic moment of ^{17}N can now be compared to the moment of its mirror nucleus ^{17}Ne. The Schmidt value of a neutron in a $p_{1/2}$ state is

$$\mu_S(^{17}Ne) = +0.638\,\mu_N\ , \tag{7.55}$$

while the experimental value of the magnetic moment is $+0.78798(53)\,\mu_N$. ^{17}Ne shows as well an outward deviation from the Schmidt lines shown in figure 7.2.
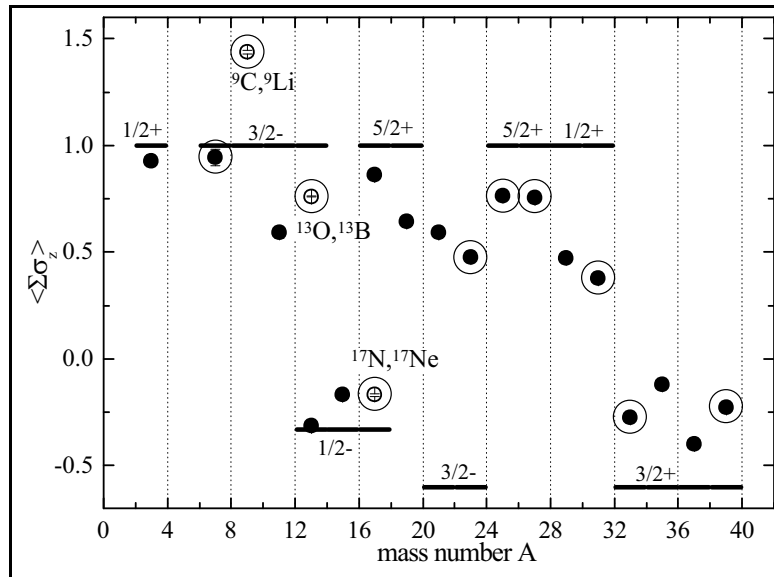
Fig. 7.7: *Isoscalar moments from experimental magnetic moments and Schmidt values according to Sugimoto [Sug73]. Experimental values are plotted as circles, from the corresponding Schmidt value as lines for J^π. The data points marked by filled circles represent data of nuclei with isospin $T = 1/2$, the open circles denote nuclei with $T = 3/2$. The plot contains data taken from [Sug73] and additional data from [Rag89]. Data not included in [Sug73] are marked by large circles.*

Now the isoscalar moment can be investigated. The experimental data available to Sugimoto [Sug73] cover a number of mirror nuclei, namely 9 self conjugate nuclei ($T = 0$), 13 isospin doublets ($T = 1/2$) including two excited states, and 4 isospin triplets ($T = 1$).

Meanwhile this collection of data can be extended in the light nuclei region to additional $T = 0, 1/2, 1$ and $T = 3/2$ pairs [Rag89]. The corresponding values of $\langle \sum \sigma \rangle$, calculated by the use of equation (7.53), are plotted in figure 7.7. The plot covers the isoscalar moments of nuclei up to the *sd* shell. It is limited to mirror pairs with $T = 1/2$ and $T = 3/2$, using data available nowadays from the sources [Rag89] supplemented by [Sto01] and ^{17}Ne from this work. The isoscalar moment of self-conjugate nuclei and $T = 1$ pairs were omitted, because those are formed by odd-odd nuclei.

Several features become obvious from Fig 7.7:

- The isoscalar moments of the majority of the mirror nuclei fall between and deviate little from the corresponding isoscalar moments Schmidt moments.

- The isoscalar moment of the $T = 3/2$ mirror pair ^{9}C-^{9}Li falls far outside the general trend.

- The $T = 3/2$ mirror pairs ^{13}O-^{13}B and even ^{17}Ne-^{17}N follow the general trend of the $T = 1/2$ nuclei.

The situation for the ($T = 1$) mirror pair ^{8}Li-^{8}B, which is not plotted in figure 7.7, is similar to the case of ^{9}C-^{9}Li. The corresponding isoscalar moment ($\langle \sum \sigma \rangle_{exp} = 1.815$) exceeds its single-particle value ($\langle \sum \sigma \rangle_{sp} = 1.33$) considerably. From these observations the conclusion is drawn that nuclei with "unusual structure", like ^{9}C [Huh98] and ^{8}B [Min92] cause a behavior deviating from the general trend of the isoscalar moments. In contrast to this, the mirror pair ^{17}N-^{17}Ne, with magnetic moments adding up to an isoscalar moment close to the Schmidt value, shows isospin symmetry of the two nuclei.

7.3.3   Discussion for ^{17}N

The statements of the previous section can be used to find a qualitative picture for the structure of ^{17}Ne. First of all, as discussed e.g. by Arima [Ari78], the general deviation of the magnetic moments and isoscalar moments from their Schmidt values can be explained by several mechanisms, namely (i) First order configuration mixing (core polarization), (ii) mesonic exchange currents (MEC), (iii) coupling of a valence nucleon to low-lying collective states, (iv) second-order configuration mixing (of states with $2\hbar\omega$ or higher).

Compared to the individual magnetic moments, the isoscalar moments are less sensitive to these mechanisms because the effects influencing the magnetic moments partly cancel out. Thus, the magnetic moments show stronger deviations from the corresponding single-particle value than the isoscalar parts. Furthermore, the first-order configuration mixing does not contribute to the moments of $p_{1/2}$ states [Ari54, Shi74]. The ^{17}N magnetic moment has been explained by Ueno *et al.* [Uen96]. In this context, also the behavior of the magnetic moments and their isoscalar parts for the pair ^{17}Ne-^{17}N can be well understood.

The exceptions from the general trend observed in figure 7.7 for $A = 8$ and $A = 9$ are probably caused by the proton-drip-line nuclei ^{8}B and ^{9}C and cannot easily be explained by the above mechanisms. ^{8}B is considered as a proton halo nucleus, which was suggested from a β-NMR measurement of the quadrupole moment by Minamisono *et al.* [Min92] and was

confirmed by Schwab *et al.* [Sch95] from a narrow momentum distribution observed in beak-up reactions. Similarly the magnetic moment of ^{9}C, probably causing the strong deviation from the trend in the isoscalar moments "may be an indication of unique structure phenomena for the drip-line nucleus" [Huh98]. These deviations imply the breaking of isospin symmetry between the mirror partners.

The isoscalar moments of the two other $T = 3/2$ mirror pairs follow the general trend of the $T = 1/2$ nuclei, which indicates isospin symmetry between the two partners. This behavior is shown also by the pair ^{17}Ne-^{17}N, even though the individual magnetic moments fall both outside the Schmidt lines.

Ueno *et al.* [Uen96] explained the magnetic moment of ^{17}N by admixtures of sd-shell configurations to the $p_{1/2}$ single-hole state. The authors investigate ^{17}N in a model assuming a core of ^{16}O, so that the ^{17}N ground state is formed by a hole in a $p_{1/2}$ proton shell and two neutrons in the sd shell. In a first approximation, the neutrons in the sd shell couple to $J^\pi = 0$, so that the proton alone is responsible for the nuclear spin of $I^\pi = 1/2^-$.

$$\psi_0 = \left| (\pi p_{1/2})^{-1} \otimes [(\nu\, sd)^2]^{J^\pi=0^+} \right\rangle^{J^\pi=1/2^-}$$

Thus, the proton configuration is uniquely assigned to a $p_{1/2}$ hole, where first-order core polarization of the protons does not contribute. Finally, the contribution of this configuration to the magnetic moment consists only of the single-particle value plus small corrections arising from MEC and second order core polarization, which is accounted for by the use of effective g-factors (see [Uen96]).

Secondly, the influence of the sd shell neutrons is investigated, with the result that the wave function contains appreciable components of the sd-shell neutron pair coupled to $J^\pi = 2^+$,

$$\psi_A = \left| (\pi p_{3/2})^{-1} \otimes [(\nu\, d_{5/2})^2]^{J^\pi=2^+} \right\rangle^{J^\pi=1/2^-} ,$$

$$\psi_B = \left| (\pi p_{3/2})^{-1} \otimes [(\nu\, s_{1/2})(\nu\, d_{5/2})]^{J^\pi=2^+} \right\rangle^{J^\pi=1/2^-} .$$

Then the ground state wave function can be described by

$$\psi(^{17}N) = c_0\psi_0 + c_A\psi_A + c_B\psi_B , \tag{7.57}$$

and the magnetic moment of ^{17}N can be explained by $|c_A|^2 + 0.73|c_B|^2 = 4.4\%$ which corresponds to an admixture of configurations with sd neutrons coupled to 2^+ between 4.4 and 6%.

Shell-model calculations with two different interactions (PSDWBT, PSDMK) justify this empirical argumentation, yielding 2.8% and 4.6%, respectively, of $J^\pi = 2^+$ admixture to the $J^\pi = 0^+$ major component.

As well interesting in the context of a possible halo structure is the ψ_0 wave function, which consists of three contributions. For ^{17}N, the shell model calculations yielded the components listed in table 7.4.

Note that the wave function of the two valence neutrons is dominated by the $0d_{5/2}$ state.

Table 7.4: *Contributions to the ground-state wave function ψ_0 of ^{17}N. The values are taken from [Uen96].*

	interaction	
configuration	PSDWBT	PSDMK
$(\pi\,p_{1/2})^{-1} \otimes [(\nu\,d_{5/2})^2]^{0^+}$	63.4%	62.8%
$(\pi\,p_{1/2})^{-1} \otimes [(\nu\,s_{1/2})^2]^{0^+}$	26.9%	25.1%
$(\pi\,p_{1/2})^{-1} \otimes [(\nu\,d_{3/2})^2]^{0^+}$	6.5%	6.7%

7.3.4 Conclusions for ^{17}Ne

As discussed above, the behavior of the magnetic moments of the mirror nuclei ^{17}N-^{17}Ne is symmetric in the isospin. Thus, the explanation given by Ueno *et al.* [Uen96] for the magnetic moment of ^{17}N can be as well adopted for ^{17}Ne without problems, suggesting a similar structure.

It remains to be discussed how a halo structure, with similar contributions of the *sd*-shell proton pair coupled to $J^\pi = 2^+$, would influence the magnetic moment of ^{17}Ne, and thus the composition of the wave function? The dominant zero-order wave function of a halo configuration has to be

$$\psi_0 = \left| [(\pi\,s_{1/2})^2]^{J^{\pi=0^+}} \otimes (\nu p_{1/2})^{-1} \right\rangle^{J^\pi=1/2^-} \quad .$$

This dominance would involve a difference to the composition of the wave function of ^{17}Ne to the magnetic moment. The leading $s_{1/2}$ proton configuration would suppress the $d_{5/2}$ admixtures, which are important for the deviation from the Schmidt value. However, from the magnetic moment itself, and from their mirror symmetry, it is clear that both nuclei, ^{17}N and ^{17}Ne, are similar in their ground-state structure.

The argument against the proton halo structure of ^{17}Ne is supported by the theoretical study of Fortune and Sherr [For01], who describe the ground state structure of ^{17}Ne with a proton pair in the *sd* shell in a ^{15}O + 2p (2s, 1d) model. In comparison with experimental excitation energies they conclude that the ground state of ^{17}Ne is dominated by 78% of a $(\pi d_{5/2})^2$ configuration with 22% of $(\pi s_{1/2})^2$ admixture. The calculations of Zhukov *et al.* [Zhu95] yield almost the same ratio of *s*-wave and *d*-wave components, although the authors argue in favor of a halo. Finally Timofeyuk *et al.* [Tim96] claims the dominance of the halo $s_{1/2}$ state over the $d_{5/2}$ configuration, but nevertheless argues against a halo. We will come back to this discussion in connection with the mean square charge radii.

Chapter 8

Nuclear Shapes and Sizes

The interpretation of the experimental differences in mean square charge radii of the neon isotopes, presented in chapter 6, is closely related to the shapes of the nuclei. The deformation properties are usually responsible for irregularities in the trend of the radii along the isotope chain. Thus, the first part of this chapter is devoted to the description of the nuclear shapes. The second part compares the experimental data with several recent microscopic theoretical calculations of the charge radii. In a third section the radius of ^{17}Ne is compared to theoretical predictions in the context of a possible halo structure.

8.1   Nuclear Shape and Nuclear Deformation

8.1.1   Shape Description by Spherical Harmonics

The shape of a nucleus, described in terms of e.g. spherical harmonics and spherical coordinates, can be related to the experimental observables such as quadrupole moments and E2 transition strengths. In the simplest model a non-spherical nucleus is represented by a liquid drop which is filled homogenously with nuclear matter and has a well defined surface. The radius vector pointing to the surface is parameterized in terms of spherical harmonics (see [Rin80], p.5ff)

$$r = R(\theta, \phi) = R_0 \left(1 + \alpha_{00} + \sum_{\lambda=1}^{\infty} \sum_{\mu=-\lambda}^{\lambda} \alpha_{\lambda\mu}^* Y_{\lambda\mu}(\theta, \phi) \right) \, , \tag{8.1}$$

where R_0 is the radius of a sphere with the same volume.

The term α_{00} accounts for the volume conservation of the nuclear "liquid drop" under deformation (assuming that the nuclear medium is incompressible). It is given by

$$\alpha_{00} = -\frac{1}{4\pi} \sum_{\lambda \geq 1, \mu} |\alpha_{\lambda\mu}|^2 \, . \tag{8.2}$$

The terms with $\lambda = 1$ describe a translation of the whole nucleus. The three parameters $\alpha_{1\mu}$ can be fixed by the condition that the origin coincides with the center of mass

$$\int_V \mathbf{r} \quad d^3 r = 0 \, . \tag{8.3}$$

In the present framework only quadrupole deformations are of interest which limits the description to $\lambda = 2$. In this case five parameters $\alpha_{2\mu}$ have to be considered. Three of them

define the rotation of the deformed body with respect to an external coordinate system. By a suitable transformation it can be changed to a body-fixed coordinate system which is aligned to the body's principal axes. In this system, only three of the five parameters are different from zero: α_{20} and $\alpha_{22} = \alpha_{2-2}$. Under these conditions it is convenient to change to the so-called "Hill-Wheeler coordinates" [Hil53], which are given by

$$
\begin{aligned}
\alpha_{20} &= \beta_2 \cdot \cos\gamma \,, \\
\alpha_{22} &= \frac{1}{\sqrt{2}} \beta_2 \cdot \sin\gamma \,, \\
\sum_\mu |\alpha_{2\mu}|^2 &= \alpha_{20}^2 + 2\alpha_{22}^2 = \beta_2^2 \,, \\
\cos\gamma &= \sqrt{\frac{\alpha_{20}^2}{\alpha_{20}^2 + 2\alpha_{22}^2}}
\end{aligned}
\tag{8.4}
$$

The corresponding expression for the vector pointing to the nuclear surface is given by

$$
R(\theta,\phi) = R_0 \left(1 + \beta_2 \sqrt{\frac{5}{16\pi}} (\cos\gamma(3\cos^2\theta - 1) + \sqrt{3}\sin\gamma\sin^2\theta\cos 2\phi) \right)
\tag{8.5}
$$

In figure 8.1 a few examples of the deformation dependence of the parameters are shown.
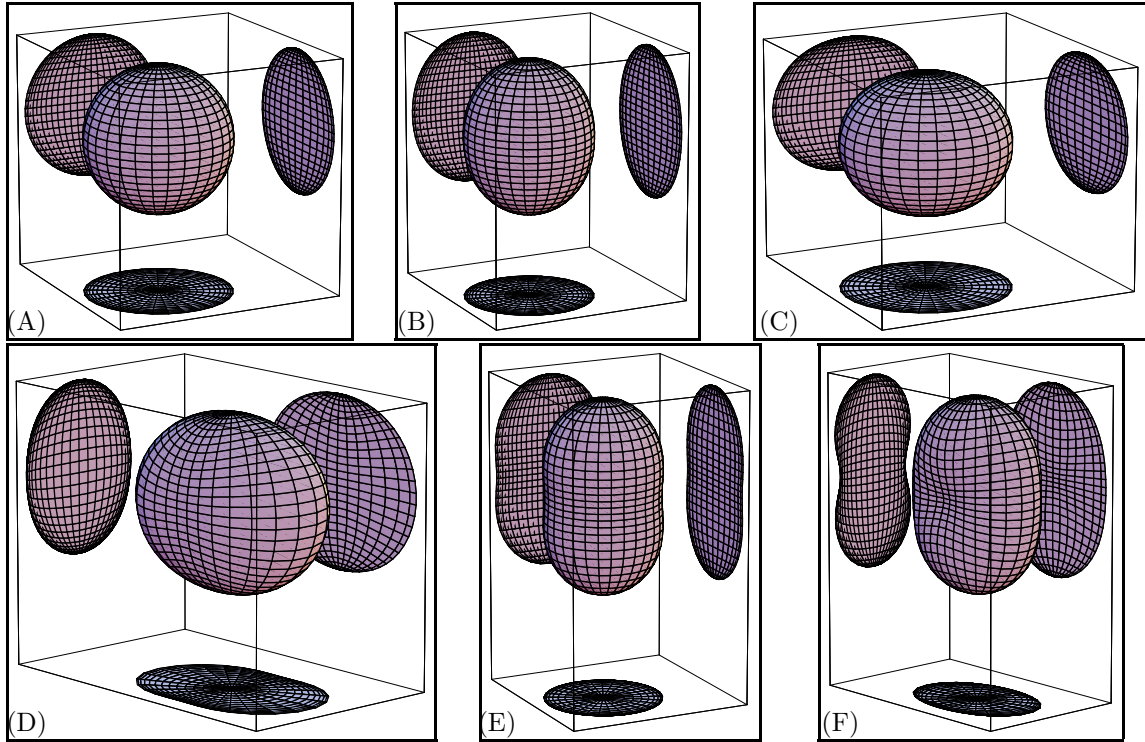
Fig. 8.1: *Examples of nuclear deformation depending on the deformation parameters. SH stands for deformation in terms of spherical harmonics, HW in terms of Hill-Wheeler coordinates*
(A) SH: $\alpha_{20} = \alpha_{22} = 0$, HW: $\beta_2 = \gamma = 0$, spherical shape
(B) SH: $\alpha_{20} = 0.2$, $\alpha_{22} = 0$, HW: $\beta_2 = 0.2$, $\gamma = 0$, prolate small def.
(C) SH: $\alpha_{20} = -0.2$, $\alpha_{22} = 0$, HW: $\beta_2 = 0.2$, $\gamma = \pi/3$, oblate small def.
(D) SH: $\alpha_{20} = 0$, $\alpha_{22} = 0.3$, HW: $\beta_2 = \sqrt{0.42}$, $\gamma = \pi/2$, triaxial def.
(E) SH: $\alpha_{20} = 0.6$, $\alpha_{22} = 0$, HW: $\beta_2 = 0.6$, $\gamma = 0$, strong prolate def.
(F) SH: $\alpha_{20} = 0.6$, $\alpha_{22} = 0.3$, HW: $\beta_2 = 0.74$, $\gamma = 0.61$, strong triaxial def.

For $\gamma = 0$ and $\gamma = \pi/3$ the resulting nuclear shapes have cylindrical symmetry with one stretched (prolate) or shortened (oblate) axis. The coordinate system describing the nuclear shape is chosen such that the coordinate system's z-axis is parallel to the symmetry axis of the nucleus. Then, these nuclear shapes are characterized by $\alpha_{22} = 0$, while $\alpha_{20} > 0$ describes prolate and $\alpha_{20} < 0$ oblate shapes. Correspondingly, prolate shapes are described in Hill-Wheeler coordinates by $\beta_2 > 0$ and $\gamma = 0$ oblate shapes by $\beta_2 > 0$, $\gamma = \pi/3$. All other parameter sets describe nuclear shapes having no axis of cylindrical or rotational symmetry, i.e. so-called triaxially deformed nuclei. As can be seen from the plots in figure 8.1 (E), (F) the parametrization of the nuclear shape in terms of spherical harmonics differs considerably from the ellipsoidal shape in the case of large deformation parameters.

All further discussion shall be limited to nuclei with rotational symmetry along the z-axis, meaning that only the deformation parameter α_{20} differs from zero. Furthermore by fixing $\gamma = 0$ and shifting the sign of the deformation to β_2, it possible to set

$$\alpha_{20} \equiv \beta_2 \,, \tag{8.6}$$

which is used as the deformation parameter in the literature.

Thus, the radius vector r of a deformed nucleus is then given by

$$r(\theta) = R_0 \left[1 + \alpha_{00} + \beta_2 Y_{20}(\theta) \right] \,. \tag{8.7}$$

In lowest order of β the ms radius of a deformed nucleus is connected to the ms spherical radius r_{sph} by [Ott89]

$$\langle r^2 \rangle = \langle r^2 \rangle_{sph} \left(1 + \frac{5}{4\pi} \beta_2^2 \right) \,. \tag{8.8}$$

8.1.2   Droplet Model Description of Nuclei

The droplet model was introduced as a refinement of the liquid drop model (LDM) of average nuclear properties. The model takes into account the effects of to the deviation of neutron and proton densities from a constant bulk value, treats the nuclear surface as diffuse, and incorporates the deformation of the nuclear shape. The nuclear radius r is expanded in a series of Legendre polynomials

$$r = nR(1 + \alpha_2 P_2 + \alpha_4 P_4 + \alpha_6 P_6 + ...) \,, \tag{8.9}$$

where volume conservation is achieved by the relation

$$n = \left(1 - \tfrac{2}{5}\alpha_2^2 - \tfrac{2}{105}\alpha_2^3 + \tfrac{2}{25}\alpha_2^4 - \tfrac{2}{35}\alpha_2^2\alpha_4 - \tfrac{1}{9}\alpha_4^2 + ... \right) \,. \tag{8.10}$$

The connection between the α_λ and the deformation parameter β_λ is given by

$$\alpha_\lambda = \sqrt{\frac{(2\lambda + 1)}{4\pi}} \beta_\lambda \,. \tag{8.11}$$

In the context of this work the ms nuclear charge radii are of interest. Following Myers *et al.* [Mye83, Mye87] this ms radius can be expressed by

$$\langle r^2 \rangle = \langle r^2 \rangle_u + \langle r^2 \rangle_r + \langle r^2 \rangle_d \,, \tag{8.12}$$

which is the general expression for protons or neutrons. This expression for the sharp nuclear radius can be used to calculate the neutron skin thickness

$$t = \tfrac{2}{3}R(I - \bar{\delta})/B_s, \tag{8.13}$$

which gives different neutron and proton radii,

$$\text{for neutrons:} \quad R_n = R + \frac{Z}{A}t, \qquad \text{for protons:} \quad R_Z = R - \frac{N}{A}t \ . \tag{8.14}$$

Note that in the following the explicit distinction between proton and neutron radius is not made.

The first term of equation (8.12) treats a uniform distribution of nucleons, including the nuclear shape. It is given as an expansion in the deformation parameters α_λ

$$\langle r^2 \rangle_u = \tfrac{3}{5}R^2 \left(1 + \alpha_2^2 + \tfrac{10}{21}\alpha_2^3 - \tfrac{27}{35}\alpha_2^4 + \tfrac{10}{7}\alpha_2^2\alpha_4 + \tfrac{5}{9}\alpha_4^2 + ... \right) \ , \tag{8.15}$$

where the overall radius R contains more details of the nuclear bulk properties than the LDM:

$$R = r_0 A^{1/3}(1 + \bar{\varepsilon}) \ , \tag{8.16}$$

$$\bar{\varepsilon} = \frac{-2\,a_2\,A^{-1/3}B_s + L\bar{\delta}^2 + c_1 Z^2 A^{-4/3}B_C}{K} \ , \tag{8.17}$$

$$\bar{\delta} = \frac{I + \tfrac{3}{16}(c_1/Q)ZA^{-2/3}B_v}{1 + \tfrac{9}{4}(J/Q)A^{-1/3}B_s} \ , \tag{8.18}$$

$$I = \frac{(N - Z)}{A} \ . \tag{8.19}$$

The different parameters used in the model are given in [Mye83]

$r_0 = 1.18$ fm, the nuclear radius constant,

$b = 0.99$ fm, the nuclear diffuseness,

$c_1 = \tfrac{3}{5}(e^2/r_0) = 0.73219$ MeV, the Coulomb energy coefficient,

$a_2 = 20.69$ MeV, the surface energy coefficient,

$J = 36.8$ MeV, the symmetry energy coefficient,

$Q = 17$ MeV, the effective surface stiffness,

$K = 240$ MeV, the compressibility coefficient, and

$L = 100$ MeV, the density symmetry coefficient.

The coefficients B_x are shape dependent and can be expressed by an expansion in terms of the deformation parameters α_λ

$$B_s = 1 + \tfrac{2}{5}\alpha_2^2 - \tfrac{4}{105}\alpha_2^3 - \tfrac{66}{175}\alpha_2^4 - \tfrac{4}{35}\alpha_2^2\alpha_4 + \alpha_4^2 + ... \tag{8.20}$$

$$B_C = 1 - \tfrac{1}{5}\alpha_2^2 - \tfrac{4}{105}\alpha_2^3 + \tfrac{51}{245}\alpha_2^4 - \tfrac{6}{35}\alpha_2^2\alpha_4 - \tfrac{5}{27}\alpha_4^2 + ... \tag{8.21}$$

$$B_v = 1 - \tfrac{1}{5}\alpha_2^2 - \tfrac{2}{105}\alpha_2^3 - \tfrac{253}{1225}\alpha_2^4 - \tfrac{4}{055}\alpha_2^2\alpha_4 + \tfrac{4}{9}\alpha_4^2 + ... \tag{8.22}$$

The second sum term of equation (8.12) for the ms radius treats the redistribution of the nucleons, and is given by

$$\langle r^2 \rangle_r = \tfrac{12}{175} C' R^2 \left(1 + \tfrac{14}{5}\alpha_2^2 + \tfrac{28}{15}\alpha_2^3 - \tfrac{29}{5}\alpha_2^4 - \tfrac{116}{15}\alpha_2^2\alpha_4 + \tfrac{5}{9}\alpha_{70}^{26} + ...\right) \ . \tag{8.23}$$

The parameter C' in this formula depends only on A and Z, and can be approximated by ($e^2 = 1.4399764$ MeV fm)

$$C' = \frac{1}{2}\left(\frac{9}{2K} + \frac{1}{4J}\right)\frac{Z\,e^2}{R_z} \approx 0.0156\,Z\,A^{1/3} \ . \tag{8.24}$$

Finally the last term of equation (8.12) takes into account the diffuseness of the nuclear surface and has the simple form

$$\langle r^2 \rangle_d = 3b^2 \ . \tag{8.25}$$

It is worth noting that this correction has no shape dependence, and is taken as a constant for all nuclides.

Additionally Myers *et al.* give a droplet-model expression for the quadrupole moment [Mye83]:

$$Q_0 = Q_u + Q_r + Q_d, \qquad \text{where } Q_d = 0 \ . \tag{8.26}$$

The contributions from the uniform distribution Q_u and the redistribution are given by

$$Q_u \ = \ \tfrac{6}{5}\,Z\,R^2 \left(\alpha_2 + \tfrac{4}{7}\alpha_2^2 - \tfrac{1}{7}\alpha_2^3 - \tfrac{94}{231}\alpha_2^4 + \tfrac{8}{7}\alpha_2\alpha_4 + ...\right) \tag{8.27}$$

$$Q_r \ = \ \tfrac{48}{175}\,C'\,Z\,R^2 \left(\alpha_2 + \tfrac{6}{7}\alpha_2^2 - \tfrac{4}{5}\alpha_2^3 - \tfrac{1984}{1155}\alpha_2^4 + \tfrac{50}{21}\alpha_2\alpha_4 + ...\right) \tag{8.28}$$

8.1.3 Particle-plus-Rotor Description

To describe the interplay between the bulk properties of the nuclear matter corresponding to a collective behavior of the nucleons and the single-particle motion of an individual particle, Bohr and Mottelson developed the particle-plus-rotor model [Boh53]. An overview is given in chapter 3.3 of [Rin80].

In this model the nucleus is described as a deformed even-even core with an appropriate number of valence particles moving in the deformed mean potential of the core. From symmetry considerations, rotation components of the core parallel to the symmetry axis of the deformed core are not allowed. Thus, the core rotates with an angular momentum $\mathbf{R}$ around an axis which is perpendicular to the axis of rotational symmetry (see Fig. 8.2). The Hamiltonian describing the system is divided into two parts. $\mathcal{H}_{coll}$ describes the collective behavior of the core, $\mathcal{H}_{intr}$ ("intrinsic" term) describes microscopically the valence particles occupying Nilsson states in the deformed potential:

$$\mathcal{H}_{tot} = \mathcal{H}_{coll} + \mathcal{H}_{intr} \ . \tag{8.29}$$

The collective part describes the rotations of the inert core

$$\mathcal{H}_{coll} = \sum_{i=1}^{3} \frac{R_i^2}{2\mathcal{J}_i} \ , \tag{8.30}$$

where $\mathcal{J}_i$ is the moment of inertia of the rotor with respect to the body-fixed coordinate system, and R_i are the components of the angular momentum of the core along the three

axes of the laboratory system. Furthermore are defined the projection of the spin on the body-fixed coordinate system $K := I_3$, and the projection of the angular momentum of the single-particle on the 3-axis of the body-fixed system $\Omega := j_3$. The orientation of the angular momenta is shown in figure 8.2 for the two limits of "strong coupling" and "weak coupling". By taking into account that the spin of an odd-A nucleus is given by $\mathbf{I} = \mathbf{R} + \mathbf{j}$ (see Fig. 8.2), the collective Hamiltonian can be separated into three parts

$$\mathcal{H}_{coll} = \mathcal{H}_{rot} + \mathcal{H}_{rec} + \mathcal{H}_{cor} \ . \tag{8.31}$$

$\mathcal{H}_{rot}$ describes the rotation of the combined system of the core and the valence particles. The recoil term $\mathcal{H}_{rec}$ acts on the valence particles only and takes into account the two-body interaction, if there is more than one valence particle. Finally there is the Coriolis term $\mathcal{H}_{cor}$ which couples the degrees of freedom of the valence particles with the ones of the rotor. It is given by

$$\mathcal{H}_{cor} = -\sum_{i=1}^{3} \frac{I_i j_i}{\mathcal{J}_i} \ , \tag{8.32}$$

and is responsible for the so-called *strong-coupling* and *weak-coupling* limits of the model. These limits are given by the proportionality of the Coriolis matrix elements to the angular momentum term ([Rin80], p.113),

$$\langle \Psi^I_{MK+1} | \mathcal{H}_{cor} | \Psi^I_{MK} \rangle \propto \sqrt{I(I+1) - K(K+1)} \sqrt{j(j+1) - \Omega(\Omega+1)} \ . \tag{8.33}$$
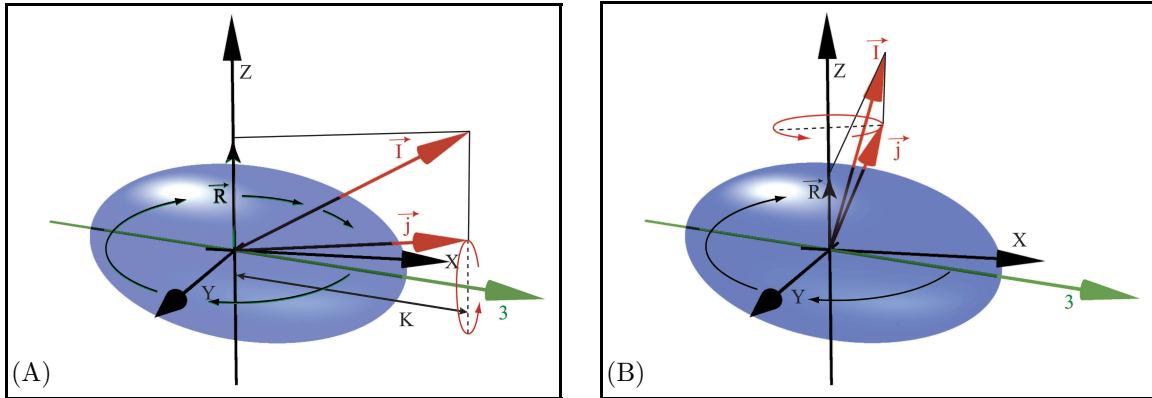
Fig. 8.2: *Illustration of the alignment of angular momenta in strong and weak coupling. Axes labelled by x,y,z belong to the external coordinate system, the 3-axis is the symmetry axis of the body-fixed coordinate system. The vector $\vec{I}$ denotes the spin of the nucleus, $\vec{j}$ the angular momentum of a single-particle, and $\vec{R}$ the angular momentum of the rotating core.*
(A) Strong coupling case.
(B) Weak coupling / rotational alignment case
Figure after Fig. 3.7 in [Rin80]

In the strong-coupling limit the angular momentum of the unpaired particle(s) follows adiabatically the rotation of the even-even core. The strong coupling limit is realized when the Coriolis matrix elements (see Eqn. (8.33)) are small compared to the level splitting of the single-particle energies in the deformed shell model [Rin80]. The Coriolis term is small, if either the spin I is small, or if the single-particle angular momenta j are small. If j is large,

the projection of j on the 3-axis Ω has to be large too for strong coupling. Strong coupling is expected for strong deformations [Rin80]. An illustration of the coupling of the various angular momenta is given in figure 8.2 (A).

In the weak coupling limit the Coriolis matrix elements are no longer negligible, which is the case for small deformations with the single-particles moving essentially in their spherical shell model orbits. This situation is found for high-spin states.

8.1.4   Spectroscopic Quadrupole Moments and Nuclear Deformation

To relate the experimental spectroscopic quadrupole moment to a *static* deformation of the nucleus, the intrinsic quadrupole moment Q_0 has to be calculated from the experimental moment. This intrinsic moment is defined in a coordinate system which is fixed to the nucleus, whereas the spectroscopic quadrupole moment is an observable in the laboratory frame. To calculate the intrinsic moment of well deformed nuclei with static deformation the expression (see e.g. [Boh75], p.45)

$$Q_s = Q_0 \frac{3K^2 - I \cdot (I+1)}{(2I+3)(I+1)} \tag{8.34}$$

has to be evaluated, where $K = I_3$ is again the projection of the spin on the 3-axis of the body-fixed system. In the case the strong coupling limit, which is normally realized in the ground state of well deformed nuclei [Boh75], it is found that $K = I = j_3$, where one valence particle alone is responsible for the nuclear spin, whereas the core particles couple to a $R = 0$ configuration. For very high spins of ground state nuclei ($K = I$) the system becomes weakly coupled, and the spectroscopic and the intrinsic quadrupole moment are equal $Q_s = Q_0$.

For fixed K and increasing spin, which corresponds to increasing angular momentum of the single-particle, the quotient $Q_s/Q_0 = -1/2$ for very high spins. Thus, the spin becomes aligned to an axis perpendicular to the axis of symmetry of the nuclear body as shown in figure 8.2 (B).

A vanishing spectroscopic quadrupole moment does not necessarily mean that the investigated nucleus has spherical shape. This is because all Q_s vanish, if $I = 0$, or $I = 1/2$, independent of Q_0. From equation (8.34) is seen that even strongly deformed nuclei can have vanishing spectroscopic quadrupole moments.

8.2   Experimental Deformation Parameters

Raman *et al.* [Ram01] published a large compilation of $B(E2)$ values, quadrupole moments β_2 parameters and related quantities. The β_2 values therein were calculated from the first order formula

$$Q_0 = \frac{3}{\sqrt{5\pi}} Z R_0^2 \beta_2 \tag{8.35}$$

A different approach was chosen in this thesis, where the deformation parameters and radii were calculated from the droplet-model expressions. This was due to two mayor weaknesses of expression (8.35): (i) The limitation to the lowest order of β_2 leads to overestimated deformations. This becomes especially important for large deformations, where higher order terms contribute substantially to the quadrupole moment. (ii) The nuclear radius is approximated

Table 8.1: *Calculated intrinsic quadrupole moments and nuclear deformation parameters from experimental data calculated for the strong coupling case by the use of the droplet model expressions and from ms charge radii. The errors are purely experimental.*

		^{21}Ne	^{23}Ne
$Q_s = Q_0$(w.c.)	[mb]	103(7.6)	141(13)
Q_0(s.c.)	[mb]	515(39)	394(36)
$\langle r^2 \rangle$	[fm^2]	8.81(8)	8.46(20)
droplet model:	β_2^{DM}(s.c.)	0.607(20)	0.471(19)
Kumar:	β_2^{Kum}(s.c.)	0.462(34)	0.370(35)

by $R_0 = r_0\,A^{1/3}$. This dependence leads to too small radii, especially for light nuclei, and thus to too large deformation parameters.

8.2.1 Deformation Properties of ^{21}Ne and ^{23}Ne

In the droplet model the nuclear deformation parameter β_2 is related to the quadrupole moment via equation (8.26). By the use of the experimental quadrupole moment, measured in the present experiment, the deformation parameter β_2 was calculated from this droplet-model expression. Because higher order βs are unknown, in the droplet-model series expansion only the two lowest orders of α_2 were taken into account. The results for ^{21}Ne and ^{23}Ne are collected in table 8.1.

The nuclear deformation can be as well related to the experimentally measured mean square charge radii. Kumar [Kum72] uses the nuclear monopole moment (i.e. the mean square charge radius) and the quadrupole moment to calculate the deformation parameter β_2 by the first order expression

$$\beta_2^{\text{Kum}} = \sqrt{\frac{\pi}{5}}\,\frac{Q_0}{Z \cdot \langle r^2 \rangle}\,. \tag{8.36}$$

The corresponding values of the nuclear deformation parameters calculated from the results of the present measurements for the strong coupling case are as well collected in table 8.1.

The two isotopes ^{21}Ne and ^{23}Ne, whose quadrupole moments are discussed here, show well deformed nuclear shapes. Assuming strong coupling for the calculation of the deformation parameters β_2 one ends up with $\beta_2 > 0.3$, which is associated with strong prolate deformation. As low-spin states are considered, the assumption of strong coupling seems to be justified.

The majority of the investigated isotopes have even-even nuclei with ground state spin $I = 0$, or odd-even ones with $I = 1/2$ which thus have vanishing spectroscopic quadrupole moments. As will be seen in the next section, the deformation parameters of these isotopes can be determined from nuclear spectroscopy data.

8.2.2 Nuclear Deformation of the Even Isotopes

The determination of the nuclear shape of even-even isotopes relies on the measurement of E2 transition probabilities, the so-called "B(E2) values" or "E2 transition strengths". These are determined from γ-ray spectroscopy measurements. The γ-ray transitions between low-lying collective states of the nucleus can have two different natures. On the one hand, they are

connected with the relaxation of quadrupolar surface *vibrations* of the nuclear shape around its spherical equilibrium. On the other hand, the observed γ-ray spectra can be connected to rotational excitation modes of a statically deformed nuclear shape.

For rotational quadrupole transitions, the transition probability is connected to the intrinsic quadrupole moment ([Boh75], p.45), by

$$B(\text{E2}; KI_1 \rightarrow KI_2) = \frac{5}{16\pi} Q_0^2 \langle I_1 K 20 | I_2 K \rangle^2 \, , \tag{8.37}$$

where $\langle I_1 K 20 | I_2 K \rangle$ is a vector addition coefficient representing the coupling of the angular momenta in the intrinsic frame. In the special case of a rotational transition from $I_1 = 2^+$ to $I_2 = 0^+$ within a band with $K = 0$, e.g. in the ground-state band of a doubly-even isotope, the intrinsic quadrupole moment can be calculated from [Ram01]

$$Q_0^2 = \frac{16\pi}{5} \times B(\text{E2}; 2^+ \rightarrow 0^+) \tag{8.38}$$

Experimental data on $B(\text{E2})$-values, Q_0 and other related quantities for even-even nuclei were compiled by Raman *et al.* [Ram01], and compared also to a number of theoretical model predictions. Similar to the β_2 from laser spectroscopy, the quadrupole moment from the corresponding $B(\text{E2})$-value was used to calculate the deformation parameters for the even-A neon isotopes. Again the droplet model expressions were employed, and the lowest two orders in α_2 were taken into account in the equations.

The β_2 expression given by Kumar [Kum72] (Eqn. (8.36)), can be rewritten in terms of the $B(\text{E2})$-value and becomes

$$\beta_2^{\text{Kum}} = \frac{4\pi}{5} \times \frac{\sqrt{B(\text{E2})}}{Z \langle r^2 \rangle} \, . \tag{8.39}$$

Furthermore, the liquid drop model gives a very simple expression for the single-particle deformation parameter $\beta_2^{(sp)}$ [Ram01], for neon with $Z = 10$

$$\beta_2^{(sp)} \approx 1.59/Z = 0.16 \, . \tag{8.40}$$

The deviation of β_2 from this parameter gives an idea how much of the transition strength has to be attributed to collective motion. All the relevant values for the properties discussed above are collected in table 8.2.

Table 8.2: *$B(E2)$-values, and related quantities for the even neon isotopes. The values are taken from [Ram01], additionally in column 6 the deformation parameter calculated with the help of equation (8.39)*

Isotope	E(2^+) [keV]	B(E2) [e^2b^2]	Q_0 [mb]	β_2^{DM} [Ram01]	β_2^{Kum} [Kum72]	$\beta_2^{DM}/\beta_2^{(sp)}$
^{18}Ne	1887.3(2)	0.0269(26)	0.519(25)	0.636(13)	0.466(45)	3.98
^{20}Ne	1663.674(15)	0.034(3)	0.584(26)	0.684(13)	0.512(45)	4.28
^{22}Ne	1274.542(7)	0.023(1)	0.481(10)	0.566(5)	0.437(19)	3.54
^{24}Ne	1981.6(4)	0.017(6)	0.41(7)	0.483(35)	0.34(14)	3.02
^{26}Ne	2018.2(3)	0.0228(41)	0.477(43)	0.540(21)	0.443(80)	3.38
^{28}Ne	1310(20)	0.027(14)	0.50(14)	0.552(65)	0.47(24)	3.45
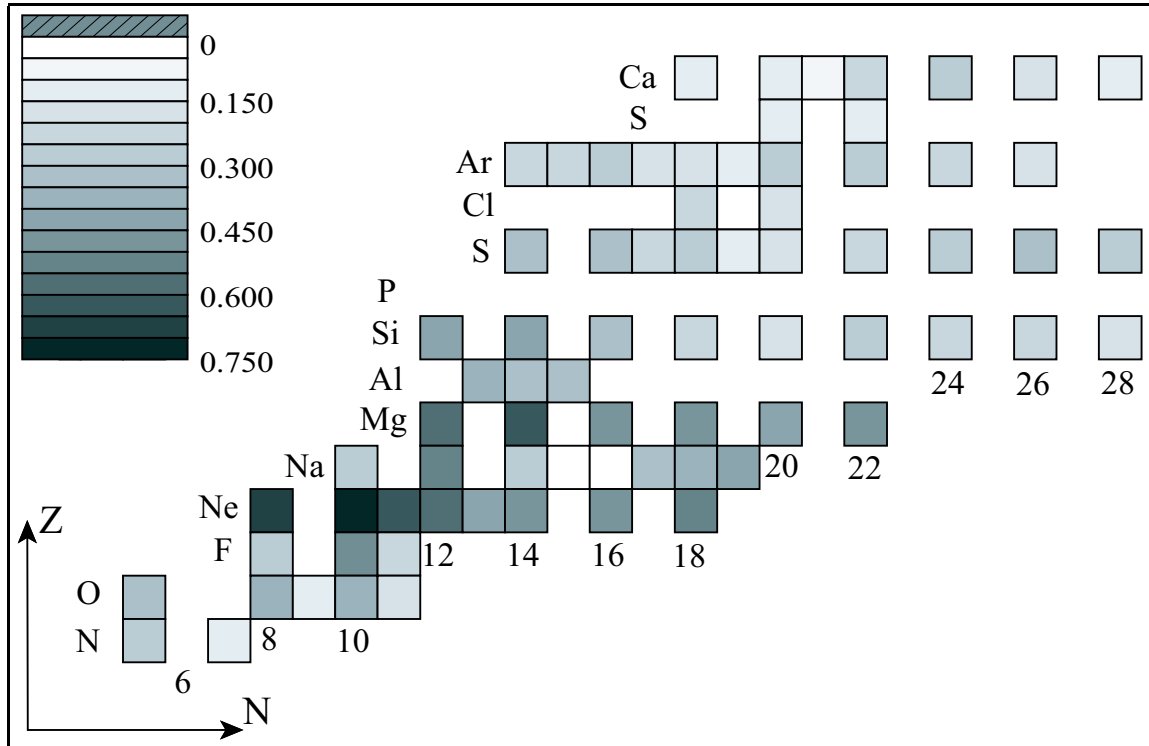
Fig. 8.3: *Plot of absolute values of the deformation parameters β_2 of nuclei in the sd shell and below. All values shown for even-even configurations are taken from [Ram01], values of odd configurations are calculated with the help of equations (8.34), and the droplet model expressions. The input parameters for the spectroscopic quadrupole moments were taken from [Rag89].*

A map of the experimentally known deformation parameters in the p and sd shell is shown in figure 8.3. It contains the values for even-even isotopes taken from [Ram01]. Odd-A configurations were calculated using the first order expression (8.35) given by Raman *et al.* [Ram01]. The input quadrupole moments for the calculation were taken from the compilation of Raghavan [Rag89]. Additional values for ^{21,23}Ne, argon [Kle96], and sodium isotopes [Kei00] are added in the plot. Large deformation parameters are indicated by dark colors, small deformation parameters by light ones.

Finally the energies of the rotational band can be used to judge about the nature of the γ-radiation. For a $K = I_3 = 0$ band of a good rotator the energies of the levels are given by ([Boh75], p.24)

$$E^{(Rot)} = \frac{\hbar^2}{2\mathcal{J}} \cdot I(I+1) \ . \tag{8.41}$$

the energies of the levels 2^+, and 4^+ of a good rotator fulfill the condition

$$\frac{E(4^+)}{E(2^+)} = \frac{10}{3} = 3.3 \ . \tag{8.42}$$

This has to be compared to the spectrum of a vibrator for which

$$\frac{E(4^+)}{E(2^+)} = 2 \ . \tag{8.43}$$

For some of the even neon isotopes the energies of the 2^+ and 4^+ levels are known as shown in table 8.3, and they can be used to characterize the nature of these states, and the corresponding nuclear shape.

Table 8.3: *Comparison of the $4^+/2^+$ level energy for some even neon isotopes. Values taken from [Fir96].*

	^{18}Ne	^{20}Ne	^{22}Ne	^{24}Ne
E(2^+) [keV]	1887.3(2)	1633.674(15)	1274.53(2)	1981.6(4)
E(4^+) [keV]	3376.2(4)	4247.7(11)	3357.2(4)	3962.18(9)
E(4^+)/E(2^+)	1.78	2.56	2.63	2.00

The $E(4^+)/E(2^+)$ ratios suggest that ^{20}Ne and ^{22}Ne can be regarded as rotators. The ratios for ^{18}Ne and ^{24}Ne indicate that the excited collective states originate from vibrations rather than rotations. Thus, the values of β_2 calculated from the quadrupole moments should not be overinterpreted. Nevertheless, if the static deformation parameter β_2 is interpreted as the rms deformation parameter $\langle\beta_2\rangle^{1/2}$ of the oscillator model, it is justifiable to use this in the calculation of the radii in the framework of the droplet model.

8.3 Mean Square Charge Radii in the Droplet Model

Using the droplet model and the deformation parameters discussed in the previous section, the deformations can be used to calculate ms nuclear radii in the framework of the droplet model (DM) developed by Myers *et al.* ([Mye74, Mye83, Mye87], and references therein).

8.3.1 Neon Radii in the Droplet Model

Table 8.4: *$\langle r^2\rangle_{DM}$ and $\delta\langle r^2\rangle_{DM}$ calculated in the droplet model by the use of deformation parameters β_2^{DM} from the droplet model expressions. Additionally radius data calculated from the droplet model by the use of deformation parameters β_2^{Kum} according to Kumar [Kum72].*

A	β_2^{DM}	$\langle r^2\rangle_{DM}$ [fm^2]	$\delta\langle r^2\rangle_{DM}^{20,A}$ [fm^2]	β_2^{Kum}	$\langle r^2\rangle_{\mathrm{Kum}}$ [fm^2]	$\delta\langle r^2\rangle_{\mathrm{Kum}}^{20,A}$ [fm^2]
18	0.636(13)	9.263(22)	-0.379(24)	0.466(45)	9.010(59)	-0.328(81)
20	0.684(13)	9.642(24)	-	0.512(45)	9.338(67)	-
21	0.607(20)	9.462(33)	-0.179(42)	0.462(34)	9.253(46)	-0.085(81)
22	0.566(5)	9.415(10)	-0.227(24)	0.437(19)	9.250(27)	-0.088(81)
23	0.462(34)	9.224(24)	-0.417(25)	0.370(35)	9.197(38)	-0.141(81)
24	0.483(35)	9.327(49)	-0.315(74)	0.34(14)	9.127(16)	-0.211(81)
26	0.540(21)	9.636(33)	-0.006(42)	0.443(80)	9.540(91)	0.201(101)
28	0.552(65)	9.818(114)	0.177(203)	0.47(24)	9.757(94)	0.418(107)

Using the droplet-model formulae, the differences in the ms charge radii with respect to ^{20}Ne can be predicted from known deformations. The ms radii are calculated from equation (8.12), and only the two lowest orders in α_2 were taken into account, similar to the calculation of the deformation parameters β_2. Higher order terms were dropped, because the mixed terms in β_2 and β_4, partly compensating the higher power terms in β_2 are unknown.

From the droplet model deformation parameters β_2^{DM}, ms radii $\langle r^2\rangle_{DM}$ and differences in ms radii $\delta\langle r^2\rangle_{DM}$ were calculated by the use of the above mentioned droplet-model expression

(8.12). The corresponding values of β_2^{DM}, $\langle r^2 \rangle_{DM}$ and $\delta \langle r^2 \rangle_{DM}$ are collected in table 8.4. In figure 8.4 this result compared with the experimental data of the present experiment.

Additionally, the deformation parameters β_2^{Kum}, calculated according to equation (8.36) were used to calculate $\langle r^2 \rangle_{Kum}$ and $\delta \langle r^2 \rangle_{Kum}$ from the corresponding droplet-model expressions. These values are not included in plot 8.4. They show worse agreement with the experimental values of $\delta \langle r^2 \rangle$ and were consequently omitted for better overview.
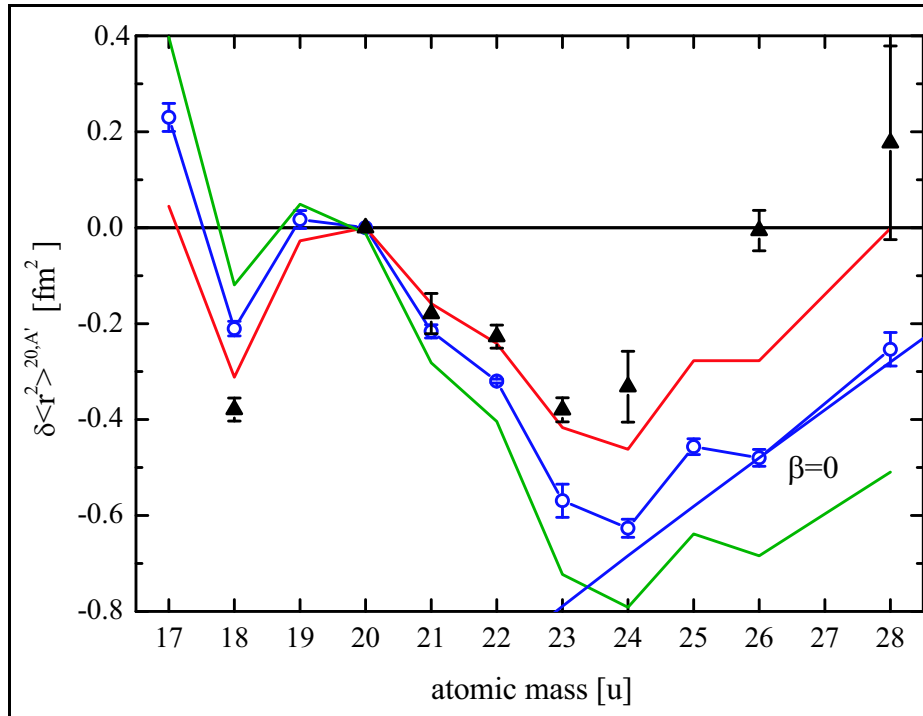
Fig. 8.4: *Comparison between experimental data and prediction from the droplet model. The open circles together with the error limits represent range of the experimental data of this work. The triangles are the predictions for $\delta \langle r^2 \rangle$ from the droplet model. The line crossing the data point of ^{26}Ne shows the $\delta \langle r^2 \rangle$ from the droplet model with constant deformation $\beta_2 = 0$ for comparison.*

8.3.2   Discussion of the Droplet-Model Description

As can be seen from figure 8.3, ^{18}Ne and ^{20}Ne are the nuclides with the largest β_2-values known in the *sd* shell according to Raman *et al.* [Ram01]. Generally the region of light neon isotopes shows large quadrupole deformations. The mid-shell nucleus ^{24}Ne seems to be the least deformed isotope, and the deformation increases again towards ^{30}Ne at $N = 20$, which is the neutron shell closure. A corresponding behavior is observed in the comparison of the energy level ratios of the lowest 2^+, and 4^+ states of the even isotopes. It shows good agreement with the rotational model based on static quadrupole deformation for the two stable neon isotopes, ^{20}Ne and ^{22}Ne. A puzzling case is ^{18}Ne with a closed $N = 8$ neutron shell, a large value of β_2 and an apparently vibrational level structure.

The radii determined by the fairly simple droplet model calculation reproduce surprisingly well the experimental data. Despite the general slope of the curve, the curvature is very

similar. This can as well be taken as support of the description in terms of well deformed nuclear shapes. This is very much in contrast to other light nuclear systems like argon [Kle96], where the deformation is small and the behavior of the radii seems to be dominated by the single-particle structure. Also for heavier systems it has been found that the semi-empirical droplet-model description is most suitable in regions of strong deformation. The agreement between the droplet model and the experimental data can even be improved by assuming oblate deformation of the isotopes ^{24,26,28}Ne as will be shown below.

8.4 Comparison with Theoretical Studies

In recent years, a number of comprehensive theoretical studies of basic nuclear properties were published employing various models. Möller *et al.* [Möl95], Lalazissis *et al.* [Lal99], and Goriely *et al.* [Gor01] calculated properties like masses, radii and deformations all over the nuclear chart with different methods. Siiskonen *et al.* [Sii99] deal more specifically with the even-even configurations of oxygen, neon, and magnesium isotopes.

8.4.1 Macroscopic-Microscopic Calculation

Table 8.5: *Relevant nuclear ground state properties from macroscopic-microscopic calculations, taken from [Möl95].*

Isotope	$M^{(MM)} - M^{(exp)}$ [MeV]	$\beta_2^{(MM)}$	$\beta_4^{(MM)}$	$\beta_6^{(MM)}$	$r_{ch}^{(MM,DM)}$ [fm]	$\delta\langle r^2 \rangle$ [fm^2]
^{18}Ne	0.005	0.109	0.150	0.0	2.8908	-0.7805
^{19}Ne	0.001	0.294	0.330	0.011	2.9690	-0.3223
^{20}Ne	0.001	0.335	0.428	0.023	3.0228	0.0
^{21}Ne	0.001	0.327	0.274	0.012	2.9974	-0.1526
^{22}Ne	0.001	0.326	0.225	0.011	3.0006	-0.1336
^{23}Ne	0.001	0.307	0.141	0.009	2.9934	-0.1767
^{24}Ne	0.010	-0.215	0.155	-0.010	2.9816	-0.2474
^{25}Ne	0.040	0.0	0.0	0.0	2.9644	-0.3495
^{26}Ne	0.070	0.0	-0.014	0.0	2.9747	-0.2882
^{27}Ne	0.280	0.0	-0.014	0.0	2.9849	-0.2280
^{28}Ne	0.390	-0.204	0.127	0.002	3.0188	-0.0242

The calculation of Möller *et al.* [Möl95] is based on a macroscopic-microscopic model which uses the finite range droplet model (FRDM) for the macroscopic description of the nuclear shape. The FRDM is a refined version of the DM with am improved description of the nuclear compressibility. The macroscopic properties are corrected by microscopic effects, namely the shell-plus-pairing correction. This correction is parameterized by several methods: BCS and the Lipkin-Nogami model for the pairing effects and the Strutinsky shell correction for the shell effects. The nine model constants of the macroscopic parameters and one microscopic parameter (Lipkin-Nogami effective pairing gap constant r_{mic}) are determined by a least squares fit to 1654 ground state masses ranging from ^{16}O to ^{263}Sg. The overall deviation

between the input and the theoretical masses is 0.669 MeV, but worse for the light-mass region with $A < 65$. The additional microscopic model constants influencing the model were determined independently from the least squares fit to the nuclear masses.

Besides other results the calculation yields nuclear deformation parameters β_2, β_4, β_6, and nuclear masses. The relevant values for the nuclei under investigation in this work are tabulated in table 8.5 (index "MM"). A comparison with the "experimental" deformation parameters calculated in the droplet model β_2^{DM} is shown in figure 8.5, where the $\beta_2^{(MM)}$ correspond to the up-triangles. Because Möller *et al.* do not give rms charge radii, the deformation parameters were used to calculate nuclear rms charge radii $r_{ch}^{(MM,DM)}$ in the framework of the droplet model according to equation (8.12). Note the values for the hexadecapole deformation β_4 which are of the same order of magnitude as β_2. Consequently these were taken into account in the droplet model calculation. A comparison between the calculated rms radii, the differences $\delta\langle r^2 \rangle$ in the ms radii (up-triangles) and the experimental data from this work is shown in figure 8.6.

8.4.2 Hartree-Fock Calculation

Table 8.6: *Relevant nuclear ground state properties from Hartree-Fock calculations, taken from [Gor01].*

Isotope	$M^{(HF)} - M^{(exp)}$ [MeV]	$\beta_2^{(HF)}$	$\beta_4^{(HF)}$	$r_{ch}^{(HF)}$ [fm]
^{18}Ne	0.7	0.18	0.0	2.96
^{19}Ne	0.2	0.19	0.01	2.94
^{20}Ne	-0.5	0.35	0.00	2.96
^{21}Ne	0.3	0.40	-0.01	2.97
^{22}Ne	-0.2	0.40	-0.04	2.96
^{23}Ne	1.3	0.29	-0.01	2.95
^{24}Ne	0.8	-0.3	-0.05	2.94
^{25}Ne	2.1	-0.19	-0.02	2.93
^{26}Ne	2.2	-0.07	0.00	2.93
^{27}Ne	3.1	-0.07	0.00	2.95
^{28}Ne	2.1	0.13	-0.01	2.98

Hartree-Fock (HF) calculations of Goriely *et al.* [Gor01] were intended to give predictions of nuclear ground state masses all over the nuclear chart. The nuclei were modelled in the framework of the Hartree-Fock method (HFBCS-1), with pairing correlations described by the BCS formalism. The nuclear force used in the calculations was of the Skyrme type (10-parameter MSk7), together with a 4-parameter δ-function pairing force and a 2-parameter phenomenological Wigner term. The parameter set was fitted to reproduce 1888 experimental ground state masses from the Audi-Wapstra tables [Aud93], for which the rms error was 0.738 MeV.

Besides the nuclear masses many other nuclear parameters were calculated. The deformations parameters β_2, β_4, and rms charge radii r_{ch}. These are collected for the neon isotopes in

table 8.6. The theoretical quadrupole deformation parameters are plotted together with the β_2^{DM} deduced from the droplet model in figure 8.5, where they appear as down-triangles. The rms charge radii and the differences in ms radii $\delta\langle r^2\rangle^{20,A}$ calculated from these are plotted as down-triangles in figure 8.6.

8.4.3   Relativistic Mean-Field Calculations

Table 8.7: *Relevant nuclear ground state properties of the even-even neon nuclei from relativistic mean-field calculations, taken from [Lal99].*

Isotope	$\beta_2^{(RMF)}$	$\beta_4^{(RMF)}$	$r_{ch}^{(RMF)}$ [fm]
^{18}Ne	0.001	0.000	3.066
^{20}Ne	0.186	0.054	3.020
^{22}Ne	0.350	0.070	3.000
^{24}Ne	0.191	0.024	2.956
^{26}Ne	0.001	0.000	2.955
^{28}Ne	0.000	0.000	2.993

The calculations of Lalazissis *et al.* [Lal99] are based one the relativistic mean field (RMF) approach. The corresponding Lagrangian uses the 9-parameter set called "NL3", and includes pairing by the use of the BCS formalism. In contrast to the two former theoretical approaches, the RMF theory is less phenomenological and is limited to even-even nuclei. The parameter set NL3 was determined by a fit to the ground-state charge radii, binding energies and neutron radii of 10 spherical nuclei [Lal97].

The predicted properties of interest are listed in table 8.7. Similarly to the prediction of the calculations presented in the previous sections, the deformation parameters β_2, the rms radii r_{ch}, and $\delta\langle r_{ch}^2\rangle$ can be found in figures 8.5, and 8.6, indicated by asterisks.

8.4.4   Hartree-Fock Calculation in the Lower sd Shell

Table 8.8: *Relevant nuclear ground state properties of the even-even neon nuclei from deformed Hartree-Fock calculations, taken from [Sii99].*

	^{18}Ne	^{20}Ne	^{22}Ne	^{24}Ne	^{26}Ne	^{28}Ne
$\beta_2^{(DHF)}$	0.00	0.38	0.33	-0.22	0.20	0.17
$r_{ch}^{(DHF)}$ [fm]	3.011	3.009	2.971	2.956	2.961	2.999

Siiskonen *et al.* [Sii99] concentrated their theoretical study on the even-even isotopes of oxygen, neon, and magnesium up to the neutron drip-line. They compare the predictions of shell model calculations and calculations using a deformed Skyrme-Hartree-Fock (DHF) model with axial symmetry and BCS pairing included. Using Skyrme forces with the parametrizations SkI6, RATP, Z_σ^*, and SkX (see references in [Sii99]) they obtain ground-state deformations and rms radii. The authors find the SkI6 parameterization to give the best overall agreement with experimental data in the O, Ne, Mg region. The results of these

model calculations for the rms nuclear charge radii r_{ch}, and deformation parameters β_2 (index "DHF") are given in table 8.8.

The deformation parameters $\beta_2^{(DHF)}$ are included in figure 8.5, indicated by diamonds. Values for $\delta\langle r^2\rangle$ were calculated from the given rms radii and are plotted together with the other data as diamonds in figure 8.6.

8.4.5 Summary of the Theoretical Results
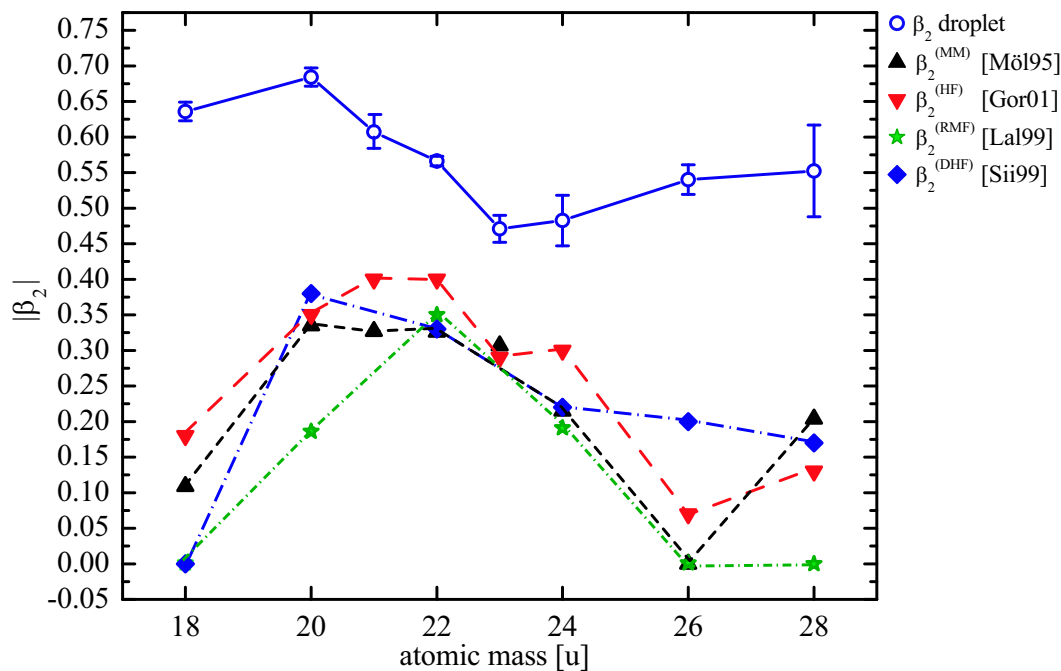
Fig. 8.5: *Comparison between experimental data of absolute deformation parameter $|\beta_2|$, calculated using the droplet model equations, compared to theoretical values ([Möl95, Gor01, Lal99, Sii99]).*

From figures 8.3 and 8.4 can be seen that the charge radii and their isotopic variation are much better reproduced by theory than the absolute values of the deformation. On the average, the different theoretical approaches predict the absolute rms charge radii r_{ch} equally well. Similar, a remarkable agreement is found in the structure of the $\delta\langle r^2\rangle$ curves given by experiment and theory. All of them show a maximum close to $A = 20$, a flat minimum in the region of $A = 24 - 26$, and increasing $\delta\langle r^2\rangle$ towards $A = 30$.

For the absolute rms radii the rms deviation from experimental values are smallest for the two HF calculations [Gor01, Sii99]. Nevertheless, the prediction of [Gor01] gives the largest deviation from the experimental reference radius of ^{20}Ne [Fri95]. This shifts the whole curve of predicted $\delta\langle r^2\rangle$ values. Also the shape of the nuclei in terms of quadrupole deformation seems to be reproduced best by the two HF models (see Fig. 8.5), although all the models predict β_2 values which are at least 30% smaller than the values derived from $B(E2)$ values assuming the rotator model. This behavior may be understood by the fact that the nuclei in this region do not behave like rigid rotors. Especially the assumption of well defined rotors has to be questioned in the case of ^{18}Ne and ^{24}Ne where the $E(4^+)/E(2^+)$ energy ratios suggest vibrational excitations. Furthermore, the calculation of β_2 is sensitive to choice of

the terms in the series expansion of Q_0 which are not negligible for large deformations.
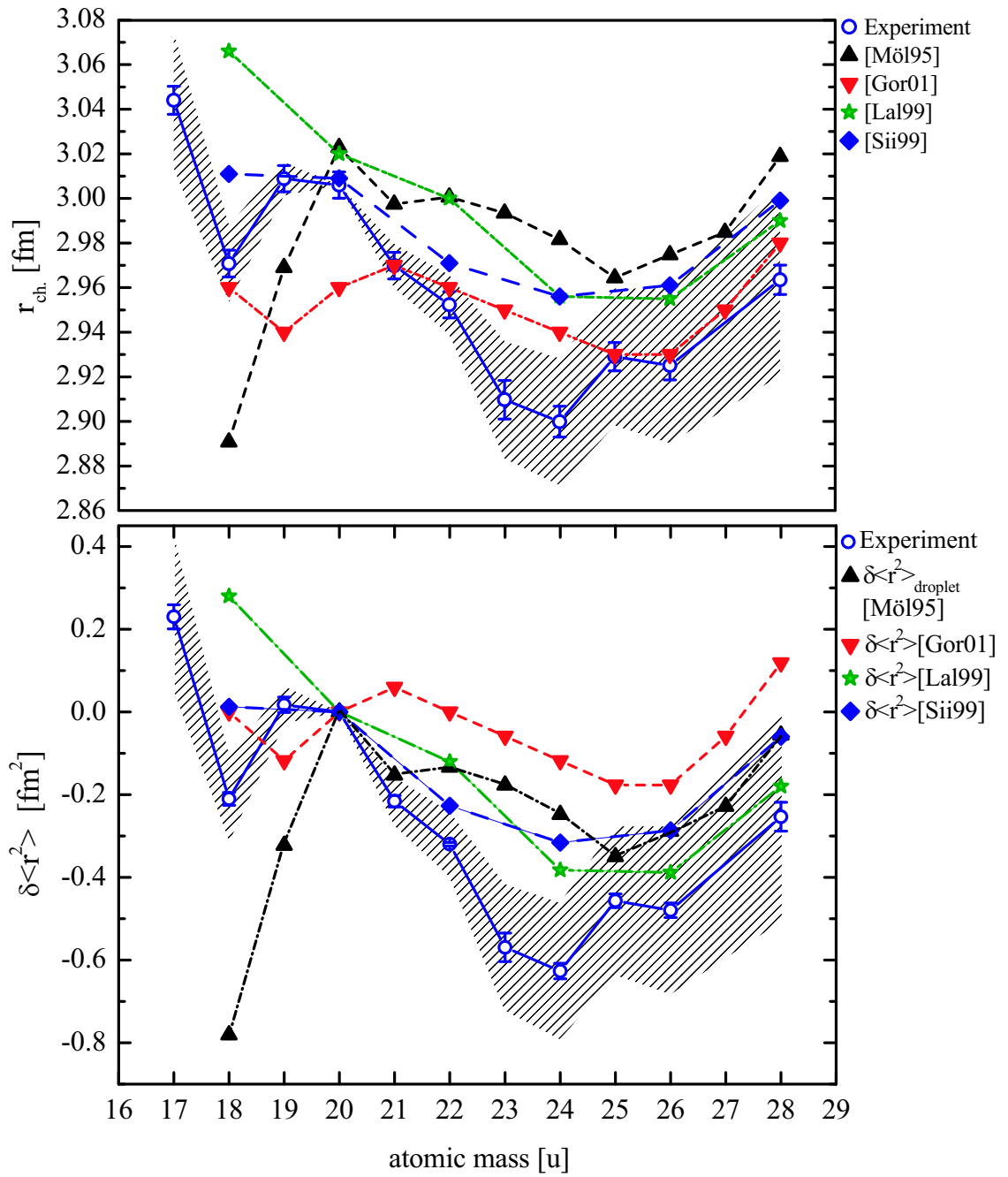
Fig. 8.6: *Comparison of experimental data of rms charge radii r_{ch}, and differences $\delta\langle r^2 \rangle$ with the-
oretical predictions [Möl95, Gor01, Lal99, Sii99].*
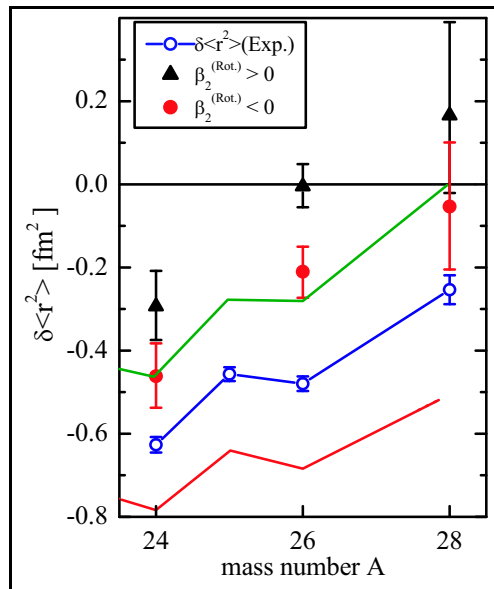
Fig. 8.7: *Comparison for the isotopes ^{24}Ne, ^{26}Ne, ^{28}Ne – prolate or oblate?*

None of the theoretical calculations predicts a large quadrupole deformation for ^{18}Ne, ^{26}Ne and ^{28}Ne. In particular, the position of ^{18}Ne at the shell closure $N = 8$ leads to spherical nuclei in the models. Siiskonen *et al.* [Sii99] attribute the discrepancy with the large experimental deformations to the failure of "the Bohr-Mottelson dynamics or of the HF results". A simple argument against the rotational character of ^{18}Ne is its $E(4^+)/E(2^+)$ energy ratio, as pointed out in section 8.2.2. It seems that the large B(E2) value as well as the large radius have their origin in a pronounced vibrational character of this nucleus. This may also explain the large scattering of the predictions for the radius of ^{18}Ne.

Very interesting is the inspection of the deformation parameters β_2 predicted by Möller *et al.* and by Goriely *et al.* in the region of $A > 23$. Both calculations yield negative deformations corresponding to an oblate shape. Lalazissis *et al.* ([Lal99], Tab. B) mention ^{24}Ne as a nucleus "with possible shape coexistence in the ground state". Their model gives a very small difference in the binding energy of prolate and oblate states. Similarly, the calculation of Siiskonen *et al.* show oblate deformation for ^{24}Ne.

As the sign of the deformation parameter cannot be determined from the B(E2) values, all β_2 were assumed to be positive in the droplet model calculations. Taking the predictions serious, and using experimental deformations with negative sign for $A \geq 24$, the droplet model leads to $\delta\langle r^2\rangle$ values which are plotted in figure 8.7. The up triangles show the earlier droplet values of $\delta\langle r^2\rangle$ from positive β_2 values, the dots show the values for negative sign. By taking the sign information seriously, the agreement between the experimental and the model values can be improved – possibly an argument for oblate deformation in this region.

In summary the calculations of Siiskonen *et al.* [Sii99] seem to give the most realistic description of nuclear ground state properties in the region of the even-even isotopes of O, Ne, and Mg. The calculation of Goriely *et al.* [Gor01] was intended for a large scale mass table. Nevertheless it yields good agreement for the radii of the heavy neon isotopes and ^{18}Ne, whereas it fails to predict the maximum in the radii observed for ^{19}Ne and ^{20}Ne. It is the only calculation predicting a moderately non-spherical shape of ^{18}Ne. The largest deviations from the experimental data are observed in the results by Möller and Nix [Möl95] obtained from macroscopic-microscopic calculations based on the FRDM. This type of model is better suited for heavy nuclei, and cannot hold for few-nucleon systems where individual particles play an important role. Also the unrealistically large hexadecapole deformation parameter β_4 predicted in the region around ^{20}Ne probably belongs into this context.

8.4.6 Conclusion for the sd-shell Isotopes with A ≥ 18

The strong deformation of ^{18}Ne found from the measured $B(E2)$ value is supported by the observation of a large experimental ms charge radius, provided that the DM is a reasonable approach for the description in terms of empirical deformation values. This assumption is strongly suggested by the success of the DM description presented in section 8.3. On the other hand, this is contrasted with the energy ratio $E(4^+)/E(2^+) = 1.78$. This can be taken as an evidence for vibrational rather than rotational excitation, which leads as well to noticeable mean square deformations and changes in the radius. Thus, ^{18}Ne cannot be considered to be a good rotator with static deformation.

^{20}Ne, which serves a the reference isotope for the ms charge radii, exhibits strong deformation, having the largest quadrupole deformation in the Bohr rotator model experimentally known in the sd shell. This finding is well known and has been discussed since a long time. The spectrum of ^{20}Ne is discussed in some length in the book of Bohr and Mottelson ([Boh75], p.96). ^{20}Ne is specified as a good rotator with strong static quadrupolar deformation. As an evidence for this is seen in the changes of $B(E2, i \rightarrow f)/B(E2, 2 \rightarrow 0)$ ratios within the ground-state band([Boh75], p.98). Similarly the $K = 2$ band $B(E2)$-value relations show values corresponding to a rotational spectrum, as well as the energies of the three levels $K^\pi = 0^+$, 2^-, and 0^-.

Many properties of ^{20}Ne such as the strong deformation can be understood by ^{16}O$+\alpha$ cluster-model [Buc75, Buc95, Duf96]. In this model the nucleus is described by a ^{16}O core (which itself can be seen as a 4-α cluster) plus an additional α-particle bound to the core. With this model it is phenomenologically easy to understand the large deformation and the quadrupole moment caused by the α-particle outside a spherical core.

The behavior of the isotopes with $A \geq 21$ can as well be understood in terms of deformation properties. The static deformation calculated for ^{21}Ne and ^{23}Ne from the spectroscopic quadrupole moments found by laser spectroscopy fits smoothly into the trend of β_2^{DM} values calculated from the $B(E2)$ values of the even isotopes. Even though the differences in ms charge radii, calculated by the use of the DM, follow the experimental $\delta\langle r^2\rangle$ very well as is shown in figure 8.4, the assumption of static deformation is again questioned from the energy ratio $E(4^+)/E(2^+)$ observed for ^{24}Ne, which indicates dynamic deformation. Unfortunately, these energy ratios are not available for ^{26}Ne and ^{28}Ne.

^{23}Ne and ^{24}Ne are found to have the smallest deformation of all neon isotopes as is seen from the plot of β_2 in figure 8.3. Assuming that the deformation of ^{24}Ne is overestimated by the $B(E2)$ values, due to vibrational excitations, ^{24}Ne seems to mark the minimum of static deformation. The occurrence of oblate deformation for the heavier isotopes, as predicted by theoretical calculations, cannot be confirmed from the $B(E2)$ values alone. However, in combination with the radii, better agreement between the experimental data and the deformed DM description is obtained if negative β_2 parameters are assumed for ^{24,26,28}Ne, corresponding to oblate deformation in this region.

Towards the neutron shell closure at $N = 20$ a decrease of deformation is expected, but the experimental data show the opposite behavior [Thi75, Det79, Gui84]. This can be seen in the context of the so-called "island of inversion" postulated for the region of $N \approx 20$ and $Z \approx 11$,

which is discussed in a number of articles (see [Pov94, Cau98, Uts99, Cau01] and references therein). The discovery of this breakdown of the shell closure goes back to measurements of the mass and the spin of ^{31}Na [Thi75], and was attributed to a shape change from spherical to prolate [Cam75]. Later experiments on magnesium, other sodium and neon isotopes showed a similar behavior of the isotopes around $N = 20$. The experimental information indicating deformed nuclei led to a shell-model interpretation by the intrusion of a $2p - 2h$ configuration (i.e. belonging to the fp shell) which is intrinsically deformed [Pov94]. The shell-model study of Utsuno *et al.* [Uts99] predicts the onset of this effect for neon isotopes with $N > 26$. The sd-shell calculation reproduces the experimental $E(2^+)$ energy of ^{26}Ne, whereas ^{28}Ne shows large discrepancies between experiment and theory. This is interpreted as arising from large $2p - 2h$ contributions to the sd-shell wave function leading to a deformed ground state in this nucleus.

8.5   Separate Discussion for ^{17}Ne

So far, the properties of ^{17}Ne were excluded from the discussion of the results. ^{17}Ne is an exceptional case in the sense that it is not an sd-shell nucleus and that proton-halo properties have been postulated and discussed in numerous publications of recent years.

8.5.1   Experimental Data from Scattering Experiments

Most of the discussion about the charge radius of ^{17}Ne goes back to the experiments of Ozawa *et al.* [Oza94]. In these experiments the nuclear matter radii of three isobars with $A = 17$ were determined from interaction cross sections using a Glauber-model analysis [Tan85]. These cross sections were measured from the transmission of ^{17}N, ^{17}F and ^{17}Ne beams with a kinetic energy of 700 MeV/u through different targets. In all cases ^{17}Ne exhibits a larger interaction cross section and thus a larger ms radius than the radii of the neighboring nucleus ^{17}F, and the mirror nucleus ^{17}N. This is interpreted as an isospin antisymmetry, explained by the assumption of a large contribution of the $(\pi s_{1/2})^2$ configuration of the two protons above the $N = 8$ shell – prerequisite for a proton halo. The data on nuclear matter radii published by Ozawa *et al.* [Oza94] can be found in the leftmost column of table 8.9.

Ozawa *et al.* are the only authors who explicitly give values for a rms charge radius r_{ch}. This is derived by folding the charge distribution of the proton with the point proton distribution which is given by the Glauber model analysis. The convolution leads to a simple expression for the rms charge radius which is given by (see e.g. [Lal99])

$$r_{ch} = \sqrt{\left(r_p^{(0)}\right)^2 + (r_p)^2} \,, \qquad \text{where } r_p^{(0)} = 0.8 \text{ fm} \,. \qquad (8.44)$$

All other publications quoted below give values for the rms proton (r_p), neutron (r_n) and matter radius (r_m). The rms charge radius in table 8.9 was calculated from r_p by the use of equation (8.44).

Table 8.9: *Data on nuclear radius parameters of ^{17}Ne from one experimental and four theoretical publications. The data marked with (*) are calculated r_p using equation (8.44). The experimental value of the present work is composed of the absolute radius given in [Fri95] and $\delta\langle r^2 \rangle$ from laser spectroscopy.*

	[Oza94]	[Zhu95] (CSF1)	[Zhu95] (CSF2)	[Tim96]	[Kit97] $(\pi d_{5/2})^2$	[Kit97] $(\pi s_{1/2})^2$	this work
r_{ch} [fm]	2.90(7)	3.05(*)	2.99(*)	2.82(*)	2.953(*)	3.21(*)	3.045(7)
r_p [fm]	2.79(7)	2.94	2.88	2.70	2.843	3.105	-
r_n [fm]	2.69(7)	2.62	2.62	2.35	2.526	2.526	-
r_m [fm]	2.75(7)	2.81	2.88	2.56	2.711	2.717	-

8.5.2 Theoretical Studies of the Structure of ^{17}Ne

Zhukov and Thompson [Zhu95] use the data of Ozawa *et al.* [Oza94] as comparison with a three-body ^{15}O+p+p model with Borromean binding structure (none of the subsystems is bound if one of the three constituents is removed). They calculated radii of ^{17}Ne from two models with two nuclear forces for each model. The results of these calculations [Zhu95] are given in table 8.9. The selected values are those from a Fadeev calculation [Ban92] with a SSC(C) force [Tou82] (CFS1), and a gaussian force [Joh90] (CFS2). The second model, the hyperharmonics method [Zhu93] yields the same radius properties as the CSF2 calculation, and is not included in the table. The authors conclude that ^{17}Ne "can be considered as a very promising candidate" for a proton halo with a proton radius exceeding the radius of the the neutron distribution by about 0.3 fm , and a proton wave function having a 26% probability of $(\pi s_{1/2})^2$, which is the typical halo configuration, and a 70% probability of $(\pi d_{5/2})^2$.

The possibility to explain the reaction cross sections by a proton halo motivated as well the theoretical study of Timofeyuk *et al.* [Tim96]. They investigated the mirror nuclei ^{17}N, and ^{17}Ne in a three body cluster model (GCM) [Bay89], where ^{17}Ne is again described by a ^{15}O+p+p, and ^{17}N by a ^{15}N+n+n configuration. Timofeyuk *et al.* [Tim96] find a shallow minimum in the center region of the calculated ^{17}Ne proton-density distribution. The authors conclude that this is a sign that the two last protons "...occupy $1s_{1/2}$ states rather than $0d_{5/2}$states", but do not give numbers for the wave-function composition. The matter distributions calculated in the model are almost indistinguishable for the two mirror partners, showing only small differences in the far tails of the radial distributions. The proton and neutron radii calculated for the two nuclei are symmetric with respect to the isospin. Hence, "the last two neutrons in ^{17}N should also occupy a $1s_{1/2}$ state rather than a $0d_{5/2}$ state", which contrasts the analysis of ^{17}N by Ueno *et al.* [Uen96]. Nevertheless, Timofeyuk *et al.* [Tim96] criticize the analysis of [Oza94] which seems to underestimate the radius of ^{17}N, and thus introduces the radial differences in comparison with ^{17}Ne. On the basis of this discussion the authors conclude that ^{17}Ne "should not be considered as a halo nucleus".

Finally Kitagawa *et al.* [Kit97] use the data of Ozawa *et al.* [Oza94] for a comparison with their results of Hartree-Fock calculations. Additionally the scattering experiment on $A = 20$ isobars [Chu96] provided experimental data on reaction cross sections and the rms nuclear charge radius of ^{20}Ne. Kitagawa *et al.* [Kit97] use these data for comparison with the theoretical calculation of the cross sections and the rms charge radius of ^{20}Ne which were

performed in the same model as ^{17}Ne. In a first step the nuclear density is modelled by a set of wave functions, which are obtained by the HF method using a Skyrme-type interaction (SGII), where the potential depth is adjusted to the empirical proton separation energy. On basis of these calculations Kitagawa *et al.* [Kit97] obtain rms matter radii, as well as the proton and neutron distribution of ^{20}Ne and for a $(\pi d_{5/2})^2$ and a $(\pi s_{1/2})^2$ configuration of the *sd*-shell proton pair of ^{17}Ne. These are tabulated in table 8.9. The Glauber model reaction cross sections were calculated from the theoretical radii and compared to the experimental data from Ozawa *et al.* [Oza94]. The HF approach of Kitagawa *et al.* [Kit97] does not lead to an unambiguous conclusion. On the one hand they point out that "the density distribution of ^{17}Ne ... shows a clear sign of a proton halo in the case that the last two protons occupy $2s_{1/2}$". This is contrasted by comparing the radii for the mirror pair ^{17}Ne-^{17}N: "...the isospin dependence is obtained in a reasonable way by the calculations with $1d_{5/2}$ valence configuration...". From this point of view "... the evidence of proton halo is still not conclusive".

8.5.3   Comparison with Data from Laser Spectroscopy
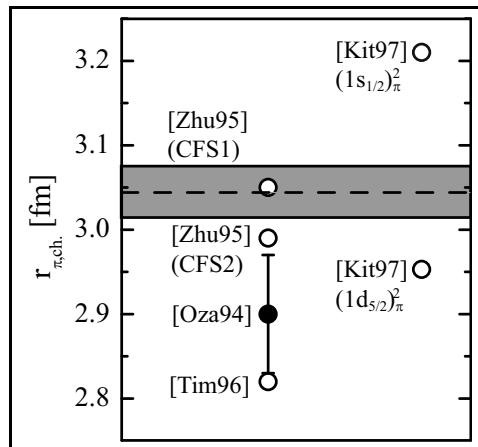
Fig. 8.8: *Comparison between the experimental data of r_{ch} from the present work and data from cross section measurements and from theory.*

The theoretical results on nuclear charge radii presented in the last section have to be compared to the data from laser spectroscopy. To do so, the absolute radius of ^{17}Ne was calculated. The input parameters are $\delta\langle r^2 \rangle^{20,17}$ of ^{17}Ne, and the experimental radius of ^{20}Ne of $r_{ch} = \langle r^2 \rangle^{1/2} = 3.006(59)$ fm published by Fricke *et al.* [Fri95]. The result is given in the last column of table 8.9. In figure 8.8 the experimental value is indicated by a dashed horizontal line, with the total error comprising the sum of the statistical and systematic error of the absolute radius of ^{17}Ne.

Similarly, the values of $\delta\langle r^2 \rangle^{20,17}$ were calculated from the experimental and theoretical input data on the absolute radii gathered in table 8.9. The corresponding comparison with the experimental value from the isotope shift is shown in figure 8.9. The data contained in the figures 8.8, and 8.9 consists of:

- The experimental value of r_{ch} and $\delta\langle r^2 \rangle$ measured by laser spectroscopy indicated by a dashed line with the error indicated as shaded area.

- Experimental rms charge radius r_{ch} given by Ozawa *et al.* [Oza94]. $\delta\langle r^2 \rangle$ calculated from the values of r_{ch} from the publication of Ozawa *et al.* [Oza94], and Fricke *et al.* [Fri95]. These data are indicated by filled circles.

- Theoretical values of r_{ch} published by Zhukov *et al.* [Zhu95], Timofeyuk *et al.* [Tim96] and Kitagawa *et al.* [Kit97]. $\delta\langle r^2 \rangle$ calculated from the theoretical values of r_{ch} for ^{17}Ne,^{20}Ne published by Kitagawa *et al.* [Kit97], indicated by open circles.
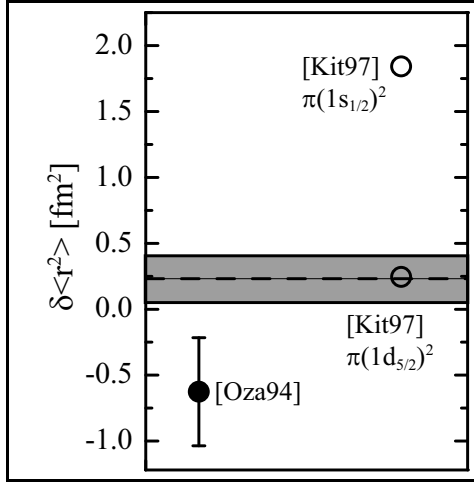
Fig. 8.9: *Comparison between the experimental data of $\delta\langle r^2\rangle$ of this work and values from cross section measurements by Ozawa et al. [Oza94] and theoretical values of Kitagawa et al. [Kit97].*

The comparison of the available data with the experimental value does not lead to a clear picture. Taking a look at the absolute radii r_{ch}, the earliest values for ^{17}Ne by Zhukov *et al.* [Zhu95] are consistent with the value from laser spectroscopy. The theoretical value of r_{ch} given by Timofeyuk *et al.* [Tim96] shows the largest deviation from the experimental value. The Hartree-Fock calculation of Kitagawa *et al.* [Kit97] does not show good agreement with experiment for either assumption about the wave function of ^{17}Ne. On the other hand these calculations underestimate systematically the charge radii, as is seen from the comparison with the known radius of ^{20}Ne given by Fricke *et al.* [Fri95]. Correcting the ^{17}Ne radius of Kitagawa by the difference between the theoretical and experimental radius of ^{20}Ne ($\delta r_{ch} = 0.096$ fm), yields an absolute radius in the $(\pi d_{5/2})^2$ state of 3.049 fm, which is consistent with the experimental value.

Unfortunately [Oza94, Zhu95], and [Tim96] published only values for ^{17}Ne but not for ^{20}Ne. Thus, a comparison of the experimental and theoretical values of $\delta\langle r^2\rangle$ is always hampered by the lack of consistently calculated theoretical of both, ^{17}Ne and ^{20}Ne. Consequently, only the experimental charge radius published by Ozawa *et al.* [Oza94] together with the absolute radius of Fricke *et al.* [Fri95] was used for comparison. The only consistent theoretical values were published by Kitagawa *et al.* [Kit97]. The systematic effect mentioned above is eliminated in the calculation of $\delta\langle r^2\rangle$. the Kitagawa value for the $(\pi d_{5/2})^2$ state is in good agreement with the value of $\delta\langle r^2\rangle$ measured by collinear laser spectroscopy.

In summary it seems that ^{17}Ne does not exhibit clear halo-nucleus behavior from the viewpoint of the data discussed above. The discussion on radii supports the picture already found by the comparison of the magnetic moments of the mirror nuclei ^{17}Ne-^{17}N (see Sec. 7.3.3): the nuclear structure of ^{17}Ne is a mixture of wave functions for the two protons above a ^{15}O core

$$^{17}\text{Ne}_{g.s.} = {}^{15}\text{O}_{g.s.} \otimes \left|\alpha\,(\pi d_{5/2})^2 + \beta\,(\pi s_{1/2})^2\right\rangle \ .$$

From the publication of Fortune and Sherr [For01], who investigated the ^{17}Ne ground state in the framework of the shell model, the contribution of the $(\pi s_{1/2})^2$ state is about 22%. This is consistent with the discussion of the nuclear moment and the value of 26% given by Zhukov [Zhu95]. But the conclusions drawn from these numbers are converse. Zhukov and Thompson consider ^{17}Ne "as a very promising candidate" for a proton halo. In contrast, Fortune and Sherr conclude from their calculations "that the $(\pi d_{5/2})^2$ configuration dominates for the last two nucleons and not $(\pi s_{1/2})^2$ as suggested by others". Furthermore Millener [Mil97] investigated isospin asymmetries in β-decays for the mirror pair ^{17}Ne-^{17}N. He finds as well a dominance of $(\pi d_{5/2})^2$ over the $(\pi s_{1/2})^2$ state.

8.6 Comparison with Unpublished RMF Data on Radii

In connection with this thesis theoretical calculations were performed by the group of Rein-
hard *et al.* [Rei01], which will be published together with the experimental data. These
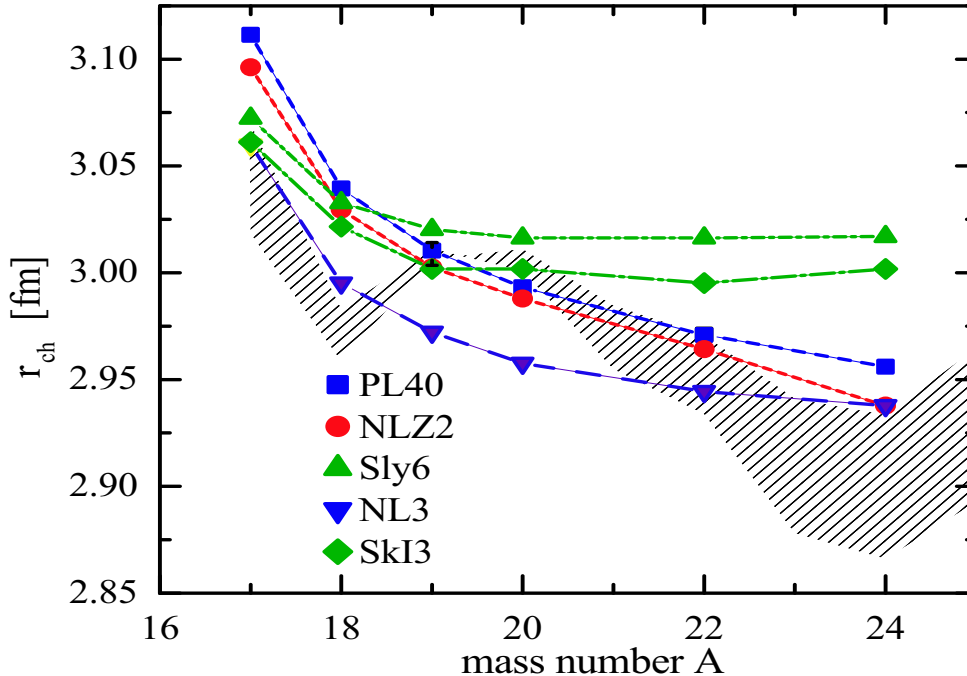
Fig. 8.10: *Comparison of experimental nuclear radii of neon with the results of
Skyrme-HF and RMF calculations of Reinhard et al. [Rei01]. The ex-
perimental value range defined by the statistical and systematic errors is
shown as grey area. The theoretical radii (dashed curves) were calculated
by the use of different interactions.*

calculations were performed in the framework of the Skyrme Hartree-Fock and the relativis-
tic mean field (RMF) model employing five different forces. The theoretical model involves
deformation properties, which only partly determine the trend of the radii. The results of the
calculations for absolute radii are plotted in figure 8.10 together with experimental results
which were calculated using the $\delta\langle r^2\rangle$ values from laser spectroscopy and the absolute radius
of ^{20}Ne from [Fri95]. At the present time these calculations are only available up to the
isotope ^{24}Ne, but work was in progress to extend the theoretical data to the range of isotopes
covered by the experiment.

As can be seen from the plot, the models are able to reproduce the general trend of the
charge radii increasing towards the proton drip-line. Still the structure of the experimental
curve cannot be reproduced in detail. Nevertheless, it is very interesting to compare exper-
iment and theory in the vicinity of ^{17}Ne. All theoretical predictions show a steep increase
of the radius from ^{18}Ne to ^{17}Ne and no shell effects for ^{18}Ne. Hence, the behavior of the
experimental data for these nuclei can be interpreted without the necessity to argue in favor
of a halo, rather suggesting a "standard" structure.

Chapter 9

Summary and Outlook

The aim of this work was the investigation of short-lived neon isotopes far off stability by collinear laser spectroscopy. The measurements took place at the on-line mass separator ISOLDE at the European nuclear physics center CERN in Geneva, Switzerland. The experimental work included the application and optimization of a method which allows to detect optical resonances under very challenging conditions – i.e. very low primary ion beam intensities, necessitating extremely high sensitivity, and very high selectivity due to otherwise overwhelming background levels. From the experimental spectra isotope shifts and hyperfine structure parameters were to be extracted to study nuclear phenomena in the lower sd shell, in the vicinity of the neutron shell closures $N = 8$ and $N = 20$. The nuclear moments, which are calculated from the hyperfine structure parameters can be used to test predictions of the single-particle structure of the odd-A nuclei in the framework of the nuclear shell model. Complementary the differences in mean square charge radii, which can be determined from the isotope shift, give information about the collective behavior of the investigated nuclei. The appropriate nuclear models of the relativistic mean field or the Hartree Fock type were to be tested with the acquired data. Of special interest in this context is the discussion about a possible proton halo structure of ^{17}Ne, which should show up in the observables accessible to laser spectroscopy.

In collinear laser spectroscopy a large Doppler shift is involved, which depends on the isotope mass and the acceleration voltage of the incoming ion beam. The transition frequency between two atomic states is determined by measuring the resonance peak position in terms of an acceleration voltage. To reach the precision required for the small field shifts of neon isotopes, the beam energy in terms of an acceleration voltage of the incoming ion beam had to be determined to better than a 2 V at a typical acceleration voltage of 60 kV.

The direct beam energy measurement was achieved by applying a new method which is based on collinear-anticollinear laser spectroscopy. In this geometry two closely lying atomic transitions are shifted into opposite directions due to the direction dependence of the Doppler shift. If the atomic levels are spaced appropriately they cross within the experimental working range of the collinear laser spectroscopy setup. Fortunately such a pair of transitions with very accurately known wave numbers was found in the atomic spectrum of ^{20}Ne. This newly implemented beam-energy measurement technique was realized by the use of the standard collinear laser spectroscopy setup with only minor modifications.

Besides the advances in measuring the beam energy, the laser system was upgraded to

achieve an improved long-term stability of the laser frequency. This improvement is important for experiments which require measuring times of several hours at stable laser conditions.

The sensitivity for laser spectroscopy on short-lived isotopes was achieved by implementing the method pioneered by A. Klein in previous measurements on argon [Kle96]. Here the method of detecting an optical resonance non-optically by collisional reionization was combined with the detection of the β-particles emitted by the radioactive isotopes. With the introduction of an additional identical detection system the signals can now be normalized to the primary beam intensity. This is necessary because the primary beam intensity varies strongly depending on the target conditions under proton bombardment. This normalization and the improvement of the laser stabilization enabled the measurement of the resonance of ^{28}Ne at an extremely low primary ion beam intensity of 50 ions per proton pulse on the target within about 4 hours.

The experiments on the odd-A neon isotopes yielded the nuclear moments which were determined from the measured hyperfine structure parameters. The magnetic moments of ^{17}Ne and ^{25}Ne are reported for the first time. The spin of ^{25}Ne was found to be 1/2. Similarly the quadrupole moment of ^{23}Ne was measured for the first time, and the accuracy of the magnetic moment was improved. The comparison of the results on ^{19}Ne and ^{21}Ne with previously known data gave excellent agreement. The nuclear moments were compared with values from nuclear shell-model calculations by A. Brown, showing fairly good agreement over the sd shell.

The magnetic moment of ^{17}Ne was interpreted separately in the framework of the isoscalar moment which can be calculated for the mirror partners ^{17}Ne and ^{17}N. Both nuclei show symmetric deviations from the general trend of $p_{1/2}$ magnetic moments but follow the systematics of the isoscalar moments. This behavior implies mirror symmetry of the two isotopes, so that the interpretation of the magnetic moment of ^{17}N which was given by Ueno *et al.* [Uen96] holds as well for ^{17}Ne.

The isotope shifts $\delta\nu_{IS}$ were measured in the full range of ^{17}Ne to ^{26}Ne, and for ^{28}Ne with respect to the reference isotopes ^{20}Ne. From these data it was possible to extract the differences in mean square nuclear charge radii $\delta\langle r^2 \rangle$. The comparison with theoretical data implies that the changes in the charge radii can be explained well by nuclear deformation effects. Very surprising for such low-A systems the radii derived from the droplet model with experimental deformation parameters match the experimental values rather well. The agreement becomes even better, if a shape transition from prolate to oblate is assumed when the mid shell is crossed at ^{24}Ne, which is supported by theoretical predictions. The behavior of the nuclear charge radii implies that the shell closure at ^{18}Ne, still showing strong deformation effects, is softened. Similarly approaching the neutron shell closure $N = 20$ does not indicate decreasing deformation for ^{28}Ne. This behavior is understood to be linked to the so-called "island of inversion", which was found to determine the nuclear structure in the vicinity of ^{31}Na and ^{32}Mg.

The comparison of the nuclear charge radius of ^{17}Ne with theoretical predictions does not lead to a conclusive picture. Nevertheless the experimental result does not support a pronounced proton halo structure of this nucleus. A structure dominated by a $d_{5/2}$ proton pair with small $s_{1/2}$ admixtures seems to be more likely.

The experimental improvements made for this work give good prospects for further measurements on short-lived isotopes in the region of light elements. Thus, the improved experimental setup was already used for studies of argon isotopes in the neutron-rich region close to stability. An extension to beyond the $N = 28$ shell closure is planned for the future. Furthermore the odd krypton isotope ^{73}Kr was investigated to complete an earlier experiment yielding the nuclear spins, moments and nuclear charge radii of neutron-deficient krypton isotopes.

The improvements achieved by developing a beam-energy measurement technique enable collinear laser spectroscopy measurements of isotope shifts with unprecedented accuracy. Besides being useful for laser spectroscopy experiments the measurement of the beam energy is of interest for other experiments like ion beam decelerators and bunching facilities, which require a precise knowledge of the actual beam energy as well. Still it will be very difficult to push the possibilities of measuring field shifts by collinear laser spectroscopy experiments towards lower masses.

Appendix A

Isotope Shift Data for all the Runs

In the tables A.1, A.2 and A.3, $\delta\nu_{line}^{20,A}$ is the frequency shift between a resonance line of an arbitrary isotope and the reference ^{20}Ne without the correction for the difference in the optical and non-optical signals. The statistical errors of the uncorrected line position $\Delta^{stat}(\delta\nu_{line})$ results from the scattering of the data, the errors from the fit of the lines are neglected, because it is found $\Delta(\delta\nu_{scatter}) >> \Delta(\delta\nu_{fit})$. The systematic errors $\Delta^{sys}(\delta\nu_{line})$ are resulting from the statistic uncertainties of the beam-energy measurement $\Delta U_{MAIN}^{stat} = \sqrt{(\Delta U_{ISOL}^{stat})^2 + (\Delta U_{plasma}^{stat})^2}$. These errors are run dependent, the run independent systematic errors of the beam-energy measurement are included later and contribute to the errors in table 6.4. The total error of the individual run $\Delta(\delta\nu_{line,corr}^{20,A})$ is given by the linear sum $\Delta^{stat}(\delta\nu_{line}) + \Delta^{sys}(\delta\nu_{line})$.

In column 5 the non-optical line correction parameter $\delta\nu_{line}^{corr}$ with its error $\Delta(\delta\nu_{line}^{corr})$ in column 6 is found. The final values of the corrected shifts $\delta\nu_{line,corr}^{20,A}$ of an individual line of a hyperfine multiplet of all the evaluated runs is presented in column 7. The data printed in bold characters are the weighted mean values for the isotope shifts $\delta\nu_{IS}^{20,A}$, with $\Delta(\delta\nu_{line,corr}^{20,A})$ as weights. The error given in parenthesis is the sum of the weighted mean error of $\Delta(\delta\nu_{line,corr}^{20,A})$ and the error of the line-position correction $\Delta(\delta\nu_{line}^{corr})$.

Table A.1: *Data on line positions and isotope shifts of ^{17,18,19}Ne.*

run	$\delta\nu_{line}^{20,A}$	$\Delta^{stat}(\delta\nu_{line})$ [MHz]	$\Delta^{sys}(\delta\nu_{line})$ [MHz]	$\delta\nu_{line}^{corr}$ [MHz]	$\Delta(\delta\nu_{line}^{corr})$ [MHz]	$\delta\nu_{line,corr}^{20,A}$ [MHz]	$\Delta\delta\nu_{line,corr}^{20,A}$ [MHz]
				^{17}Ne			
$F_i = 5/2 \to F_f = 5/2$				wmv $\delta\nu_{line,corr}^{20,A}$=-3473.951(0.978) MHz			
09/98	-3476.081	0.526	0.960	1.474	0.123	-3474.607	1.486
10/99	-3475.552	1.378	0.104	1.473	0.122	-3474.079	1.482
04/00	-3472.798	2.622	0.068	1.422	0.117	-3471.376	2.690
$F_i = 5/2 \to F_f = 3/2$				wmv $\delta\nu_{line,corr}^{20,A}$=-1084.715(2.448) MHz			
10/99	-1086.188	2.344	0.104	1.473	0.122	-1084.715	2.448
$F_i = 3/2 \to F_f = 5/2$				wmv $\delta\nu_{line,corr}^{20,17}$=-5135.118(2.822) MHz			
10/99	-5136.591	2.718	0.104	1.473	0.122	-5135.118	2.822
$F_i = 3/2 \to F_f = 3/2$				wmv $\delta\nu_{line,corr}^{20,17}$=-2749.918(1.150) MHz			
09/98	-2745.783	1.980	0.960	1.474	0.123	-2744.309	2.940
10/99	-2752.563	1.195	0.104	1.473	0.122	-2751.090	1.299
04/00	-2750.387	4.504	0.068	1.422	0.117	-2748.965	4.572
						$\delta\nu_{\mathbf{IS,corr}}^{\mathbf{20,17}} = \mathbf{-3183.847(1.169)}$ **MHz**	
				^{18}Ne			
09/98	-1996.088	0.574	0.606	1.487	0.123	-1994.601	1.180
10/99	-2001.479	1.458	0.065	1.474	0.122	-2000.005	1.523
04/00	-1996.516	0.539	0.043	1.478	0.122	-1995.038	0.582
						$\delta\nu_{\mathbf{IS,corr}}^{\mathbf{20,18}} = \mathbf{-1995.484(0.616)}$ **MHz**	
				^{19}Ne			
$F_i = 5/2 \to F_f = 5/2$				wmv $\delta\nu_{line,corr}^{20,19}$=-248.695(0.742) MHz			
09/98	-252.576	2.741	0.286	1.487	0.123	-251.089	3.027
10/99	-251.737	0.910	0.031	1.474	0.121	-250.263	0.941
04/00	-246.664	1.294	0.020	1.478	0.122	-245.186	1.314
$F_i = 5/2 \to F_f = 3/2$				wmv $\delta\nu_{line,corr}^{20,19}$=-5968.290(3.360) MHz			
09/98	-5961.881	9.462	0.679	1.487	0.123	-5960.394	10.141
10/99	-5970.738	3.530	0.031	1.474	0.121	-5969.264	3.561
$F_i = 3/2 \to F_f = 5/2$				wmv $\delta\nu_{line,corr}^{20,19}$=3723.331(1.003) MHz			
09/98	3722.460	0.653	0.679	1.487	0.123	3723.947	1.332
10/99	3721.048	1.495	0.031	1.474	0.121	3722.522	1.526
$F_i = 3/2 \to F_f = 3/2$				wmv $\delta\nu_{line,corr}^{20,19}$=-1995.401(0.489) MHz			
09/98	-1989.295	1.223	0.286	1.487	0.123	-1987.808	1.509
10/99	-1998.213	0.599	0.031	1.474	0.121	-1996.739	0.630
04/00	-1996.848	0.883	0.020	1.478	0.122	-1995.370	0.903
						$\delta\nu_{\mathbf{IS,corr}}^{\mathbf{20,19}} = \mathbf{-947.424(0.741)}$ **MHz**	

Table A.2: *Data on line positions and isotope shifts of* $^{21,22,23,24}Ne$.

run	$\delta\nu_{line}^{20,A}$	$\Delta^{stat}(\delta\nu_{line})$ [MHz]	$\Delta^{sys}(\delta\nu_{line})$ [MHz]	$\delta\nu_{line}^{corr}$ [MHz]	$\Delta(\delta\nu_{line}^{corr})$ [MHz]	$\delta\nu_{line,corr}^{20,A}$ [MHz]	$\Delta(\delta\nu_{line,corr}^{20,A})$ [MHz]
				^{21}Ne			
09/98	873.255	0.756	0.262	-optical-	-optical-	873.255	1.018
03/99	873.674	1.013	0.263	-optical-	-optical-	873.255	1.276
10/99	874.288	1.788	0.028	0.750	0.031	875.038	1.847
04/00	877.761	1.359	0.019	1.515	0.125	879.276	1.503
07/00	872.063	1.313	0.060	1.552	0.128	873.615	1.501
11/99	875.620	1.303	0.024	1.525	0.126	877.145	1.453
					$\delta\nu_{\mathbf{IS,corr}}^{\mathbf{20,21}} = \mathbf{874.940(0.556)}$ **MHz**		
				^{22}Ne			
05/99	1662.692	0.607	0.134	-optical-	-optical-	1662.692	0.741
10/99	1663.703	0.426	0.054	-optical-	-optical-	1663.703	0.480
04/00	1664.500	0.389	0.035	-optical-	-optical-	1664.500	0.424
07/00	1662.791	0.345	0.113	-optical-	-optical-	1662.791	0.458
11/00	1663.593	0.179	0.055	-optical-	-optical-	1663.593	0.234
					$\delta\nu_{\mathbf{IS,corr}}^{\mathbf{20,22}} = \mathbf{1663.595(0.170)}$ **MHz**		
				^{23}Ne			
05/99	2391.848	1.576	0.192	1.580	0.130	2393.428	1.768
10/99	2392.888	1.977	0.077	1.570	0.129	2394.458	2.054
					$\delta\nu_{\mathbf{IS,corr}}^{\mathbf{20,23}} = \mathbf{2393.810(1.379)}$ **MHz**		
				^{24}Ne			
05/99	3049.902	0.927	0.245	1.592	0.132	3051.494	1.172
10/99	3054.632	0.635	0.099	1.567	0.129	3053.199	0.734
07/00	3051.031	1.001	0.208	1.549	0.127	3052.580	1.209
11/00	3049.263	0.979	0.101	1.571	0.130	3050.834	1.080
					$\delta\nu_{\mathbf{IS,corr}}^{\mathbf{20,24}} = \mathbf{3053.643(0.752)}$ **MHz**		

Table A.3: *Data on line positions and isotope shifts of $^{25,26,28}Ne$.*

| run	$\delta\nu_{line}^{20,A}$	$\Delta^{stat}(\delta\nu_{line})$ [MHz]	$\Delta^{sys}(\delta\nu_{line})$ [MHz]	$\delta\nu_{line}^{corr}$ [MHz]	$\Delta(\delta\nu_{line}^{corr})$ [MHz]	$\delta\nu_{line,corr}^{20,A}$ [MHz]	$\Delta(\delta\nu_{line,corr}^{20,A})$ [MHz]
^{25}Ne							
$F_i = 5/2 \rightarrow F_f = 5/2$				wmv $\delta\nu_{line,corr}^{20,25}$=4028.792(0.604) MHz			
05/99	3049.902	1.457	0.295	1.585	0.131	4032.615	1.752
07/00	4026.683	1.653	0.250	1.573	0.130	4028.256	1.903
11/00	4026.715	0.563	0.121	1.563	0.129	4028.278	0.684
$F_i = 5/2 \rightarrow F_f = 3/2$				wmv $\delta\nu_{line,corr}^{20,25}$=976.238(1.069) MHz			
05/99	975.132	0.905	0.295	1.585	0.131	976.717	1.200
11/00	972.828	2.236	0.121	1.563	0.129	974.391	2.357
$F_i = 3/2 \rightarrow F_f = 5/2$				wmv $\delta\nu_{line,corr}^{20,25}$=6144.093(1.475) MHz			
05/99	6142.724	1.608	0.295	1.585	0.131	6177.309	1.903
11/00	6142.205	2.213	0.121	1.563	0.129	6143.768	2.334
$F_i = 3/2 \rightarrow F_f = 3/2$				wmv $\delta\nu_{line,corr}^{20,25}$=3094.609(0.457) MHz			
05/99	3098.029	0.841	0.295	1.585	0.131	3099.614	1.136
07/00	3092.077	0.849	0.250	1.573	0.130	3093.650	1.099
11/00	3092.079	0.310	0.121	1.563	0.129	3093.642	0.560
$\delta\nu_{\mathbf{IS,corr}}^{\mathbf{20,25}} = \mathbf{3654.737(0.659)}$ **MHz**							
^{26}Ne							
05/99	4213.748	0.930	0.340	1.558	0.129	4215.306	1.270
07/00	4212.800	0.681	0.288	1.573	0.130	4214.373	0.969
11/00	4215.575	0.728	0.139	1.578	0.130	4217.153	0.867
$\delta\nu_{\mathbf{IS,corr}}^{\mathbf{20,26}} = \mathbf{4215.791(0.706)}$ **MHz**							
^{28}Ne							
05/99	5209.326	0.956	0.421	1.512	0.125	5210.838	1.377
11/00	5200.871	3.162	0.160	1.494	0.123	5202.365	3.322
$\delta\nu_{\mathbf{IS,corr}}^{\mathbf{20,28}} = \mathbf{5209.596(1.396)}$ **MHz**							

Appendix B

Line Compression Mechanism in Accelerated Ion Beams

B.1 General Idea of Compression Mechanism

As described in [Kau76], the velocity distribution of the ion/atom beam experiences a compression which is dependent on the acceleration voltage. To the knowledge of the author there is no analytical formula available in the literature which describing the velocity distribution resulting from this phenomenon. Attempts were made to explain similar effects, as an example Field *et al.* [Fie89]) investigate the compression of the velocity distribution of a cloud of atoms accelerating in the gravitational field of a planet. However, the velocity bunching in accelerated ion beams was not yet described by an analytical formula. In the framework of this thesis the exact description of the line shape was desirable, and an attempt was made to describe the line shape compression analytically.
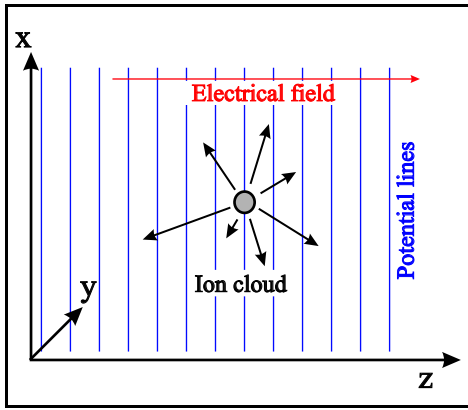
Fig. B.1: *An ion cloud expanding in an electrical field. The arrows indicate the starting velocities.*

In a simple picture a cloud of ions expands with thermal energies from one point in all directions of space, each ion with a starting velocity $\vec{v} = (v_x, v_y, v_z)$. The starting point is $\vec{x} = (0,0,0)$, their velocity distribution should be Maxwellian. It is assumed that the ion density is small enough that repulsive forces due to their electrical charge are negligible. The expansion takes place in a homogeneous electrical potential, which has a constant gradient in z-direction $\frac{\partial \phi}{\partial z} = const$ whereas the potential is constant in the other directions. The electrical field causes a force in +z direction, and depending on the starting velocity the ions will only be able to escape to +z as shown in figure B.1.

The kinetic energy gain of the ions is dependent on their starting position in the electrical potential, i.e. the position where their velocity z-component is zero. An ion starting with a velocity 0 will gain kinetic energy according to

$$\Delta E_{kin} = \frac{\partial \phi}{\partial z} \Delta z. \tag{B.1}$$

An ion starting with a velocity component in the +z-direction will have an initial kinetic energy, which adds to the gain from the field potential energy. Ions starting with velocities in the negative z-direction will be stopped and then accelerated by the field. Because the distance they have to travel in the field is bigger, their gain from potential energy is bigger as well – actually equal to their kinetic energy at the beginning. Finally all the ions with the same absolute starting velocity will end up in the same energy regime of the accelerated ions, independent of their starting velocities' z-directions
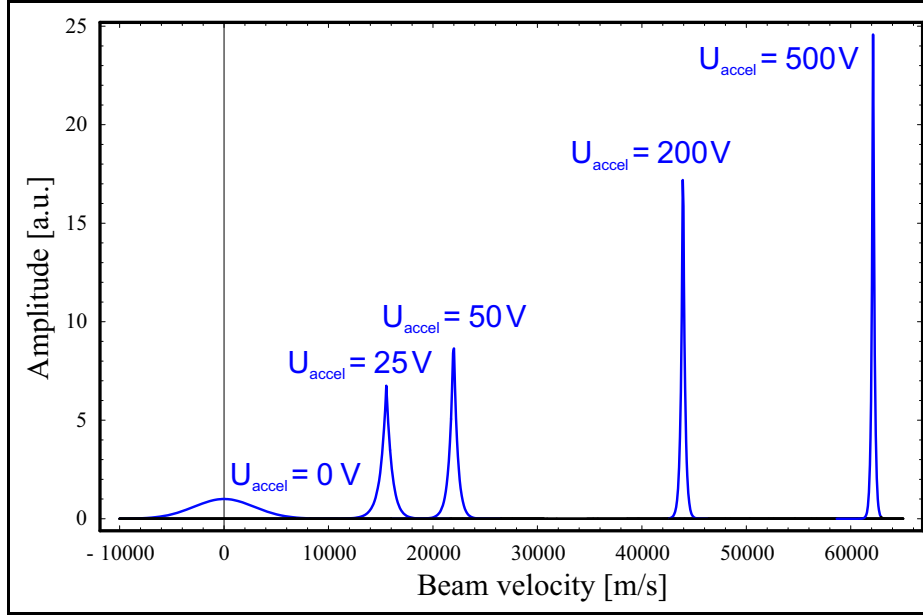
Fig. B.2: *Velocity compression of a Maxwell shaped distribution. The voltages indicated are the acceleration voltages used for the different profiles. The initial distribution at zero velocity is of Maxwellian type. An ion temperature of 0.9 eV ≈ 20000 K is assumed. This corresponds to a typical value of a rf plasma ion source such as used at ISOLDE [Wol].*

As an approximation a Maxwell distribution for the ion velocities in the z-direction is assumed

$$P(v_z) = \left(\frac{m}{2\pi kT}\right)^{1/2} \cdot e^{-mv_z^2/2kT}. \tag{B.2}$$

Or written in terms of momenta:

$$P(p_z) = \left(\frac{m}{2\pi kT}\right)^{1/2} \cdot e^{-p_z^2/2mkT} ., \tag{B.3}$$

which is an expression for the kinetic energy. The kinetic energy of the ions after acceleration is expressed by:

$$E_{kin} = \frac{p_z'^2}{2m} = \underbrace{\frac{p_z}{|p_z|} \cdot \frac{p_z^2}{2m} + eU}_{X} \tag{B.4}$$

$$\Rightarrow p_z' = 2m\frac{X}{|X|}\sqrt{|X|} \tag{B.5}$$

The factor $p_z/|p_z|$ and $X/|X|$ is needed to indicate the ion's direction $\pm z$. Replacing p_z in equation (B.3) yields an expression for the accelerated velocity distribution which compresses with increasing acceleration as shown in figure B.2:

$$
\begin{aligned}
P(p_z') &= \left(\frac{m}{2\pi kT}\right)^{1/2} \cdot e^{-p_z'^2/2mkT} \\
&= C \cdot e^{-(\frac{p_z}{|p_z|} \cdot \frac{p_z^2}{2m} + eU)^2/(2kT \times |\frac{p_z}{|p_z|} \cdot \frac{p_z^2}{2m} + eU|)}
\end{aligned}
\tag{B.6}
$$

The norm constant C is given by preservation of the integral under the curve. In parallel to this thesis the line shape problem was investigated by another group at Mainz. Stefan Götte derived an analytical formula for the normalization constant [Göt02]

$$
C = N_0 \sqrt{\frac{m}{2\pi kT}} \cdot \frac{1}{\exp\left[\sqrt{\frac{eU}{kTc^2}}\right]^2 \left(1 - \operatorname{erf}\left[\sqrt{\frac{eU}{kT}}\right]\right)} ,
\tag{B.7}
$$

where N_0 is the initial area under the Gaussian distribution inside the ion source. In figure B.2 the velocity bunching effect is clearly visible even for very small acceleration voltages. In practice the acceleration voltage will not be below 40 kV. Plotting of distributions at high voltages was omitted for better visualization of the effect.

B.2 Compression Factor for Linewidth

After having derived the expression for the linewidth compression it is interesting to investigate the linewidths resulting from the acceleration. Unfortunately, an analytical expression for the FWHM could not be calculated. To get an idea about the magnitude of the compression a numerical approach was chosen. In figure B.3 the dependence of width on voltage
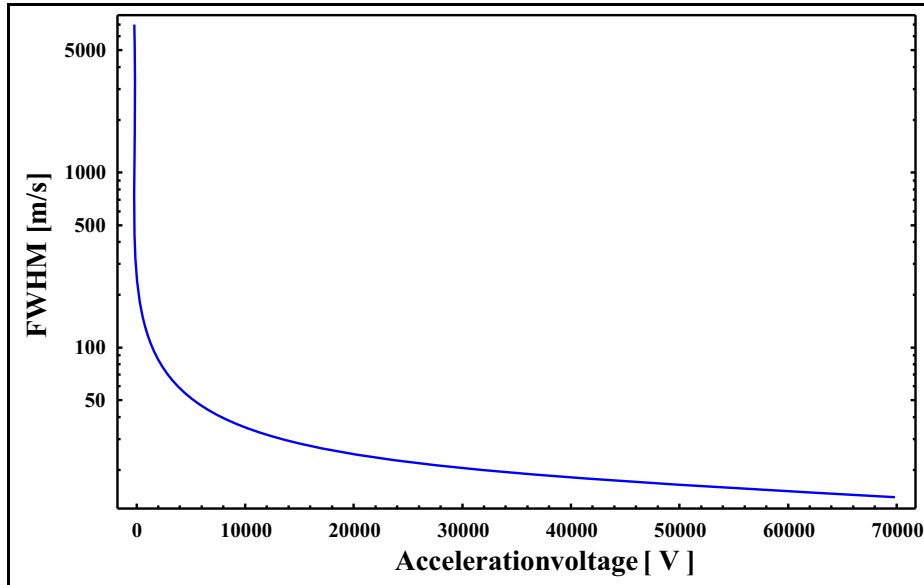
Fig. B.3: *Behavior of the linewidth of the compressed velocity distribution as a function of the acceleration voltage. The initial parameters are the same as in figure B.2.*

dependence is plotted. The plot has a logarithmic ordinate, which represents the distribution width in m/s. As can be seen, the distribution width decreases significantly with increasing acceleration voltage. With acceleration voltages of about 60 kV a reduction by a factor of 1000 of the width of the velocity distribution can be expected.

Assuming an initial ion energy spread of 0.9 eV, corresponding to about 20000 K, which is the typical order of magnitude for ions in a plasma ion source, the initial Doppler width of the "spectroscopic" transition of ^{20}Ne "inside the ion source" is given by ([Dem98], p.68)

$$\Delta\nu_D = \frac{\nu_0}{c}\sqrt{8kT\ln(2)/m} = 11.05 \text{ GHz} . \tag{B.8}$$

Using the compression factor of 1000 at an ion-beam energy of 60 keV, residual Doppler linewidths in the order of 11 MHz are found. This corresponds to the residual Doppler width typically observed in experimental spectra.

B.3   Ions in Ion Sources

The principle outlined in the previous paragraph can be adapted to the situation inside a real plasma ion source. Inside the source cavity the space is filled with the burning plasma. The physics of ion sources and plasmas can be found in books like [Bro89]. Inside the plasma the potential is constant, external fields are shielded from the interior region, quite similar to the way a metal excludes electric fields from its interior. at the plasma borders a boundary layer is formed between the plasma itself and the exterior region. This boundary layer is called plasma sheath, and the potential inside the plasma drops to the potential of the outside wall within the sheath thickness, given by the Debye length:

$$\lambda_D = \sqrt{\frac{\epsilon_0 kT_e}{e^2 n_e}} . \tag{B.9}$$

Where T_e is the electron temperature, which is of the order of several eV (1 eV $\hat{=}$ 23216 K) in the case of a discharge ion source [Bro89] similar to those used at ISOLDE. The parameter n_e, the so-called plasma density, is the number of electrons emitted by the ions of charge state q_i with number n_i:

$$\sum q_i n_i = n_e . \tag{B.10}$$

When an external electrical field is applied on the plasma, the field can penetrate the plasma only to a depth given by the high voltage sheath thickness:

$$d_{\text{sheath}} = \lambda_D \sqrt{\frac{U_{external}}{kT_e}} \tag{B.11}$$

The effect of the penetrating external potential and the thickness of the plasma layer is shown schematically in figure B.4.
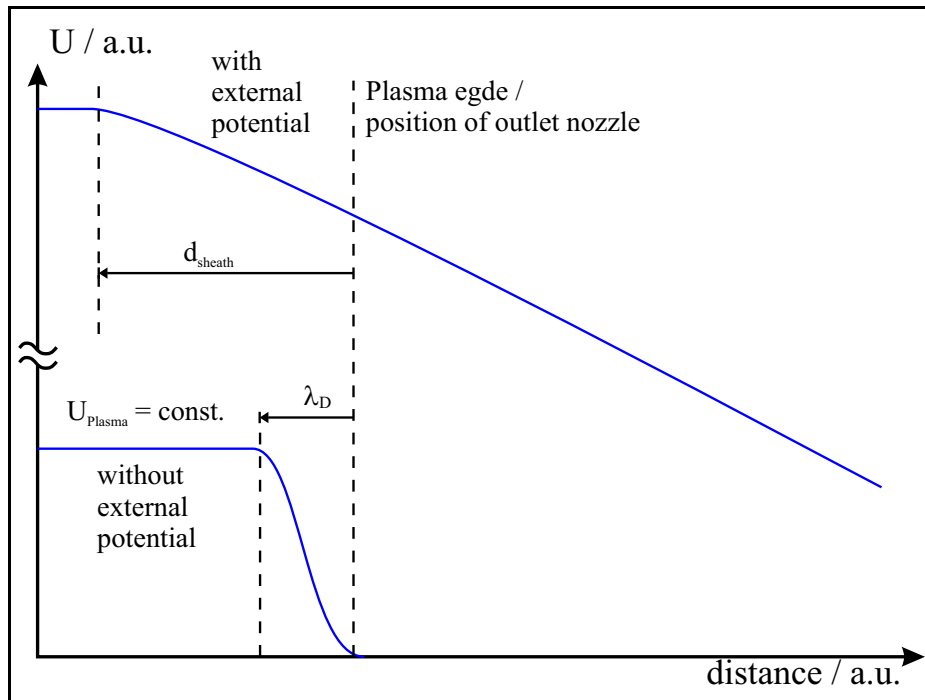
Fig. B.4: *Potential distribution at the plasma edge. The dimensions shown in this figure are not to scale, the depth of the plasma sheath is underestimated in comparison with λ_D.*

Two important effects can be explained by the slope-like structure of the potential at the ion source nozzle. On the one hand is a potential slope necessary for the velocity compression. On the other hand the unknown acceleration potential can be attributed to the potential step at the outlet orifice of the source . The total acceleration potential is extremely sensitive to the position of ionization. If it takes place at the potential step, big differences between the applied electrical voltages and the beam energy can be the result. The dependence on the ion source conditions is supported by the measurements done in this work. The experimental results of the measurements are presented in chapter 5.

Appendix C

Small Formula Collection for Collinear Laser Spectroscopy

In the literature the equations governing the physics of collinear can unfortunately only be found in the simplified non-relativistic formulation. The purpose of this formula collection is to give the full relativistic formulation of these equation together with a number of expression which are useful in the daily experimental work.

C.1 Basic Equations

- Doppler shifted frequency ν_D of an atomic resonance frequency ν_0:

$$\nu_D = \nu_0 \pm \delta\nu_D = \nu_0 \times \frac{1 \pm \beta}{\sqrt{1 - \beta^2}} \tag{C.1}$$

- Relativistic factor β in dependence of the acceleration voltage:

$$\beta = \frac{v}{c} = \sqrt{1 - \frac{m^2 c^4}{(eU + mc^2)^2}} \tag{C.2}$$

- Doppler shifted resonance frequency as a function of the acceleration voltage:

$$\nu_D = \nu_0 \times \frac{mc^2 + e\,U \pm \sqrt{eU(2mc^2 + eU)}}{mc^2} \tag{C.3}$$

C.2 Differential Doppler Shift

The Differential Doppler shift $\delta\nu_{diff}$ is given by the Doppler shift in MHz per volt acceleration voltage:

$$\delta\nu_{diff} = \frac{\partial\nu_D}{\partial U} = \frac{\nu_0}{m\,c^2} \left(e + \frac{e\,(mc^2 + eU)}{\sqrt{eU\,(2\,m\,c^2 + eU)}} \right) \tag{C.4}$$

In the case of ^{20}Ne the differential Doppler shift at 60 keV beam energy is $\delta\nu_{diff} = 10.35$ MHz/V.

C.3 Isotopic Doppler Shift

A useful quantity for experimental purposes is the so-called "isotopic Doppler shift", the frequency difference caused by the difference in mass between two isotopes:

$$\delta\nu_{iso} = \nu_D^{(1)} - \nu_D^{(2)} \ , \text{ where } \nu_0^{(2)} = \nu_0 + \delta\nu_{IS} \tag{C.5}$$

$$
\begin{aligned}
\Rightarrow \delta\nu_{iso} = {} & \frac{\nu_0}{m_1 c^2}\left[e\,U^{(1)} + \sqrt{e\,U^{(1)}(2c^2 m_1 + e\,U^{(1)})} \,\right] \\
& - \delta\nu_{IS} \\
& - \frac{(\nu_0 + \delta\nu_{IS})}{m_2 c^2}\left[e\,U^{(2)} + \sqrt{U^{(2)}e(2m_2 c^2 + e\,U^{(2)})} \,\right]
\end{aligned}
\tag{C.6}
$$

Here $U^{(1)}$ and $U^{(2)}$ represent the resonance positions for the two isotopes (mass m_1 and m_2) under investigation. The differential Doppler shift is defined as the frequency difference for the case $U^{(1)} = U^{(2)}$. Taking as an example the isotopic Doppler shift between the isotopes ^{20}Ne, and ^{21}Ne ($\delta\nu_{IS} = 875$ MHz) at a beam energy of 60 keV, it is found that $\delta\nu_{iso} = 29.10$ GHz.

C.4 Isotope Shift

The isotope shift $\delta\nu_{IS}$ has to be calculated from the line positions $U^{(1)}$ and $U^{(2)}$ of the corresponding isotopes. From these line positions the isotope shift becomes:

$$
\delta\nu_{IS} = \nu_0 \times \left\{ \frac{m_2 e\,U^{(1)} - m_1 e\,U^{(2)}}{m_1\left[m_2 c^2 + e\,U^{(2)} + \sqrt{e\,U^{(2)}(2m_2 c^2 + e\,U^{(2)})} \,\right]} \right.
$$

$$
+ \frac{m_2\sqrt{e\,U^{(1)}(2m_1 c^2 + e\,U^{(1)})}}{m_1\left[m_2 c^2 + e\,U^{(2)} + \sqrt{e\,U^{(2)}(2m_2 c^2 + e\,U^{(2)})} \,\right]}
$$

$$
\left. - \frac{m_1\sqrt{e\,U^{(2)}(2m_2 c^2 + e\,U^{(2)})}}{m_1\left[m_2 c^2 + e\,U^{(2)} + \sqrt{e\,U^{(2)}(2m_2 c^2 + e\,U^{(2)})} \,\right]} \right\}
\tag{C.7}
$$

where m_1, m_2 represent the atomic mass of the corresponding isotope.

Appendix D

Small Formula Collection for Beam Energy Measurement

D.1   Acceleration Voltage from Collinear/Anticollinear Excitation

The measurement of the true ion beam energy relies on collinear/anticollinear excitation of two closely lying atomic levels of one isotope.

$$
\begin{aligned}
\nu_L \;&=\; \frac{\nu_0^{(1)}}{mc^2} \cdot \left[mc^2 + U^{(1)}e + \sqrt{U^{(1)}e(2mc^2 + U^{(1)}e)} \, \right] \qquad \text{(collinear)} \\
&=\; \frac{\nu_0^{(2)}}{mc^2} \cdot \left[mc^2 + U^{(2)}e - \sqrt{U^{(2)}e(2mc^2 + U^{(2)}e)} \, \right] \qquad \text{(anticollinear)} , \quad \text{(D.1)}
\end{aligned}
$$

The line positions of the two resonance lines can be written in terms of main acceleration voltage and post-acceleration voltage:

$$
U^{(1),(2)} = U_{calib} + U_{post}^{(1),(2)} \tag{D.2}
$$

Solving for U_{calib} yields an expression for the calibrated beam energy (acceleration voltage)

$$
\begin{aligned}
U_{calib} \;=\;& \frac{\left(\nu_0^{(1)} + \nu_0^{(2)}\right)\sqrt{m^2c^4\left(\nu_0^{(2)} - \nu_0^{(1)}\right)^2 + e^2\nu_0^{(1)}\nu_0^{(2)}\left(U_{post}^{(2)} - U_{post}^{(1)}\right)^2}}{2e\left(\nu_0^{(2)} - \nu_0^{(1)}\right)\sqrt{\nu_0^{(1)}\nu_0^{(2)}}} \\
&- \frac{1}{2}\left(U_{post}^{(2)} + U_{post}^{(1)}\right) - \frac{mc^2}{e} \; . \tag{D.3}
\end{aligned}
$$

The line positions in terms of the post-acceleration voltage is given by:

$$
U_{post}^{(1),(2)} = U_{prema}^{(1),(2)} \times D_{div} + U_{DAC}^{(1),(2)} \times F_{cal}^{(1),(2)} \times D_{div} \tag{D.4}
$$

For small separations of the collinear and anticollinear line one finds

$$
U_{prema}^{(1)} = U_{prema}^{(2)} \quad , \quad F_{cal}^{(1)} = F_{cal}^{(2)} \tag{D.5}
$$

D.2   Divider Ratio from Collinear/Anticollinear Excitation of two Isotopes

If the ion beam energy was determined twice by using the collinear/anticollinear method by the use of two isotopes, the divider ratio can be calculated. The part of the acceleration

voltage, which is constant in time for the two isotopes, is

$$U_{stat}^{(1)} = U_{ISOL} + U_{plasma}^{(1)} + U_{prema}^{(1)} \times D_{div} \tag{D.6}$$

$$U_{stat}^{(2)} = U_{ISOL} + U_{plasma}^{(2)} + U_{prema}^{(2)} \times D_{div} . \tag{D.7}$$

U_{ISOL} and U_{prema} are electrically measured voltages, and U_{plasma} is the unknown offset voltage measured by collinear laser spectroscopy. The voltage divider ratio can be calculated from

$$D_{div} = \frac{U_{stat}^{(1)} - U_{stat}^{(2)}}{U_{prema}^{(2)} - U_{prema}^{(1)}} . \tag{D.8}$$

Note that the measured beam energy and the divider ratio are coupled quantities. Thus, the determination of both requires an iterative calculation. It was found that this iteration converged for the present measurements.

Appendix E

General Quantum Mechanics Formulae

E.1   Wigner-Eckart Theorem

For further information see [Hey94], p.50f, [Sak95], p.238f, or [Gre96], p.35f. The Wigner-Eckart theorem is used for the calculation of matrix elements of spherical tensor operator components $\hat{T}_\kappa^{(k)}$. With its help it is possible to separate the part which is only dependent on projection quantum numbers – "m-quantum numbers" – and the other part that depends on other properties (radial, angular momentum, etc.) of the operator and the state vectors.

Take a matrix element of the irreducible spherical tensor operator $\hat{T}_\kappa^{(k)}$ between angular-momentum states of the form $|\alpha jm\rangle$. The corresponding matrix element is given by

$$\langle \alpha jm|\hat{T}_\kappa^{(k)}|\alpha' j'm'\rangle .$$ (E.1)

Using the Wigner-Eckart theorem we can split projection and other parts and can write the reduced matrix element

$$\langle \alpha jm|\hat{T}_\kappa^{(k)}|\alpha' j'm'\rangle = (-1)^{j-m} \begin{pmatrix} j & k & j' \\ -m & \kappa & m' \end{pmatrix} \langle \alpha j||\hat{T}^k||\alpha' j'\rangle ,$$ (E.2)

where the matrix coefficient in the equation is given by the Wigner $3j$-symbols

$$\begin{pmatrix} j_1 & j_2 & j_z \\ m_1 & m_2 & m_3 \end{pmatrix} = \frac{(-1)^{j_1-j_2-m_3}}{\sqrt{2j_3+1}} \langle j_1 m_1, j_2 m_2 | j_3 - m_3 \rangle .$$ (E.3)

The reduced matrix element is defined implicitly by equation (E.2), and is symbolized by the double-bar $\langle \, || \, || \, \rangle$.

Appendix F

List of Publications and Conference Contributions

F.1 Publications

- W. Geithner, U. Georg, S. Kappertz, M. Keim, P. Lievens, R. Neugart, M. Neuroth, L. Vermeeren, S. Wilbert
  "Measurement of nuclear moments and radii by collinear laser spectroscopy and by beta -NMR spectroscopy."
  Hyperfine-Interactions (Netherlands), vol.129, no.1-4, p.271-88, 2000.

- B. Ittermann, M. Füllgrabe, M. Heemeier, F. Kroll, F. Mai, K. Marbach, P. Meier, D. Peters, G. Welker, W. Geithner, S. Kappertz, S. Wilbert, R. Neugart, P. Lievens, U. Georg, M. Keim
  "beta -NMR in II-VI semiconductors."
  Hyperfine-Interactions (Netherlands), vol.129, no.1-4, p.423-41, 2000.

- W. Geithner, K.M. Hilligsøe, S. Kappertz, G. Katko, M. Keim, S. Kloos, G. Kotrotsios, P. Lievens, K. Marinova, R. Neugart, L. Vermeeren, S. Wilbert:
  "Accurate isotope shift measurements on short-lived neon isotopes"
  APAC'99: Euroconference on atomic physics at accelerators – laser spectroscopy and applications, Mainz, Germany, 19.-24. September 1999
  Hyperfine Interactions (Netherlands), vol. 127, no. 1-4, p.117-120, 2000.

- B. Ittermann, M. Füllgrabe, M. Heemeier, F. Kroll, F. Mai, K. Marbach, P. Meier, D. Peters, H. Thiess, G. Welker, H. Ackermann, H.J. Stöckmann, W.D. Zeitz, W. Geithner, S.Kappertz, S. Wilbert, R. Neugart, P. Lievens, U. Georg, M. Keim:
  "Implanted light dopants in ZnSe"
  Hyperfine Interactions vol. 120-121, p.403-407, 1999.

- W. Geithner, S. Kappertz, R. Neugart, S. Wilbert, V. Sebastian, M. Keim, P. Lievens, L. Vermeeren, V.N. Fedoseyev, V.I. Mishin, U. Köoster:
  "Measurement of the magnetic moment of the one neutron halo nucleus ^{11}Be"
  Physical Review Letters, vol. 83, no. 19, p.3792-3725, 1999

- S. Kappertz, W. Geithner, G. Katko, M. Keim, G. Kotrotsios, P. Lievens, R. Neugart, L. Vermeeren, S. Wilbert:
  "Measurement of the magnetic moments of ^{7}Be and of the halo nucleus ^{11}Be"
  2nd International Conference on Exotic Nuclei and Atomic Masses, Bellaire, MI, USA, 23.-27. June 1998 / Edited by B.M. Sherill, D.J. Morrissey, J. David, C.N. Davids, AIP conference proceedings 455, p.110-113, 1998

- S. Wilbert, B.A. Brown, W. Geithner, U. Georg, S. Kappertz, M. Keim, P. Lievens, R. Neugart, M. Neuroth, L. Vermeeren:
  "β-NMR measurements of the nuclear quadrupole moments of $^{20,26-31}$Na"
  2nd International Conference on Exotic Nuclei and Atomic Masses, Bellaire, MI, USA, 23.-27. June 1998 / Edited by B.M. Sherill, D.J. Morrissey, J. David, C.N. Davids, AIP conference proceedings 455, p.142-145, 1998

F.2 Conference Contributions

Poster: W. Geithner, S. Franchoo, K.M. Hilligsøe, S. Kappertz, M. Keim, P. Lievens, K. Marinova, R. Neugart, H. Simon, L. Vermeeren, L. Weissman, S. Wilbert, and the ISOLDE collaboration
"Laser spectroscopy measurements of isotope shifts and nuclear moments of short-lived neon isotopes"
ENAM2001: 3rd international conference on exotic nuclei and atomic masses, Hämeenlinna, Finland, 2.-7. July 2001

Poster: W. Geithner, S. Kappertz, P. Lievens, K. Marinova, R. Neugart, and the ISOLDE collaboration
"Nuclear spin and moments of ^{73}Kr and odd-even staggering in the radii of light krypton isotopes"
ENAM2001: 3rd international conference on exotic nuclei and atomic masses, Hämeenlinna, Finland, 2.-7. July 2001

Poster: W. Geithner, K.M. Hilligsøe, S. Kappertz, M. Keim, P. Lievens, K. Marinova, R. Neugart, H. Simon, L. Vermeeren, S. Wilbert, the ISOLDE collaboration:
"Accurate Isotope Shift Measurements of Short-Lived Neon Isotopes",
Spring meeting of the German physical society (Deutsche Physikalische Gesellschaft – DPG), Berlin, April 2001.

Talk: W. Geithner, K.M. Hilligsøe, S. Kappertz, M. Keim, P. Lievens, K. Marinova, R. Neugart, H. Simon, L. Vermeeren, S. Wilbert, the ISOLDE collaboration:
"Das magnetische Moment von ^{17}Ne",
Spring meeting of the German physical society (Deutsche Physikalische Gesellschaft – DPG), Erlangen, March 2001.

Talk: W. Geithner, S. Kappertz, M. Keim, S. Kloos, P. Lievens, K. Marinova, R. Neugart, L. Vermeeren, S. Wilbert, the ISOLDE collaboration:

"Kernradien von $^{17-28}$Ne aus Messungen der Isotopieverschiebung",
Spring meeting of the German physical society (Deutsche Physikalische Gesellschaft – DPG), Dresden, March 2000.

Poster: W. Geithner, K.M. Hilligsøe, S. Kappertz, M. Keim, S. Kloos, P. Lievens, K. Marinova, R. Neugart, L. Vermeeren, S. Wilbert, the ISOLDE collaboration:
"Accurate isotope shift measurements on short-lived neon isotopes",
APAC'99: Euroconference on atomic physics at accelerators – laser spectroscopy and applications, Mainz, Germany, 19.-24. September 1999.

Talk: W. Geithner, S. Kappertz, M. Keim, G. Kotrotsios, P. Lievens, R. Neugart, L. Vermeeren, S. Wilbert, the ISOLDE collaboration:
"Messungen der Isotopieverschiebungen von $^{17-22}$Ne und des magnetischen Moments von ^{17}Ne",
Spring meeting of the German physical society (Deutsche Physikalische Gesellschaft – DPG), Freiburg, March 1999.

Talk: W. Geithner, S. Kappertz, M. Keim, G. Kotrotsios, P. Lievens, R. Neugart, L. Vermeeren, S. Wilbert, the ISOLDE collaboration:
"Kerneigenschaften aus den Isotopieverschiebungen und Hyperfeinstrukturen von $^{17-22}$Ne",
Spring meeting of the German physical society (Deutsche Physikalische Gesellschaft – DPG), Heidelberg, March 1999.

Talk: W.Geithner, M. Keim, S. Wilbert, S. Kappertz, R. Neugart, P. Lievens, L. Vermeeren, the ISOLDE collaboration:
"Isotopieverschiebung im lithiumähnlichen ^{7,9,10}Be$^+$ und das magnetische Moment von ^{7}Be",
Spring meeting of the German physical society (Deutsche Physikalische Gesellschaft – DPG), Konstanz, March 1998.

Bibliography

[Ami83] **Amin, S.**; Crossed-beam Spectroscopy of Neon: Precision Measurements if three ^{20}Ne Wavelengths; *J. Opt. Soc. Am.*; vol. 73(6); 1983; pp. 862–863.

[Ant78] **Anton, K.-R.; Kaufman, S.-L.; Klempt, W.; Neugart, R.; Otten, E.-W. and Schinzler-B.**; Narrowed optical lines observed in laser method for use with accelerated beams.; *Hyperfine Interact.*; vol. 4(1-2); 1978; pp. 87–90.

[Ari54] **Arima, A. and Horie, H.**; Configuration Mixing and Magnetic Moments of Nuclei; *Prog. Theor. Phys. (Japan)*; vol. 11; 1954; pp. 509–511.

[Ari78] **Arima, A.**; Nuclear Moments and Nuclear Structure; *Hyperfine Interact.*; vol. 4; 1978; pp. 151–164.

[Arn82] **Arnold, E.; Kühl, T.; Otten, E.-W. and von Reisky, L.**; Collinear laser spectroscopy of the Balmer-alpha line; *Phys. Lett. A*; vol. 90(8); 1982; pp. 399–401.

[Arn87] **Arnold, E.; Bonn, J.; Gegenwart, R.; Neu, W.; Neugart, R. Otten, E.; Wendt, K. and the ISOLDE Collaboration**; Nuclear Spin and Magnetic Moment of ^{11}Li; *Phys. Lett. B*; vol. 197(3); 1987; pp. 311–314.

[Arn92] **Arnold, E. et al.**; Quadrupole moment of ^{11}Li; *Phys. Lett. A*; vol. 281; 1992; pp. 16–19.

[Arn94] **Arnold, E. et al.**; The quadrupole moment of the neutron-halo nucleus ^{11}Li; *Z. Phys. A*; vol. 349; 1994; pp. 337–338.

[Aud93] **Audi, G. and Wapstra, A.**; The 1993 atomic mass evaluation; *Nucl. Phys. A*; vol. 565(1); 1993; pp. 1–27.

[Auf87] **Aufmuth, P.; Heilig, K. and Steudel, A.**; Changes in mean square charge radii from optical isotope shifts; *At. Data Nucl. Data Tables*; vol. 37(3); 1987; pp. 455–490.

[Bab63] **Babushkin, F.**; Isotope shift of spectral lines; *Soviet Physics JETP (USA)*; vol. 17; 1963; pp. 1118–1122.

[Bal] Balzers Hochvakuum GmbH; Postfach 437, CH-8037 Zürich; Product catalog 1996: Composants pour la technique du vide.

[Ban92] **Bang, J. and Thompson, I.**; Three body calculations for Li; *Phys. Lett. B*; vol. 279; 1992; pp. 201–206.

[Bar70]   **Barrett, R.**; *Phys. Lett. B*; vol. 33; 1970; p. 388.

[Bas97]   **Basar, G.; Basar, G.; Büttgenbach, S.; Kröger, S. and Kronfeldt, H.-D.**;
          Parametric investigation of the isotope shift in odd configurations of Ne I; *ZZ. Phys.
          D*; vol. 39; 1997; pp. 283–289.

[Bay89]   **Baye, D. and Descouvement, P.**; in Proceedings of the 5th International Con-
          ference in Clustering Aspects in Nuclear and Subnuclear Systems; vol. 58; Physical
          Society of Japan; 1989.

[Bel83]   **Belfrage, C.; Grafström, P.; Kröll, S. and Svanberg, S.**; Doppler-Free Laser
          Spectroscopy Measurement on a Ne Discharge for Determination of ^{22}Ne-^{20}Ne Iso-
          tope Shift; *Phys. Scripta*; vol. 27; 1983; pp. 367–370.

[Boh50]   **Bohr, A. and Weisskopf, V.**; The Influence of Nuclear Structure on the Hyperfine
          Structure of Heavy Elements; *Phys. Rev.*; vol. 77; 1950; pp. 94–98.

[Boh53]   **Bohr, A. and Mottelson, B.**; *Matematisk-fysiske meddelelser Kongelige Danske
          Videnskabernes Selskab*; vol. 27(16); 1953; p. 1.

[Boh75]   **Bohr, A. and Mottelson, B.**; Nuclear Structure (Nuclear Deformations); vol. 2;
          World Scientific (Singapore, New Jersey, London, Hong Kong); reprint 1998 edn.;
          1975.

[Bor89a] **Borchers, W.**; Kernstrukturuntersuchungen an Xenon- und Radon-Isotopen mit
          Hilfe einer neuen Nachweistechnik für die kollineare Laserspektroskopie; Ph.D. thesis;
          Institut für Physik, Johannes Gutenberg Universität Mainz; Staudingerweg 7, 55128
          Mainz; 1989.

[Bor89b] **Borchers, W.; Arnold, E.; Neu, W.; Neugart, R. and Wendt, K.**; Xenon
          Isotopes far from Stability Studied by Collisional Ionization Laser Spectroscopy;
          Phys. Lett. B; vol. 216(1); 1989; pp. 7–10.

[Bra83]   **Bransden, B. and Joachain, C.**; Physics of atoms and moleculs; Longman Sci-
          entific & Technical; reprint 1995 edn.; 1983.

[Bre33]   **Breit, G. and Wills, L.**; Hyperfine Structure in Intermediate Coupling; *Phys.
          Rev.*; vol. 44; 1933; pp. 470–490.

[Bro82]   **Brown, B.; Wildenthal, B.; Chung, W.; Massen, S.; Bernas, M.; Bern-
          stein, A. and Miskimen, R.**; Isovector $E2$ matrix elements from electromagnetic
          transitions in the $s-d$ shell: Experiment and shell-model calculations; *Phys. Rev.
          C*; vol. 26(5); 1982; pp. 2247–2272.

[Bro87]   **Brown, B. and Wildenthal, B.**; Empirically optimum M1 operator for sd shell
          nuclei; *Nucl. Phys. A*; vol. 474; 1987; pp. 290–306.

[Bro88a] **Brown, B.; Richter, W.; Julies, R. and Wildenthal, B.**; Semi-empirical
          effective interactions for the 1s-0d shell; *Annals of Physics*; vol. 182; 1988; pp. 191–
          236.

[Bro88b] **Brown, B. and Wildenthal, B.**; Status of the nuclear shell-model; *Ann. Rev. Nucl. Part. Sci.*; vol. 38; 1988; pp. 29–66.

[Bro89] **Brown, I.**; The Physics and Technology of Ion Sources; John Wiley and Sons; 1989.

[Bro98a] **Brown, B.**; New Skyrme interaction for normal and exotic nuclei; *Phys. Rev. C*; vol. 58(1); 1998; pp. 220–231.

[Bro98b] **Brown, B.**; The Structure of Light Nuclei; in Proceedings of 4th Course of the International School of Heavy Ion Physics. Exotic Nuclei, Erice, Italy, 11-20 May 1997; 1998.

[Bro01a] **Brown, B.**; The nuclear shell-model towards the drip lines; *Prog. Part. Nucl. Phys.*; vol. 47; 2001; pp. 517–599.

[Bro01b] **Brown, B.**; Shell-model values of selected electromagnetic nuclear moments; 2001; Private Communication.

[Buc75] **Buck, B.; Dover, C. and Vary, J.**; Simple potential model for cluster states in light nuclei; *Phys. Rev. C*; vol. 11(5); 1975; pp. 1803–1821.

[Buc95] **Buck, B.; Merchant, A. and Perez, S.**; Systematics of alpha-cluster states above double shell closures; *Phys. Rev. C*; vol. 51(2); 1995; pp. 559–565.

[Büt84] **Büttgenbach, S.**; Magnetic Hyperfine Anomalies; *Hyperfine Interact.*; vol. 20; 1984; pp. 1–64.

[Cam75] **Campi, X.; Flocard, H.; Kerman, A. and Koonin, S.**; Shape transition in the neutron rich sodium isotopes; *Nucl. Phys. A*; vol. 251; 1975; pp. 193–205.

[Car86] **Carchidi, M.; B.H., W. and Brown, B.**; Quadrupole moments of sd shell nuclei; *Phys. Rev. C*; vol. 34(6); 1986; pp. 2280–2297.

[Cau98] **Caurier, E.; Nowacki, F.; Poves, A. and Retamosa, J.**; Shell-model study of the neutron rich isotopes from oxygen to silicon; *Phys. Rev. C*; vol. 58(4); 1998; pp. 2033–2040.

[Cau01] **Caurier, E.; Nowacki, F. and Poves, A.**; Shell-model studies of neutron-rich nuclei; *Nucl. Phys. A*; vol. 693; 2001; pp. 374–382.

[Chu96] **Chulkov, L. et al.**; Interaction cross sections and matter radii of A=20 isobars; *Nucl. Phys. A*; vol. 603(2); 1996; pp. 219–237.

[Coh] Coherent Laser Division; 3210 Porter Drive, Palo Alto, California 94304; Coherent CR-699 Ring Dye Laser Manual.

[Cra49] **Crawford, M. and Schawlow, A.**; Electron-Nuclear Potential Fields from Hyperfine Structure; *Phys. Rev.*; vol. 76; 1949; pp. 1310–1317.

[Del76] **Delsart, C. and Keller, J.**; Hyperfine structure in ^{21}Ne using laser-induced absorption line narrowing.; *Opt. Comm.*; vol. 16(3); 1976; pp. 388–391.

[Dem98] **Demtröder, W.**; Laser Spectroscopy; Springer (Berlin, Heidelber, New York); 2nd edn.; 1998.

[Det79] **Detraz, C. et al.**; Beta decay of Na and their descendants; *Phys. Rev. C*; vol. 19(1); 1979; pp. 164–176.

[Dob68] **Dobson, D. and Brown, S.**; Nuclear Magnetic Moment of Ne^{23}; *Bull. Am. Phys. Soc.*; vol. 13; 1968; p. 173.

[Duc72] **Ducas, T.; Feld, M.; Ryan Jr., L.; Skribanowitz, N. and Javan, A.**; Hyperfine Structure of Excited States and Quadrupole Moment of ^{21}Ne Using Laser-Induced Line-Narrowing Techniques; *Phys. Rev. A*; vol. 5; 1972; pp. 1036–1043.

[Duf76] **Dufay, M.; Carré, M.; Gaillard, M.; Meunier, G.; Winter, H. and Zgainski, A.**; High-Resolution Studies in Ion Beams with Laser-Induced Resonances; *Phys. Rev. Lett.*; vol. 37(25); 1976; pp. 1678–1681.

[Duf96] **Dufour, M.; Descouvement, P. and Baye, D.**; Microscopic description of the $\alpha+^{16}$O system in a multicluster model; *Phys. Rev. C*; vol. 50(2); 1996; pp. 795–801.

[Eng74] **Engfer, R.; Schneuwly, H.; Vuilleumier, J.; Walter, H. and Zehnder, A.**; Charge-distribution parameters, isotope shifts, isomer shifts, and magnetic constants from muonic atoms; *At. Data Nucl. Data Tables*; vol. 14; 1974; pp. 509–597.

[Fed93] **Fedorov, D.; Jensen, A. and Riisager, K.**; General properties of halos; *Phys. Lett. B*; vol. 312; 1993; pp. 1–5.

[Fer33] **Fermi, E. and Segrè, E.**; Zur Theorie der Hyperfeinstruktur; *ZZ. Phys.*; vol. 82; 1933; pp. 729–749.

[Fia92] **Fiander, D. and Fowler, A.**; A 60 kV modulator for the target voltage of an on-line isotope separator; in 20th Power Modulator Symposium; Myrtle Beach South Carolina, USA, 23-25 June 1992; 1992.

[Fie89] **Field, D. and Gray, M.**; Kinematic compression and expansion of the velocity distributions of particles and gas flows; *Phys. Rev. A*; vol. 40(4); 1989; pp. 1976–1982.

[Fir96] **Firestone, R. and Shirley, V.**; Table of the Isotopes, 8th edition; John Wiley & Sons; 1996.

[For01] **Fortune, H. and Sherr, R.**; Structure of ^{17}Ne ground state; *Phys. Lett. B*; vol. 503; 2001; pp. 70–72.

[Fri95] **Fricke, G.; Berhardt, C.; Heilig, K.; Schaller, L.; Schellenberg, L.; Shera, E. and De Jager, C.**; Nuclear Ground State Charge Radii from Electromagnetic Interactions; *At. Data Nucl. Data Tables*; vol. 60(2); 1995; pp. 178–285.

[Fuk91] **Fukuda, M. et al.**; Neutron halo in ^{11}Be studied via reaction cross sections; *Phys. Lett. B*; vol. 268(3-4); 1991; pp. 339–344.

[Gei00] **Geithner, W. et al.**; Measurements of Moments and Radii of light Nuclei by Collinear Fast-Beam Laser Spectroscopy and β-NMR; 2000.

[Geo90] **Georg, U.**; Untersuchungen zum Stoßionisations-Nachweis bei kollinearer Laserspektroskopie am Xenon; Master's thesis; Institut für Physik, Johannes Gutenberg Universität; Staudingerweg 7, 55128 Mainz; 1990.

[Gor01] **Goriely, S.; Tondeur, F. and Pearson, J.**; A Hartree-Fock nuclear mass table; *At. Data Nucl. Data Tables*; vol. 77; 2001; pp. 311–381.

[Göt02] **Götte, S.**; Die thermische Breite von Linienformen bei kollinearer Laserspektroskopie; 2002; Private Communication.

[Gre96] **Greiner, W. and Maruhn, J.**; Nuclear Models; Springer (Berlin, Heidelberg, New York); 1996.

[Gro58] **Grosof, G.; Buck, P.; Lichten, W. and Rabi, I.**; Quadrupole moment of Ne^{21}; *Phys. Rev. Lett.*; vol. 1(6); 1958; pp. 214–215.

[Gui84] **Guillemaud-Mueller, D. et al.**; β-decay schemes of very neutron-rich sodium isotopes and their descendants; *Nucl. Phys. A*; vol. 426(1); 1984; pp. 37–76.

[Gui95] **Guimaraes, V. et al.**; Structure of light proton-rich nuclei near the drip-line; *Nucl. Phys. A*; vol. 588; 1995; pp. 161c–164c.

[Gut94] **Guthörlein, G. and Windholz, L.**; Optogalvanic spectroscopy – a useful tool in atomic and plasma physics; *Journal of Optics Research*; vol. 2(3/4); 1994; pp. 171–187.

[Han87] **Hansen, P. and Jonson, B.**; The neutron Halo of Extremely Neutron-Rich Nuclei; *EuroPhys. Lett.*; vol. 4(4); 1987; pp. 409–414.

[Han95] **Hansen, P.; Jensen, A. and Jonson, B.**; Nuclear Halos; *Ann. Rev. Nucl. Part. Sci.*; vol. 45; 1995; pp. 591–634.

[Hey94] **Heyde, K.**; The Nuclear Shell-Model; Springer (Berlin, Heidelberg, New York); 1994.

[Hil53] **Hill, D. and Wheeler, J.**; *Phys. Rev.*; vol. 89; 1953; p. 1102.

[Hub78] **Huber, G. et al.**; Spins, magnetic moments, and isotope shifts of $^{21-31}$Na by high resolution laser spectroscopy of the atomic D_1 line; *Phys. Rev. C*; vol. 18(5); 1978; pp. 2342–2354; rapid communication.

[Huh98] **Huhta, M. et al.**; Anomalous p-shell isoscalar magnetic moment: remeasurement of ^{9}C and the influence of isospin nonconservation; *Phys. Rev. C*; vol. 57(6); 1998; pp. R2790–R2793; rapid communication.

[Hus78] **Husson, X. and Grandin, J.**; Hyperfine structure in the $2p^5 3p$ configuration of ^{21}Ne; *J. Phys. B*; vol. 11(8); 1978; pp. 1393–1398.

[Hyt]   Hytec Electronics Ltd.; 5 Cradock Road, Reading, Berkshire, RG2 0JT, England; Manual: DAC 670 MK2 CAMAC opto isolated dual 18 Bit.

[Jac83]   **Jackson, D.**; Klassische Elektrodynamik; Walter de Gruyter (Berlin, New York); 2nd edn.; 1983.

[Jam75]   **James, F. and Roos, M.**; MINUIT – a system for function minimization and analysis of the parameter errors and correlations; *Comp. Phys. Comm.*; vol. 10(6); 1975; pp. 343–367.

[Jen01]   **Jensen, A.; Garrido, E.; Riisager, K. and Fedorov, D.**; Survey of halos: Structure, occurrence conditions, and high energy breakup reaction mechanisms; *RIKEN Rev.*; vol. 39; 2001; pp. 3–10.

[Joh90]   **Johannsen, L.; Jensen, A. and Hansen, P.**; The Li nucleus as a three-body system; *Phys. Lett. B*; vol. 244; 1990; pp. 357–356.

[Jon01]   **Jonson, B.**; On the physics of halo nuclei; *Nucl. Phys. A*; vol. 690(1-3); 2001; pp. 151–162.

[Jul]   Julie Research Laboratories, Inc.; 211 West 61st Street, New York, N.Y. 10023; Manual: Instruction manual model KV-10R voltage divider.

[Jun82]   **Juncar, P. and Pinard, J.**; Instrument to measure wave numbers of CW and pulsed laser lines: the sigmameter; *Rev. Sci. Inst.*; vol. 53(7); 1982; pp. 939–948.

[Kau76]   **Kaufman, S.**; High-resolution laser spectroscopy in fast beam; *Opt. Comm.*; vol. 17(3); 1976; pp. 309–312.

[Kei95]   **Keim, M. et al.**; Laser spectroscopy measurements of $^{72-96}$Kr spins, moments and charge radii; *Nucl. Phys. A*; vol. 586; 1995; pp. 219–239.

[Kei00]   **Keim, M. et al.**; Measurement of the electric quadrupole moments of $^{26-29}$Na; *European Physical Journal A*; vol. 8(1); 2000; pp. 31–40.

[Kep]   Kepco, Inc.; 131-38 Sanford Ave., Flushing, NY 11352, USA; Manual: Kepco Model BOP 500M instruction manual.

[Kin84]   **King, W.**; Isotope Shifts in Atomic Spectra; Plenum Press – New York and London; 1984.

[Kit97]   **Kitagawa, H.; Tajima, N. and Sagawa, H.**; Reaction cross sections and radii of A=17 and A=20 isobars; *Z. Phys. A*; vol. 358; 1997; pp. 381–387.

[Kle95]   **Klein, A.**; Bestimmung von Kernmomenten und -radien kurzlebiger Argon-Isotope durch kollineare Laserspektroskopie mit hochempfindlichem Radioaktivitätsnachweis; Ph.D. thesis; Institut für Physik, Johannes Gutenberg Universität Mainz; Staudingerweg 7, 55128 Mainz; 1995.

[Kle96] **Klein, A. et al.**; Moments and mean square charge radii of short-lived argon iso-
         topes; *Nucl. Phys. A*; vol. 607; 1996; pp. 1–22.

[Klu74] **Kluge, H. and Sauter, H.**; Levelcrossing Experiments in the First Excited $^1P_1$
         States of the Alkaline Earth; *ZZ. Phys.*; vol. 270; 1974; pp. 295–309.

[Kon92] **Konz, E.; Kraft, T. and Rubahn, H.-G.**; Optical determination of the ^{20,22}Ne
         3s-3p specific mass shift; *Applied Optics*; vol. 31(24); 1992; pp. 4995–4997.

[Kop58] **Kopfermann, H. and Schneider, E.**; Nuclear Moments; Academic Press Inc. –
         New York; 1958.

[Kot99] **Kotrotsios, G.**; Laserspektroskopie-Untersuchungen an stabilen Neon-Isotopen;
         Master's thesis; Institut für Physik, Johannes Gutenberg Universität; Staudingerweg
         7, 55128 Mainz; 1999.

[Kug93] **Kugler, E.**; The ISOLDE Facility at the CERN PS Booster; *Nucl. Inst. Meth. in
         Physics Research B*; vol. 79; 1993; pp. 322–325.

[Kum72] **Kumar, K.**; Intrinsic Quadrupole Moments and Shapes of Nuclear Ground States
         and Excited States; *Phys. Rev. Lett.*; vol. 28; 1972; pp. 249–253.

[Kuo66] **Kuo, T. and Brown, G.**; *Nucl. Phys.*; vol. 85; 1966; p. 40.

[Kuo67] **Kuo, T.**; *Nucl. Phys. A*; vol. 103; 1967; p. 71.

[Lal97] **Lalazissis, G.; König; D. and Ring, P.**; New parameterization for the La-
         grangian density of the relativistic mean field theory; *Phys. Rev. C*; vol. 55(1); 1997;
         pp. 540–543.

[Lal99] **Lalazissis, G.; Raman, S.; D. and Ring, P.**; Ground-state properties of even-
         even nuclei in the relativistic mean-field theory; *At. Data Nucl. Data Tables*; vol. 71;
         1999; pp. 1–40.

[Ley]   Leybold Vakuum GmbH; Bonner Strasse 498, D-50968 Köln; Das Gasreibungsvaku-
         ummeter VISCOVAC VM 211.

[Lid00] **Lide, D.** (Editor); CRC Handbook of Chemistry and Physics; CRC Press, New
         York; 81st edn.; 2000.

[Lie96] **Lievens, P. et al.**; On the odd-even staggering of mean-square charge radii in the
         light krypton region; *EuroPhys. Lett.*; vol. 33(1); 1996; pp. 11–16.

[LT57]   **La Tourrette, J.; Quinn, W. and Ramsey, N.**; Magnetic Moment of ^{21}Ne;
         Phys. Rev.; vol. 107; 1957; p. 1202.

[Mac82] **MacArthur, D.; Calaprice, F.; Hallin, A.; Schneider, M. and Schreiber,
         D.**; Nuclear magnetic moment of ^{1}9Ne with possible applications to other radioactive
         gas isotopes; *Phys. Rev. C*; vol. 26(4); 1982; pp. 1753–1756.

[May49] **Mayer, M.**; On Closed Shells in Nuclei II; *Phys. Rev.*; vol. 75; 1949; pp. 1969–1970.

[May55] **Mayer, M. and Jensen, J.**; Elementary Theory of Nuclear Shell Structure; Whiley (New York); 1955.

[Mel] Melles Griot; Lilienthalstrasse 30-32, D-64625 Bensheim; Melles Griot Product Catalog 1996: Optics, Opto-Mechanics, Lasers, Instruments.

[Mil97] **Millener, D.**; First-forbidden β decay of ^{17}N and ^{17}Ne; *Phys. Rev. C*; vol. 55(4); 1997; pp. R1633–R1636.

[Min92] **Minamisono, T. et al.**; Proton halo of ^{8}B disclosed by its giant quadrupole moment; *Phys. Rev. Lett.*; vol. 69(14); 1992; pp. 2058–2061.

[Miz01] **Mizusaki, T.; Otsuka, T.; Honma, M. and Brown, B.**; Spherical-deformed shape coexistence for the fp shell in the nuclear shell-model; *Phys. Rev. C*; vol. 63(044306); 2001.

[Moh98] **Mohr, P. and Taylor, B.**; CODATA Recommended Values of the Fundamental Physical Constants: 1998; *Journal of Physical and Chemical Reference Data (USA)*; vol. 28(6); 1998; pp. 1713–1852.

[Möl95] **Möller, P.; Nix, J.; Myers, W. and Swiatecki, W.**; Nuclear ground-state masses and deformations; *At. Data Nucl. Data Tables*; vol. 59; 1995; pp. 185–381.

[Moo71] **Moore, C.**; Atomic Energy Levels Vol. III, NSRDS-NBS 35; National Bureau of Standards (U.S.); 1971.

[Mue83] **Mueller, A. et al.**; Spins, moments and charge radii of Barium isotopes in the range $^{122-146}$Ba determined by collinear fast-beam laser spectroscopy; *Nucl. Phys. A*; vol. 403; 1983; pp. 243–262.

[Mye74] **Myers, W. and Swiatecki, W.**; The Nuclear Droplet Model for Arbitrary Shapes; *Annals of Physics*; vol. 84; 1974; pp. 186–210.

[Mye83] **Myers, W. and Schmidt, K.-H.**; An update on droplet-model charge distributions; *Nucl. Phys. A*; vol. 410; 1983; pp. 61–73.

[Mye87] **Myers, W. and Rozmej, P.**; The Contribution of Collective Zero-Point Motion to Mean-Square Charge Radii; *Nucl. Phys. A*; vol. 470; 1987; pp. 107–118.

[Neu77] **Neugart, R.; Kaufman, S.; Klempt, W.; Moruzzi, G.; Otten, E.-W. and Schinzler, B.**; High-resolution spectroscopy in fast atomic beams.; vol. III of *Laser Spectroscopy*; Jackson Lake Lodge, WY, USA, 4-8 July 1977; 1977.

[Neu81] **Neugart, R.**; Laser Spectroscopy on Mass-Separated Radioactive Beams; *Nucl. Inst. Meth. in Physics Research*; vol. 186(1-2); 1981; pp. 165–175.

[Neu86] **Neugart, R.; Klempt, W. and Wendt, K.**; Collisional Ionization as a Sensitive Detection Scheme in Collinear Laser-Fast-Beam Spectroscopy; *Nucl. Inst. Meth. in Physics Research B*; vol. 17; 1986; pp. 354–359.

[Neu88] **Neugart, R.**; Nuclear Moments From Laser Spectroscopy; *Hyperfine Interact.*; vol. 43; 1988; pp. 441–456.

[Nil55] **Nilsson, S.**; *Matematisk-fysiske meddelelser Kongelige Danske Videnskabernes Selskab*; vol. 29(16); 1955; p. 68.

[NIS99] **NIST – National Institute of Standards and Technology**; NIST Standard Reference Database #78 – Atomic Spectra Database; Online in the Internet: http://physics.nist.gov/cgi-bin/AtData/main_asd; 1999.

[Noy59] **Noya, H.; Arima, A. and Horie, H.**; Nuclear Moments and Configuration Mixing; *Prog. Theor. Phys. supplement (Japan)*; vol. 8; 1959; pp. 33–112.

[Odi65] **Odintsov, V.**; Isotopic Shift in the Spectrum of Neon; *Optics and Spectroscopy*; vol. 18(3); 1965; pp. 205–206.

[Ott77] **Otten, E.**; Hyperfine and isotope shift measurements far off stability by optical pumping; in Atomic Physics; vol. 5; 1977.

[Ott89] **Otten, E.**; Nuclear Radii and moments of unstable isotopes; in Treatise on heavy-ion science, (Edited by **Bromley, D.**); vol. 8; Plenum Publishing Corporation; 1989; pp. 517–638.

[Oza94] **Ozawa, A. et al.**; Interaction cross sections and radii of the mass number A=17 isobar (^{17}N, ^{17}F and ^{17}Ne); *Phys. Lett. B*; vol. 334; 1994; pp. 18–22.

[Oza00] **Ozawa, A.; Kobayashi, T.; Suzuki, T.; Yoshida, K. and Tanihata, I.**; New Magic Number $N = 16$, near the Neutron Drip Line; *Phys. Rev. Lett.*; vol. 84(24); 2000; pp. 5493–5495.

[Pou82] **Poulsen, O.**; Velocity and high voltage measurements using resonant collinear, fast-beam / laser interactions; *Nucl. Inst. Meth.*; vol. 202; 1982; pp. 503–509.

[Pov94] **Poves, A. and Retamosa, J.**; Theoretical study of the very neutron-rich nuclei around $N = 20$; *Nucl. Phys. A*; vol. 571; 1994; pp. 221–241.

[PRE] PREMA Präzisionselektronik GmbH; Robert Bosch Strasse 6, 55129 Mainz, Germany; Manual: 6040 integrierendes Präzisionsmultimeter.

[Pri99] **Pritychenko, B.; Glasmacher, T.; Cottle, P. and Fauerbach, M.**; Role of intruder configurations in ^{26,28}Ne and ^{30,32}Mg; *Phys. Lett. B*; vol. 461; 1999; pp. 322–328.

[Rac42] **Racah, G.**; On a New Type of Vector Coupling in Complex Spectra; *Phys. Rev.*; vol. 61; 1942; p. 537.

[Rag89] **Raghavan, P.**; Table of nuclear moments; *At. Data Nucl. Data Tables*; vol. 42(2); 1989; pp. 190–209 (last missing).

[Ram01] **Raman, S.; Nestor, C. and Tikkanen, P.**; Transition Probabilities, $B(E2)$, from the Ground to the first-excited 2^+ State of even-even nuclides; *At. Data Nucl. Data Tables*; vol. 78; 2001; pp. 1–128.

[Rei01] **Reinhard, P.; Bender, M.; Buervenich, T.; Reiss, C.; Maruhn, J. and Greiner, W.**; Nuclear charge radii of neon isotopes by relativistic mean field model; 2001; Private Communication.

[Ric91] **Richter, W.; van der Merwe, M.; Julies, R. and Brown, B.**; New effective interactions for the 0f1p shell; *Nucl. Phys. A*; vol. 523; 1991; pp. 325–353.

[Rin80] **Ring, P. and Schuck, P.**; The Nuclear Many-Body Problem; Springer (Berlin, Heidelberg, New York); 2nd edn.; 1980.

[Ros32] **Rosenthal, E. and Breit, G.**; The Isotope Shift in Hyperfine Structure; *Phys. Rev.*; vol. 41; 1932; pp. 459–470.

[Sag84] **Sagawa, H. and Brown, B.**; E2 core polarization for *sd* shell single-particle states calculated with a Skyrme-type interaction; *Nucl. Phys. A*; vol. 430(1); 1984; pp. 84–98.

[Sak95] **Sakurai, J.**; Modern Quantum Mechanics; Addison-Wesley; rev. edn.; 1995.

[Sch]   Schott Glaswerke; Schott Glaswerke, P.O. Box 2480, D-55014 Mainz, Germany; Optical Glas Filters, Cat. Nr.: 3555.

[Sch55] **Schwartz, C.**; Theory of the hyperfine structure; *Phys. Rev.*; vol. 97(2); 1955; pp. 380–403.

[Sch95] **Schwab, W. et al.**; Theory of the hyperfine structure; *Phys. Rev.*; vol. 97(2); 1995; pp. 380–403.

[Sem64] **Semenov, R. and Strugach, B.**; The possibility of determining intermediate coupling coefficients from experimental spectra; *J. Opt. Soc. Am.*; vol. XXX(XXX); 1964; pp. 428–430.

[Sha63] **de Shalit, A. and Talmi, I.**; Nuclear Shell Theory; Academic Press (New York, London); 1963.

[Shi74] **Shimizu, K.; Ichimura, M. and Arima, A.**; Magentic moments and GT-type β-decat matix elements in nuclei with a *LS* doubly closed shell plus or minus one nucleon; *Nucl. Phys. A*; vol. 226; 1974; pp. 282–318.

[Sii99] **Siiskonen, T. and Lipas, P.**; Shell-model and Hartree-Fock calculations for even-mass O,Ne, and Mg nuclei; *Phys. Rev. C*; vol. 60(034312); 1999; pp. 1–5; electronic paper.

[Ste51] **Sternheimer, R.**; On Nuclear Quadrupole Moments; *Phys. Rev.*; vol. 84(2); 1951; pp. 244–253.

[Sto01] **Stone, N.**; Table of nuclear magnetic dipole and electric quadrupole moments; 2001; Oxford Physics Preprint(Clarendon Laboratory).

[Sug73] **Sugimoto, K.**; Nuclear Moments of Conjugate Nuclei; in Proceedings of the International Conference on Nuclear Moments and Nuclear Structure, 1972; vol. 1973 of *J. Phys. Soc. Japan*; The Physical Society of Japan; 1973.

[Tan85] **Tanihata, I. et al.**; Measurements of interaction cross sections and nuclear radii in the light *p*-shell region; *Phys. Rev. Lett.*; vol. 55; 1985; pp. 2676–2679.

[Tan90] **Tanihata, I.**; Neutron halos and exotic modes; *Nucl. Phys. A*; vol. 520; 1990; pp. 411–425.

[Tan01] **Tanihata, I.**; Nuclear Radii and Change in Shell Structure: A Halo Driven New Magic Number N=16; *Nucl. Phys. A*; vol. 682; 2001; pp. 114c–123c.

[Thi75] **Thibault, C.; Klapisch, R.; Rigaud, C.; Poskanzer, A.; Prieels, R.; Lessard, L. and Reisdorf, W.**; Direct measurement of the masses of Li and Na with an on-line mass spectrometer; *Phys. Rev. C*; vol. 12(2); 1975; pp. 644–657.

[Tim96] **Timofeyuk, N.; Descouvemont and Baye, D.**; Microscopic calculation of ^{17}Ne and ^{17}N properties in a three-cluster generator-coordinate method; *Nucl. Phys. A*; vol. 600; 1996; pp. 1–19.

[Tou82] **de Tourreil, R. and Sprung, D.**; Super-soft-core nucleon-nucleon interaction with π-, ρ- and ω-exchange contributions; *Nucl. Phys. A*; vol. 242; 1982; pp. 445–460.

[Uen96] **Ueno, H. et al.**; Magnetic moments of ^{17}N and ^{17}B; *Phys. Rev. C*; vol. 53(5); 1996; pp. 2142–2151.

[Uts99] **Utsuno, Y.; Otsuka, T.; Mizusaki, T. and Honma, M.**; Varying shell gap and deformation in $N \sim 20$ unstable nuclei studied by the Monte Carlo shell-model; *Phys. Rev. C*; vol. 60(054315); 1999; pp. 1–8.

[Vee02] **Veeco Applied EPI**; Vapor Pressure Data for Selected Elements; Online in the Internet: http://www.epimbe.com/pages/vp_data.htm; 2002.

[Ver92] **Vermeeren, L.; Silverans, R.; Lievens, P.; Klein, A.; Neugart, R.; Schulz, C. and Buchinger, F.**; Ultrasensitive Radioactive Detection of Collinear-Laser Optical Pumping: Measurements of Nuclear Charge Radius of ^{50}Ca; *Phys. Rev. Lett.*; vol. 68(11); 1992; pp. 1679–1682.

[Ves85] **Veseth, L.**; Many-body calculations of atomic isotope shifts; *J. Phys. B*; vol. 18; 1985; pp. 3463–3480.

[War92a] **Warburton, E. and Brown, B.**; Effective interactions for the $0p1s0d$ shell-model space; *Phys. Rev. C*; vol. 46(3); 1992; pp. 923–944.

[War92b] **Warburton, E.; Brown, B. and Millener, D.**; Large-basis shell-model treatment of $A = 16$; *Phys. Lett. B*; vol. 293(1-2); 1992; pp. 7–12.

[Wik78] **Wik, T. and Bennett, S.**; Doppler-free, linear, single photon spectroscopy of metastable atoms and molecules; *Phys. Rev. Lett.*; vol. 40(16); 1978; pp. 1080–1083.

[Wil79] **Wildenthal, B. and Chung, W.**; Implications of experimental magnetic moment values in light nuclei for the presence and characteristics of mesonic exchange currents; in Mesons in nuclei, (Edited by **Rho, M. and Wilkinson, D.**); North Holland (Amsterdam, New York, Oxford); 1979; pp. 721–753.

[Wil84] **Wildenthal, B.**; Empirical strengths of spin operators in nuclei; in Prog. Part. Nucl. Phys., (Edited by **Wilkinson, D.**); vol. 11; Pergamon Press (Oxford); 1984; p. 5.

[Win76] **Wing, W.; Ruff, G.; Lamb, W. and Spezeski, J.**; Observation of the Infrared Spectrum of the Hydrogen Molecular Ion MD^+; *Phys. Rev. Lett.*; vol. 36(25); 1976; pp. 1488–1491.

[Wol] **Wolf, B.**; Ion temperature of ions in a typical rf plasma ion source; Private Communication.

[Wol32] **Wolfe, H.**; Multiplet Splitting and Intensities of Intercombination Lines Part I; *Phys. Rev.*; vol. 41; 1932; pp. 443–458.

[Zha87] **Zhao, P.**; High-precision measurement of ^{20}Ne and ^{22}Ne transitions; *J. Opt. Soc. Am. B*; vol. 4(5); 1987; pp. 644–647.

[Zhu93] **Zhukov, M.; Danilin, B.; Fedorov, D.; Bang, J.; Thompson, I. and Vaagen, J.**; Bound state properties of Borromean halo nuclei: He and Li; *Physics Reports*; vol. 231(4); 1993; pp. 151–199.

[Zhu95] **Zhukov, M. and Thompson, I.**; Existence of proton halos near the drip line; *Phys. Rev. C*; vol. 52(6); 1995; pp. 3505–3508.

Lebenslauf

1. Persönliche Daten

Name:	Ralf <u>Wolfgang</u> Geithner
Geburtsdatum:	22.08.1969 in Mainz / Deutschland
Adresse:	An der Allee 81
	D-55122 Mainz
Nationalität:	Deutsch
Familienstand:	Ledig

2. Schulausbildung

Gymnasium:

<u>Juli 1986 - Mai 1989:</u>   Staatliches Gymnasium Mainz Gonsenheim
Leistungsfächer:
Mathematik, Physik, Erdkunde,
Englisch (mündl. Prüfungsfach)

<u>Mai 1989:</u>   Beendigung des Gymnasiums mit Abschluss
Abitur

3. Wehrdienst:

<u>06.06.1989 – 31.08.1990:</u>   Diez/Lahn

4. Universitätsausbildung

Diplomstudien:

<u>Oktober 1990 - November 1996:</u>   Physik Johannes Gutenberg-Universität Mainz

<u>23.09.1992:</u>   Abschluss Vordiplom-Prüfungen

<u>Juni 1995 - September 1996:</u>   Diplomarbeit in der Gruppe von Prof. R. Neugart,
Thema:
"Untersuchungen zum Transfer von Cäsiumionen
in eine magneto-optische Falle".

<u>29.11.1996:</u>   Beendigung des Physik-Studiums
mit Ablegen der Diplom-Hauptprüfung.

Doktorarbeit:

<u>Januar 1997:</u>   Beginn mit der Doktorarbeit mit kernphysi-
kalischer Themenstellung in der Gruppe
von Prof. R. Neugart,
Thema:
"Nuclear spins, moments and radii of short lived
neon isotopes by collinear laser spectroscopy."

Zweite Phase der Doktorarbeit:

<u>April 1999:</u>   Migration nach Genf (Schweiz) als Koordinator
für die Experimente der Gruppe unter
Prof. Neugart. Fortsetzung der Studien
an radioaktiven Neon-Isotopen.

<u>21.08.2002:</u>   Abschluss der Promotion mit Ablegen der
mündlichen Doktorprüfung.

Sonstige universitäre Studien:

Oktober 1991 - April 1992:   einführende Studien in Geographie und Spanisch